THE UNIVERSITY OF OKLAHOMA

GRADUATE COLLEGE

IN-SITU STRESS DETERMINATION IN POROUS FORMATION

A Dissertation

SUBMITTED TO THE GRADUATE FACULTY

in partial fulfillment of the requirements for the

degree of

DOCTOR OF PHILOSOPHY

By

MAURO BLOCH

Norman, Oklahoma

1999

UMI Number: 9943698

UMI®

UMI Microform 9949698

Bell & Howell Information and Learning Company
300 North Zeeb Road
P.O. Box 1346
Ann Arbor, MI 48106-1346

IN-SITU STRESS DETERMINATION IN POROUS FORMATION

A DISSERTATION APPROVED

FOR THE SCHOOL OF PETROLEUM AND GEOLOGICAL ENGINEERING

BY

James Forgotson Jr.

To my Family.

Acknowledgments

I would like to express my appreciation to my advisor Dr. Jean-Claude Roegiers and to Dr. Lizengh Cui for their help and suggestions in conducting the research work for this dissertation. Thanks are also due to other members of my advisory committee: Dr. Faruk Civan, Dr. James Forgotson, Dr. Anuj Gupta, and Dr. Roy Knapp for sharing with me their rich professional experience, to the members of the Rock Mechanics Institute at the University of Oklahoma, and to my colleagues at the University of Oklahoma and Petrobras' Research Center in Brazil – CENPES.

Special thanks to Cezar A.S. Monteiro, for the endless technical discussions and friendly support.

Finally, thanks to Petrobras from financial support, which made this work possible, and to the CENPES management, for their constant confidence in my technical capabilities.

Contents

List of Figures

List of Tables

Abstract

Knowledge of the in-situ stress field is often critical in several aspects of well design, being one of the most important parameters in reservoir management: well-bore stability, hydraulic fracture propagation and production optimization. The economic importance of reliable in-situ stress measurements can be gaged by the high cost involved in decisions like: defining the well locations and attitudes with respect to the target reservoir; determining the proper drilling fluid density; sand control in poorly and unconsolidated reservoirs; and, optimum production and recovery.

Recent research done by the oil industry has improved the accuracy of such in-situ stress measurements. Equipment and methodologies have been developed in the last 50 years, based upon physical principles that would allow the computation of the stress field from rock samples relaxation, or from measurements performed on the rock formation itself in the field. This study concentrates on a core-based technique: the anelastic strain recovery (ASR), with emphasis on the stress magnitudes determination only.

Anelastic strains are caused by the formation of a microcrack population in the core, due to the stress relief after coring, when the rock samples expand in all directions. Modelling the rock behavior for computing the in-situ stress magnitudes from ASR focused on the viscoelastic aspects of the physical process. Nevertheless,

core contraction has been reported in many occasions, indicating that other processes may affect the rock behavior under specific conditions, which are not well represented by a viscoelastic approach.

Recognizing the potential relevance of pore pressure effects when dealing with rocks, a new procedure is presented for simulating the rock anelastic strain behavior using a fully coupled poroviscoelastic model. One needs to realize that the fluid that is allowed to escape during core retrieval introduces a contraction which could mask or even overshadow the rock expansion due to the stress relief. Different rocks and field conditions were simulated by the model indicating that, depending on the rock permeability and the initial stress field, pore pressure diffusion can provide an explanation for observed rock contractions.

A new formulation is also proposed for computing the in-situ stress magnitudes based on the back-analysis of anelastic strain measurements: the rock anelastic strains generated by the poroviscoelastic model are adjusted to experimental strain measurements through a multidimensional fitting algorithm, leading to the original stress magnitudes by optimizing the curve-fitting. The validity of this approach was checked using a synthetic example, confirming the method reliability.

The procedure has been applied to field samples from Brazil's Northeast onshore wells, where the purely viscoelastic approach was unable to compute the stress magnitudes due to core shrinkage. Compression tests were carried out in the laboratory in order to determine the rock elastic, viscoelastic and poroelastic parameters necessary for the rock characterization in the poroviscoelastic model. The obtained strain curve-fittings were very reasonable, and the computed stresses were confirmed via other sources of information: regional shallow earthquakes and microfracturing.

In spite of the simplifying assumptions (plane strain and radial fluid flow are two of the most important ones), the method was able to fill a gap by considering coupled poroviscoelastic effects in the anelastic process. Further investigations are proposed, like adding thermal effects and a more careful examination of the rock experimental creep behavior, in order to improve the model representativeness.

Chapter 1

Introduction

In-Situ stresses are basically the result of the burial and lithification of sedimentary materials. Temperature changes, chemical and physicochemical processes, like mineral precipitation and recrystallization, are constantly modifying the rock structure and, consequently, the stress field. Tectonic movements affect the stress field by creating faults, fractures and foldings, which added to erosion, may generate a complex geological pattern resulting in directional tectonic stress components. Rigorously speaking, the in-situ stresses should be measured at each specific depth where any further excavation is planned. In regions with low tectonic activity or similar geological structures, the local in-situ stress, measured at one particular location, can be extrapolated to other sites, allowing the engineer to improve the new excavation design from already available data.

Knowledge of the in-situ stress is extremely important for civil and mining engineering applications, not only for safety purposes, but also for allowing larger percentage of minerals recovery. The in-situ stress estimation is, nevertheless, a difficult job. Several methods were developed for measuring the in-situ stress field at shallow depths (Lama and Vutukuri, 1978a; Goodman, 1980), leaving the petroleum engineering the task of developing the techniques necessary for deeper and harsher environments.

1.1 Relevance of In-Situ Stress Measurements in the Oil Industry

It is recognized nowadays that in-situ stresses play a major role in practically all the stages of oil exploration, deeply affecting the success rate in well drilling and well stimulation, as well as affecting oil production (Warpinski and Teufel, 1986 and 1991).

Roegiers and Vandamme (1999) pointed out that even estimating the reserves-in-place must take into account the increase in the effective in-situ stresses, during well production, which will obviously affect the total amount of recoverable hydrocarbons.

According to Guenot and Santarelli (1988), the in-situ stress field, together with the rock mechanical strength, strongly affects wellbore stability. Economically speaking, Fjær *et al.* (1992) pointed out that it would be interesting if several wells could be drilled from just one offshore platform, achieving different targets. The borehole inclination, nevertheless, is very often limited by stability considerations, when the stress concentration due to the in-situ stress field combined with the wellbore orientation and the rock mechanical strength may become unbearable (Ong and Roegiers, 1996). However, there are also situations where conventional vertical wells may fail due to extremely high horizontal in-situ stress anisotropy, and the targeted reservoir can only be achieved via a deviated borehole (Roegiers and Vandamme, 1999). One way to overcome this problem, and sometimes the only one, is to align the well with the most favorable direction, i.e., minimizing the stress contrast at the wellbore wall.

In spite of the great importance in drilling, the most evident influence of in-situ stresses in oil exploration comes from well stimulation by hydraulic fracturing. In-Situ stresses play a major role defining the fracture dimensions, orientation and the breakdown pressure for initiating the hydraulic fracture at the borehole wall, as attested by a huge number of researchers, among which Hubbert and Willis (1957), Haimson (1978), Nolte (1982), Haimson and Huang (1989) and Yale and Ryan (1994). The success of a hydraulic fracturing treatment is so much dependent on the in-situ stresses that microhydraulic fracturing tests are routinely performed before larger hydrofrac stimulations, in order to obtain stress data for optimizing the design of the main fracturing (Daneshy *et al.*, 1986).

Once a hydraulic fracture is propagated away from the wellbore, it will become perpendicular to the direction of the minimum in-situ stress (Hubbert and Willis 1957, Haimson, 1978). Based on this, whenever the need of hydraulic fracturing for production enhancement is foreseen, the well locations with respect to the target reservoir must be defined according to the in-situ stress orientation, in order to achieve an optimum drainage area (Smith, 1979), as shown in Figure 1.1, while still maintaining stability and guarantee operational success. Roegiers and Vandamme (1999), evaluated the gain in production to be as high as 30 %, whenever the drilling pattern was defined according to the most favorable direction for fracturing.

In the early years of hydraulic fracturing, it was assumed that hydraulic fractures propagated with a constant height, confined to the pay zone due to shale barriers above and below the reservoir rock. This initial concept was contradicted later on: although there was a natural barrier helping to confine the fracture height, the main factor was the horizontal in-situ stress contrast at different depths (Nolte, 1982).

Several evidences of the major influence of in-situ stresses in hydraulic fracture containment were confirmed via laboratory experiments. (Warpinski *et al.*, 1982a), mineback field tests (Warpinski *et al.*, 1982b, Warpinski and Teufel, 1991) and numerical studies (Yew and Chiou, 1983; Ben Naceur and Toubul, 1987; Fung *et al.*, 1987; Vandamme *et al.*, 1987; Mukherjee *et al.*, 1992). Figure 1.2 shows the fracture behavior observed in mineback experiments.

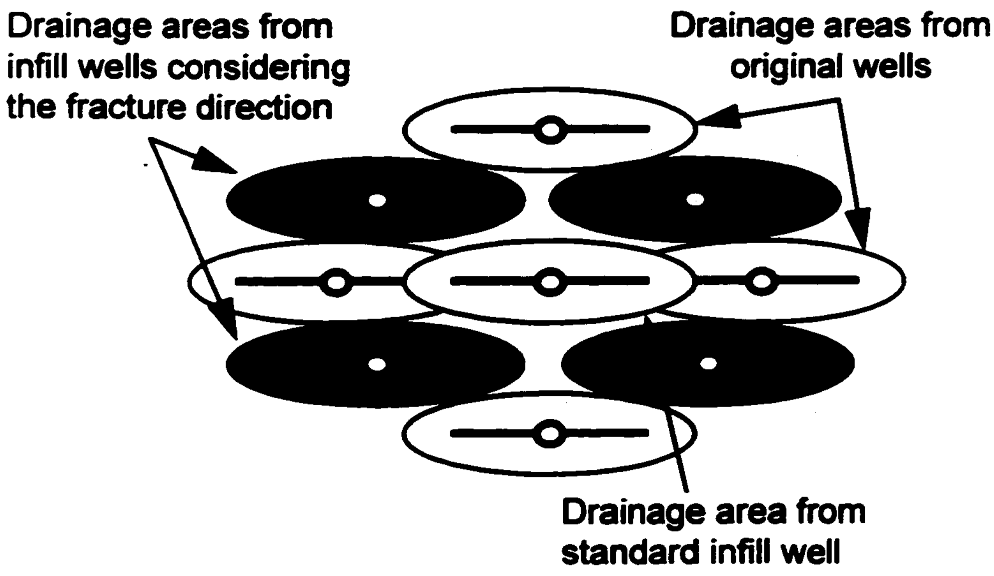

Figure 1.1: Taking advantage of knowing the fracture orientation for optimizing on the well placement.

In-Situ stresses are also relevant for estimating well stability during production. Reservoirs constituted of unconsolidated or poorly consolidated sandstones can produce large amounts of formation particles, leading to premature erosion of the surface equipment, costly oil-sand separator and sometimes total collapse of the well, due to the cavities generated around the casing (Cook *et al.*, 1994). Sanding is a complex phenomenon, being a function of the pressure drawdown and the stress concentration around the perforations, which in turn is dictated by the original in-situ stress field, as well as the 'stress cage' around the borehole, among other rock mechanical parameters (Coates and Denoo, 1981; Morita *et al.*, 1987; Pennington and Edwards, 1994).

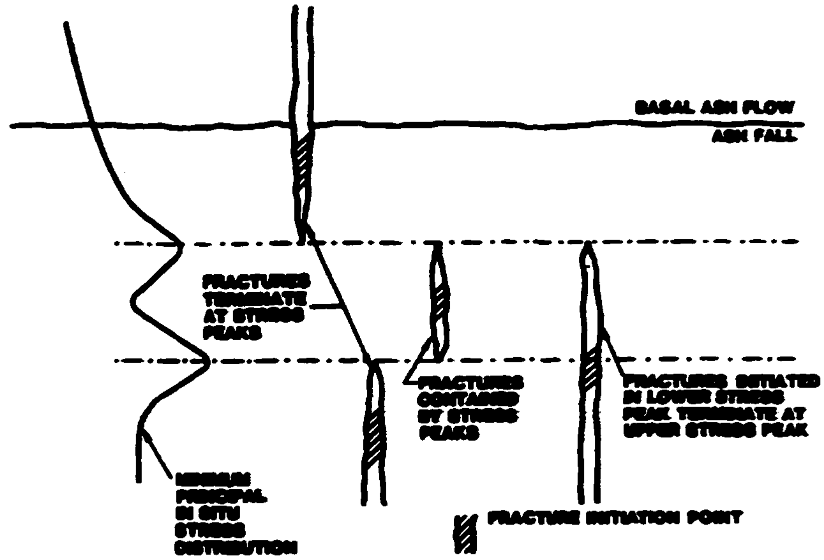

Figure 1.2: Hydraulic fracture behavior after Warpinski and Teufel (1991), as observed in mineback experiments.

1.2 Inferring the Principal In-Situ Stresses

Any stress state can be represented by three mutually perpendicular components, called principal stresses: σ_1, σ_2 and σ_3, respectively the maximum, intermediate and minimum principal stress components. From now on, every time the term 'in-situ stresses' is mentioned in this dissertation, they must be understood, also, as the principal stresses at a specific depth.

Calculating the vertical in-situ stress from the overburden due to the weight of the overlying rock material is a common practice in the oil industry, generally performed by integrating the density log from a nearby well (Bruce, 1990):

$$\sigma_z = \int_0^z \rho(z) g dz \tag{1.1}$$

where,

$$\begin{cases} \sigma_z \text{ is the total vertical overburden;} \\ \rho \text{ is the rock density;} \\ g \text{ is the acceleration of gravity; and,} \\ z \text{ is the depth measured from the surface.} \end{cases}$$

Equation (1.1) is very acceptable when the analyzed region is free from tectonics effects due to geological anomalies. Brady and Brown (1985) pointed out, for example, that the vertical stress component might be less than the value calculated from Equation (1.1) in the axial plane of an anticlinal fold.

The effective[1] horizontal stresses, σ'_x and σ'_y, can be assumed to depend only on the rock elastic behavior, as a first approximation. Thus, a basin without tectonic deformations will have equal horizontal stress magnitudes in any direction. Furthermore, σ'_x and σ'_y will be a function of σ'_z, due to Poisson's effects (Roegiers and Vandamme, 1999):

$$\sigma'_x = \sigma'_y = K_0 \sigma'_z \tag{1.3}$$

where K_0 can be deduced from the equations of elasticity. Assuming, for example $\varepsilon_x = \varepsilon_y = 0$, provides:

$$\sigma'_x = \sigma'_y = \frac{\nu}{1-\nu}\sigma'_z \tag{1.4}$$

where ν is the material Poisson's ratio.

Equation (1.4) gives $0 < K_0 \leq 1$, since $0 < \nu < 0.5$. The ratio between the average horizontal and vertical stresses, however, can vary significantly: from 0.2 to 1.5, at larger depths, and from about 1 up to 10 or 12 at shallow depths (Fjær *et al.*, 1992). Equation (1.4) is, therefore, a very rough estimate, implicitly assuming that

[1]Biot's effective stress law states that:

$$\sigma'_i = \sigma_i - \alpha_i p \tag{1.2}$$

where:

$$\begin{cases} \sigma'_i \text{ is the effective stress in the } i\text{-direction;} \\ \sigma_i \text{ is the total stress in the } i\text{-direction;} \\ \alpha_i \text{ is the effective stress coefficient in the } i\text{-direction;and,} \\ p \text{ is the pore pressure.} \end{cases}$$

the sediments deform elastically and the rock properties remained constant over geological times. In fact, as mentioned before, erosion, diagenesis and cementation are a few examples of common processes that may produce a quite remarkable horizontal stress anisotropy, leading to $\sigma'_x \neq \sigma'_y \neq K_0\sigma'_z$.

Determining the horizontal in-situ stresses became, then, a 'must' for the oil industry. A total of 20 techniques used in the oil industry are listed in Table 1.1 (Hill *et al.*, 1994; Roegiers and Vandamme, 1999). The utilization of any technique, nevertheless, is restricted by the 'built-in' theoretical assumptions, testing conditions, experimental limitations and mathematical modelling inherent to each method, as discussed in Chapter 2.

Most of the methods presented in Table 1.1 are capable of providing only the in-situ stress orientation. Three methods, nevertheless are more general: Anelastic Strain Recovery (ASR); Differential Strain Curve Analysis (DSCA); and microhydraulic fracturing, allowing also the computation of the in-situ stress magnitudes. The ASR method has a major advantage over the other methods since it allows inferring the stress magnitudes, provided that the stress relief mechanism is well understood, whatever the well inclination.

In a typical ASR test, the deformation of core samples is monitored for 48 hours after removal from the coring barrel. Figure 1.3 shows the portable equipment used by Petrobras for running ASR tests in the field (TerraTek, 1995).

If the sample is isotropic and homogeneous, and the strain recovery can be assumed linear viscoelastic, the strain relief will be uniform with time. Thus, the principal strain orientations determined by the ASR test will be aligned with the principal in-situ stress (Warpinski and Teufel, 1986; El Rabaa, 1988). A few models for inferring the in-situ stress magnitudes from the relative magnitudes of the principal strains measured in the ASR test were developed by Blanton (1983), Warpinski

Table 1.1: In-situ stress determination methods.

Core-Based Methods	
1	anelastic strain recovery (ASR)
2	differential strain curve analysis (DSCA)
3	circumferential velocity anisotropy (CVA)
4	differential wave velocity analysis (DWVA)
5	axial point load test
6	petrographic examination of microcracks
7	overcoring of archived core
8	drilling induced fractures in core
9	direct observation of overcored open-hole stress test fractures
Borehole-Based Techniques	
10	microhydraulic fracturing
11	borehole breakouts
12	borehole deformation
13	borehole imaging of drilling induced fractures
14	directional gamma-ray logging
Near-Wellbore Techniques	
15	microseismic logging
16	earth tilt survey
Geological Indicators	
17	earthquake focal mechanisms
18	fault slip data
19	surface mapping of neotectonic joints
20	volcanic vent alignment

Figure 1.3: ASR testing equipment. The box on the left holds the temperature controller and signal conditioners for the displacement transducers. A lap top for data acquisition is shown in the center. Up to two samples may be placed in the sample chamber on the right, which has the purpose of keeping temperature and humidity constant during the ASR test. Each sample is instrumented with 12 Linear Variable Displacement Transducers (LVDT).

and Teufel, (1986) and Matsuki and Takeuchi (1990), based on the viscoelasticity theory.

A major limitation of the previous ASR models is the assumption that rock samples will always expand after coring, due to the stress relief. This assumption is implicit in the viscoelastic model for computing the stress magnitudes (Blanton and Teufel, 1986), leading to wrong values whenever the rock shows some contraction. Core contraction has been reported in many field cases (Blanton and Teufel, 1983; Lessi *et al.*, 1988; Perreau *et al.*, 1989; Butterworth *et al.*, 1991; Ramos *et al.*, 1994; Breretron, 1995); and a few attempts have been made to explain it. Butterworth *et al.* (1991) mentioned that, in some cases, this core contraction may be only apparent, being caused by the spring loaded sensor tips, which may dig into the samples by deteriorating the rock at the contact point. Assuming that the sensor tips are not influencing the measurements, three additional potential factors have been considered to explain rock contraction: high Poisson's ratio; temperature changes; and poroelastic effects (Blanton, 1983 and 1986; Warpinski and Teufel, 1986; Breretron *et al.*, 1995).

Based solely on the elasticity theory it is easy to see that rock contractions may occur in the direction of the minimum in-situ stress for rocks with high Poisson's ratio under high deviatoric stresses: the rock expansion due to the relief of the minimum stress would be smaller than the rock contraction due to the expansion in the direction of the maximum in-situ stress.

Correcting the strain measurements for the temperature variation is an initial step whenever analyzing ASR data. This is usually done by measuring the rock coefficient of linear thermal expansion, and adding or subtracting the thermal deformation due to the temperature changes from the total strain measurement when performing ASR tests. A more appropriate way, however, would be to consider the thermal effects coupled to the rock deformation due to the stress relief and pore pressure diffusion.

Coupled effects of pore pressure diffusion and solid deformations have been, nevertheless, totally neglected by the current viscoelastic models for computing the stress magnitudes from ASR. Several reasons may be listed for this, like assuming that pore volume deformations are too small or homogeneous, equally affecting the rock deformations in all the directions, thus irrelevant for models using the relative magnitude of the principal strains as input for computing the stresses. It must also be noticed that the importance of the poroelasticity theory was not so widespread in the oil industry by the 80's. In fact, only a few publications mentioned poroelasticity effects, mainly in hydraulic fracturing (Roegiers and Ishijima, 1983; Schmitt and Zoback, 1989; Detournay *et al.*, 1989; Haimson and Huang, 1989; Boone and Detournay, 1990; Boone *et al.*, 1991a and 1991b).

Advances in the poroelasticity theory after Detournay and Cheng (1993), and the perception of its relevance when dealing with the deformations of porous media like saturated rocks, made this theory more and more palatable to petroleum related problems, improving the theoretical explanation of field problems and helping the understanding of the rock behavior in several oil field applications.

This dissertation focuses on the application of the poroelasticity theory to the modelling of the coring process. The purely mathematical approach, presented by Breretron (1995) for highlighting the poroelastic effects on the core deformation after coring, is taken several steps further: a fully coupled poroelastic formulation for computing the radial strain in cylindrical geometries (previously derived by Detournay and Cheng, 1993) is made time-dependent by the Viscoelastic Principle of Correspondence — VCP (as presented by Abousleiman *et al.*, 1996), constituting a new poroviscoelastic model for analyzing the effects of pore pressure diffusion in

ASR.

1.3 Potential Importance of Poroelasticity on the Anelastic Strain Recovery

It is easy to accept that changes in the pressure at the core boundary during the trip of the coring barrel out of the borehole will cause a pressure redistribution inside the core, up until a new homogeneous pore pressure level is reached via diffusion. The pore pressure variation will most probably lead to changes in the pore volume. These changes may, in some cases, be large enough to affect the rock expansion due to the stress relief after coring. It is also easy to prove that the rate of the pore pressure diffusion depends mainly on the rock permeability and fluid viscosity: it will be faster for rocks with higher permeability and fluids with lower viscosities. In other words, poroelastic effects may be irrelevant for higher permeability rocks, since they will be over by the time the sample is brought to the surface.

After recognizing the importance of the pore fluid diffusion in ASR, it became a common practice for the oil service companies to wrap the sample up in plastic or to paint the core with impermeable paints, in order to avoid the loss of fluids during the ASR test (El Rabaa, 1986; Owen *et al.*, 1988). This procedure, nevertheless, is unable to stop the internal pressure redistribution process in low permeability rocks, started when the sample was cored and slowly progressing even after the sample is removed from the coring barrel. The ASR results, thus, are not free from poroelastic effects in low permeability rocks. Breretron *et al.* (1995) showed that complex deformation patterns in ASR tests, presented in Figure 1.4, could be explained by a combination of strains generated by stress relief and pore pressure variations, assuming that both processes compete with one another depending upon the magnitudes of the rock stresses, the permeability and the pore pressure.

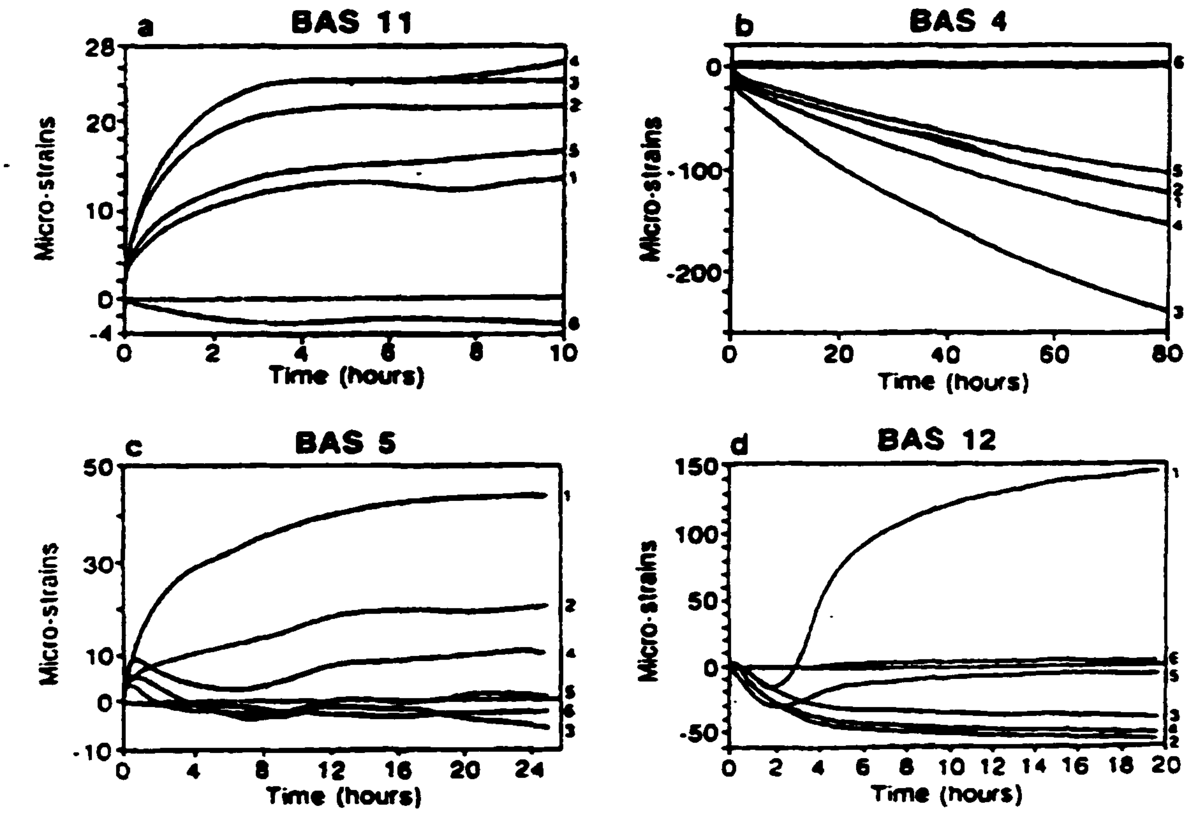

Figure 1.4: Anelastic strain recovery from four different wells (BAS 11, 4, 5 and 12), after Breretron et al. (1995).

Considering the anelastic strain from the purely viscoelastic model presented by Warpinski and Teufel (1989), to be in the form of:

$$\varepsilon(t) = \varepsilon_\infty \left(1 - e^{-\frac{t}{\tau}}\right) \tag{1.5}$$

where ε_∞ is the rock asymptotic strain level at $t \rightarrow \infty$ and τ is the relaxation time for the anelastic deformation, both parameters being exclusively related to the stress relief. Assuming now the pore pressure response as:

$$\beta(t) = -\beta_\infty \left(1 - e^{-\frac{t}{\lambda}}\right) \tag{1.6}$$

where β_∞ is the rock final strain level and λ is the pore pressure relaxation time, both constants are uniquely related to the pore pressure dissipation in this case. The total strain in a hypothetical ASR test can then be represented by adding $\varepsilon(t)$ and $\beta(t)$. The negative sign in Equation (1.6) means that the contraction caused by the pore pressure reduction is taken as negative, while the expansion caused by the stress relief computed by Equation (1.5) is taken as positive.

By playing with the time constants of these two equations (τ and λ), Breretron *et al.* (1995) showed that the deformation patterns in Figure 1.4 can be reproduced from Equations (1.5) and (1.6) for three different cases (Figures 1.5 to 1.10).

Curve 'C', in Figure 1.5, shows that the initial contraction followed by expansion, in the direction 1 of the ASR results for BAS 12 (Figure 1.4d), can be reproduced if the magnitude and relaxation time of the stress relief and pore pressure diffusion process are such that:

$$\begin{cases} \varepsilon_\infty = 150; \\ \tau = 10; \\ \beta_\infty = 25; \text{ and,} \\ \lambda = 0.5; \end{cases}$$

Assuming a larger recovery time, let's say 10 hours, a behavior similar to directions 1 to 5 in BAS 11 (Figure 1.4a), and directions 1 and 2 in BAS 5 (Figure 1.4c), are reproduced in Figure 1.6. This figure presents the same curves as in Figure 1.5, but with a 10 hours measuring delay.

Assuming that the magnitudes of the solid deformation due to the stress relief and pore pressure variation are the same ($\varepsilon_\infty = \beta_\infty$), but having the relaxation times given by: $\lambda = 3\tau$, the behavior shown in curve 'C', Figure 1.8, which are derived from Figure 1.7, match the ones measured for BAS 4 (Figure 1.4b), showing pure contraction.

By keeping the relaxation times equal ($\lambda = \tau$), and having ($\beta_\infty = 3\varepsilon_\infty$) in the last example, curves 'C' from Figure 1.9 and 1.10 are comparable to the results for orientations 2, 3 and 4, in BAS 12 (Figure 1.4d).

Although purely mathematical, this analysis proves that the pore pressure variation can provide a reasonable explanation for the ASR results. A more complete formulation, coupling the pore fluid diffusion and solid deformation, nevertheless, is still lacking in the in-situ stress determination literature. This formulation is exactly the subject of the present study, as shown in the next section.

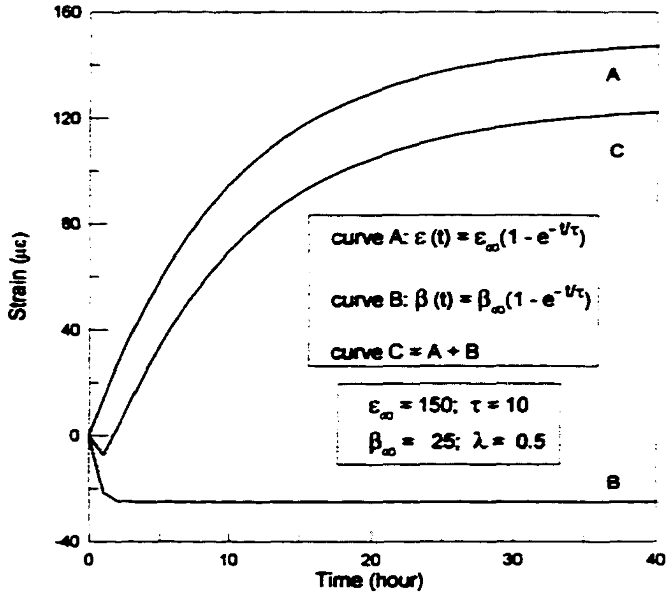

Figure 1.5: Anelastic strain patterns due to: A - stress relief; B - pore pressure diffusion; C = A + B (case 1).

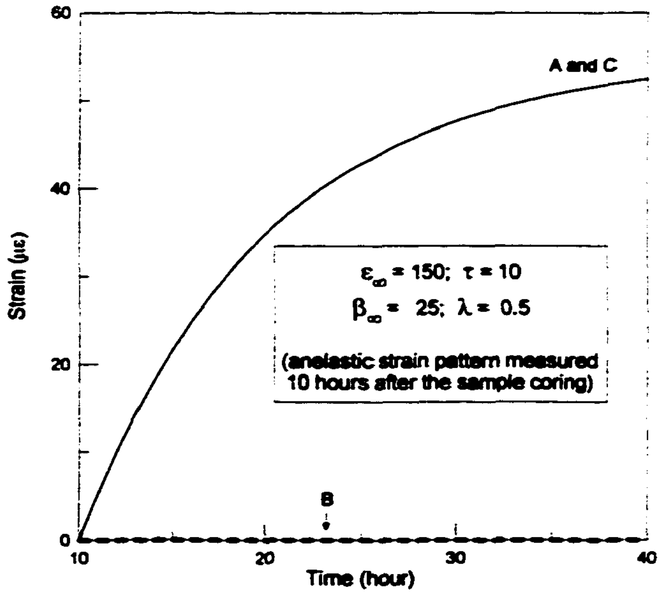

Figure 1.6: Anelastic strain patterns due to: A - stress relief; B - pore pressure diffusion; C = A + B, measured 10 hours after coring (case 1).

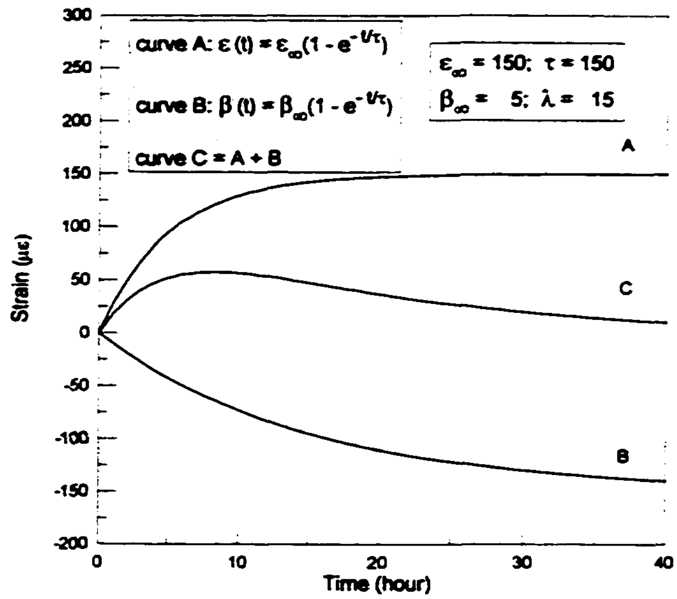

Figure 1.7: Anelastic strain patterns due to: A - stress relief; B - pore pressure diffusion; C = A + B (case 2).

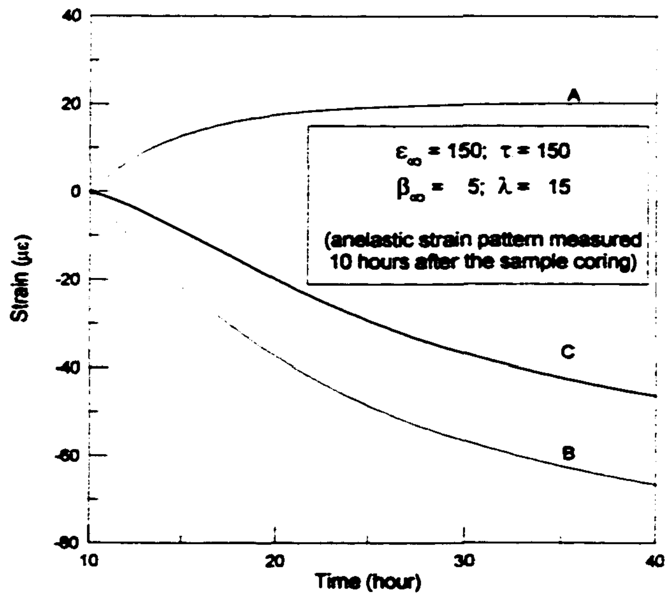

Figure 1.8: Anelastic strain patterns due to: A - stress relief; B - pore pressure diffusion; C = A + B, measured 10 hours after coring (case 2).

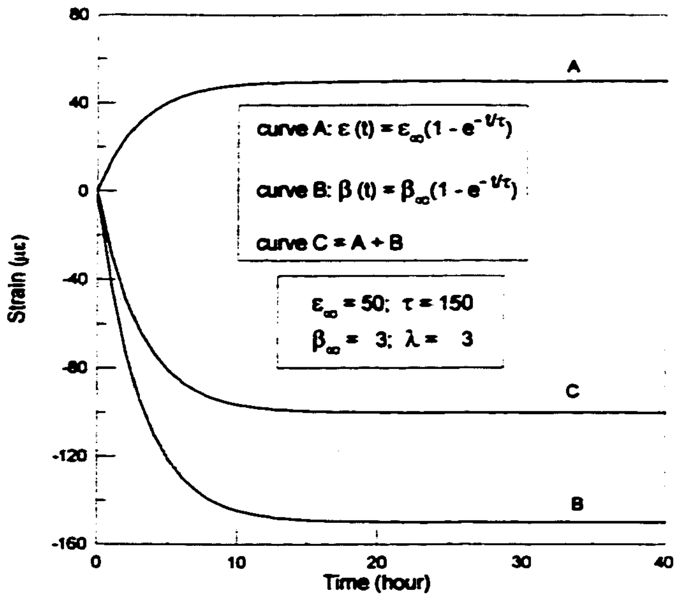

Figure 1.9: Anelastic strain patterns due to: A - stress relief; B - pore pressure diffusion; C = A + B (case 3).

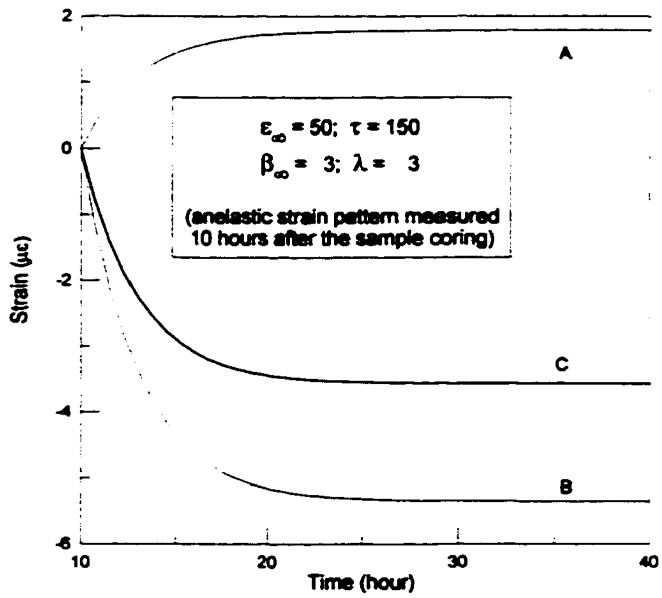

Figure 1.10: Anelastic strain patterns due to: A - stress relief; B - pore pressure diffusion; C = A + B, measured 10 hours after coring (case 3).

1.4 Objectives, Initial Assumptions and Dissertation Outline

This dissertation presents a new model for the ASR process under the poroviscoelastic theory. The new approach intends to improve the simulation of the rock anelastic deformations. The rock viscoelastic behavior is represented by the modified Kelvin model (Flügge, 1975), allowing each rock parameter to change independently during the deformation process, contrary to the existing viscoelastic formulations which assume a single viscoelastic function for the rock volumetric strain (Blanton, 1983 and 1986).

The major advance with the poroviscoelastic approach is to provide a mechanical explanation for the core contraction, frequently observed in ASR tests, which none of the existing viscoelastic models (Blanton, 1983; Warpinski and Teufel, 1986) handle properly, since viscoelastic formulations cannot include pore shrinkage effects. The final goal of the new approach is to allow the computation of the stress magnitudes whatever the rock anelastic strains are: expansion, contraction or expansion and contraction mixed, filling a gap in the existing ASR literature.

1.4.1 Objectives

The objectives of this study can be summarized as follows:

- Develop a model capable of reproducing any strain trajectory as a function of the rock properties, initial stress field and drilling conditions, prescribed as boundary conditions during coring.

- Define a suitable set of rock properties for analyzing the coring process within a poroviscoelastic approach from laboratory experiments and conduct a parametric study.

- Verify the influence of poroviscoelasticity in the rock anelastic strain generated by coring.
- Quantify, experimentally, the creep effect on the rock elastic properties in order to define the ones that may play some role in the anelastic deformations, and attribute an exclusive time-dependency function to them.
- Confirm the importance of the pore pressure diffusion process in rock shrinkage by analyzing the strain response in different materials.
- Compute the in-situ stresses from the anelastic strain measured in the ASR test based on the poroviscoelastic formulation.
- Develop a methodology for back-analyzing ASR field data in order to compute the magnitude of horizontal in-situ stresses.
- Compute the horizontal in-situ stresses for specific depths in five Petrobras' wells.

1.4.2 Assumptions

The geometry analyzed in this dissertation is cylindrical, and the principal stresses are assumed to be longitudinal and radial to the cylinder axis. In the case of a vertical wellbore, for example, the principal stresses would be exactly the vertical and horizontal ones.

Four initial assumptions are necessary for analyzing the coring process and consequent anelastic strain recovery (a few other assumptions are presented in Chapter 3, since they are intrinsic to the poroelastic formulation discussed in that chapter):

1. Plane strain conditions: the core was considered to be infinitely long; so that the vertical strain is negligible and does not affect the radial deformations.

This assumption was kept on, even when considering the 3" x 6" sample used in the ASR test, as a first approach.

2. Axisymmetry: the adopted poroelastic formulation is valid only for axisymmetric loading (Detournay and Cheng, 1993), i.e., the stresses are defined based on the radial position. In order to adapt this condition to the rock actual stress field, the stresses were decomposed in hydrostatic and deviatoric components, represented respectively by P_0 and S_0 in Figure 1.11. While the hydrostatic loading (Figure 1.11b) leads to volumetric changes, and is very much affected by the pore fluid, the rock response to the deviatoric loading (Figure 1.11c) is completely elastic (Abousleiman *et al.*, 1996); hence, not influenced by the pore fluid. Thus, based on the problem linearity, the hydrostatic case was solved by the poroviscoelastic approach and later on added to the viscoelastic solution for the deviatoric loading, simulating the actual stress field.

3. Homogeneity: whenever macro-variations in the rock constituent are detected, before or after the ASR test (sometimes rocks heterogeneities are not visible until the test is done and the samples are sawed), the results must be disregarded, since the measured strains, and thus the stress computation, would be affected by the local heterogeneities.

4. Isotropic: although it is also possible to consider poroelastic effects in transversely isotropic rocks (Cui *et al.*, 1996; Cheng, 1997), the formulation developed in this dissertation assumes the rock to be isotropic, simplifying the equations, reducing the necessary input rock parameters and, consequently, the experimental tests.

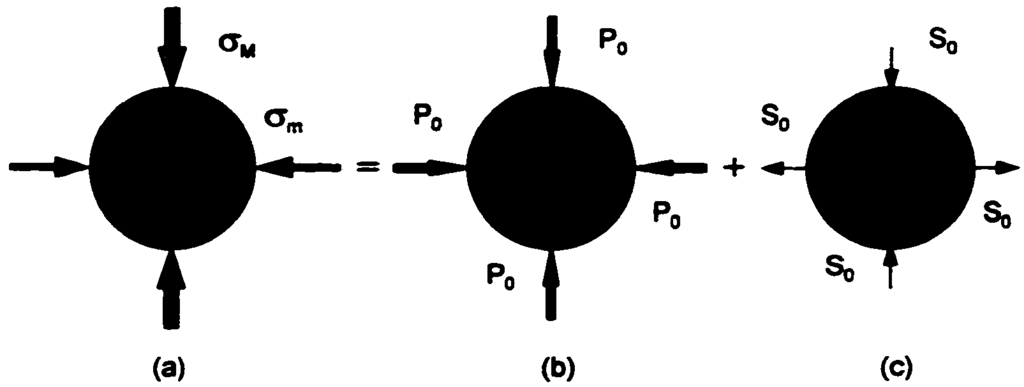

Figure 1.11: Decomposition of the stress field around the core.

1.4.3 Dissertation Outline

Following the introductory chapter, Chapter 2 of this dissertation reviews several methods for in-situ stress determinations. The methods are briefly described, highlighting their applications, procedures, advantages, weaknesses and limitations. Previous works, presenting and applying the ASR technique, are more deeply analyzed, since they constitute the basis for the study presented in this dissertation.

Chapter 3 describes the poroelastic formulation and the viscoelastic model which are combined for constituting the new poroviscoelastic approach for the ASR process. The boundary conditions for simulating the coring process are presented and introduced into the poroelasticity governing equations, providing closed-form solutions for computing the radial strain at the core outer surface, and the pore pressure distribution inside the core. This procedure is then inverted, allowing the computation of the original radial in-situ stress and the reservoir pressure.

A comparison between the results generated from a Fortran code with the poroviscoelastic formulation and previous results from the literature are shown in Chapter 4. The data from the literature is not related to coring, but to classical cylinder problems which were previously solved by Detournay and Cheng (1993), and

Abousleiman *et al.* (1996). The long term elastic and viscoelastic solutions are also compared to the code results, showing that the poroviscoelastic approach do converge to the elastic and viscoelastic values, as the pore pressure inside the core reaches an equilibrium with the environment.

A parametric study is also presented in Chapter 4 for comparing the code results with different rock input data. This study revealed that not considering some of the rock properties as time-dependent, as in the existing viscoelastic approach, makes a large difference in the strain pattern.

In Chapter 5 a methodology is presented for back-analyzing ASR data in order to compute the horizontal in-situ stress magnitudes. The inversion problem is solved with the help of a multidimensional numerical code — the Simplex algorithm. The method is successfully applied to ASR tests in five oil wells in Brazil, South America, which have presented complex ASR pattern.

The rock data needed for the computations in Chapter 5 were gathered from experimental tests on the samples previously tested for ASR. Chapter 6 presents the experimental procedures and results. The tests focused on getting the necessary input parameters for a standard data set for a poroviscoelastic analysis. The performed creep tests, aimed not only in providing the necessary input data but also defining which rock elastic properties are more relevant for the process.

The summary and conclusions of the dissertation are presented in Chapter 7, as well as an outline for the extension of the realized work.

Chapter 2

Critical Literature Review

The determination of the underground stress field has always been a challenging job for mining and civil engineering, but for the petroleum industry the scenario is even more complex. Although several techniques are available for shallower depths excavation like overcoring and flat-jack methods (Lama and Vutukuri, 1978a; Goodman, 1980), oil wells can reach targets at 4,700 m (Pereira, 1990) and offshore wells are drill nowadays at more than 1,700 m below the sea level (Petroleum Review, 1998), making in-situ stress measurements a difficult and expensive task. In spite of the harsh environment, the oil industry has been able to develop a few methods for inferring the in-situ stress field. Not all of them, nevertheless, are capable of providing a complete description of the stress field, i.e., magnitude and orientation of the principal stresses.

According to Hill *et al.* (1994), the available methods for inferring the original stress field can be divided into core-based tests, like Anelastic Strain Recovery (ASR) and Differential Strain Curve Analysis (DSCA); borehole-based techniques, like microhydraulic fracturing and breakouts from wireline logs; near-wellbore techniques, which includes measuring the orientation of hydraulic fracturing initiation and propagation; and, regional geologic indicators, like existing faulting regime or even the world stress map.

Core-based techniques are more economical, since they do not occupy the drilhole exclusively for the test, specially if coring is already planned for that specific well. On the other side, the results may be influenced by the testing environment, since the core is not anymore under the exact in-situ conditions. Borehole techniques have the initial advantage of gathering data directly from the underground. Nevertheless, they are more expensive, because of the surface and downhole equipment needed, and very often difficult to interpret.

Because of the uncertainties and limitations associated with each method, the industry tendency is to apply more than one technique in the same field and compare the results, increasing the data interpretation reliability. This procedure is not the best approach for the problem, but has been applied quite often (Brumley *et al.*, 1994; Zheng, 1999).

A description of some of the most common methods for inferring the in-situ stresses in oil wells is presented next, highlighting the physical background of each technique, its advantages and disadvantages.

2.1 Core-based Methods

Core-based methods for inferring the in-situ stresses are sometimes preferred when coring is already in the drilling schedule for, for example, geological description, like in the case of exploratory wells. There is a wide variety of core-based techniques, which most of the times can only provide the in-situ stress orientation. The ASR technique is analyzed with special emphasis in this chapter, not only because it can provide the complete stress field, but also because its physical background and theoretical formulation constitute the main subject of this dissertation. The DSCA is also discussed in details, since it usually represents and alternative to the ASR, also providing the complete stress tensor.

2.1.1 Anelastic Strain Recovery (ASR)

The main goal of the ASR technique is to determine the in-situ stress field based on the rock deformations due to the stress relief that naturally occurs after coring. The most accepted theoretical basis for the strain relaxation process assumes that sand grains become stressed during burial and lithify. The stored energy within the grain may vary in different directions, depending on the amount of stress that was applied along each orientation. When a rock stratum is cored, the sand grains attempt to expand elastically as soon as the existing stresses are relieved, but they are held back by the cement bond. Many of these bonds will eventually be broken, forming a microcrack population which is typically represented by an anelastic deformation process, where most of the microcracks are preferentially aligned with the previous stress field (Hill *et al.*, 1994). Measuring the rock principal strains caused by such microcrak openings would lead to the direction of the principal stresses.

The idea of a population of oriented microcracks spread throughout the whole core was confirmed through acoustic emission tests and P-wave velocity measurements in the laboratory, which have presented a strong correspondence with the strain recovery pattern (Teufel, 1983a and 1983b; Butterworth *et al.*, 1991). ASR tests on sub-cores plugged from a core several years after its recovery, however, have also shown typical ASR curves (Butterworth *et al.*, 1991), leading to a different line of thought regarding the physical mechanisms: only the outer part of the core would be involved in the relaxation process, and/or the process may be significantly influenced by paleostresses locked in the core. Nevertheless, none of these observations seems to be definitive, and the physical principles behind the ASR process are still open to investigations.

In spite of the lack of a complete explanation for the process, the reliability of the stress field derived from ASR tests has been confirmed in many situations by comparison with other methods like hydraulic fracturing (Blanton and Teufel, 1983; Teufel, 1985a), and lab tests with synthetic sandstones (Wang *et al.*, 1997). There are also occasions in which the ASR tests were unsuccessful: in unconsolidated sandstones (Ramos *et al.*, 1994); because of a long time gap between coring and testing (Brumley *et al.*, 1994); and the impossibility of computing the stress magnitudes due to core contraction (Siqueira *et al.*, 1996a; 1996b; 1997a; 1997b; and, 1997c).

Testing Procedure

The testing procedure assumes that the strain measured in the ASR test after removing the core from the coring barrel is proportional to the total strain since coring, and hence, also proportional to the pre-existing state of stress. It should be emphasized, nevertheless, that this is only true if the rocks are also considered isotropic, homogeneous and linearly viscoelastic.

Since the strain variation after cutting the core decays exponentially with time, the ASR tests are performed as soon as the sample becomes available at the drilling rig. To further reduce the time between coring and testing, the sample is usually taken from the bottom part of the whole core, which is the last one to be cored before pulling the coring barrel.

The ASR test consists in acquiring the core deformation in several directions, until the rock reaches equilibrium. The first ASR tests, nevertheless, were inconsistent due to the strain measuring procedure, which used strain gages glued to the surface of unsealed saturated samples (Teufel, 1982 and 1983a). Silicon spray coating (Teufel, 1985a) or polyurethane wrapping (Teufel, 1985b) were then introduced in order to seal the core and avoid moisture evaporation; at the same time, strain gages were replaced by clip-on gauges, increasing the measurements reliability. Oil baths (Perreau *et al.*, 1989) or inert silicon-based fluids (Butterworth *et al.*, 1991) were later used in order to control the temperature, humidity and external vibrations .

during the tests.

Gathering the Orientation of the Principal In-Situ *Stresses*

Coring for ASR tests is generally oriented in order to associate the strain directions measured in the test with the wellbore azimuth. When an oriented coring tool is not available, geophysical logs like the formation microscanner and paleomagnetic techniques can also be used for orienting the samples (Butterworth *et al.*, 1991), even though with less accuracy. Considering, for example, the strain measurement along six directions, the orientation of the principal strains would be obtained by computing the eigenvectors of:

$$\begin{bmatrix} \varepsilon^i_{xx} & \dfrac{\varepsilon^i_{xx} - 2\varepsilon^i_{aa} + \varepsilon^i_{yy}}{2} & \dfrac{\varepsilon^i_{zz} - 2\varepsilon^i_{bb} + \varepsilon^i_{xx}}{2} \\ \dfrac{\varepsilon^i_{xx} - 2\varepsilon^i_{aa} + \varepsilon^i_{yy}}{2} & \varepsilon^i_{yy} & \dfrac{\varepsilon^i_{yy} - 2\varepsilon^i_{cc} + \varepsilon^i_{zz}}{2} \\ \dfrac{\varepsilon^i_{zz} - 2\varepsilon^i_{bb} + \varepsilon^i_{xx}}{2} & \dfrac{\varepsilon^i_{yy} - 2\varepsilon^i_{cc} + \varepsilon^i_{zz}}{2} & \varepsilon^i_{zz} \end{bmatrix} \tag{2.1}$$

where the superscript i means time step and the strain orientations are shown in Figure 2.1.

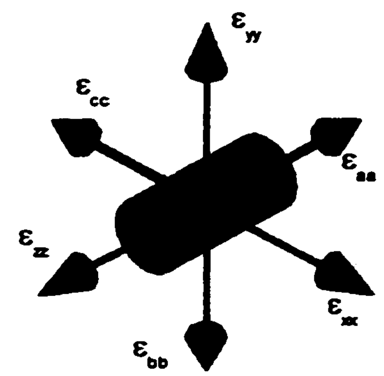

Figure 2.1: Typical orientation for the strain measurements.

Computing the principal stress orientation from ASR tests can be considered fairly accurate for isotropic homogeneous rocks (Teufel, 1982 and 1983a; El Rabaa and Meadows, 1986; Owen *et al.*, 1988; El Rabaa, 1988). Rock samples, however, may have hidden heterogeneities, not visible from the core external surface, which can affect the rock deformation anisotropically, misleading the principal strain orientations. Several ASR results, for example, were discarded by Graves (1995), after examining samples previously tested for ASR and finding out inner heterogeneities.

Computing the Principal In-Situ *Stress Magnitudes*

The first formulation for computing the stress magnitudes from ASR tests was a viscoelastic approach presented by Blanton (1983), which was applied with reasonable results (Blanton and Teufel, 1983; Teufel, 1983b, 1985a and 1985b). It is worth noticing, however, that only rock expansion was reported in the earlier applications, leaving the doubt if the method would work fine having the core presented contraction instead of expansion. Solutions were obtained for both isotropic and transversely isotropic cores, based on the following basic assumptions:

1. the original in-situ stress was assumed to drop to the atmospheric pressure instantaneously at the coring instant;

2. the vertical stress was assumed to be one of the principal stresses, equal to the overburden;

3. the anelastic strain, $\varepsilon_{ij}(t)$, was equated to:

$$\varepsilon_{ij}(t) = S_{ijkl} \int_0^t V(t-\tau) \frac{\partial \sigma'_{kl}(\tau)}{\partial t} d\tau \tag{2.2}$$

where:

$$\left\{ \begin{array}{l} S_{ijkl} \text{ is the compliance matrix (function of the rock Young's modulus and} \\ \text{Poisson's ratio);} \\ V(t-\tau) \text{ is a global compliance function;} \\ (t-\tau) \text{ is a time interval; and,} \\ \sigma'_{kl}(t) \text{ is the effective stress history.} \end{array} \right.$$

A more realistic approach for the conditions immediately after coring is taken in this dissertation, considering an instantaneous drop from the original stresses and formation static pressure to the drilling fluid pressure, followed by a gradual decrease to the atmospheric pressure as the core is retrieved. Assuming the vertical stress to be a principal one represents the situation in tectonically relaxed basins, which is very reasonable as a first approach.

It is clear from Equation (2.2) that considerations on the physical mechanisms involved in the anelastic process were intentionally avoided by choosing a global compliance function. In opposition to this approach, a spring-dashpot arrangement was used for simulating the rock anelastic behavior in this dissertation (Chapter 3), allowing any of the rock elastic parameters (Young's modulus, drained and undrained bulk modulus and grain bulk modulus) to represent the rock viscous characteristics..

A gradual linear unloading to the atmospheric pressure was also proposed in a new formulation by Blanton and Teufel (1986) and adopted by Terratek (1995), improving the viscoelastic model. Knowing the vertical effective stress (σ'_{11}) *à priori*, the horizontal stresses (σ'_{22} and σ'_{33}) in this approach are given by:

$$
\begin{aligned}
\sigma'_{22} &= \sigma'_{11}\left[\frac{w_{22} - DV_m(1-\alpha)p}{w_{11} - DV_m(1-\alpha)p}\right] \\
\sigma'_{33} &= \sigma'_{11}\left[\frac{w_{33} - DV_m(1-\alpha)p}{w_{11} - DV_m(1-\alpha)p}\right]
\end{aligned}
\tag{2.3}
$$

having:

$$
w_{ij} = \frac{(1-2\nu)\,\Delta\varepsilon_{ij} + \nu\Delta\varepsilon_{kk}}{(1+\nu)(1-2\nu)} \tag{2.4}
$$

$$
\begin{cases}
\Delta\varepsilon_{ij} = \varepsilon_{ij}(t_2) - \varepsilon_{ij}(t_1) \\
\Delta\varepsilon_{kk} = \varepsilon_{kk}(t_2) - \varepsilon_{kk}(t_1)
\end{cases}
\tag{2.5}
$$

and,

$$
V_m = D_n\left(e^{\dfrac{-(t_1-\tau_0)}{n}} - e^{\dfrac{-(t_2-\tau_0)}{n}}\right)\left[\left(\frac{n}{\Delta t}\right)\left(e^{\dfrac{\Delta t}{n}} - 1\right) - 1\right] \tag{2.6}
$$

where:

$$\begin{cases} D \text{ is the compliance modulus } (D = 1/E) \\ \alpha \text{ is Biot's effective stress coefficient;} \\ p \text{ is the porepressure;} \\ \nu \text{ is the rock Poisson's ratio;} \\ \Delta\varepsilon_{ij} \text{ and } \Delta\varepsilon_{kk} \text{ are the variations in the principal and volumetric strains;} \\ D_n \text{ and } n \text{ are the creep parameters of the analyzed rock;} \\ (t_1 - \tau_0) \text{ is the time elapsed since the beginning of the ASR test and a} \\ \text{referential time, } \tau_0; \\ (t_2 - \tau_0) \text{ is the time elapsed since the end of the ASR test and } \tau_0\text{; and,} \\ \Delta t = (t_1 - \tau_0)\,. \end{cases}$$

Even though core contraction has been recognized and attributed to high Poisson's ratios and high deviatoric stresses, Equations (2.3) to (2.6) show that the above method may fail whenever the rock shows contraction: since D and Vm are positive constants, having negative values for $\Delta\varepsilon_{ij}$ and $\Delta\varepsilon_{kk}$ (Equations 2.5) may change the sign between the horizontal and vertical principal stresses, related in Equation (2.3), leading to an absurd condition of a tensile in-situ stress.

Warpinski and Teufel (1986) developed another viscoelastic model also applicable to cases with contraction in all gages, even though no considerations were made about the reasons for the rock shrinkage. The model was designed for vertical boreholes only, assuming three horizontal gauges and a vertical one. Instead of only one global compliance function, as in Blanton's model (1983), two independent creep compliances, one in distortion (J_1) and another one in dilatation (J_2), were defined for describing the rock viscoelastic behavior.

The idea of splitting the deformation into distortional and dilatational behavior is similar to the procedure followed in this dissertation, where the load was divided into deviatoric and hydrostatic loading in order to compute the original stresses (Chapter 5). Warpinski and Teufel (1989), nevertheless, considered the dilatational effects (which includes pore pressure diffusion) irrelevant in the stress computation, which was based solely on distortional strains.

The advantages and disadvantages of the two existing viscoelastic models were discussed in details by Blanton (1989) and Warpinski & Teufel (1989), highlighting that Blanton's model was applicable only in the absence of pore fluid diffusion and core contraction. Even though more general, computing J_1 and J_2 for Warpinski & Teufel's model is somehow cumbersome, and was still to be optimized by the authors.

Further developments on Warpinski and Teufel's model (1989) were presented by Matsuki and Takeuchi (1990 and 1991), for computing the in-situ stress field from ASR tests on deviated wells at a geothermal field in Japan. In spite of a completely different testing setup, with cubic samples and strain gages, the formulation was the same as in Warpinski and Teufel's model (1989), and there were no concerns with poroelastic effects.

Pore pressure effects were first investigated by Breretron (1995), with a simple mathematical approach for reproducing ASR patterns observed in cores from offshore wells in the Indian Ocean. The good matching obtained by representing the rock behavior with emphasis on the pore pressure diffusion (Figures 1.5 to 1.10), together with advances in the application of the poroelasticity theory to rock mechanics problems (Detournay and Cheng, 1993; Abousleiman *et al.*, 1996), motivated the search for a new and more complete formulation.

Summary of the Method Advantages

1. possibility of determining the complete stress field with just one test;
2. test is relatively easy and cheap to perform;
3. there is no need for altering the job schedule for the well, since the samples can be obtained using coring for other purposes. Nevertheless, oriented coring tools should be used.

4. can be applied in situations where microfrac is not recommended for stress measurements: *(i)* due to the risk of severe borehole stability problems, stuck tools and well control (uncased open holes); *(ii)* difficulties for isolating a specific zone;

5. can be used in deviated wells provided that the strain relaxation is measured along a minimum of six directions, in order to allow the computation of the full strain tensor (Equation 2.1);

6. greater accuracy for determining the principal stress orientations; and,

7. the test is non-destructive: the samples remain available for any other purpose after the ASR test.

ASR Limitations

1. the physical principles are not completely understood: several factors remain undefined, as anisotropy effects in the thermal and pore pressure diffusion processes;

2. only applicable in well consolidated rocks: ASR tests on unconsolidated and poorly consolidated sandstones presented transducer embedment in the soft matrix and absence of measurable strains (Ramos *et al.*, 1994);

3. need of oriented cores: the tools for oriented coring are not completely reliable, sometimes rotation or lack of scribe marks makes part of the core useless (Owen *et al.*, 1988; Ramos *et al.*, 1994);

4. the models for computing the stress magnitudes are complex, needing several rock parameters as input data;

5. cores with a microcrack fabric due to tectonics or other causes cannot be tested since the stress would be released by the existing fractures, with no relation to the original stresses orientations (Warpinski and Teufel, 1986; El Rabaa, 1986; Kuhlman *et al.*,1992);

6. the validity of assuming a linear viscoelastic behavior for rocks may be questionable: if the principal strain directions change during the test it should be discarded because of anisotropic viscous behavior;

7. the error calculating the minimum in-situ stress magnitude is higher than measurements with microfracturing; and,

8. large time lost between drilling and starting the test may result in small displacements during the test, affecting the accuracy of the strain measurements (Brumley *et al.*, 1994).

2.1.2 Differential Strain Curve Analysis

The Differential Strain Curve Analysis (DSCA) is a laboratory technique also based on the formation of an oriented population of microcracks in the core due to the in-situ stress relief upon coring. The DSCA consists in analyzing the strain *versus* pressure curves from hydrostatic compression tests on rock samples. These tests intend to revert the expansion process by compressing the rocks beyond its original state of stress. Since only dry rock samples are tested in the DSCA, no considerations are made regarding pore pressure diffusion effects. Thus, rock contraction after coring does not affect the method, allowing for a much simpler formulation in the stress calculation.

Two main assumptions are made in the DSCA technique: the volumetric density of the microcracks is proportional to the in-situ stress magnitudes; and, subjecting the sample to a hydrostatic pressurization would revert the expansion process in any specific direction (Strickland and Ren, 1980), i.e., the deformation caused by closing the microcracks is considered analogous to the deformation in the opening phase. The first assumption was confirmed by acoustic emission experiments (Teufel, 1989), and allow the computation of the in-situ stress ratio by considering it to be proportional to the ratio between the magnitude of the strains generated by closing the cracks in the compression test. The second hypothesis assumes that the strain relaxation process is reversible. The creation of irregular surfaces in the microcrack opening phase, however, will surely demand more energy for being closed, configuring an irreversible process.

The intrinsic assumptions for the DSCA method, nevertheless, appears to be good enough for the needs of the oil industry, and the technique has provided good results in several conditions (Strickland and Ren, 1980; Ren and Roegiers, 1983; Teufel, 1984; Owen *et al.*, 1988; Kuhlman *et al.*, 1992).

Testing Procedure

Samples for the DSCA test are generally cubic, although cylindrical cores have also been used (Ramos and Rathmell, 1989). Strain gages are glued onto the samples for measuring the strain in several directions, allowing also a statistical analysis of the obtained results because of the duplicity in the measuring directions (Figure 2.2).

The hydrostatic compression curve for sedimentary rocks generally presents two distinct slopes, separated by a transition zone (Figure 2.3): the initial slope is attributed to the closing of microcracks and pore spaces, while the last slope is considered to represent the intrinsic compressibility of the constituent minerals in the rock matrix. Assuming a linear crack closure, the strain due to the cracks alone can be computed for each measured direction by subtracting out the matrix portion

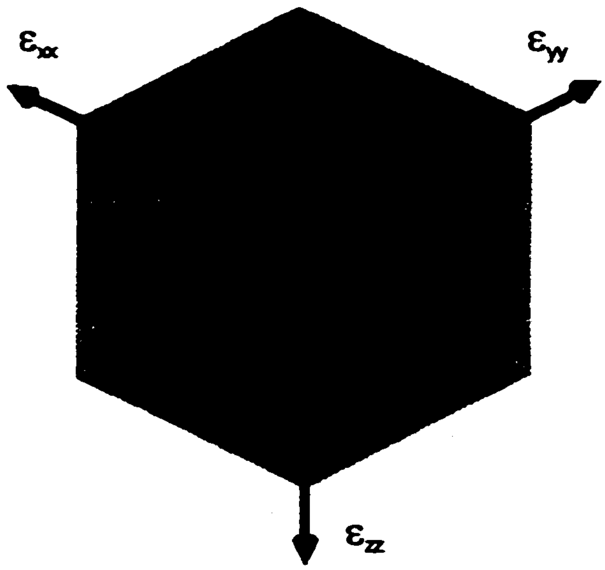

Figure 2.2: Strain gage positioning on the cubic sample.

from the total strain (Strickland and Ren, 1980; Ren and Roegiers, 1983):

$$\Delta\varepsilon_{ij}^{c} = \Delta\varepsilon_{ij}^{t} - \Delta\varepsilon_{ij}^{m} \tag{2.7}$$

where:

$\Delta\varepsilon_{ij}^{c}$ is the specific strain change (per unit of pressure) due to the complete or partial closing of all the cracks in the ij-direction;
$\Delta\varepsilon_{ij}^{t}$ is the total specific strain change (matrix plus cracks and pores) in the i-direction; and,
$\Delta\varepsilon_{ij}^{m}$ is the matrix specific strain change in the i-direction;.

Determining the In-Situ *Stress Field*

Similarly to the procedure for the ASR, the principal strain magnitudes are computed by the eigenvalues of the matrix presented in Equation (2.1), while the principal strain orientations are given by the eigenvectors of the same matrix. Taking advantage of the extra strain measurements, several matrixes can be solved, increasing the results reliability.

Once the ratio between the principal strains are known, the ratio between the

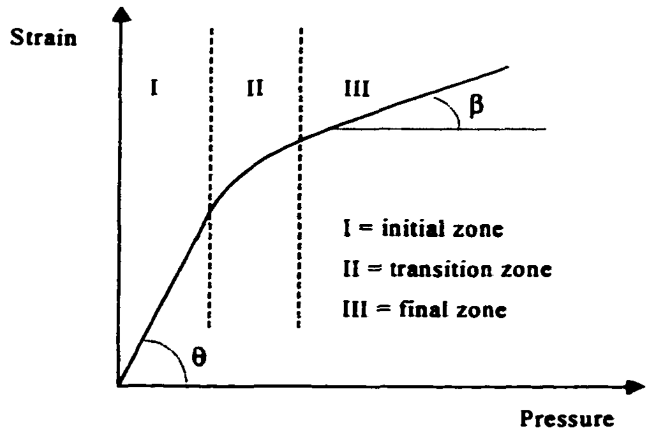

Figure 2.3: Typical compression curve for sedimentary rock samples.

principal stress magnitudes can also be computed, considering the stress-strain relations from linear elasticity. The in-situ stress field will be completely defined if another source of data, like microfracturing, provides the minimum in-situ stress.

It must be pointed out that although the ASR and DSCA methods are based on the same basic principles, a few differences between this two methods, shown in Table 2.1, must be taken into account whenever comparing their results. These differences arise from the fact that rock formations may have been subjected to larger stresses in its geological history, leaving a microcracking pattern that would be reflected in a testing procedure like the DSCA.

Table 2.1: Comparison between ASR and DSCA methods.

DSCA	ASR
- reflects the cumulative effect of all loadings and unloadings in the stress history of the rock;	- limited to the present state of stress;
- based on the rock complete strain relief;	- only the strain ocurring after recovering the core from the well is considered;

Summary of the DSCA Capabilities

1. good reliability when compared to other methods;

2. free from poroelastic and thermal effects;

3. the results are easier to analyze; and,

4. cheaper when compared to microfracturing.

Summary of the Method Disadvantages

1. need of some kind of core orientation, as in the ASR method;

2. like the ASR technique, the DSCA method cannot be used if a microcrack fabric can be detected at depth, before coring. Perreau *et al.* (1989), for example, obtained stress orientations 90^o from the correct azimuth when applying the DSCA and ASR methods, because of naturally fractured samples;

3. preparing cubic samples is more difficult than using cylindrical cores;

4. poorly cemented rocks are not suitable for epoxy-bonding of strain gages;

5. strain gages are not very practical for rock testing, i.e., the test setup is more complex when compared to the ASR ready-to-use apparatus. The construction of a strain measuring ring for triaxial testing with rock cubes would improve this aspect; and,

6. large strains cannot be measured by strain gages (Ramos *et al.*, 1994).

2.2 Field Methods

Hydraulic fracturing and breakout analyses are two of the most applied field methods for in-situ stress determination (Haimson, 1988; Nolte, 1989). While microhydraulic fracturing is the most reliable technique for gathering the minimum in-situ stress magnitude (Warpinski, 1989), breakouts can provide the orientation of the horizontal in-situ stresses (Gough and Bell, 1982). The rock mechanics literature for the oil industry presents an impressive amount of research about in-situ stress determination based on hydraulic fracturing and quite a few on breakout analyses. Only a few aspects of both methods principles, advantages and limitations, are presented in this section, to be compared to the ASR technique.

2.2.1 Hydraulic Microfracturing

Small volume injection jobs have been extensively used by the oil industry preceding major fracturing treatments, serving to diagnose the fracturing behavior of mainly low-permeability, hard rock formations, and allowing the determination of the minimum in-situ stress magnitude ($\sigma_{h\,\min}$), from the pressure decline curve (Warpinski and Smith, 1989).

The most interesting feature of hydraulic fracturing is determining the rock strength under the in-situ conditions. The logistic complexity of a hydrofrac, nevertheless, makes other methods, like core-based methods, more attractive and economical.

Experimental Procedure

A microfrac test can be defined as a hydrofrac job where no more than 500 l of fracturing fluid are pumped into a portion of the borehole, sealed off with a straddle packer, at a flow rate lower than 50 l per minute (de Bree, 1989). As the internal fluid pressure increases, the tangential stress at the borehole wall becomes tensile at a critical region, according to the 'Kirsch solution' (Goodman, 1980), initiating the fracture. If more fluid is pumped into the formation, the fracture will propagate perpendicular to the minimum far-field stress, since this direction requires the least pressure to fracture the formation. In vertical wellbores, the fracture trace at the borehole wall coincides with the minimum far-field stress (Figure 2.4), allowing the determination of the stress orientation from borehole methods.

Situations do exist in which microfracturing cannot be applied: open hole mi-

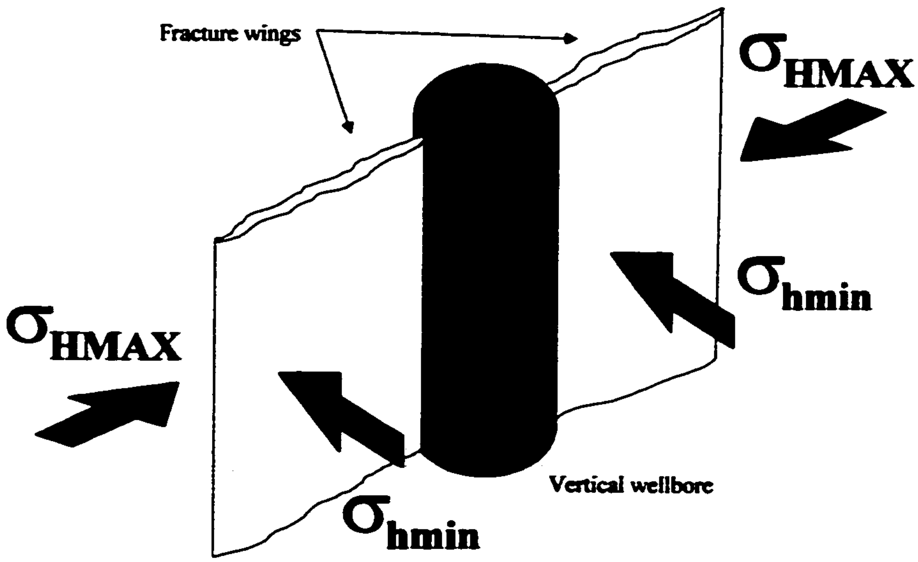

Figure 2.4: Vertical hydraulic fracture.

crofracturing are generally preferred, because there is no interference from perforation damages, casing and cement annulus (Warpinski, 1989), but stability concerns and potential well control problems may prioritize cementing and casing the borehole. Moreover, the interaction between the drilling fluid and shaly formations very often produces an irregular borehole diameter, causing problems to packer installation and potential leaks that can mask the pressure curve (Bloch *et al.*, 1997).

Computing the In-Situ *Stress Magnitudes*

The theoretical pressure-time curve for microfracturing allows identifying the breakdown pressure at which the crack is formed, P_b, the instantaneous shut-in pressure, *ISIP*, immediately after pumping stops and eventually a reopening pressure, P_r, if more than one cycle is performed (Figure 2.5).

Considering the fracture to propagate perpendicular to the minimum in-situ stress, the *ISIP* recorded in the field can be assumed equal to $\sigma_{h\,\min}$ (Cornet and Valete, 1984; Warpinski, 1989; Economides and Nolte, 1989). Nevertheless, the

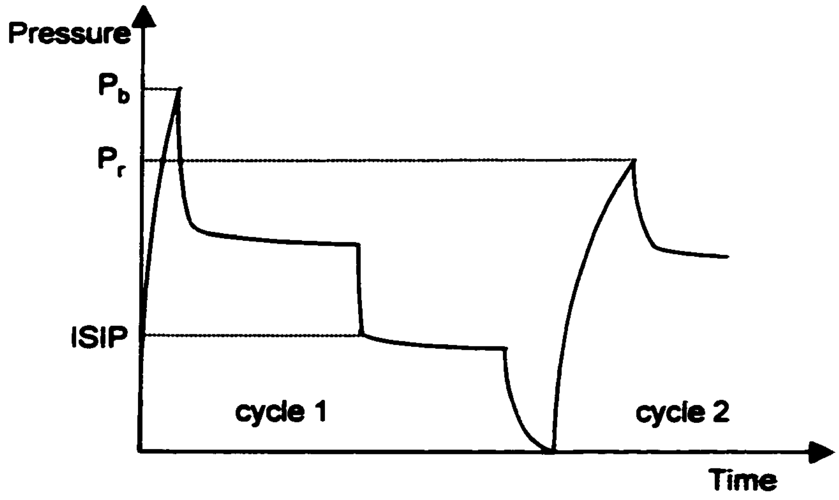

Figure 2.5: Ideal pressure-time curve (as recorded from the surface): P_b is the breakdown pressure; P_r is the re-opening pressure; and *ISIP* is the instantaneous shut-in pressure.

interpretation of the pressure records is not always straightforward, mainly if the rock permeability allows high fluid flow into the formation, disturbing the pattern of the pressure-time curve. Even though several methods have been developed for improving the pressure decline analysis, and the correct ISIP determination (Warpinski and Smith, 1989), the stress computation may become rather subjective.

Microfracs can also provide the maximum horizontal in-situ stress magnitude (σ_{HMAX}) from Equations (2.8) or (2.9) (Haimson and Huang, 1990; Economides and Nolte, 1989), which are valid only for uncased boreholes, where the pressure record is not affected by the perforations. If the borehole wall is assumed impermeable due to mudcake buildup, one must use Equation 2.8; on the other hand, assuming that there are no barriers to fluid flow into the formation during the fracturing, poroelastic effects must be considered, and Equation (2.9) should be used:

$$P_{b_{upper}} = 3\sigma_{h\,\min} - \sigma_{HMAX} + T_0 - p \tag{2.8}$$

$$P_{b_{lower}} = \frac{3\sigma_{h\min} - \sigma_{HMAX} + T_0 - 2\eta p}{2(1-\eta)} \tag{2.9}$$

where:

P_b is the breakdown pressure, measured when the fracture starts to propagate;
$\sigma_{h\min}$ is assumed equal to the $ISIP$;
T_0 is the rock tensile strength, which can be obtained from rock laboratory tests or assumed as $T_0 = P_b - P_r$ (Goodman, 1980);
p is the pore pressure; and,
η is the poroelastic stress coefficient, defined as:

$$\eta = \alpha\frac{(1-2\nu)}{2(1-\nu)} \tag{2.10}$$

where Poisson's ratio, ν , and Biot's poroelastic effective stress coefficient, α, must be determined from laboratory tests.

Gathering the In-Situ *Stress Orientation*

There are several methods for detecting the fracture orientation from hydrofrac jobs. They can be subdivided into real-time methods, like: tiltmeters and downhole seismic tools (Lacy, 1984), and post-test methods, like: impression packers (Meehan, 1994); borehole televiewers; multiple radioactive tracer logs; gamma ray logs and pulse neutron logs (Mullen *et al.*, 1996; Morales *et al.*, 1997) and overcoring (Yale *et al.*, 1992). The techniques based on the fracture trace along the wellbore wall are only applicable to vertical boreholes, since the fracture at the wall is aligned to the far-field minimum in-situ stress. Most of these methods, nevertheless, may fail with microfracs, because of the small dimensions of the created fractures. Determining the horizontal stress orientation from microfracs remain thus, a major shortcoming for the method.

Hydraulic Fracturing Advantages for Computing the In-Situ *Stress Field*

1. most reliable method for directly determining $\sigma_{h\min}$ (Teufel, 1982); and,

2. the stress is determined exactly under the in-situ conditions.

1. stopping the drilling job and removing the drilling string for a microfrac test means increasing the rig operational time, and therefore the drilling cost, besides running into potential well stability problems;

2. borehole sloughing and creep in shale formations can make it difficult to isolate the zone of interest in order to perform the microfrac (Khulman, 1990); and,

3. need of a larger hydrofrac combined to another technique for verifying the stress orientation.

2.2.2 Breakouts

Breakouts are defined as intervals where the cross-section of vertical wellbores is non-circular due to fracturing of the borehole wall, as a consequence of a non-hydrostatic horizontal stress field. Based once more on the 'Kirsch solution' for circular openings under compression (Goodman, 1980), and low borehole internal pressure, the rock spalling in breakouts can be associated to the orientation of the minimum horizontal in-situ stress, since the tangential stress concentration produces a critical region in that direction.

Wellbore breakouts have been observed in several areas of North America and Europe (Gough and Bell, 1982; Podrouzeck and Bell, 1985; Bell and Babcock, 1986; Paillet and Kim, 1987; Bell, 1990; Bell *et al.*, 1992; Zoback and Peska, 1995; Fejerskov and Bratli, 1998) and analyzed by experimental tests (Haimson and Herrick, 1989; Martin *et al.*, 1994), proving to be a reliable indicator of the horizontal principal stress orientations. In opposition to ASR strain measurements, the rock deformation in breakouts is huge and clearly identifies the stress orientation, without having to compute the strain tensor. Breakouts occurrence, nevertheless, is conditioned by the horizontal stress contrast: it has to be large enough so that the stresses at the critical region may exceed the rock strength, leading to failure.

The borehole elongation (Figure 2.6) can be identified by several commercial logging tools, like the conventional four-arms dipmeter, and more sophisticated logging tools, which can send images of the borehole wall to the surface based upon changes on the formation microresistivity (Morrison and Thibodaux, 1984; Seiler *et al.*, 1994); differences in the acoustic travel time at a cross section of the wellbore (Taylor, 1983); and, echoes amplitude from ultrasonic scanners (Hayman *et al.*, 1994).

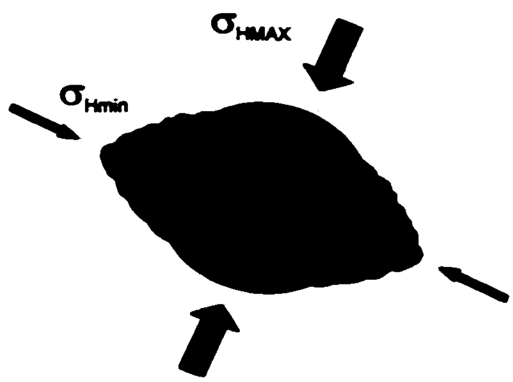

Figure 2.6: Breakout cross-section: the long axis of the breakout is parallel to the minimum horizontal principal stress.

It is important to correctly distinguish between breakouts and other causes of borehole ellipticity, including drilling pipe wear and washouts. Fejerskov and Bratli (1998), for example, reported a large problem for differentiating borehole breakouts from drilling-induced keyseats even at low hole inclination. Bell *et al.* (1992), proposed a limiting inclination of 5^0 in order to allow breakout identification in a well.

Also the rock permeability seems to play some role in breakout identification:

Podrouzek and Bell (1985) pointed out that more permeable sandstones usually have a limited amount of breakouts because of the strengthening provided by mudcake armouring of the borehole walls. Bell *et al.* (1991) confirmed that there is a higher probability of detecting breakouts in brittle rocks like shale, shale-rich or carbonate intervals than in sandstones.

Using breakouts for establishing the horizontal in-situ stress orientations for a specific region requires studying a large number of wells (depending on the size of the area 25 to 50 wells may be needed, according to Bell *et al.*, 1991) in order to confirm the observations. Furthermore, each well must show breakouts over several thousands meters, in order to provide a reliable statistical analysis and lead to the stress distribution pattern. There are situations, however, where even a positive breakout identification may be helpless for determining the stress orientations: Bell *et al.* (1992) attributed the inconsistent breakout results for the stress regime of the southwestern part of the Aquitaine Basin (France), to both weak horizontal stress anisotropy and geomechanical discontinuities.

Several researchers attempted to define a correlation between breakouts and in-situ stress magnitudes (Zoback *et al.*, 1985; Haimson and Herrick, 1989; Haimson and Song, 1995; Zoback and Peska, 1995). None of these works, nevertheless, analyzed the kinematical aspect of failure (Detournay and Roegiers, 1986), relating only the size and shape of the breakouts to the stress field. Furthermore, based on the numerical simulations by Zheng *et al.* (1988), breakouts cross-sections cannot be uniquely related to the magnitude of the original in-situ stress, i.e., the same rock under the same initial stress condition can produce different breakouts geometries, depending on the rock stress history.

Computing the stress magnitudes from breakouts seems to be in a stage even more initial than in the ASR method. The initial consensus of a shear failure

(Zheng *et al.*, 1988; Haimson and Song, 1993) has been revised by Germanovich *et al.* (1994), indicating that breakouts are most probably caused by the tensile failure of pre-existing cracks, which propagate parallel to the free surface of the borehole. A better understanding of the mechanisms behind breakouts is still required before computing the stress magnitudes, and the method remains, nowadays, as a valuable tool for determining only the horizontal in-situ stress orientation.

Advantages of Using Breakouts for In-Situ *Stress Determination*

1. the principal horizontal stress orientation is detected under in-situ conditions, improving the method reliability;
2. the method has been widely validated for vertical wellbores; and,
3. in-situ stress information can be gathered from logging tools routinely used for analyzing borehole ellipticity.

Disadvantages of Using Breakouts for In-Situ *Stress Determination*

1. only the stress field orientation is provided;
2. only applicable for vertical boreholes;
3. not always available since it depends on the stress anisotropy and rock strength; and,
4. can be erroneously identified from drill pipe wear, keyseats and washouts.

Chapter 3

A Poroviscoelastic Formulation for the Strain Relaxation Process

The principal steps for deriving the poroviscoelastic equations for the strain relaxation process are explained in this chapter. The indicial notation, as defined by Chen and Saleeb (1982), was used in most of the cases, in order to abbreviate the equations. Nevertheless, the extended form of the vectors' and tensors' components was also used in a few key-equations for a better comprehension of the physical meaning.

Since the main goal of the model was to verify the influence of the pore fluid diffusion on the core deformations, the governing equations and parameters are presented for the case of fully coupled poroelasticity. In order to be more realistic, the rock properties are allowed to change during the core relaxation, i.e., a time-dependence (viscous behavior) was also included by means of the Viscoelastic Correspondence Principle — VCP (Flügge, 1975); providing, finally, the complete poroviscoelastic solution.

The core deformations are modelled from the initial coring time until they become negligibly small; this process may be shorter or longer, depending on the rock permeability and mechanical properties[1]. The boundary conditions for the model

[1]Experimental results on siltstones presented negligible strains after 12 hours testing (Butterworth *et al.*, 1991); the anelastic strain was completed within 6 to 10 hours in unconsolidated

are the variation in the stress and pore pressure at the core outer surface, during tripping out of the borehole. These conditions, together with the rock properties and the chosen viscous model, are assumed to define a specific radial displacement *versus* time curve, and then lead to a unique estimate of the in-situ stresses.

Although numerical solutions using finite or boundary elements are applied in most poroelasticity problems, the geometry analyzed in this dissertation is sufficiently simple, that a closed-form solution could be derived. The differential equations were solved in the Laplace domain, and then numerically inverted to the time domain, via the Stehfest inversion method (Stehfest, 1970b).

The model main outputs are:

(i) the radial displacements for the complete anelastic process. This behavior will then be compared to the available viscoelastic approach; quantifying the influence of poroelasticity to the ASR process;

(ii) the pore pressure distribution history, in an attempt to explain the core deformation pattern; and,

(iii) the in-situ radial stress or initial reservoir pressure from the radial displacements measured in the field with the ASR device; comparing with the stresses predicted by the conventional viscoelastic models.

3.1 Modeling the Coring Process

Modeling the coring process took into account two distinct types of deformations the core exhibits when cut away from the rock mass: elastic, in a first stage, and anelastic as a second and final stage. The stress and pore pressure at the core boundary were assumed to drop instantaneously to the drilling fluid pressure as coring started,

sandstones (Ramos *et al.*, 1994); while tests on shales in a Saskatchian potash mine still presented measurables strains after 10 days (Roegiers, 1999).

whatever the drilling conditions: overbalanced, balanced or underbalanced. A linear pressure decline was further assumed during the trip out of the borehole.

3.1.1 Strain Variation

The strain behavior[2] immediately after coring is shown in Figure 3.1. The elastic process is represented by a straight line from A to B, at the coring instant ($t = \tau_0$), while the anelastic process, which begins with the sample still inside the coring barrel, is represented from B to E. At C ($t = \tau_1$) the sample reaches the surface, and the preparation for the ASR test takes from C to D ($t = t_1$): generally speaking, two pieces of the whole core are cut, polyurethane wrapped or painted for preventing moisture evaporation, and placed into the ASR constant temperature testing chamber. The displacement transducers are then adjusted around the sample, as shown in Figure 3.2, and the data acquisition is performed from D to E ($t = t_2$), when the strain variation becomes negligeable.

The reason why sealing paint is applied for preventing moisture evaporation is to avoid pore deformations due to diffusion and subsequent pore pressure redistribution. Whatever the process used for avoiding moisture evaporation from the sample surface, pore fluid redistribution in an ASR test cannot be avoided, since it has already started at the moment of drilling, and continued throughout tripping, because of the pore pressure variation at the core external surface.

3.1.2 Stress and Pore Pressure Variation

The original radial stresses at the core boundary were assumed to become instantaneously equal to the drilling fluid pressure at the instant of coring, as well as the pore pressure at the core surface. The core is then under a hydrostatic stress field, having the total radial stress equal to the pore pressure at the core surface and equal

[2] *(i)* the rock temperature can be assumed to equalize before the test;
(ii) vibration effects during the tests are minimized by the testing apparatus design.

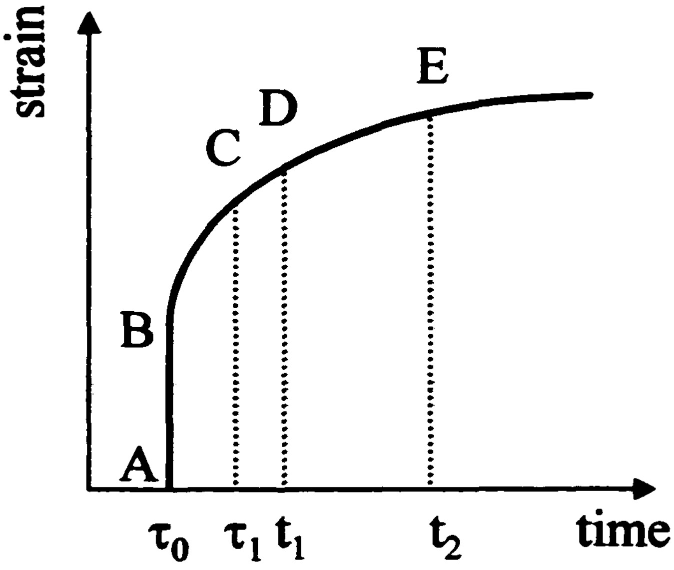

Figure 3.1: Strain variation during coring.

Figure 3.2: A rock sample wrapped in plastic and instrumented with the displacement transducers.

to the drilling fluid pressure at the coring depth. As the whole core travels up to the surface, the drilling fluid pressure is gradually reduced to zero. The variation in the drilling fluid pressure, during the trip out of the borehole, was modelled as linear, i.e.:

$$\frac{dp}{dt} = -\rho g \frac{dh}{dt} \tag{3.1}$$

where,

$$\begin{cases} dp/dt \text{ is the variation in the drilling fluid pressure;} \\ \rho \text{ is the drilling fluid density;} \\ g \text{ is the local gravity acceleration; and,} \\ dh/dt \text{ is the coring barrel speed (assumed to be constant).} \end{cases}$$

The negative sign in Equation (3.1) indicates that p is decreasing with time. Figure 3.3 shows schematically the assumed changes in the radial stress and pore pressure at the core surface for overbalanced, balanced and underbalanced drilling conditions[3].

3.2 Poroviscoelastic Approach

Whenever the pore pressure at the core external surface changes, the pressure inside the core is affected, leading to a diffusion-type redistribution process. As discussed in the literature review chapter, the solid deformations due to changes in the pore pressure inside the rock are greatly overlooked by purely viscoelastic models for computing stresses from the rock anelastic deformations. A more accurate approach must take poroviscoelastic effects into account, considering that the strains measured in ASR do include pore deformations (although sometimes negligible), because of the unavoidable pore pressure redistribution during coring.

The mechanical response of a fluid-saturated porous material to changes in the pressure and/or flow across its boundaries is governed by a coupled time-dependent

[3]If an impermeable mudcake covers the core an alternative boundary condition should be taken considering the no-flow condition.

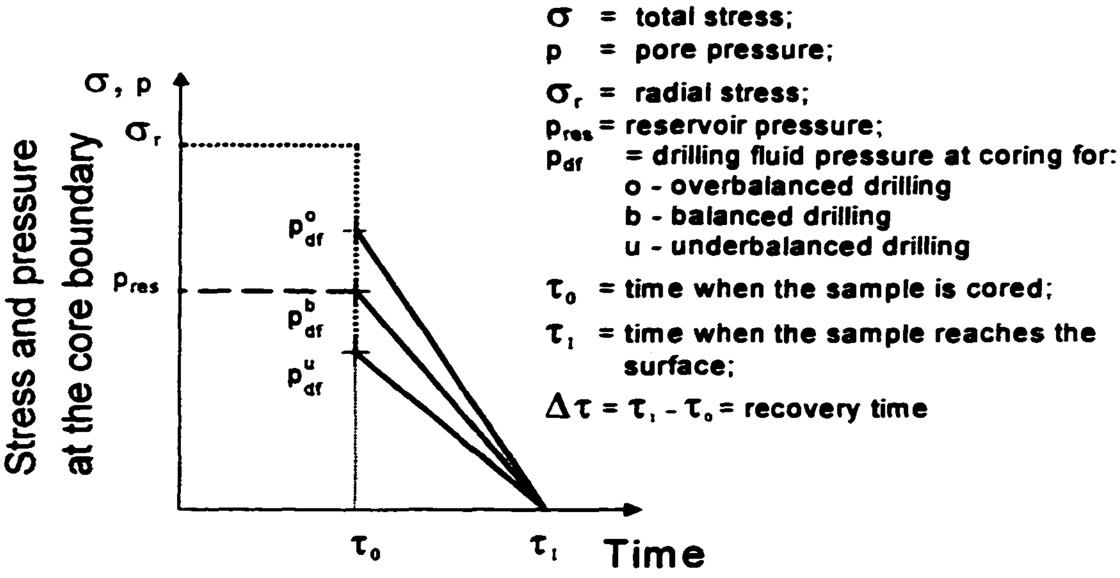

Figure 3.3: Total stress and pore pressure histories at the external surface of a core during coring and tripping out of the borehole.

deformation/diffusion process. Reductions in the pore pressure during tripping, for example, will lead to shrinkage of the pore volume, potentially masking some or all of the overall expansion due to the stress relief process. The influence of poroviscoelasticity is obviously dependent on the rock physical and mechanical properties, as well as on the pore fluid viscosity. Temperature effects can also play an important role in the rock deformations occurring after coring. Nevertheless, temperature effects are not analyzed in this dissertation.

The main questions to be answered by the poroviscoelastic model are:

(i) In which types of rocks can the strain generated by poroviscoelastic effects significantly affect the total strain measured in the ASR test?

(ii) What error is incurred when the poroviscoelastic effects are ignored? and,

(iii) Is there a way to overcome the complexity of computing in-situ stresses using a poroviscoelastic approach for the ASR test?

The poroviscoelastic model utilized in this study is based on the linear poroelastic analysis for cylindrical rock cores published by Detournay and Cheng (1993). The coupled poroelasticity theory, in turn, can be seen as an extension of the elasticity theory, but adding the coupling of the porous media deformations with the fluid flow through the pore spaces. A few assumptions are necessary for the application of linear poroelasticity to the cylinder problem:

- axisymmetric geometry;
- porous media is considered isotropic and homogeneous;
- small strains and displacements, so that they can be assumed to be linear;
- plane strain conditions;
- strains and stresses are proportional;
- body forces can be neglected;
- pores are interconnected in such a way that there is free flow;
- porous media is fully saturated;
- pore fluid is Newtonian and incompressible; and,
- temperature variations are not taken into account.

Under these assumptions, the rock deformations are further assumed to be homogeneous in the radial direction (independent of the angular position) and the radial strains are obviously only a function of the radial position in the rock. In other words, the situation analyzed is that of equal horizontal stresses. The plane strain condition is a simplifying assumption which is applicable to ASR once the core length is much larger than the diameter, while still in the coring barrel. Since the rock was previously assumed to be isotropic and homogeneous, there is no reason to believe that the pore pressure diffusion process will not be equally spread throughout the whole sample.

3.2.1 Governing Equations in Poroelasticity

The modern poroelasticity theory was initiated by Biot (1941), and a new formulation was presented by Rice and Cleary (1976), redefining some of the physical constants in the way they are used in this dissertation. Four independent constants plus the rock permeability are necessary for deriving all the relevant parameters in an isotropic poroelastic medium. It should be noted, however, that the basic constants cannot be randomly chosen: two of them must represent the rock drained behavior, while the two others must be associated to the fluid flow aspects.

Another two aspects were still considered in this dissertation for determining the basic constants: *(i)* facility and reliability for measuring the constants in the laboratory; and, *(ii)* need of including the viscous effects into the governing equations. The chosen basic parameters, finally, were:

$$\left\{ \begin{array}{l} \text{Young's modulus, } E; \\ \text{bulk modulus, } K; \\ \text{grain bulk modulus, } K_s; \\ \text{grain bulk modulus, } K_s; \\ \text{undrained bulk modulus, } K_u\text{; and,} \\ \text{rock permeability, } k. \end{array} \right.$$

The set of governing equations for analyzing the stress-strain behavior in the coupled theory of linear poroelasticity includes the basic equations of fluid mechanics, fluid flow in porous media and rock mechanics. These equations are:

- Equilibrium equation:

$$\sigma_{ij,j} = 0 \tag{3.2}$$

- Darcy's law:

$$q_i = -\kappa p_{,i} \tag{3.3}$$

where,

$$\left\{\begin{array}{l} q_i \text{ is the flowrate in the } x_i\text{-direction;} \\ \kappa \text{ is the mobility, defined as the ratio between the rock permeability} \\ \text{and the fluid absolute viscosity } (k/\mu)\text{; and,} \\ p_{,i} \text{ is the pressure gradient in the i-direction.} \end{array}\right.$$

- Continuity equation:

$$\frac{\partial \zeta}{\partial t} + q_{i,i} = 0 \tag{3.4}$$

where ζ is defined as the change in the fluid volume per unit volume of porous material during the diffusive fluid mass transport, computed as:

$$\zeta = \frac{\Delta V_f}{V} \tag{3.5}$$

where ΔV_f is the amount of fluid entering or leaving a Representative Elementary Volume-REV[4]; and V is the volume of the REV.

- Constitutive equations for poroelasticity:

The stress-strain relationship can be written as:

$$\sigma_{ij} = 2G\varepsilon_{ij} + \frac{2G\nu}{1-2\nu}\varepsilon\delta_{ij} - \alpha p\delta_{ij} \tag{3.6}$$

where,

$$\left\{\begin{array}{l} G \text{ is the shear modulus;} \\ \nu \text{ is Poisson's ratio;} \\ \delta_{ij} \text{ is the Kronecker delta function } (\delta_{ij} = 1 \text{ for } i = j \text{ and} \\ \delta_{ij} = 0 \text{ for } i \neq j)\text{; and,} \\ \alpha \text{ is Biot's effective stress coefficient, which for isotropic} \\ \text{rocks is given by:} \end{array}\right.$$

[4]REV is an infinitesimal cell, large enough when compared to the pore and to grain sizes to be considered representative.

$$\alpha = 1 - \frac{K}{K_s} \tag{3.7}$$

where K is the bulk modulus and K_s is the grain modulus.

It is interesting to note that having the pore pressure $p = 0$ in Equation (3.6) will reproduce the elastic constitutive equations. Equation (3.6) can also be written in terms of the fluid content variation as:

$$\sigma_{ij} = 2G\varepsilon_{ij} + \frac{2G\nu_u}{1-2\nu_u}\varepsilon\delta_{ij} - \alpha M\zeta\delta_{ij} \tag{3.8}$$

where M is known as Biot's modulus, given by:

$$M = \frac{2G(\nu_u - \nu)}{\alpha^2 (1-2\nu)(1+\nu_u)} \tag{3.9}$$

and ν_u is the undrained Poisson's ratio.

- A Navier-type equation for the displacement u_i is obtained by substituting Equation (3.8) in Equation (3.2):

$$G\nabla^2 u_i + \frac{G}{1-2\nu_u} u_{k,ki} = \alpha M\zeta_{,i} \tag{3.10}$$

The diffusion equation for the fluid content is then given by:

$$\frac{\partial\zeta}{\partial t} - c\nabla^2\zeta = 0 \tag{3.11}$$

where c is the rock diffusivity, given by:

$$c = \frac{2\kappa G(1-\nu)(\nu_u - \nu)}{\alpha^2(1-2\nu)^2(1-\nu_u)} \tag{3.12}$$

Under hydrostatic stress conditions, which results in an axisymmetric problem, the Laplacian operator is given by:

$$\nabla^2 = \left(\frac{\partial^2}{\partial r^2} + \frac{1}{r}\frac{\partial}{\partial r}\right) \tag{3.13}$$

Application of such Laplace transformation to the various quantities involved in Equation (3.11) allows the time derivative to be eliminated:

$$\mathfrak{L}\left[\frac{\partial \zeta}{\partial t}\right] = s\tilde{\zeta} - \zeta(0) \tag{3.14}$$

where,

$$\begin{cases} \mathfrak{L} \text{ denotes the Laplace transform;} \\ \tilde{} \text{ represents the function in the Laplace domain;} \\ s \text{ is the Laplace variable; and,} \\ \zeta(0) = 0. \end{cases}$$

Using (3.13) and (3.14), Equation (3.11) can be rewritten as:

$$\frac{d^2\tilde{\zeta}}{dr^2} + \frac{1}{r}\frac{d\tilde{\zeta}}{dr} - \frac{s}{c}\tilde{\zeta} = 0 \tag{3.15}$$

The general solution of Equation (3.15) has already been derived by Detournay and Cheng (1993) as:

$$\tilde{\zeta} = D_1 I_0(\xi) \tag{3.16}$$

where,

D_1 is an integration constant;

I_0 is the modified Bessel function of first kind and order zero;

$$\begin{cases} \xi = r\sqrt{\dfrac{s}{c}} \\ \beta = R\sqrt{\dfrac{s}{c}} \end{cases} \tag{3.17}$$

and, R is the rock core external radius.

A relationship between the volumetric strain and the variation of fluid content can be obtained by considering the Navier Equation (3.10) in the radial direction only:

$$\frac{\partial \varepsilon}{\partial r} = \frac{\eta}{GS}\frac{\partial \zeta}{\partial r} \tag{3.18}$$

where,

η is the poroelastic stress coefficient, given by:

$$\eta = \frac{\alpha (1 - 2\nu)}{2 (1 - \nu)} \tag{3.19}$$

S is the storage coefficient, computed as:

$$S = \frac{(1 - \nu_u)(1 - 2\nu)}{M (1 - \nu)(1 - 2\nu_u)} \tag{3.20}$$

The volumetric strain in the Laplace domain can be written by substituting Equation (3.16) into Equation (3.18), and integrating both sides of the resulting expression:

$$\tilde{\varepsilon} = \frac{\eta}{\beta G S} D_1 I_0(\xi) + D_2 \tag{3.21}$$

The volumetric strain, ε, can be written in cylindrical coordinates as:

$$\varepsilon = \varepsilon_r + \varepsilon_\theta + \varepsilon_z \tag{3.22}$$

Considering the symmetry of the cylinder problem in the above:

$$\begin{cases} \varepsilon_r = \dfrac{\partial u_r}{\partial r} \\ \varepsilon_\theta = \dfrac{u_r}{r} \\ \varepsilon_z = \dfrac{\partial w}{\partial z} \end{cases} \tag{3.23}$$

Taking into account the plane strain assumption, i.e.:

$$\varepsilon_z = 0 \tag{3.24}$$

The volumetric strain can be finally derived by replacing Equations (3.23) and (3.24) into Equation (3.22):

$$\varepsilon = \frac{1}{r}\frac{\partial}{\partial r}(r u_r) \tag{3.25}$$

The radial displacements in the Laplace domain are then obtained by integrating Equation (3.25) using Equation (3.21):

$$\tilde{u}_r = D_1 \frac{\eta R}{\beta G S} I_1(\xi) + D_2 \frac{r}{2} \tag{3.26}$$

where D_1 and D_2 are integration constants to be defined by the boundary conditions.

Two boundary conditions are needed for computing D_1 and D_2. They will be initially imposed as the variation of pore pressure and radial stress at the core external surface.

The variation of pore pressure can also be written as:

$$p = M\left(\zeta - \alpha\varepsilon\right) \tag{3.27}$$

Using the strain definitions for the plane strain problem (Equations 3.22 to 3.24) and transforming Equation (3.27) into the Laplace domain:

$$\tilde{p} = M\left[\tilde{\zeta} - \alpha\left(\frac{\partial\tilde{u}}{\partial r} + \frac{\tilde{u}}{r}\right)\right] \tag{3.28}$$

From Equation (3.26):

$$\frac{\partial\tilde{u}}{\partial r} = \frac{\eta D_1}{GS}\left[I_0(\xi) - \frac{I_1(\xi)}{\xi}\right] + \frac{D_2}{2} \tag{3.29}$$

Finally, the expression for the pore pressure variation is obtained in the Laplace domain by inserting Equations (3.16), (3.29) and (3.26) into Equation (3.28):

$$\tilde{p} = D_1\left[MI_0(\xi)\left(1 - \frac{\eta\alpha}{GS}\right)\right] - \alpha M D_2 \tag{3.30}$$

The radial stresses can be derived from Equation (3.8) in cylindrical coordinates and for plane strain conditions:

$$\sigma_r = 2G\varepsilon_r + \frac{2G\nu_u}{1-2\nu_u}\left(\varepsilon_r + \varepsilon_\theta\right) - \alpha M\zeta \tag{3.31}$$

Equation (3.31) can then be rearranged and transformed into the Laplace domain, giving:

$$\tilde{\sigma}_r = D_1\frac{2\eta}{S}\left[\left(\frac{1-\nu_u}{1-2\nu_u} - \frac{\alpha MS}{2\eta}\right)I_0(\xi) - \frac{I_1(\xi)}{\xi}\right] + D_2\frac{G}{1-2\nu_u} \tag{3.32}$$

Summarizing, the integration constants D_1 and D_2 can now be computed from the initial boundary conditions through Equations (3.30) and (3.32).

3.2.2 Boundary Conditions

The general procedure for analyzing linear poroelasticity problems should take into account the linear characteristics and isolate the physical phenomena by considering several fundamental loading modes. These modes are then superimposed, representing a variety of boundary conditions. Table 3.1 shows a total of eight different loading modes at the cylinder external surface, as described by Abousleiman and Cui (1998).

Table 3.1: Loading modes utilized in the cylinder problem.

Mode	σ_r	$\tau_{r\theta}$	p	ε_z	q_r
I	$-P_0(t)$		0		
IA	$-P_0(t)$				0
II	0		$p_0(t)$		
IIA	0				$\dot{Q}(t)/2\pi r$
III	$-S_0 cos2\theta$	$S_0 sin2\theta$			
IV			0	$\dot{\varepsilon}(t)$	
IVA				$\dot{\varepsilon}(t)$	0

Obs.: compression is assumed negative.

where,

σ_r is the radial stress;
$\tau_{r\theta}$ andτ_{rz} are the shear stresses;
p is the pore pressurein the rock sample;
ε_z is the axial strain imposed on the rock sample;
q_r is the radial flow at the cylinder surface;
P_0(t) is a time-dependent radial loading on the cylinder surface;
S_0 is the amplitude of a sinusoidal loading;
p_0(t) is a time-dependent radial loading on the cylinder surface;
$\dot{\varepsilon}(t)$ is an axial strain rate; and,
$\dot{Q}(t)$ is the fluid flow rate across the cylinder surface per unit depth.

Modes I and II can represent the coring problem under hydrostatic conditions, having the radial stress and pore pressure at the core surface as boundary conditions. Modes IA and IIA can also represent the coring problem, having the fluid flow at the core external surface, instead of the pore pressure, as a second boundary

Table 3.2: Summary of the boundary conditions at the core surface.

Mode	Boundary Condition
I and II	radial stress pore pressure
IA and IIA	radial stress flow rate
III	radial stress tangential stress
IV	pore pressure axial strain rate
IVA	axial strain rate flow rate

condition. These four initial modes (I to IIA) are plane strain problems, since the strain perpendicular to the $r\theta$-plane is assumed to be zero.

Mode III deals with the deviatoric stresses, which are vectorial components, not affecting the rock volume (Roegiers and Vandamme, 1999); and thus, were not included in the poroelastic analysis. Nevertheless, they will be added later on (chapter 5), to fully describe the actual stress field obtained from ASR data.

Modes IV and IVA consider generalized plane strain conditions (the axial strain is not a function of the radial position), typical of laboratory compression tests under constant axial strain rate; this will not be used for simulating the coring process.

Table 3.2 summarizes the boundary conditions for each loading mode. Only loading Modes I and II were used as boundary conditions for the poroelastic analysis of the coring problem, leaving Modes IA, IIA for future work.

The final derivation for the radial displacement equation in Modes I and II is presented next: constants D1 and D2 are evaluated from a set of two equations, according to the known boundary condition, finally providing the desired formula.

Mode I: boundary conditions: $\sigma_r = -P_0(t)$; $p_0 = 0$ at $r = R$:

Radial displacements:

Letting $\tilde{p}_0 = 0$ in Equation (3.30), and $\bar{\sigma}_r = -\tilde{P}_0(s)$ in Equation (3.32), the following system of two equations is set up and solved for D_1 and D_2:

$$\begin{cases} -\tilde{P}_0 = D_1 \dfrac{2\eta}{S}\left[\left(\dfrac{(1-\nu_u)}{(1-2\nu_u)} - \dfrac{\alpha MS}{2\eta}\right) I_0(\xi) - \dfrac{I_1(\xi)}{\xi}\right] + D_2 \dfrac{G}{1-2\nu_u} \\ D_1\left[MI_0(\xi)\left(1-\dfrac{\eta\alpha}{GS}\right)\right] - \alpha M D_2 = 0 \end{cases} \tag{3.33}$$

The radial displacement for loading Mode I is given by replacing D_1 and D_2 from Equations (3.33) into Equation (3.26):

$$\tilde{u}_r = \tilde{P}_0 \frac{r}{2G} \frac{(1-2\nu_u)(1-\nu) I_0(\beta) + 2(\nu_u - \nu)\dfrac{I_1(\xi)}{\xi}}{(1-\nu) I_0(\beta) - 2(\nu_u - \nu)\dfrac{I_1(\beta)}{\beta}} \tag{3.34}$$

where $\tilde{P}_0$ is a function of the Laplace variable, s, to be defined by the variation imposed on the radial stress during coring.

Equation (3.34) can be checked for large times at $r = R$ (at the core boundary): letting $t \to \infty$ means $s \to 0$; then knowing that $I_0(0) = 1$ and $I_1(0) = 0$, and applying L'Hospital rule (Abramowitz and Stegun, 1970) for computing $\lim_{x \to 0} \dfrac{I_1(x)}{x} = 0$, the linear elastic solution is retrieved (the complete derivation of this equation under the linear elasticity theory is shown in Appendix A):

$$u_r = \frac{-P(t)R}{2G}(1-2\nu) \tag{3.35}$$

For small times, when the rock behavior is mostly undrained: $t \to 0$ and, hence, $s \to \infty$, and the displacement is still given by Equation (3.35), replacing ν by ν_u.

Pore pressure variations:

With D_1 and D_2 from Equations (3.33) now substituted into Equation (3.30), the pore pressure is given by:

$$\tilde{p} = \tilde{P}_0 \frac{(1-\nu)\left[I_0(\beta) - I_0(\xi)\right]}{(1-\nu) I_0(\beta) - 2(\nu_u - \nu)\dfrac{I_1(\beta)}{\beta}} \tag{3.36}$$

Mode II: boundary conditions: $\sigma_r = 0$; $p = p_0(t)$ at $r = R$:

Radial displacements:

Applying the Laplace transform to the boundary conditions once more: $\tilde{p} = \tilde{p}_0(s)$, and $\tilde{\sigma}_r = 0$. Another system of two equations can be solved for D_1 and D_2, using Equation (3.30) and Equation (3.32) again:

$$\begin{cases} D_1 \dfrac{2\eta}{S}\left[\left(\dfrac{1-\nu_u}{1-2\nu_u} - \dfrac{\alpha M S}{2\eta}\right) I_0(\xi) - \dfrac{I_1(\xi)}{\xi}\right] = -D_2 \dfrac{G}{1-2\nu_u} \\ \tilde{p}_0 = D_1\left[M I_0(\xi)\left(1 - \dfrac{\eta\alpha}{GS}\right)\right] - \alpha M D_2 \end{cases} \tag{3.37}$$

Likewise Mode I, the radial displacements for Mode II are given by replacing D_1 and D_2 from Equations (3.37) into Equation (3.26):

$$\tilde{u}_r = \tilde{p}_0 \frac{r}{2G} \frac{2\eta(1-\nu)(1-2\nu_u) I_0(\beta)/\beta + \dfrac{I_1(\xi)}{\xi}}{(1-\nu) I_0(\beta) - 2(\nu_u - \nu)\dfrac{I_1(\beta)}{\beta}} \tag{3.38}$$

Pore pressure variations:

Replacing D_1 and D_2 from Equations (3.37) in Equation (3.30):

$$\tilde{p} = \tilde{p}_0 \frac{(1-\nu) I_0(\xi) - 2(\nu_u - \nu)\dfrac{I_1(\beta)}{\beta}}{(1-\nu) I_0(\beta) - 2(\nu_u - \nu)\dfrac{I_1(\beta)}{\beta}} \tag{3.39}$$

Time-dependent boundary conditions

Computing the radial displacement and pore pressure distributions in the poroelastic formulation for both Modes I and II is now a question of defining the time-dependent boundary conditions. They must be defined in the time domain first, and then transformed to the Laplace domain.

a) Boundary conditions in the time domain:

It is important to realize that the general poroelastic formulation assumes only a variation of the initial radial stress and pore pressure, without taking into account the initial state itself. In other words, the theory of poroelasticity, as presented, is always dealing with 'deltas', over the initial conditions. The initial stress state, nevertheless, is exactly the final goal of simulating the coring process, and the way for including the initial stress and pore pressure in the poroelasticity equations was to subtract two 'delta' loadings: the first one consisted in inputting a constant condition (initial subsurface radial stress and reservoir pressure); while the second one imposes a two-step function, ending at the constant initial condition. The first loading minus the second perfectly simulates the decrease in the stresses during coring. The second loading pattern was suitably chosen for representing the three possible drilling conditions: overbalanced, balanced and underbalanced.

Figures 3.4 to 3.7 show the loading decomposition for simulating the coring process, where:

σ_r is the radial stress at the core external surface;
p_{df} is the drilling fluid pressure;
t^* is the recovery time (time for the cored sample to reach surface, when the pressure at the core external radius becomes atmospheric); and,
p_{res} is the initial reservoir pressure.

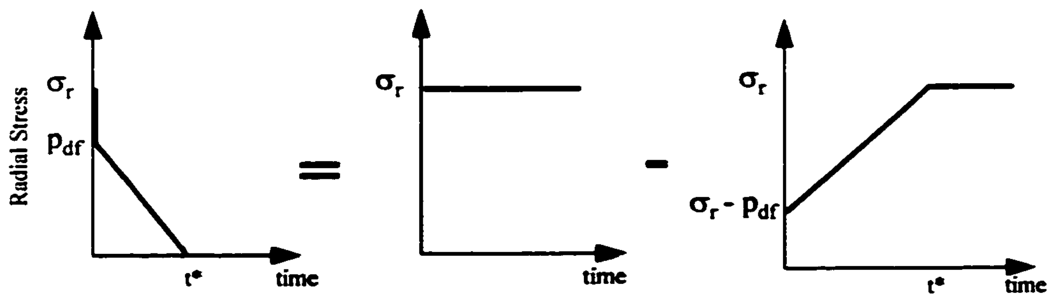

Figure 3.4: Variation of the radial stress at the core boundary.

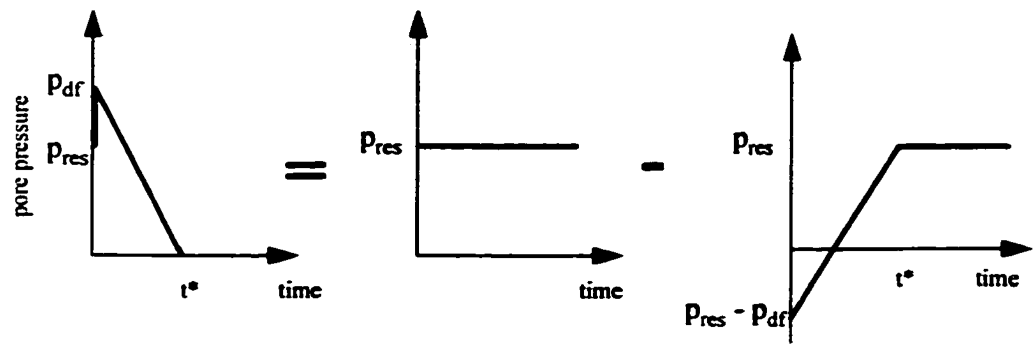

Figure 3.5: Variation of the pore pressure at the core boundary during overbalanced drilling.

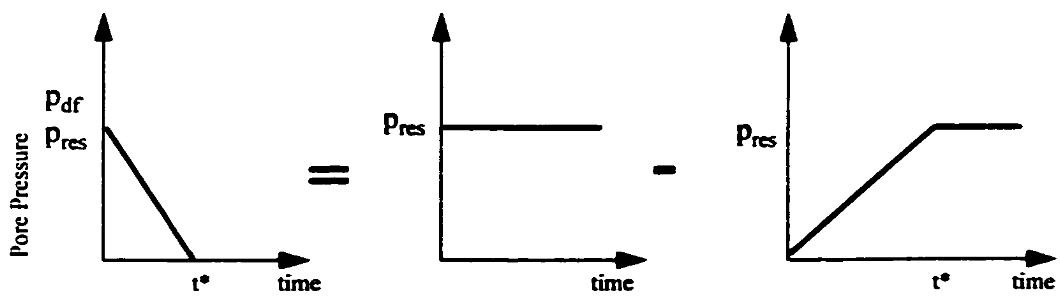

Figure 3.6: Variation of the pore pressure at the core boundary during balanced drilling.

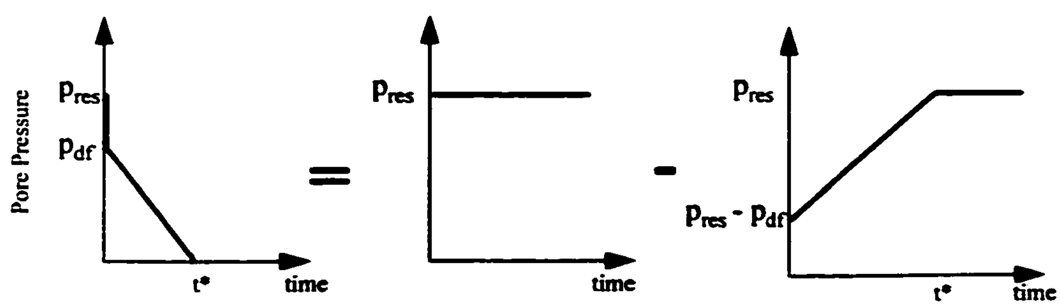

Figure 3.7: Variation of the pore pressure at the core boundary during underbalanced drilling.

As stated above, Figures 3.5 to 3.7 present the boundary conditions for computing the stresses and pore pressures histories in the core. When computing the core radial displacements, nevertheless, the core initial dimensions are not important, and the variation imposed by the second loading pattern can be applied alone for identifying rock expansion or contraction, simply by assuming that decreasing the radial stress leads to core expansion while decreasing the pore pressure means overall contraction. This convention sign will be applied later on, still in this chapter, for deriving the radial displacements for Modes I and II combined.

Functions $P_0(t)$ and $p_0(t)$, respectively the change in the radial stress and pore pressure at the core boundary, can then be defined by a single general equation, which will reproduce the variation in pressure and stress shown in Figures 3.4 to 3.7, depending on the drilling fluid pressure and reservoir pressure input:

$$L = \left\{ \left[\frac{L_0 - (L_0 - p_{df})\, t}{t^*} + (L_0 - p_{df}) \right] H(t) - \right.$$
$$\left. \left[\frac{L_0 - (L_0 - p_{df})\, t}{t^*} + (L_0 - p_{df}) \right] H(t - t^*) + L_0 H(t - t^*) \right\} \tag{3.40}$$

where,

$$\begin{cases} L \text{ represents the rock stresses at the core external surface;} \\ L_0 \text{ is the in-situ radial stress } (\sigma_r) \text{ or reservoir pressure } (p_{res})\text{; and,} \\ H(t) \text{ is the Heaviside step function, defined as:} \end{cases}$$

$$\begin{cases} H(t) = 0, \text{ for } t < 0 \\ H(t) = 1, \text{ for } t > 0 \\ H(t - t^*) = 0, \text{ for } t < t^* \\ H(t - t^*) = 1, \text{ for } t > t^* \end{cases} \tag{3.41}$$

The generality of Equation (3.40) can be checked out by confirming that it reproduces the pore pressure history at the core boundary for each drilling condition, before it reaches the surface ($t < t^*$):

i) overbalanced drilling

The pressure variation in this case is such that:

$$p_{res} - p_{df} < 0 \tag{3.42}$$

Using Equation (3.42) into Equation (3.40), and assuming ($t < t^*$), gives:

$$p = \frac{p_{res} - (p_{res} - p_{df})\,t}{t^*} + (p_{res} - p_{df}) \tag{3.43}$$

which is the equation of a line, as shown in Figure 3.8a, that correctly reproduces the pressure variation in Figure 3.5.

ii) balanced drilling

For this condition one has:

$$p_{res} - p_{df} = 0 \tag{3.44}$$

Using Equation (3.44) into (3.40):

$$p = \frac{p_{res} t}{t^*} \tag{3.45}$$

which is the equation of a line passing through the origin of the pressure *versus* time plot, shown in Figure 3.8b, that matches the variation represented in Figure 3.6.

iii) underbalanced condition

In this situation:

$$p_{res} - p_{df} > 0 \tag{3.46}$$

Replacing Equation (3.46) into Equation (3.40) reproduces exactly the same pressure variation as in the overbalanced case (Equation 3.43), but now $p_{res} > p_{df}$ at the coring instant, and the pressure variation shown in Figure 3.8c is identical to the one presented in Figure 3.7.

b) Boundary conditions in the Laplace domain:

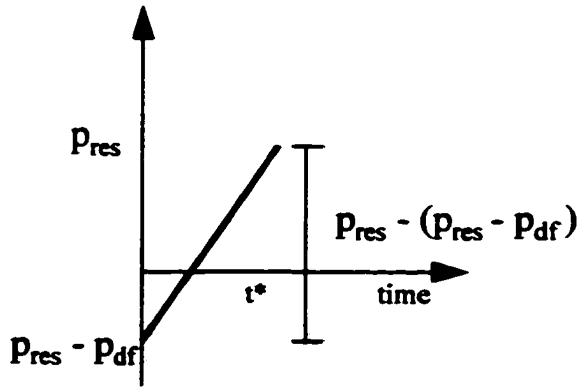

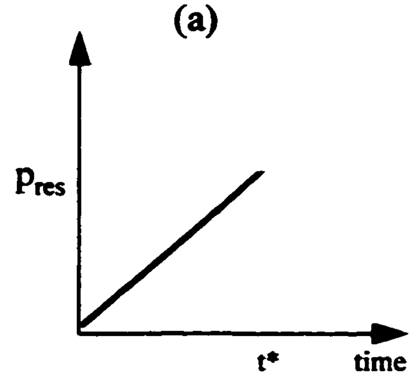

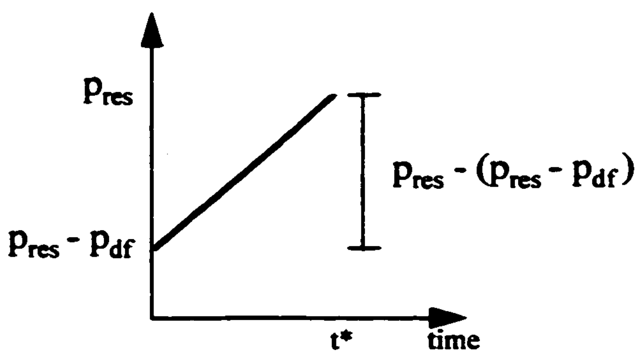

Figure 3.8: Variation of the pore pressure at the core boundary for different drilling conditions before reaching the surface: (a) overbalanced drilling; (b) balanced drilling; (c) underbalanced drilling.

The next step is to define $\bar{P}_0$ and $\bar{p}_0$, respectively the change in the radial stress and pore pressure at the core boundary, in the Laplace domain. The Laplace transform of a Heaviside function is given by (Kreyszig, 1993):

$$\begin{cases} \mathfrak{L}\left[H(t-k)\right] = \dfrac{1}{s}e^{-ks} \\ \mathfrak{L}\left[(t-k)H(t-k)\right] = \dfrac{1}{s^2}e^{-ks} \end{cases} \tag{3.47}$$

where k is a constant.

Using Equation (3.47) into Equation (3.40) gives the boundary conditions for the stress and pore pressure variation in the Laplace domain for loading Modes I and II, respectively:

$$\bar{P}_0 = \frac{p_{df}}{s}\left[\frac{\left(1-e^{-t^*s}\right)}{t^*s} - 1\right] + \frac{\sigma_r}{s} \tag{3.48}$$

$$\bar{p}_0 = \frac{p_{df}}{s}\left[\frac{\left(1-e^{-t^*s}\right)}{t^*s} - 1\right] + \frac{p_{res}}{s} \tag{3.49}$$

Radial displacements and pore pressure distributions

The boundary conditions for computing the radial displacements and pore pressure distributions are completely defined by Equations (3.48) and (3.49) in terms of the in-situ radial stress, σ_r, the initial reservoir pressure, p_{res}, the drilling fluid pressure, p_{df}, and the recovery time, t^*.

i) Radial displacements:

Inserting Equation (3.48) into Equation (3.34) gives the radial displacement for Mode I loading:

$$\tilde{u}_r = \left\{ \frac{p_{df}}{s} \left[\frac{\left(1 - e^{-t^* s}\right)}{t^* s} - 1 \right] + \frac{\sigma_r}{s} \right\} \frac{r}{2G} \frac{(1 - 2\nu_u)(1 - \nu) I_0(\beta) + 2(\nu_u - \nu) \dfrac{I_1(\xi)}{\xi}}{(1 - \nu) I_0(\beta) - 2(\nu_u - \nu) \dfrac{I_1(\beta)}{\beta}} \tag{3.50}$$

It is useful to simplify the above expression by defining:

$$\begin{cases} TFAC^6 = \dfrac{p_{df}}{s} \left[\dfrac{\left(1 - e^{-t^* s}\right)}{t^* s} - 1 \right] \\ D_3 = (1 - \nu) I_0(\beta) - 2(\nu_u - \nu) \dfrac{I_1(\beta)}{\beta} \\ D_4 = (1 - 2\nu_u)(1 - \nu) I_0(\beta) + 2(\nu_u - \nu) \dfrac{I_1(\xi)}{\xi} \end{cases} \tag{3.51}$$

leading to a new form of Equation (3.50); i.e.:

$$\tilde{u}_r = \frac{r}{2G} \frac{D_4}{D_3} \left(TFAC + \frac{\sigma_r}{s} \right) \tag{3.52}$$

By the same token, inserting Equation (3.49) into Equation (3.38) gives the radial displacements for Mode II:

$$\tilde{u}_r = \left\{ \frac{p_{df}}{s} \left[\frac{\left(1 - e^{-t^* s}\right)}{t^* s} - 1 \right] + \frac{p_{res}}{s} \right\} \frac{r}{2G} \frac{2\eta(1 - \nu)(1 - 2\nu_u) I_0(\beta)/\beta + \dfrac{I_1(\xi)}{\xi}}{(1 - \nu) I_0(\beta) - 2(\nu_u - \nu) \dfrac{I_1(\beta)}{\beta}} \tag{3.53}$$

Using once more the simplifying expressions from (3.51), and defining also:

$$D_5 = 2\eta(1 - \nu)(1 - 2\nu_u) \frac{I_0(\beta)}{\beta} + \frac{I_1(\xi)}{\xi} \tag{3.54}$$

a new form of Equation (3.53), analogous to Equation (3.52), can be written as:

$$\tilde{u}_r = \frac{r}{2G} \frac{D_5}{D_3} \left(TFAC + \frac{p_{res}}{s} \right) \tag{3.55}$$

A simple and straightforward expression can be finally written for the total radial displacements for Modes I and II combined:

$$\tilde{u}_r = \frac{r}{2GD_3} (D_4 STIL - D_5 PTIL) \tag{3.56}$$

where,

$$STIL = TFAC + \frac{\sigma_r}{s} \tag{3.57}$$

and,

$$PTIL = TFAC + \frac{p_{res}}{s} \tag{3.58}$$

The negative sign inside Equation (3.56) means only that Modes I and II have different effects on the rock deformations. In other words, rock expansion, due to the radial stress relief (expressed by the term D_4STIL), was considered positive, while rock contraction, due to the pore pressure decrease (expressed by the term D_5PTIL), was considered negative.

ii) Pore pressure distribution:

The pore pressure variation due to Mode I loading can be equated by introducing Equation (3.48) into Equation (3.36):

$$\tilde{p} = \left\{ \left[\frac{\left(1 - e^{-t^* s}\right)}{t^* s} - 1 \right] + \frac{\sigma_r}{s} \right\} \frac{(1-\nu)\left[I_0(\beta) - I_0(\xi)\right]}{(1-\nu)\, I_0(\beta) - 2\,(\nu_u - \nu)\, \dfrac{I_1(\beta)}{\beta}} \tag{3.59}$$

Defining now:

$$D_6 = (1-\nu)\left[I_0(\beta) - I_0(\xi)\right] \tag{3.60}$$

and using $TFAC$ and D_3, previously defined in Equations (3.51), Equation (3.59) can be simplified to:

$$\tilde{p} = \frac{D_6}{D_3}\left(TFAC + \frac{\sigma_r}{s}\right) \tag{3.61}$$

The pore pressure in loading Mode II can be obtained by inserting Equation (3.49) into Equation (3.39):

$$\tilde{p} = \left\{ \frac{p_{df}}{s} \left[\frac{\left(1 - e^{-t^* s}\right)}{t^* s} - 1 \right] + \frac{p_{res}}{s} \right\} \frac{(1-\nu)\, I_0(\xi) - 2(\nu_u - \nu)\dfrac{I_1(\beta)}{\beta}}{(1-\nu)\, I_0(\beta) - 2\,(\nu_u - \nu)\, \dfrac{I_1(\beta)}{\beta}} \tag{3.62}$$

Defining:

$$D_7 = (1-\nu)\, I_0(\xi) - 2(\nu_u - \nu) I_1(\beta)/\beta \tag{3.63}$$

Equation (3.62) simplifies to:

$$\bar{p} = \frac{D_7}{D_3}\left(TFAC + \frac{p_{res}}{s}\right) \tag{3.64}$$

The pore pressure variation for Modes I and II combined is then given by adding Equations 3.61 and 3.64:

$$\bar{p} = \frac{(D_6 STIL + D_7 PTIL)}{D_3} \tag{3.65}$$

where $STIL$ and $PTIL$ are given by Equations (3.57) and (3.58), respectively.

Equation (3.65) is analogous to the one obtained for the radial displacements (Equation 3.56). In the pore pressure analysis, nevertheless, both loading Modes I and II generate the same type of pore pressure variation (decreasing the radial stress and the pore pressure at the core boundary reduces the pore pressure inside the core), the terms $D_6 STIL$ and $D_7 PTIL$ must then be added.

In-Situ radial stress and initial reservoir pressure

i) In-Situ radial stress:

The in-situ radial stresses can be computed now as a function of the radial displacements and the reservoir initial pressure (for Modes I and II combined) by simply expressing the stress from Equation (3.56), using Equation (3.57):

$$\frac{\sigma_r}{s} = \frac{\left(2GD_3\frac{\tilde{u}_r}{r} + D_5 PTIL\right)}{D_4} - TFAC \tag{3.66}$$

The numerical inversion of the right-hand side of Equation (3.66) will give, then, the desired in-situ radial stress, since:

$$\mathfrak{L}^{-1}\left(\frac{\sigma_r}{s}\right) = \sigma_r \tag{3.67}$$

ii) Initial pore-pressure:

The same procedure can be adopted for computing the initial reservoir pressure as a function of the radial displacements, expressing it from Equation (3.56), and using Equation (3.58):

$$\frac{p_r}{s} = \frac{\left(D_4 STIL - 2GD_3\frac{\tilde{u}_r}{r}\right)}{D_5} - TFAC \tag{3.68}$$

Inverting now the right hand side of Equation (3.68) will give the initial reservoir pressure:

$$\mathfrak{L}^{-1}\left(\frac{p_r}{s}\right) = p_r \tag{3.69}$$

3.3 Including the Viscoelastic Effects

Until now the analysis of the coring process has been restricted to poroelastic effects. The anelastic process, however, is characterized by time-dependent deformations, in which the rock properties are most probably not constant. The rock viscous characteristics may then play some role in the deformation process. A simple way to include the viscous effect in the poroelastic equations is to use the Viscoelastic Correspondent Principle (VCP). This method states that the governing equations for an elastic problem can also be used for deriving the viscoelastic response, if the elastic constants are replaced by their time-dependent equivalent functions, expressed in terms of the Laplace transforms (Flügge, 1975). This idea can be further extended to the poroelastic formulation, and the poroviscoelastic response would be obtained by replacing the poroelastic constants by their poroviscoelastic correspondent ones.

A basic question to be answered before applying the viscoelasticity theory is the kind of time-dependence that is under consideration, i.e., is the viscous stress-strain behavior of rocks governed by linear or non-linear differential equations? The strain response of ASR tests is generally assumed to be exponential (Warpinski, 1986; Warpinski and Teufel, 1986; Breretron, 1995), and this can be confirmed by examining the field data presented in this dissertation (Chapter 5), regardless of the expansion/contraction characteristics of these curves. Since exponential solutions are typically derived from linear constitutive equations (Flügge, 1975), the linear theory of viscoelasticity will be assumed in the analysis of the cylindrical problem.

Viscous effects are present whenever a material shows increasing deformation under constant loading (creep). In order to compute the creep constants it is necessary, first, to define a proper viscoelastic model. According to Flügge (1975) several viscoelastic models can be applied for representing the behavior of solid materials (Kelvin solid; 3-parameter solid; 4-parameter solid etc.). They all show a combination of the basic elements: springs and dashpots, for simulating, respectively, the elastic and the viscous aspects of the solid deformation.

The model chosen in this dissertation is the linear three-parameter solid model (also called modified Kelvin model), shown in Figure 3.9, which is considered to better represent an exponential relaxation process like ASR (Flügge, 1975; Warpinski, 1986; Warpinski and Teufel, 1986; Abousleiman *et al.*, 1996). The question now is which rock property is responsible for creep: is it only a bulk characteristic? a solid grain property? or both of them? Two sources of information can be used for answering these questions: the experimental tests, shown in Chapter 6, where the creep behavior was measured for several rock properties; and the parametric analysis, shown in Chapter 4, where the viscous behavior was attributed to different rock parameters and the results compared. The viscoelastic formulation is presented here in terms of the bulk modulus and the volumetric strain, which are considered to best represent the rock 'bulk' behavior in the anelastic deformation process. This analysis, however, is totally analogous if any of the other four elastic constants (E, G, K_s, K_u), is chosen for describing the material viscoelastic behavior.

The model is composed of two parts: a spring and a Kelvin element (spring and dashpot in a parallel configuration) in series, having K_1 and K_2 as the spring constants and μ_K as the dashpot viscosity coefficient. P_c is the confining pressure applied to the system.

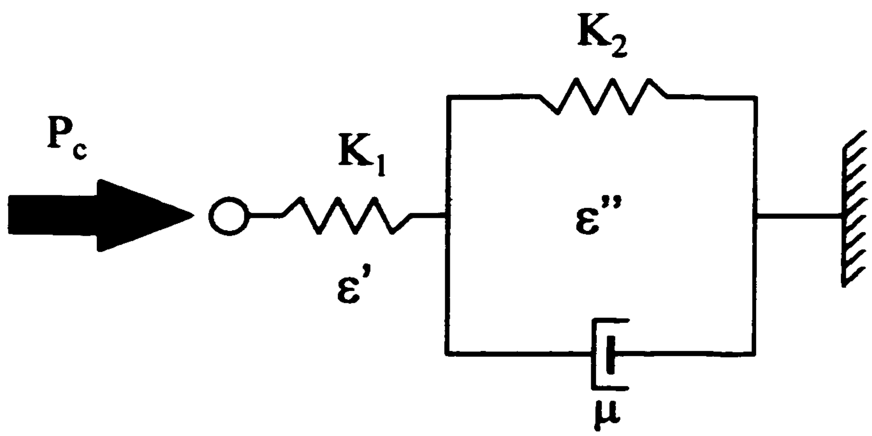

Figure 3.9: Three-parameter modified Kelvin model.

If a three-parameter solid model is loaded, an instantaneous elastic deformation, ε', appears due to the spring constant K_1:

$$P_c = K_1 \varepsilon' \tag{3.70}$$

If P_c is kept constant for period of time, the initial deformation (ε') is followed by a 'delayed elastic behavior', when K_2 and μ_K start to play some role and the stress-strain equation for the Kelvin element is given by:

$$P_c = K_2 \varepsilon'' + \mu_K \dot{\varepsilon}'' \tag{3.71}$$

The total strain is given by the sum of the strains in each element:

$$\varepsilon = \varepsilon' + \varepsilon'' \tag{3.72}$$

The constitutive relation for the model is derived by applying the Laplace transform to Equations (3.70) and (3.71), considering K_1, K_2 and μ_K to be constants:

$$\begin{cases} \bar{P}_c = K_1 \bar{\varepsilon}' \\ \bar{P}_c = (K_2 + s\mu_K)\bar{\varepsilon}'' \end{cases} \tag{3.73}$$

Rearranging and adding Equations (3.73) leads to:

$$\bar{P}_c(K_2 + s\mu_K) + \bar{P}_c K_1 = K_1 \bar{\varepsilon}'(K_2 + s\mu_K) + (K_2 + s\mu_K)\bar{\varepsilon}'' K_1 \tag{3.74}$$

Transforming Equation (3.74) back into the time domain, and using Equation (3.72), gives:

$$(K_1 + K_2)P_c + \mu_K \dot{P}_c = K_1 K_2 \varepsilon + K_1 \mu_K \dot{\varepsilon} \tag{3.75}$$

Considering now:

$$P_c = P_{c_0} H(t) \tag{3.76}$$

where,

$$\begin{cases} P_{c_0} \text{ is a constant; and,} \\ H(t) \text{ is the Heaviside unit step function, given by:} \end{cases}$$

$$\begin{cases} H(t) = 0, \; t < 0 \\ H(t) = 1, \; t > 0 \end{cases} \tag{3.77}$$

The total strain for the model can be finally derived in the Laplace domain, by inserting Equation (3.76) into Equation (3.75) and applying the Laplace transform:

$$\bar{\varepsilon} = \bar{P}_c \left[\frac{(K_1 + K_2) + s\mu_K}{K_1 K_2 + s K_1 \mu_K} \right] \tag{3.78}$$

where:

$$\bar{P}_c = \frac{P_{c_0}}{s} \tag{3.79}$$

The correspondent bulk modulus can be explicited by inverting Equation (3.78):

$$\bar{K} = \frac{\bar{P}_c}{\bar{\varepsilon}} = \left[\frac{K_1 K_2 + s K_1 \mu_K}{(K_1 + K_2) + s\mu_K} \right] \tag{3.80}$$

Having derived the viscoelastic correspondent parameter, it is necessary to define a procedure for determining the model constants: K_1, K_2 and μ_K. Assuming that the relationship between the confining pressure and volumetric strain under creep can be described by:

$$\varepsilon(t) = P_{\infty} J(t) \tag{3.81}$$

where $J(t)$ is the compliance function in strain per unit of applied pressure, and is written as (Flügge, 1975):

$$J(t) = \frac{1}{K_1}\left(1 + \frac{K_1}{K_2} - \frac{K_1}{K_2} e^{-\frac{K_2 t}{\mu_K}}\right) \tag{3.82}$$

The coefficients of $J(t)$ can be empirically evaluated by fitting the strain *versus* time curve in creep tests where P_{∞} is known (Abousleiman *et al.*, 1996). At time $t = 0$, from Equation (3.82):

$$J(t = 0) = \frac{1}{K_1} \tag{3.83}$$

and then:

$$K_1 = \frac{Pc}{\varepsilon_1} = K \tag{3.84}$$

In other words, $t = 0$ means the beginning of the creep phase, which can also be understood as the ending of the elastic region, where $K_1 = K$.

K_2 can be computed by knowing K_1 and considering that for longer times, as $t \to \infty$:

$$J(t \to \infty) = \frac{1}{K_1} + \frac{1}{K_2} \tag{3.85}$$

In order to get an explicit form for K_2 it is necessary to insert Equation (3.85) into Equation (3.82), giving:

$$K_2 = \frac{K_1}{\frac{K_1}{K_{\infty}} - 1} \tag{3.86}$$

where K_{∞} is defined as P_c/ε_{∞}, and is always smaller than K_1, since for longer times the material will show a larger deformation, i.e.:

$$\varepsilon_{\infty} > \varepsilon_1 \text{ leads to } K_1 = \frac{P_c}{\varepsilon_1} > K_{\infty} = \frac{P_c}{\varepsilon_{\infty}} \tag{3.87}$$

The limiting case would be when the material shows no creep: $K_\infty = K_1$, and then K_2 is infinitely large.

The viscosity coefficient, μ_K, can be determined using K_1 and K_2, previously calculated, and $J(t)$ taken from the curve-fitting equation at any time t:

$$\mu_K = -\frac{K_2 t}{\ln\left[\dfrac{K_2}{K_1} + 1 - K_2 J(t)\right]} \tag{3.88}$$

It is clear, from the equations just derived for the viscoelastic approach, that including viscous effects in the governing equations of poroelasticity will increase the number of parameters needed to fully describe the rock deformation process: at least two more constants (K_2, and μ_K) are needed if K_1 is not constant.

3.3.1 Relationship Among the Poroelastic Parameters

Several theoretical approaches can be applied depending on which basic parameter or which combination of basic parameters is chosen for exhibiting the rock 'primary' viscous characteristics, as described by the modified Kelvin model. The remaining parameters will also have a 'secondary' time-dependency, since they are expressed by constitutive relations, available in the rock mechanics and poroelasticity literature (Biot, 1941; Jaeger and Cook, 1979; Detournay and Cheng, 1993), as a function of the basic parameters.

Assuming, for example, E, K, K_s and K_u to be the basic input parameters for a poroviscoelastic analysis, and choosing the bulk modulus K as the only rock property exhibiting a primary viscous behavior, the viscoelastic correspondent parameters would be given by the following set of expressions:

$$\bar{G} = \frac{3\bar{K}E}{9\bar{K} - E} \tag{3.89}$$

$$\bar{\nu} = \frac{3\bar{K} - 2\bar{G}}{2\,(3\bar{K} + \bar{G})} \tag{3.90}$$

$$\bar{\alpha} = 1 - \frac{\bar{K}}{K_s} \tag{3.91}$$

$$\bar{\nu}_u = \frac{3K_u - 2\bar{G}}{2(3K_u + \bar{G})} \tag{3.92}$$

$$\bar{\eta} = \frac{\bar{\alpha}\,(1 - 2\bar{\nu})}{2\,(1 - \bar{\nu})} \tag{3.93}$$

$$\bar{M} = \frac{2\bar{G}\,(\bar{\nu}_u - \bar{\nu})}{\alpha^2\,(1 - 2\bar{\nu}_u)\,(1 - 2\bar{\nu})} \tag{3.94}$$

$$\bar{S} = \frac{(1 - \bar{\nu}_u)\,(1 - 2\bar{\nu})}{\bar{M}\,(1 - \bar{\nu})\,(1 - 2\bar{\nu}_u)} \tag{3.95}$$

3.3.2 Solutions in the Time-domain

Because of the complexity of the equations in the Laplace domain, there's no analytical inversion method for computing displacements and/or pressure distributions in the time domain. A numerical inversion is then necessary. The Stehfest algorithm, first published in January 1970 (Stehfest, 1970a), and corrected in October 1970 (Stehfest, 1970b) was chosen due to it's relative simplicity, wide application and easier programming (Detournay and Cheng, 1993; Ferreira, 1996; Cui and Abousleiman, 1998). The general form of the numerical inversion is (Stehfest, 1970b):

$$F(t) = \frac{\ell og(2)}{t} \sum_{i=1}^{n} V_i F\left[i\frac{\ell og(2)}{t}\right] \tag{3.96}$$

where,

$F(t)$ is the numerical inversion of the Laplace transform $F\left[i\frac{\ell og(2)}{t}\right]$;

$i\frac{\ell og(2)}{t}$ is the Laplace variable, s;

$$V_i = (-1)^{\frac{n}{2}+i} \sum_{k=b}^{j} \frac{k^{\frac{n}{2}}(2k)!}{\left(\frac{n}{2} - k\right)!(k)!(k-1)!(i-k)!(2k-i)!} \tag{3.97}$$

$$b = \text{integer}\left(\frac{i+1}{2}\right) \tag{3.98}$$

$$j = \min\left(i, \frac{n}{2}\right) \tag{3.99}$$

$$\begin{cases} n > 4 \\ n = \text{ even} \end{cases} \tag{3.100}$$

Theoretically speaking, the greater the value of n, the higher the accuracy of $F(t)$. Typical values for n, when dealing with equations in the poroelasticity theory, range between 8 and 16 (Ferreira, 1996). Several tests were performed comparing the numerical inversion of functions with known analytical inversion and the stability of the poroviscoelastic solutions for different values of n. Identical results were found for n between 8 and 12, and $n = 8$ was adopted in this dissertation. Figures 3.10 and 3.11 show the code fluxogram.

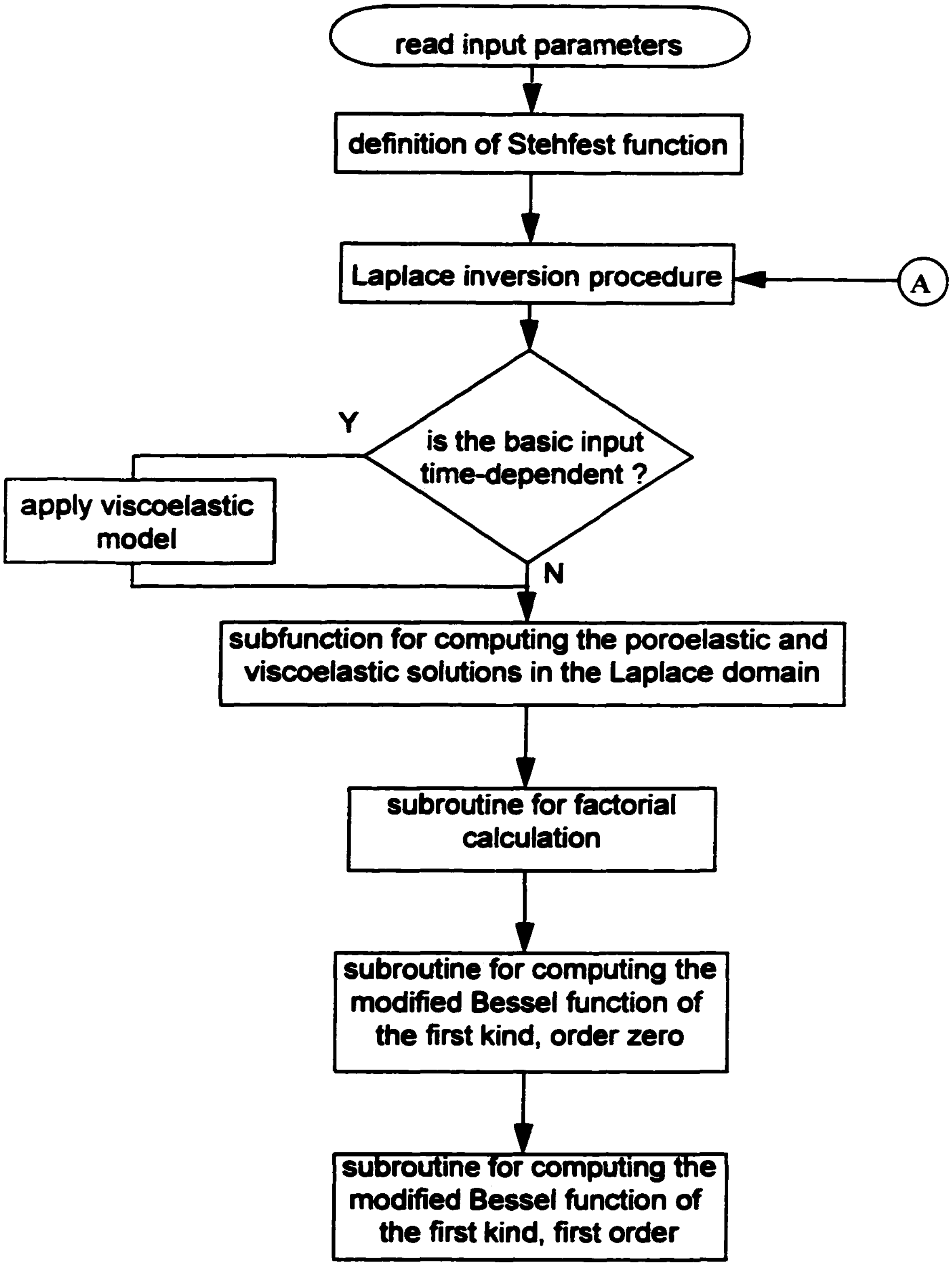

Figure 3.10: Fluxogram of the code main routines.

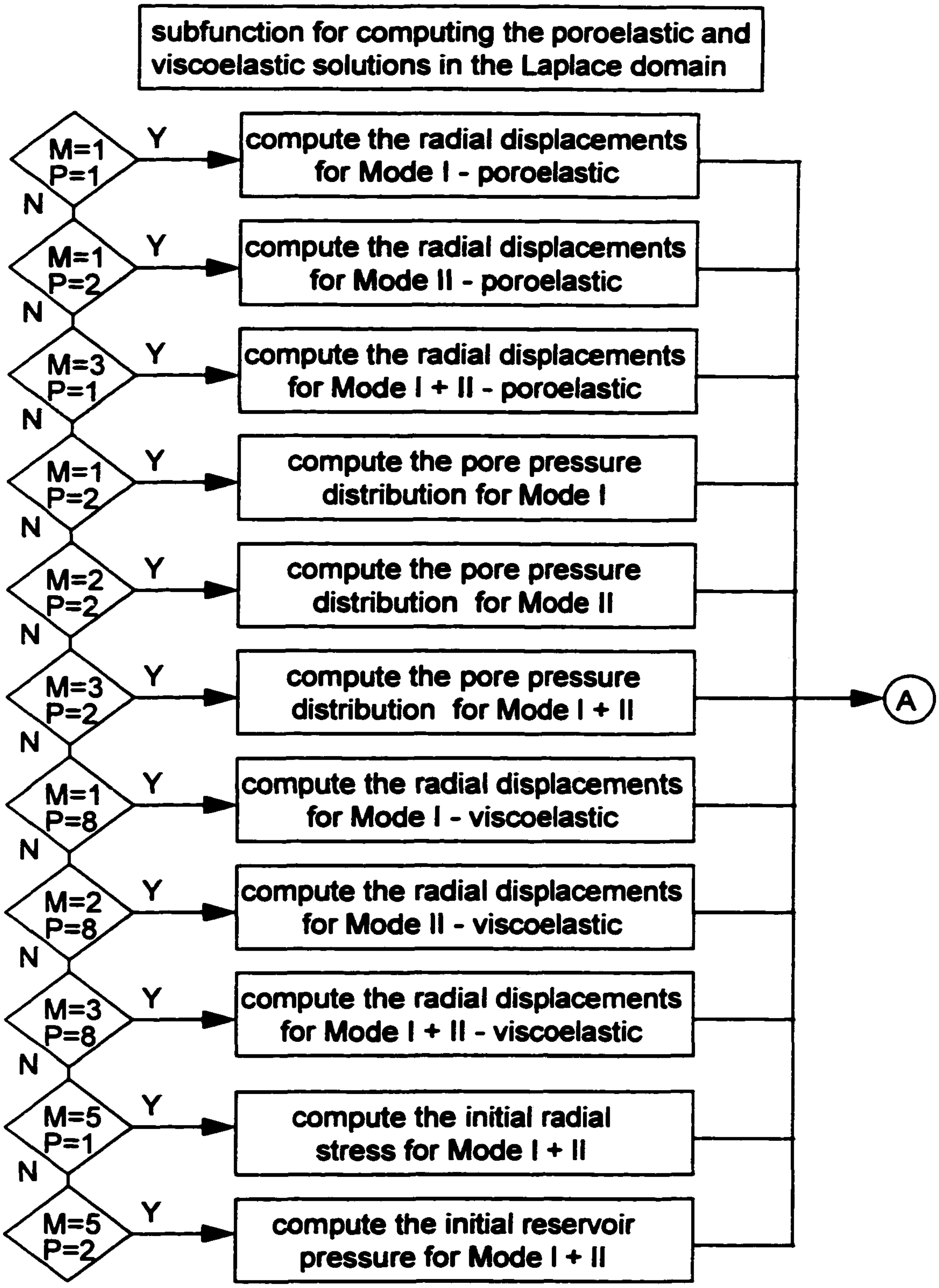

Figure 3.11: Fluxogram of the subroutine for the solutions in the Laplace domain. M and P are input parameters for defining the desired calculation.

Chapter 4

Model Validation and Parametric Analysis

A Fortran code has been developed for solving the poroelastic and poroviscoelastic axisymmetry equations derived in the previous chapter for a cylindrical geometry. Loading modes I, II, III and IV, presented in Table 3.1, can be computed isolated or combined, depending on a flag condition defined in the input data file. Mode III, as stated before, does not affect the pore pressure, and is not included in this chapter, although included in the developed code. Mode IV is presented just for comparison with the published literature.

The code outputs an ASCII table with only two columns: time and the desired solution. Table 4.1 lists the solutions that are presented in this dissertation. This output is then used as an input for a graphic software package, for plotting the curves presented in the next sections.

Table 4.1: Program output.

Output	Modes I, II and IV		Modes I and II	
	poroelastic	poroviscoelastic	elastic	viscoelastic
Radial displacement	✓	✓	✓	✓
Pore pressure distribution	✓	✓		
In-Situ radial stress	✓	✓	✓	✓
Initial reservoir pressure	✓	✓		

The four basic poroelastic parameters used in the code are exactly the ones defined in Chapter 3: E, K, K_s and K_u. These parameters can be independently assumed to be constant or time-dependent, according to the modified Kelvin model, if their viscous characteristics are available from experimental tests. In this case, the input data file should provide E_1, E_2, μ_E, K_1, K_2, μ_K, etc., depending on which parameters have the time-dependency attribute. The rock permeability, k, is the fifth rock physical property needed as input data. The complete (standard) input data for the developed code is shown from Table 4.2[1] to Table 4.4.

Table 4.2: Rock properties needed for the poroelastic and poroviscoelastic approach.

Elastic	E	K	K_s	K_u
Viscoelastic	E_1, E_2, μ_E	K_1, K_2, μ_K,	K_{s1}, K_{s2}, μ_K	K_{u1}, K_{u2}, μ_K
Permeability			k	

Table 4.3: Pore fluid data and cylindical geometry.

Pore fluid data	Cylinder geometry
viscosity, μ_f	core diameter, D

Table 4.4: Boundary conditions needed for computing specific solutions under loading Modes I and II.

Radial displacement and pore pressure distribution	In-Situ radial stress	Initial reservoir pressure
$\sigma_r(t)$	$u_r(t)$	$u_r(t)$
$p_{res}(t)$	$p_{res}(t)$	$\sigma_r(t)$
t^*	t^*	t^*
p_{df}	p_{df}	p_{df}

4.1 Model Validation

Three procedures were applied for validating the Fortran code:

[1] If, for example, Young's modulus is assumed to be constant, the code takes $E = E_1$; if the bulk modulus is assumed constant $K = K_1$; and so on.

(i) The pore pressure distribution and the radial displacements computed by the code were compared to previous results published by Detournay and Cheng (1993) and Abousleiman *et al.* (1996), using the same rock input data and boundary conditions.

(ii) The poroelastic and poroviscoelastic solutions for larger times were compared to the elastic and viscoelastic solutions, respectively. Since the effects of pore pressure must be dissipated for larger times, one should expect the poroelastic solutions to provide exactly the same results as the elastic ones, while the poroviscoelastic solutions should be identical to the viscoelastic ones, if the same viscous model is applied.

(iii) An 'inversion-check' was performed by using the radial displacements generated by specific initial stresses, reservoir pressure and drilling conditions, as input data for gathering the same initial conditions back. This check is very interesting, since it shows the code ability for providing the initial stresses as a function of the rock strain, ultimate goal of an ASR analysis.

4.1.1 Literature Comparison

Loading Modes I, II and IV have been chosen for comparing the results of the developed code with the published literature, since the solution for these modes is available for specific boundary conditions: *(i)* constant load for Modes I and II ($P(t) = P_0$ and $p(t) = p_0$); and, *(ii)* constant axial strain rate for Mode IV ($\varepsilon(t) = \varepsilon_0$). Detournay and Cheng (1993) have derived the poroelastic solutions for Modes I and II, while Abousleiman *et al.* (1996) have derived the poroelastic solution for Mode IV and the poroviscoelastic solutions for Modes I, II and IV. The literature comparison is not related to the coring process, since the poroviscoelasticity theory has never been applied to coring before. It is intended to be a check on the program output.

(i) Comparison with Detournay and Cheng (1993):

The pore pressure distribution at the center of a cylindrical rock sample was presented by Detournay and Cheng (1993) for Mode I loading, in the poroelastic approach, together with the curve for the homogeneous diffusion. The input data for this simulation is shown in Table 4.5[2].

Table 4.5: Conditions for the comparison with Detournay and Cheng (1993).

Poisson's ratio	$\nu = 0.15$
Undrained Poisson's ratio	$\nu_u = 0.31$
Diffusivity coefficient	$c = 10^{-4}\ m^2/s$
Loading	$\sigma_r = P_0$
Sample diameter	$D = 2\ cm$

The pore pressure at the center of the cylinder was obtained by letting $r = 0$ in Equation (3.36) and transforming the boundary condition into the Laplace domain:

$$\tilde{P}_0 = \frac{P_0}{s} \tag{4.1}$$

The pure diffusion solution was computed in the Laplace domain (Detournay and Cheng, 1993) and can be written as:

$$\tilde{p} = \tilde{P}_0 \left[1 - \frac{I_0(\xi)}{I_0(\beta)} \right] \tag{4.2}$$

The curves shown in Figure 4.1 perfectly match the published results.

An interesting feature of Figure 4.1 is the initial rise in pore pressure in the poroelastic solution, compared to the monotonic pressure decline in the pure diffusion solution. This effect, known as the *Mandel-Cryer effect* (Cui *et al.*, 1996; Cui and Abousleiman, 1998), can be explained considering that the pore pressure

[2]It should be noted that although only three rock parameters are presented in this table as input data for the poroelastic solution, the diffusivity coefficient is not a primary data, depending not only on the drained and undrained Poisson's ratios, but also on the rock shear modulus, permeability and Biot's effective stress coefficient, as shown in Equation (3.12). This brings the number of needed parameters back to four, plus the permeability, as stated before.

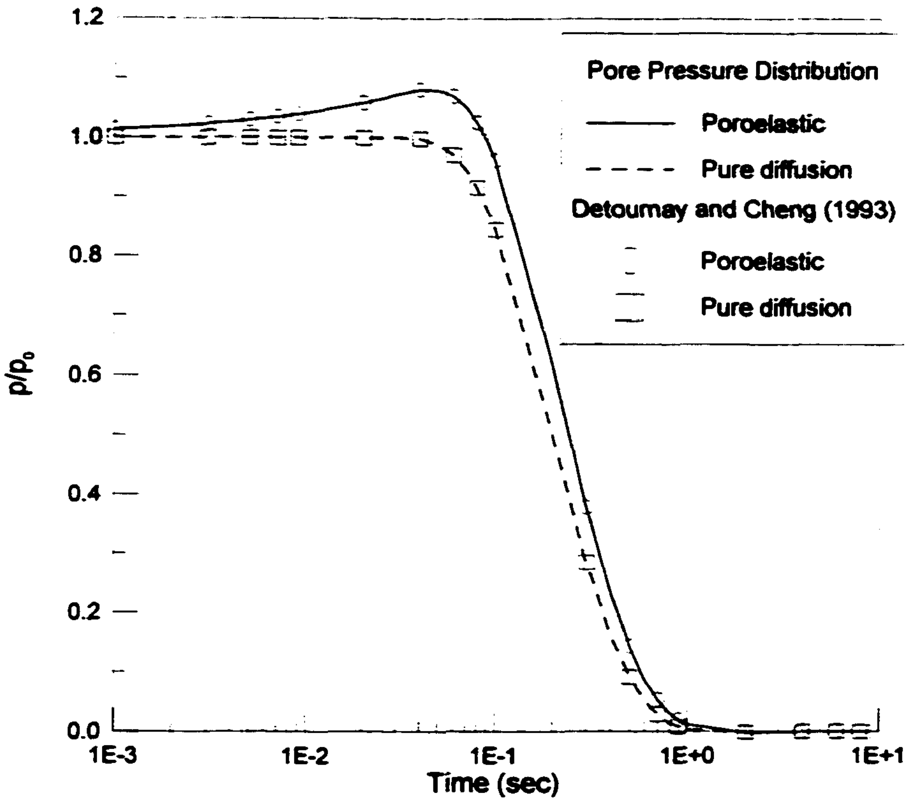

Figure 4.1: Pore pressure at the center of a cylindrical core under Mode I loading: poroelastic approach and pure diffusion solution.

dissipation starts near the rock external surface. Due to the compatibility requirement. as the core outer layer experiences a stress relief, load is transferred to the inner layer, causing an additional pore pressure rise before the excess pore pressure is dissipated and the sample returns to its initial condition.

(ii) Comparison with Abousleiman *et al.* (1996):

Abousleiman *et al.* (1996) presented the solutions for the radial displacements and pore pressure distributions of a cylindrical rock sample using both the poroelastic and poroviscoelastic approaches, in Modes I, II and IV. The properties of three different rock types were used by these authors in their simulation: Berea sandstone, Danian Chalk and a typical shale from the North Sea, having a constant load as boundary condition for the radial stress and pore pressure.

In order to compare their results with the ones from the code developed in this dissertation, the input data had to be modified, in order to use exactly the same basic input parameters. Table 4.6 shows the rock input parameters utilized by Abousleiman *et al.* (1996), while Table 4.7 shows the fluid properties used in the simulations. The sample radius was taken as 10 cm.

Table 4.6: Rock data for the comparison with Abousleiman et al. (1996).

Rock type	G (10^9 Pa)	K (10^9 Pa)	K_s (10^{10} Pa)	ϕ (%)	k (m^2/s)
Berea sandstone	6.0	8.0	3.6	19.0	1.9×10^{-8}
Danian Chalk	2.2	3.3	1.2	23.0	1.0×10^{-12}
Shale	0.8	1.1	3.4	30.0	1.0×10^{-19}

Table 4.7: Fluid properties.

Fluid	μ (Pa.sec)	K_f (Pa)
Water	1.0E-3	3.3E09

Since the rock porosity, ϕ, and the fluid compressibility, K_f, were used as input data, instead of an undrained rock parameter (like the undrained bulk modulus, chosen in this dissertation), it was necessary to compute Skempton's pore pressure coefficient, B, from:

$$B = \frac{\frac{1}{K} - \frac{1}{K_s}}{\frac{1}{K} - \frac{1}{K_s} + \phi\left(\frac{1}{K_f} - \frac{1}{K_s}\right)} \tag{4.3}$$

where,

$$\begin{cases} K \text{ is the rock bulk modulus;} \\ K_s \text{ is the grain bulk modulus;} \\ \phi \text{ is the rock porosity; and,} \\ K_f \text{ is the fluid compressibility.} \end{cases}$$

This way, the undrained Poisson's ratio, ν_u, could be computed from:

$$\nu_u = \frac{3\nu + \alpha B(1 - 2\nu)}{3 - \alpha B(1 - 2\nu)} \tag{4.4}$$

Poroelastic solution:

The solution for the radial displacements and pore pressure distributions under the poroelasticity theory was computed according to Table 4.8. The boundary conditions are:

Table 4.8: Equations used for the solving the poroelastic problem.

Mode	Radial displacement	Pore pressure distribution
I	3.34	3.36
II	3.38	3.39

$$\begin{cases} \tilde{P}_0 = \frac{P_0}{s}, \text{ for Mode I} \\ \tilde{p}_0 = \frac{p_0}{s}, \text{ for Mode II} \end{cases} \tag{4.5}$$

In Mode IV, an axial strain rate $\dot{\varepsilon}_0 = 0.01\ \mu\varepsilon/\sec$, typical for uniaxial compression tests, was simulated, and the equations for computing the radial displacements and pore pressure distributions are (Abousleiman *et al.*, 1996):

$$\tilde{u}_r = \varepsilon_0 \frac{r}{2s^2} \frac{\nu_u (1-\nu) I_0(\beta) - (\nu_u - \nu) \left[\frac{I_1(\beta)}{\beta} + \frac{I_1(\xi)}{\xi} \right]}{D_3} \tag{4.6}$$

$$\tilde{p} = \varepsilon_0 \frac{G}{s^2} \frac{(\nu_u - \nu)}{\eta} \frac{I_0(\beta) - I_0(\xi)}{D_3} \tag{4.7}$$

Poroviscoelastic solution:

The rock viscoelastic behavior was restricted by Abousleiman *et al.* (1996) to the bulk modulus, assuming $K_2 = K_1 = K$ and $\mu_K / K_2 = 2$ days, in the modified Kelvin model, for all the three rock types. Based on the VCP, already discussed in Chapter 3, the same equations showed in Table 4.8 for deriving the poroelastic solution, were applied again for computing the poroviscoelastic solution, with the same boundary conditions. In this case, nevertheless, the corresponding rock parameters were utilized.

The plots obtained, shown from Figures 4.2 to 4.7, exactly reproduce the poroviscoelastic and poroelastic results presented by Abousleiman *et al.* (1996).

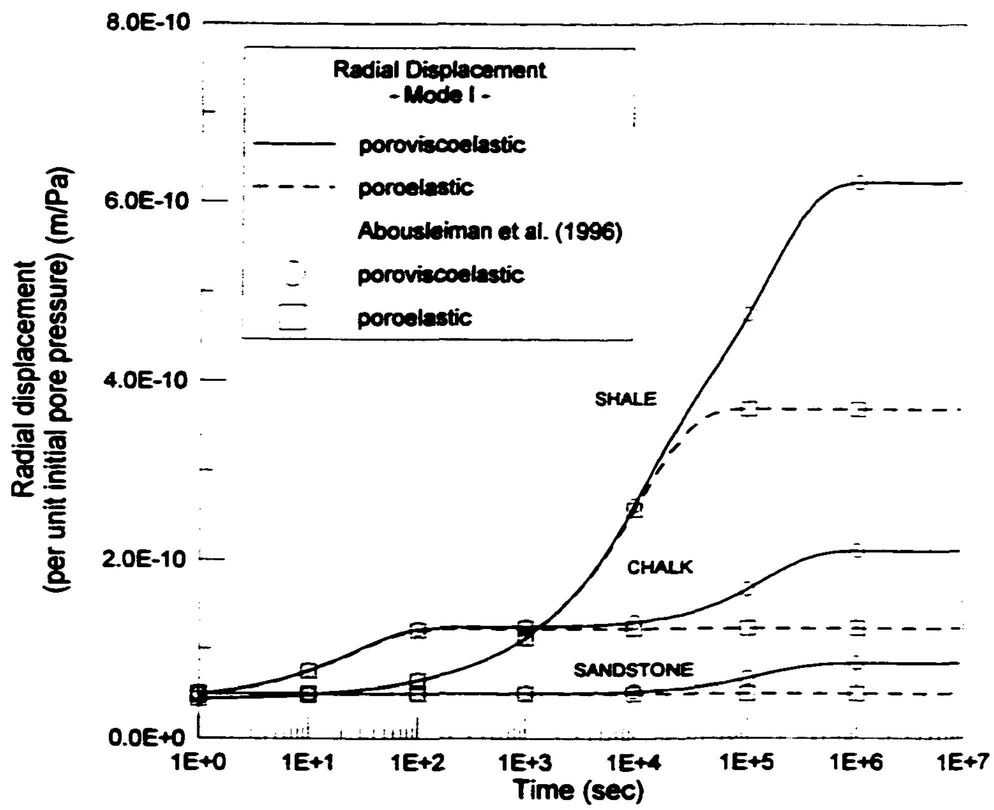

Figure 4.2: Radial displacement as a function of time for Mode I loading.

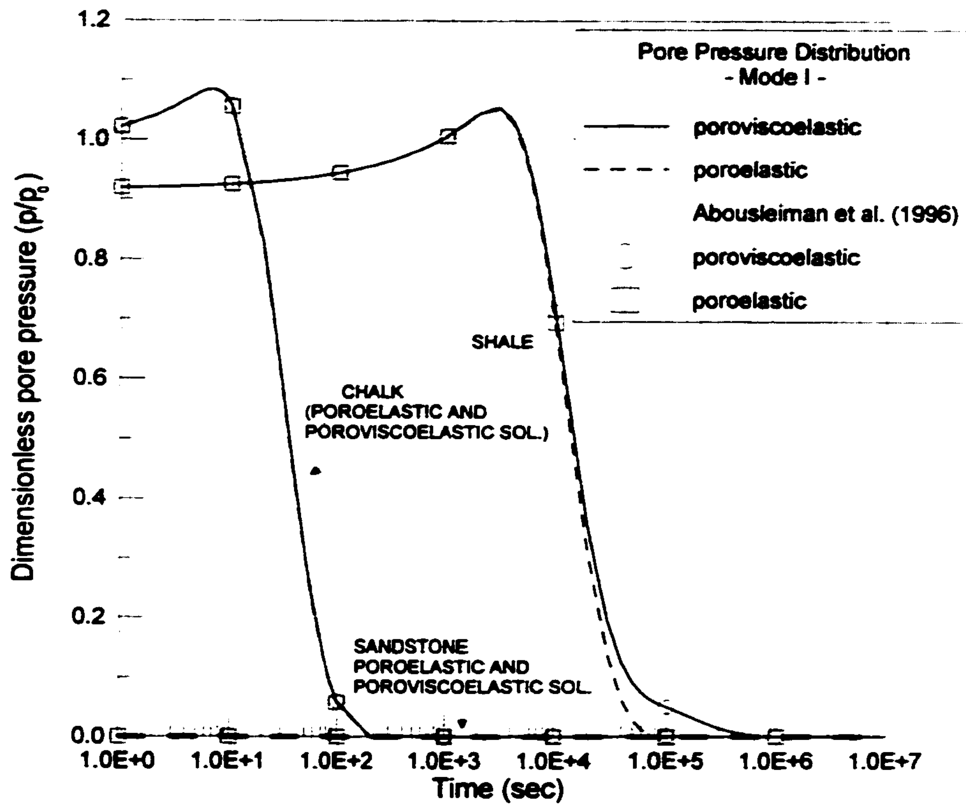

Figure 4.3: Pore pressure distribution at the center of the cylinder for Mode I loading.

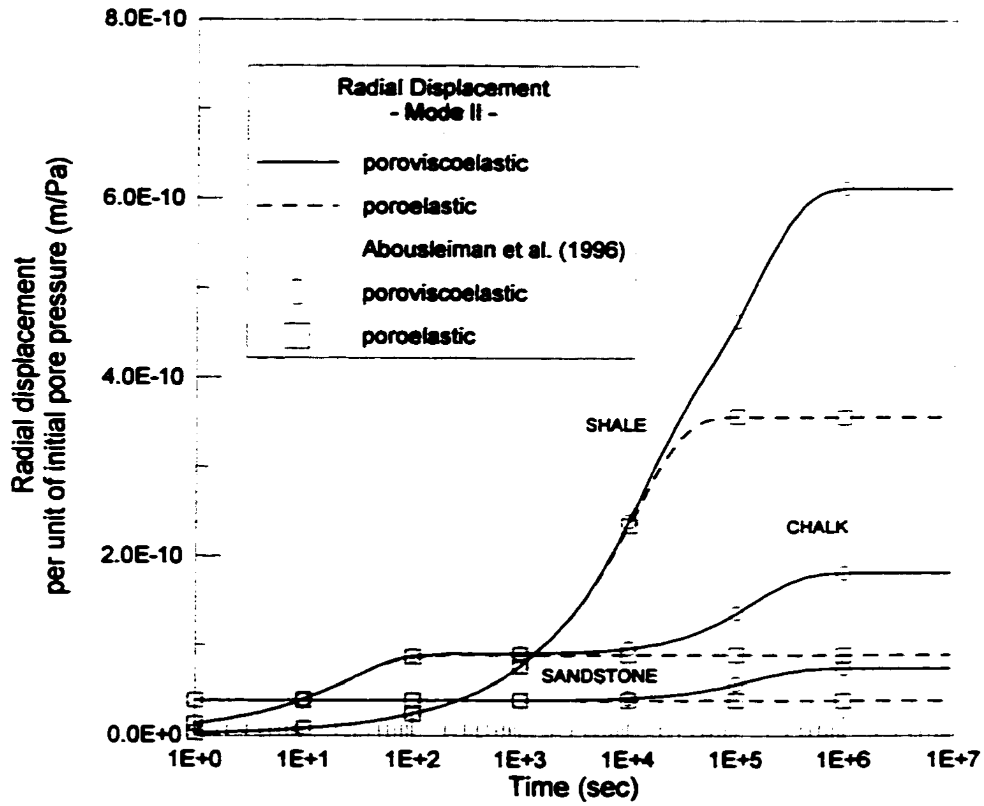

Figure 4.4: Radial displacement as a function of time for Mode II loading.

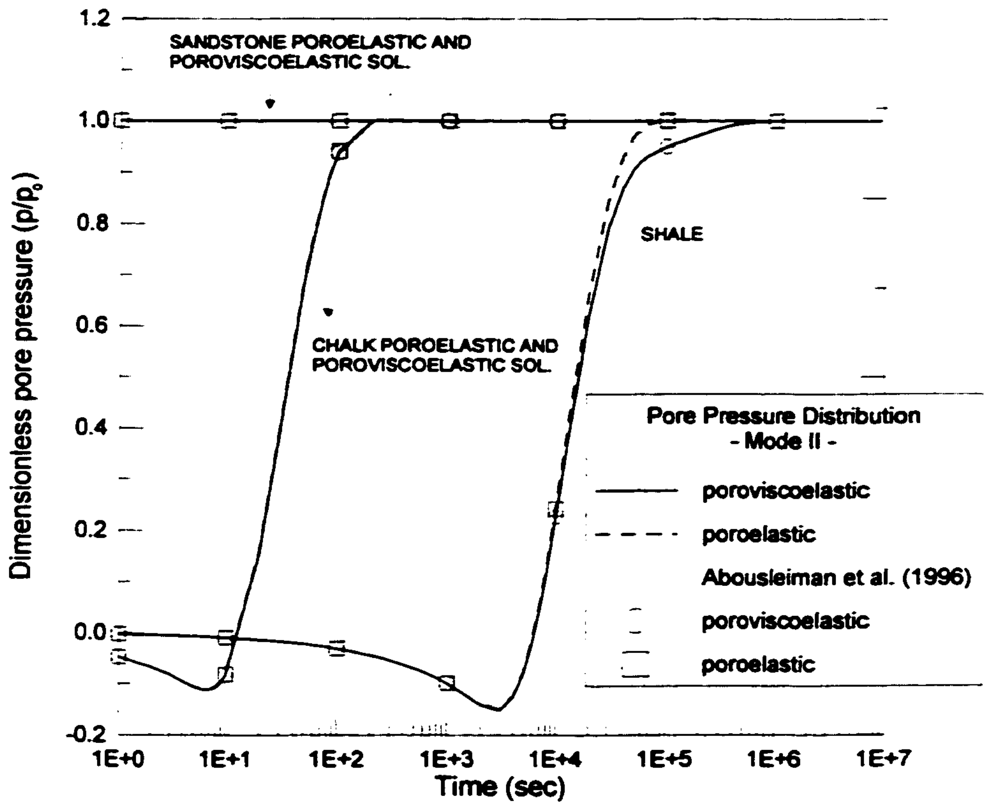

Figure 4.5: Pore pressure distribution at the center of the cylinder for Mode II loading.

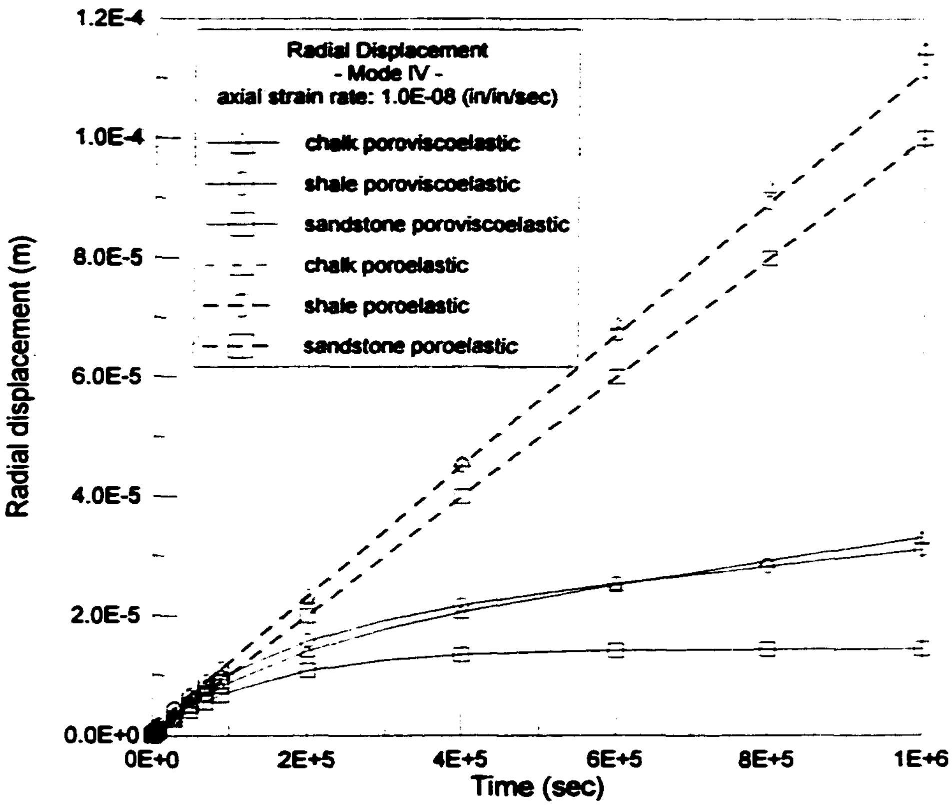

Figure 4.6: Radial displacement as a function of time for Mode IV loading. The symbols in this figure still represent Abousleiman et al.(1996) solutions.

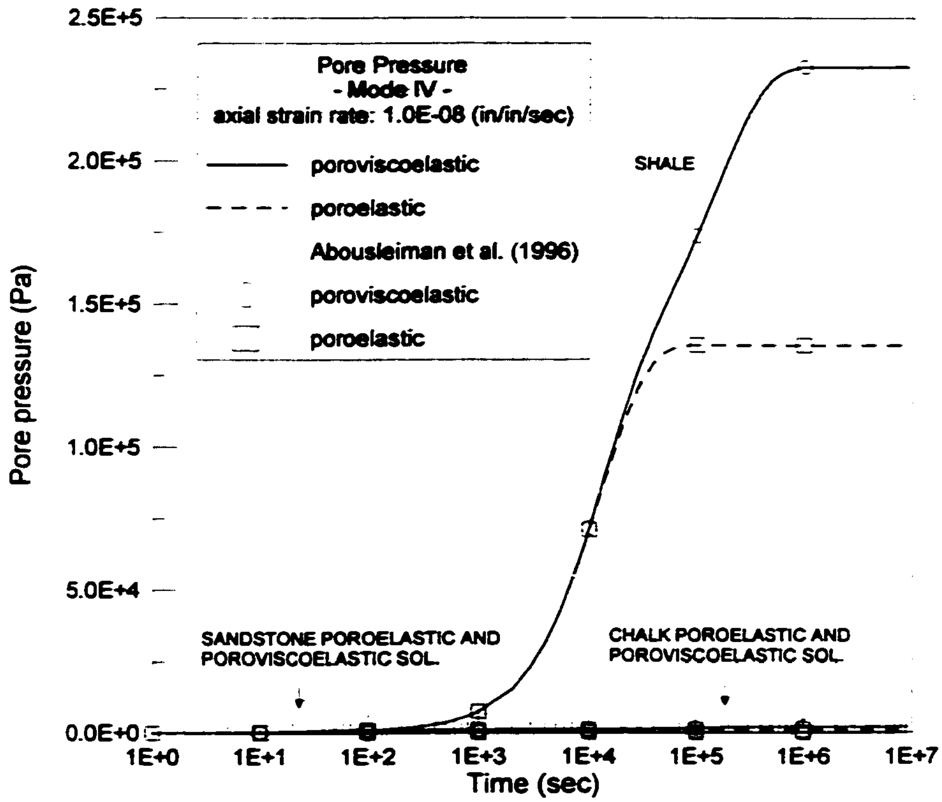

Figure 4.7: Pore pressure distribution at the center of the cylinder for Mode IV loading.

4.1.2 Long Term Solution

The total displacement computed from the poroelastic solution in mixed Modes I and II must reproduce the classical elastic solution allowing sufficient time for the pore pressure to equilibrate all over the core, after a change in the core boundary stress and/or pore pressure.

In order to verify if this behavior was reproduced by the developed code, the poroelastic solution was computed assuming E, K, K_s, K_u and the permeability, k, as the basic rock data input. The rock properties used in the simulation are presented in Table 4.9 (Abousleiman *et al.*, 1996), while the hypothetical boundary conditions are shown in Table 4.10.

Table 4.9: Rock properties used in the simulation.

Rock type	E (10^9 Pa)	K (10^9 Pa)	K_s (10^{10} Pa)	K_u (10^9 Pa)	k (m^2/s)
Sandstone	14.40	8.00	3.60	15.25	1.0 x 10^{-13}
Chalk	5.40	3.30	1.20	7.70	1.0 x 10^{-17}
Shale	1.85	1.10	3.40	9.25	1.0 x 10^{-19}

Table 4.10: Boundary conditions for the comparison between poroelastic and elastic solution.

σ_r (MPa)	p_{res} (MPa)	p_{df} (MPa)	t^* (hours)
1.30	1.27	1.27	2:00

The elastic solution was computed by Equation (A.14), derived in Appendix A, which was applied in two ways: the first one, by considering the initial radial stress and pore pressure as time-dependent, according to Equation 3.40; and secondly, assuming constant stress and constant pore pressure, as a 'quick' check. The material properties needed for applying Equation (A.14) were taken from the data given in

Table 4.9, using:

$$G = \frac{3KE}{9K - E} \tag{4.8}$$

$$\nu = \frac{3K - 2G}{2\,(3K + G)} \tag{4.9}$$

$$\alpha = 1 - \frac{K}{Ks} \tag{4.10}$$

The parameters resulting from these calculations are shown in Table 4.11.

Table 4.11: Rock parameters for computing the radial displacement in the poroelastic and elastic solution.

Rock type	G (GPa)	ν	α
Sandstone	6.00	0.20	0.78
Chalk	2.20	0.23	0.72
Shale	0.76	0.22	0.97

Figures 4.8 and 4.9 show a good match between the poroelastic and the two elastic solutions. The larger the rock permeability, the faster the pore pressure dissipates and poroelastic and elastic solutions become the same, as expected. The elastic solution, with a constant load as boundary condition, is a very simplified assumption, missing the whole deformation process, indicating only the final displacement.

Based on the VCP, the poroviscoelastic and viscoelastic solutions were computed from the poroelastic and elastic solutions, assuming once more that $K_2 = K_1 = K$ and that $\mu_K/K_2 = 2$ days, in the modified Kelvin model. Figures 4.10 and 4.11 show a good match between the poroviscoelastic and the viscoelastic approach. The curves, as a matter of fact, are identical for higher permeability rocks, like chalk and sandstone, while in shales they match only for larger times.

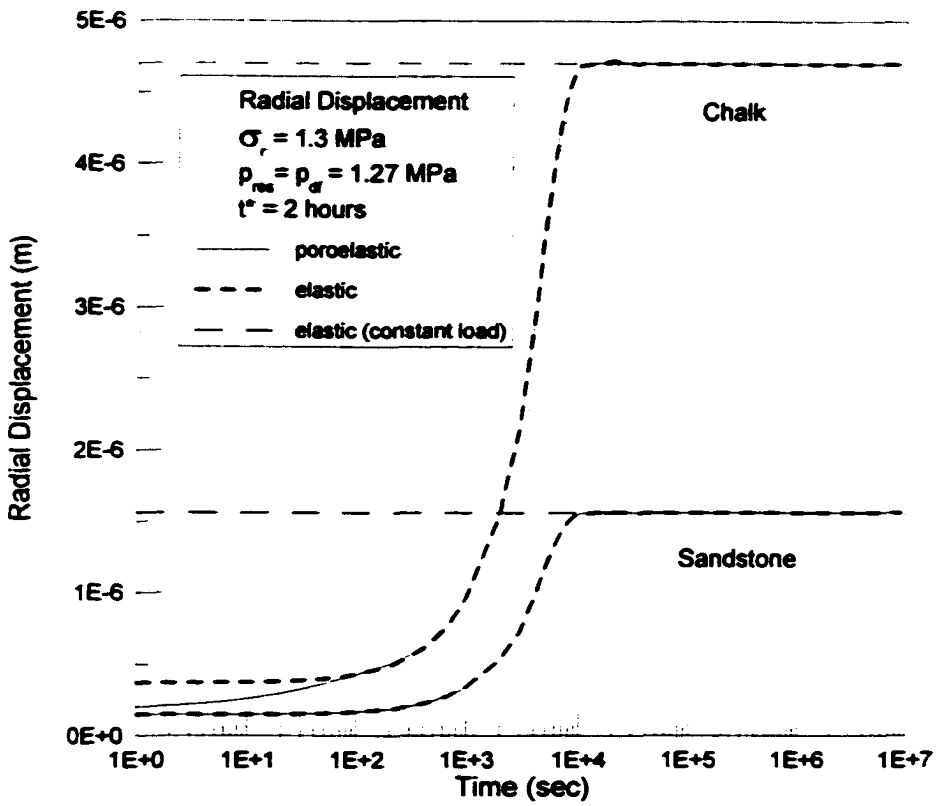

Figure 4.8: Poroelastic and elastic solutions for the radial displacement of a sandstone and a chalk sample.

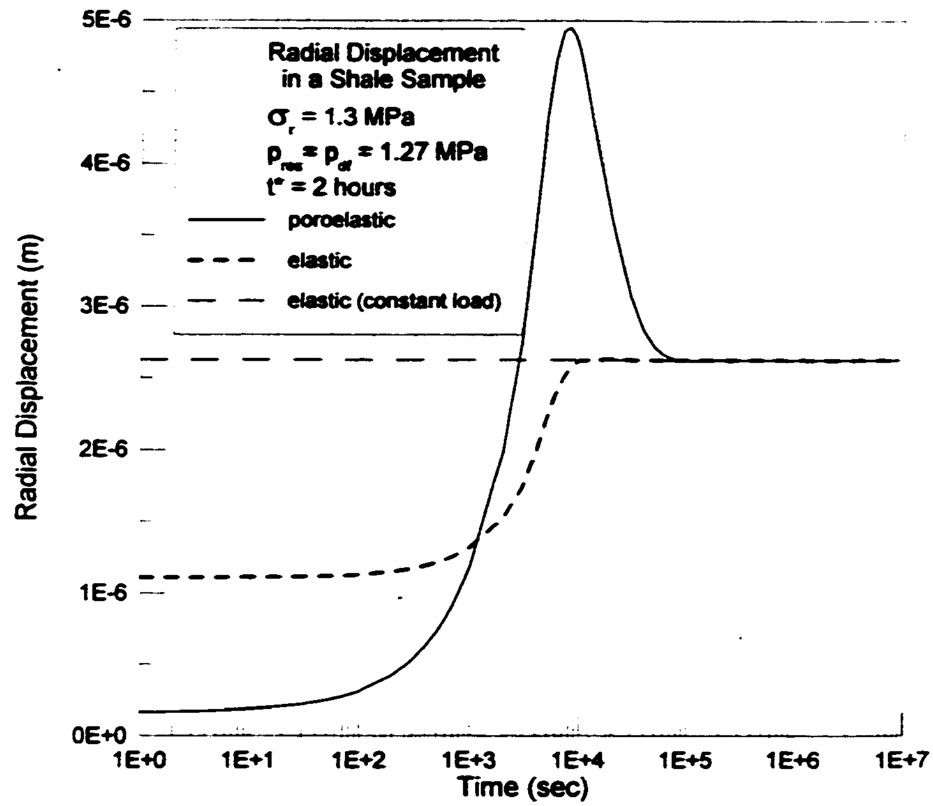

Figure 4.9: Poroelastic and elastic solutions for the radial displacement of a shale sample.

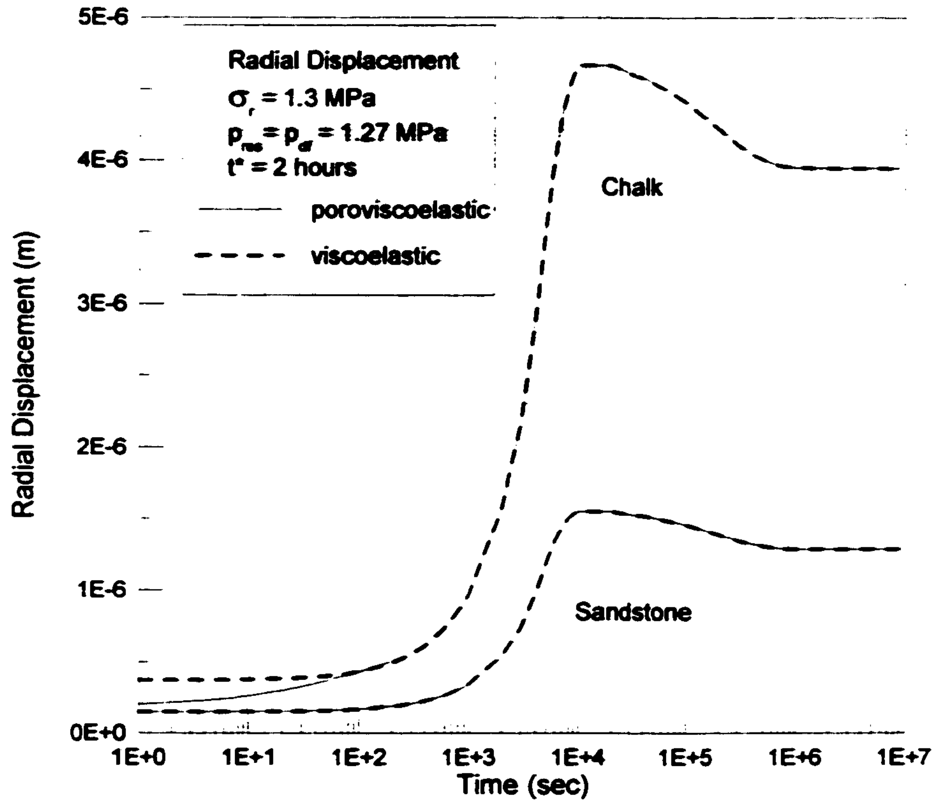

Figure 4.10: Radial displacement in the poroviscoelastic and viscoelastic approach for sandstone and chalk.

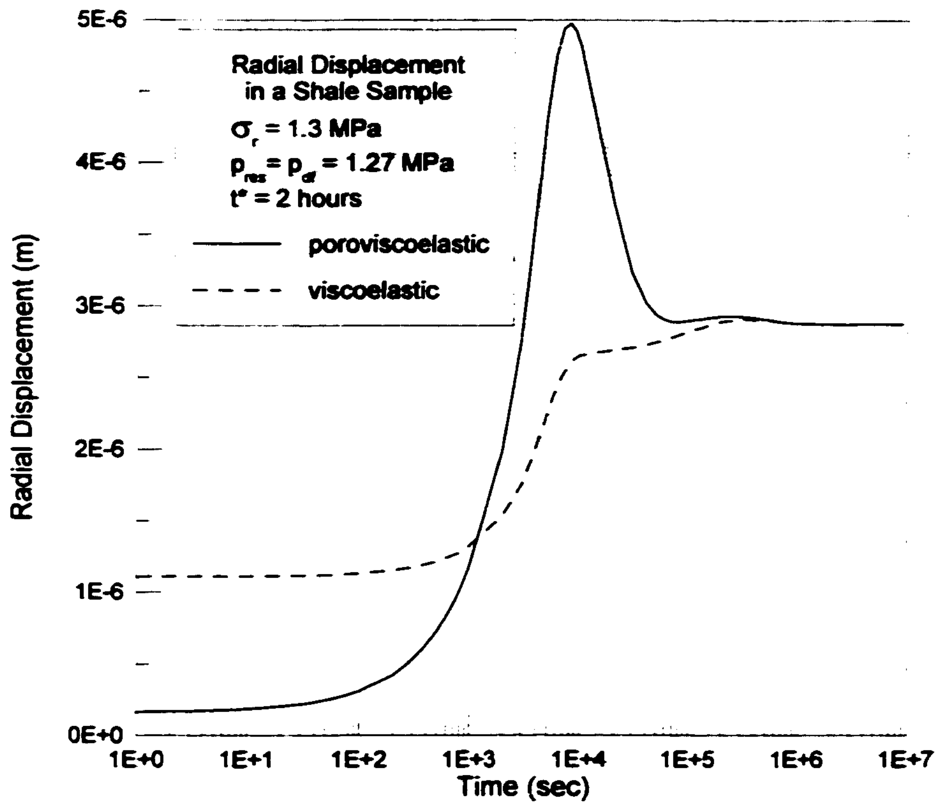

Figure 4.11: Radial displacement in the poroviscoelastic and viscoelastic approach for a shale sample.

4.1.3 The Inversion Check

The inversion check aimed at verifying the code ability for computing the radial in-situ stress and the reservoir initial pressure from a given radial displacement. A hypothetical stress field was initially defined and the numerical radial displacement computed from Modes I and II combined. This data, was then used as input for reproducing the initial stress field.

The inversion process was tested for a shale sample (the shale properties used in this simulation are shown in Table 4.9), in the poroviscoelastic approach. Once more the time-dependent behavior was restricted to the bulk modulus, having $K_2 = K_1 = K$ and $\mu_K/K_2 = 2$ days. The boundary and drilling hypothetical conditions applied for computing the radial displacement are listed in Table 4.12.

Table 4.12: Boundary conditions for computing the radial displacement.

In-Situ radial stress	$\sigma_r = 5.0$ MPa
Initial reservoir pressure	$p_{res} = 1.27$ MPa
Recovery time	$t^* = 8$ hours
Core radius	$r = 0.1$ m
Drilling fluid pressure:	
Overbalanced drilling	$p_{df} = 2.0$ MPa
Balanced drilling	$p_{df} = 1.27$ MPa
Underbalanced drilling	$p_{df} = 1.0$ MPa

According to Equations (3.66) and (3.67), the radial in-situ stress computed in this inversion check must be constant, as confirmed by Figure 4.12. By the same token, the reservoir initial pressure, computed by Equations (3.68) and (3.69), must also be constant, as shown in Figure 4.13. This test confirms the method capability for computing the initial stresses from the displacement data.

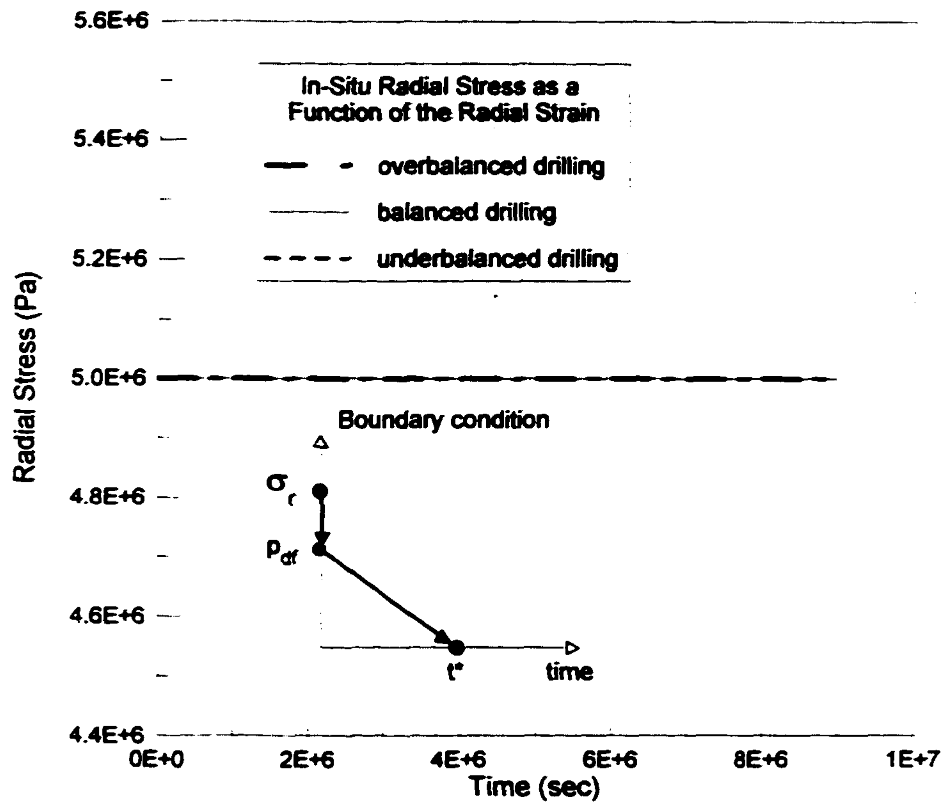

Figure 4.12: In-Situ radial stress computed from the radial displacement for the analyzed case.

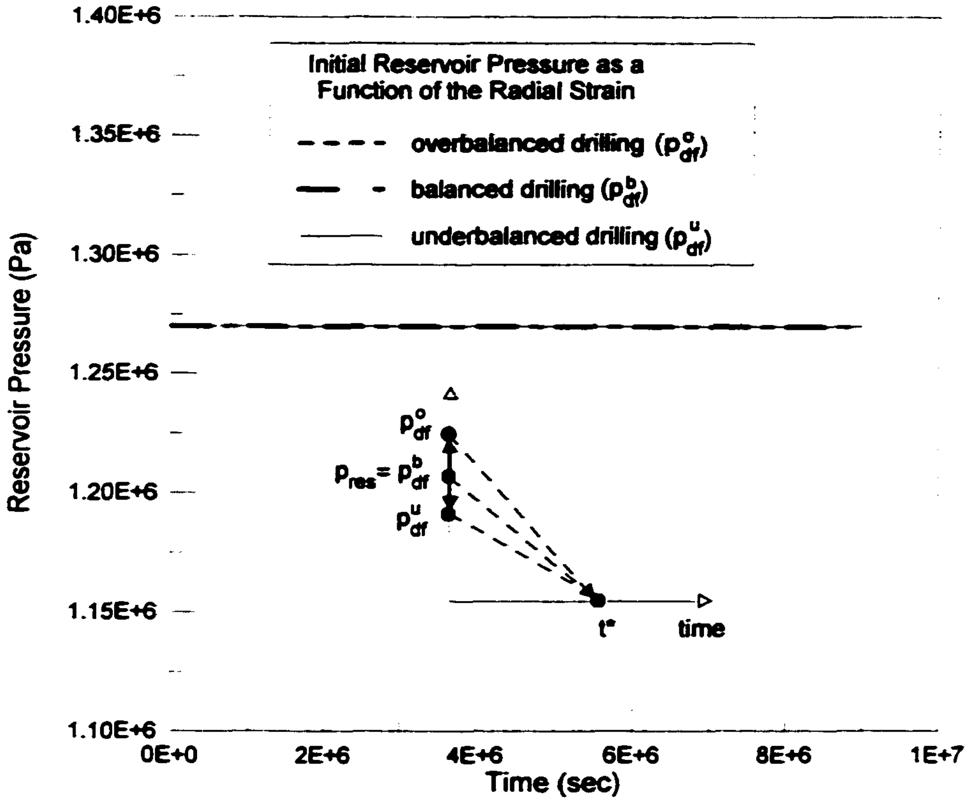

Figure 4.13: Initial reservoir pressure computed from the radial displacement for the analyzed case.

4.2 Parametric Analyses

It has been stated before that the shape of the strain *versus* time curve is important because it defines a unique in-situ stress-anelastic strain relationship. Based on this, parametric analyses were carried out aiming at identifying the conditions that can influence the anelastic strain behavior. The analyzed conditions were based on:

(i) choosing different sets of rock properties as input data;

(ii) defining the time-dependent rock properties;

(iii) the drilling conditions (overbalanced, balanced and underbalanced);

(iv) the ratio between the in-situ radial stress and the initial reservoir pressure; and,

(v) recovery time;

Although E, K, K_s, and K_u have already been defined as the 'standard' set of input rock properties, the shear modulus, G, was also included in these parametric analyses, to make it more general.

The viscous behavior was assumed as:

$$\begin{cases} X_1 = X_2 \\ \mu_X = 2\ days \end{cases} \tag{4.11}$$

where $X = E, G, K, K_s, K_u$.

The rock input parameters for the parametric analyses are shown in Table 4.13: the shale data is from Abousleiman *et al.* (1996), while the sandstone parameters were taken from well C (Chapter 6).

Table 4.13: Rock data used in the parametric study.

Rock Type	E (GPa)	K (GPa)	G (GPa)	K_s (GPa)	K_u (GPa)	k (m^2/s)	ϕ (%)
Shale	1.85	1.10	0.75	34.0	9.25	$1.0x10^{-19}$	30.0
Sandstone	2.65	-	0.43	112.0	-	$1.0x10^{-15}$	19.0

In order to verify the influence of each of the basic parameters on the radial strain, a series of cases were performed by varying the time-dependent input parameters, as shown in Table 4.14. Several ratios of in-situ stress/reservoir pressure as well as drilling conditions were tested.

Table 4.14: Analyzed input conditions.

Case	Time-Dependent Parameter	Constant Parameter
1	E	K, K_s, K_u
2	K and E	K_s, K_u
3	K	E, K_s, K_u
4a	$G(G_2 = G_1)$	K, K_s, K_u
4b	$G(G_2 = 3G_1)$	K, K_s, K_u
5a	K and $G(G_2 = G_1)$	K_s, K_u
5b	K and $G(G_2 = 3G_1)$	K_s, K_u
6	K, E, K_s, K_u	-

Figure 4.14 shows that assuming the time-dependent properties as the bulk modulus and/or Young's modulus will lead to small differences at the end of the anelastic strain recovery process. The same can be said about choosing $K(t)$ and/or $G(t)$ as the primary time-dependent properties (Figure 4.15). Comparing these two figures, it can be seen that the final strain will be exactly the same, whenever the same conditions (4.11) are taken into account for all the three parameters (K, E and G). In reality, one should not expect different rock properties to have exactly the same variation, although the results are still very similar, when one assumes, for example, that $G_2 = 3G_1$ (case b in Figure 4.15).

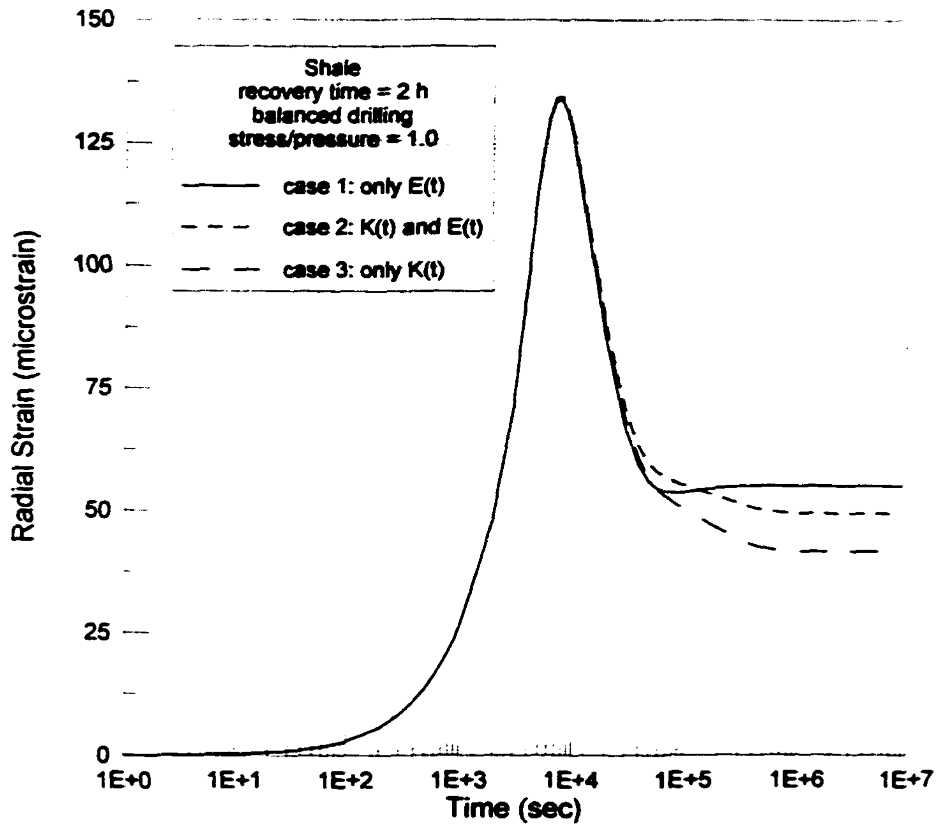

Figure 4.14: Variation of the radial strain as a function of time assuming K(t) and/or E(t) as the basic time-dependent parameters.

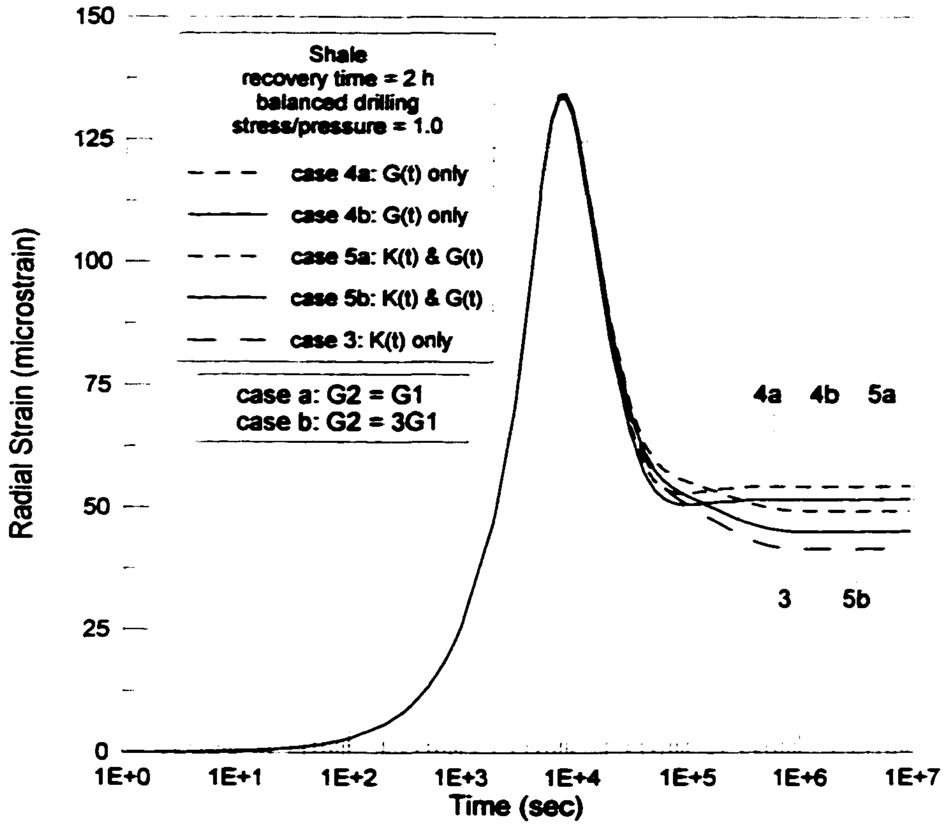

Figure 4.15: Variation of the radial strain as a function of time assuming K(t) and/or G(t) as the basic time-dependent parameters.

A more general assumption considering all the four basic elastic parameters as time-dependent is presented in Figure 4.16, for different ratios between the initial radial stress and the reservoir pressure. Once more, the effect on the strain *versus* time curve is very small. The situation where the initial radial stress and the reservoir pressure are almost the same (stress/pressure = 1.02) is shown in greater detail in Figure 4.17. This figure shows that the relationship between the initial radial stress and the reservoir pressure plays an important role in defining if the rock deformation pattern will show expansion, shrinkage or a combination of both. A large stress relief will dominate the process, leading to core expansion only, whenever the in-situ radial stress is much larger than the initial reservoir pressure. If the ratio initial stress/reservoir pressure is close to 1, and depending on the rock physical properties, pronounced rock shrinkage may occur.

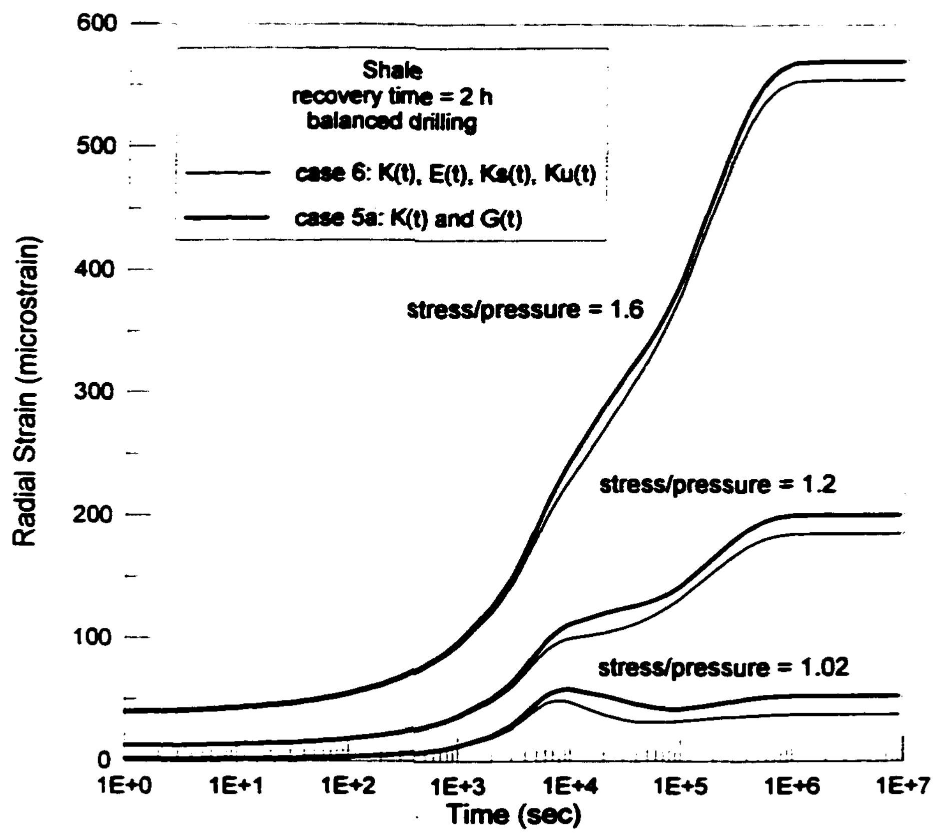

Figure 4.16: Comparison of the radial strain as a function of time assuming 2 and 4 time-dependent parameters.

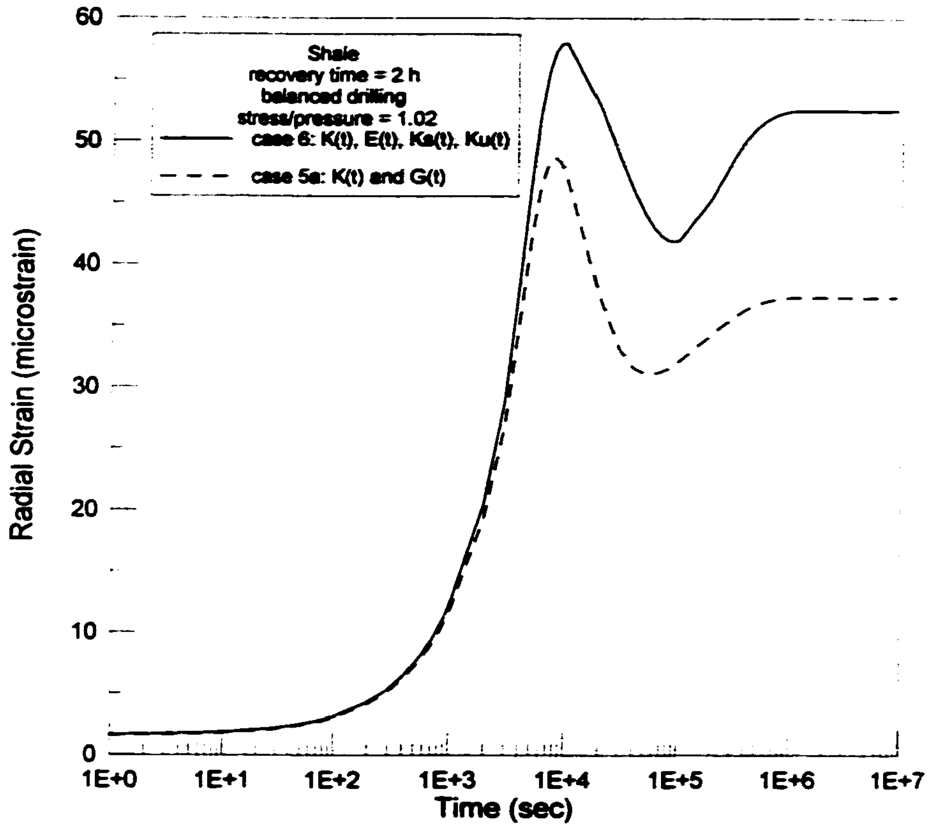

Figure 4.17: Comparison of the radial strain as a function of time for 2 and 4 time-dependent parameters and initial stress/reservoir pressure = 1.02.

The influence of the creep parameters in the radial strain is shown in Figure 4.18. As expected, the final strain is just a function of the ratio K_2/K_1: higher K_2/K_1 leads to larger radial strains. The term μ/K_2 is related to the process duration: keeping K_2/K_1 constant, higher μ/K_2 leads to a faster stress stabilization. When K_2/K_1 is large (K_2/K_1=17 in Figure 4.18), the radial displacement becomes insensitive to μ/K_2.

Figures 4.19 and 4.20 show that the drilling condition can only produce a small variation in the deformation pattern (less than 1%) for a relatively short period of time.

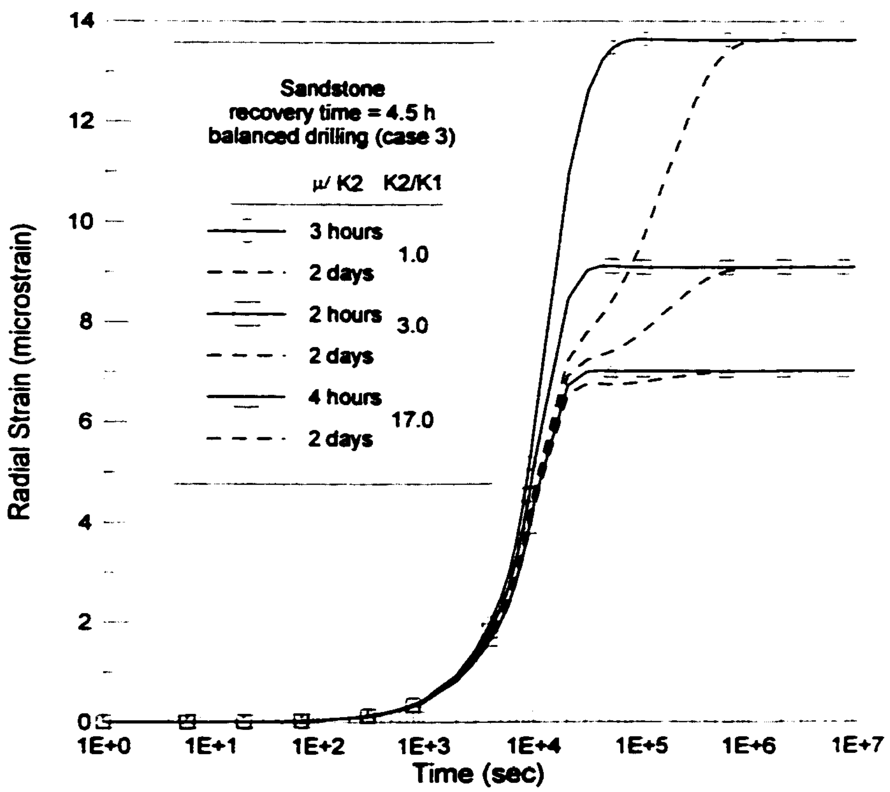

Figure 4.18: Influence of the creep parameters on the strain versus time curve assuming only K(t).

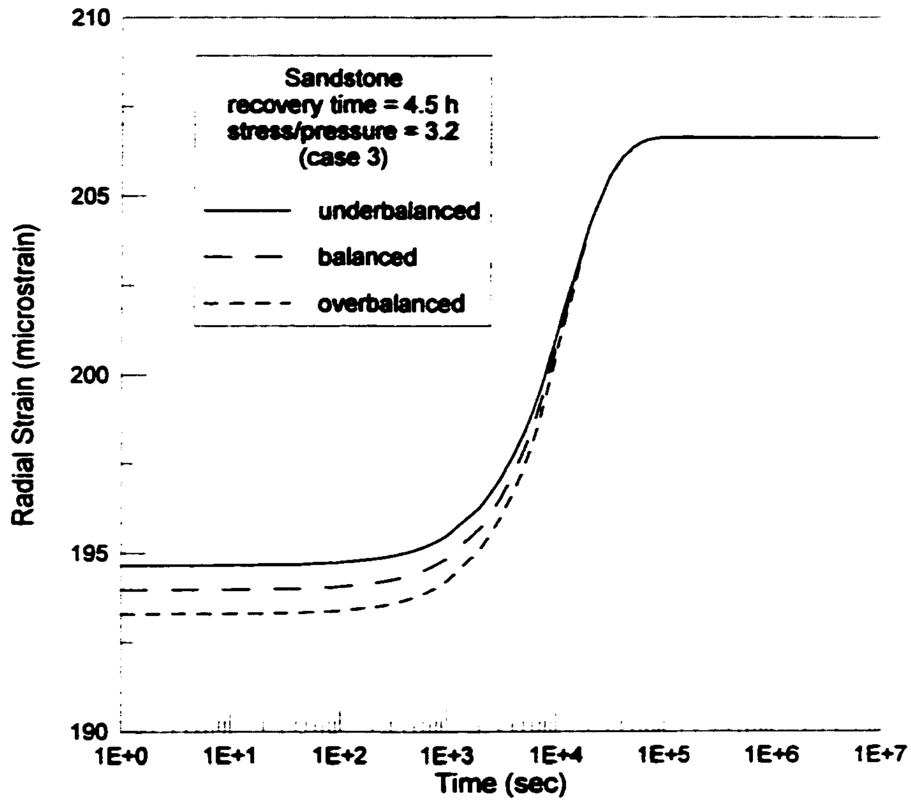

Figure 4.19: Influence of the drilling conditions on the radial strain as a function of time for a sandstone sample.

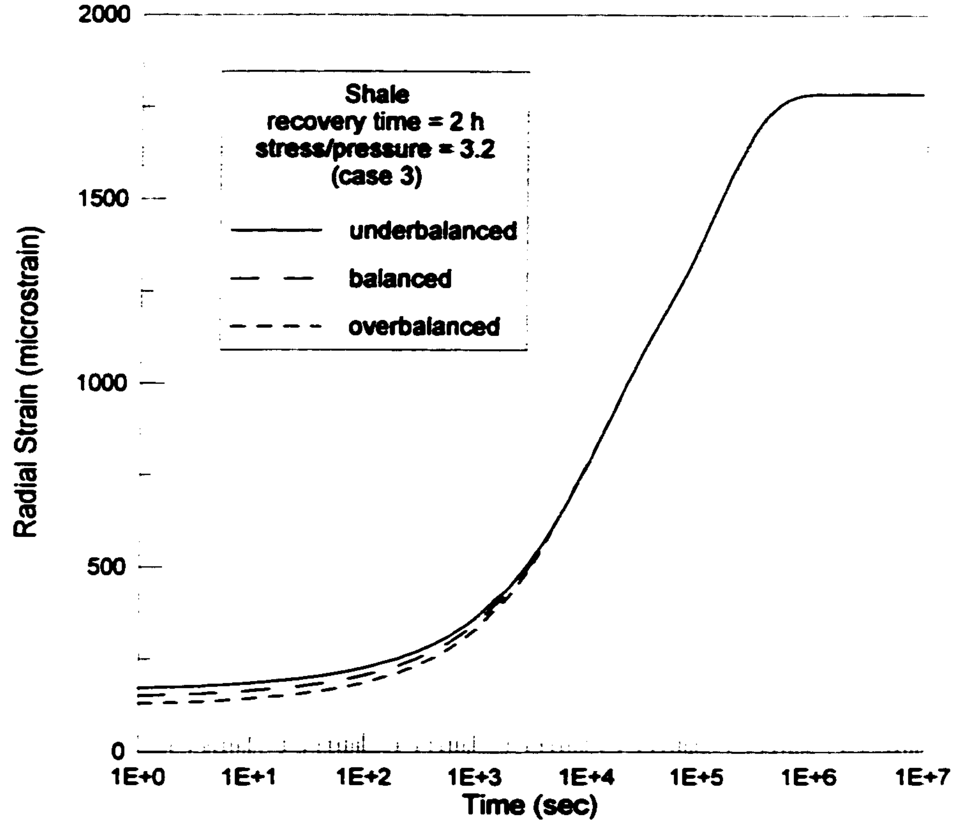

Figure 4.20: Influence of the drilling conditions on the radial strain as a function of time for a shale sample.

The sensitivity of the radial deformations with respect to Biot's coefficient, α, was also tested. Three different conditions were verified:

(i) $\alpha = \alpha(t)$, computed from Equation (3.91) and assuming $K = K(t)$;

(ii) $\alpha = \alpha_0$, where α_0 is the initial value of α, obtained from Equation (3.91) for $K(\ t = 1$ sec); and,

(iii) $\alpha = \alpha_f$, where α_f is the final value of α, also computed from Equation (3.91) for $K(t = 9E + 6$ sec).

Figure 4.21 shows that a variation of only 1.6 % of α ($\alpha_0 = 0.968$; $\alpha_f = 0.984$), but it can lead to quite different shapes and magnitudes of the strain *versus* time curve. The rock final strain can be up to 100% greater when $\alpha_0 = 0.968$ is used, instead of $\alpha(t)$.

4.3 Summary

Summarizing Chapter 4, it can be said that all the goals were attained in the validation procedure:

(i) previous literature results were matched;

(ii) the numerical long-term solution was identical to the analytical one; and,

(iii) the inversion perfectly reproduced the hypothetical input stress field.

The interesting conclusions regarding the parametric analyses are:

(i) there is no need for using more than one rock property for including the rock viscoelastic characteristics;

(ii) the anelastic strain curve is very sensitive to the ratio between the initial radial stress and the reservoir pressure: higher ratios meaning negligible deformations due to pore contraction;

(iii) the creep parameters play an important role in the anelastic strain pattern;

(iv) the drilling conditions can only produce a small variation in the beginning

of the rock deformations. After a certain time the rock strain pattern is unique for overbalanced, balanced and underbalanced drilling conditions;

(v) Biot's coefficient, which has been usually neglected by the oil industry, plays an important role in the ASR, whenever poroelastic effects are relevant; and,

(vi) low permeability rocks, like shales, or rocks with high clay content, are most prone to present shrinkage in the ASR.

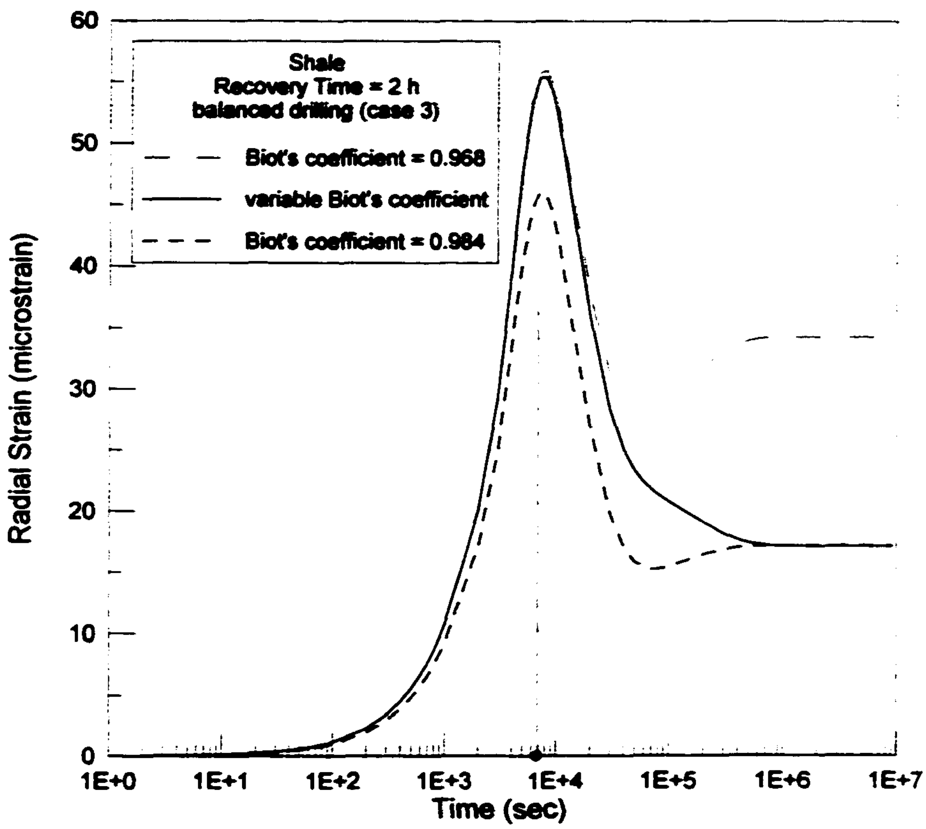

Figure 4.21: Influence of Biot's coefficient on the radial strain as a function of time for the poroviscoelastic approach.

Chapter 5

Model Application: Field Cases

Up to now the poroviscoelastic model has been used only for determining the influence of poroviscoelasticity in the ASR process after coring, using synthetic examples. In this chapter it will be applied for computing the maximum and minimum horizontal in-situ stresses, σ_{HMAX} and $\sigma_{h\min}$, from ASR actual measurements in the field.

Due to the model limitations, the stress field in the previous analyses was assumed to be hydrostatic, and loading Modes I and II, which are the only ones that may present poroelastic effects, were enough for describing the rock deformation. This led to the computation of the hydrostatic component of the in-situ stress, P_0. In order to enable the model to compute a more general stress field, it was necessary to add Mode III (which is free from poroelastic effects), for representing the strains caused by the deviatoric stresses, S_0.

Considering now that the stress field around the core can be decomposed as shown in Figure 1.11, and knowing that:

$$\begin{cases} P_0 = \dfrac{\sigma_{HMAX} + \sigma_{h\min}}{2} \\ S_0 = \dfrac{\sigma_{HMAX} - \sigma_{h\min}}{2} \end{cases} \tag{5.1}$$

the principal horizontal in-situ stresses can be finally computed as:

$$\begin{cases} \sigma_{HMAX} = P_0 + S_0 \\ \sigma_{h\min} = P_0 - S_0 \end{cases} \tag{5.2}$$

where P_0 is the hydrostatic stress component and S_0 is the deviatoric stress component, as presented in Table 3.1, assuming further that $\theta = 0^o$ corresponds to σ_{HMAX}, and consequently $\theta = 90^o$ is associated with $\sigma_{h\,\min}$.

The application can be summarized in the following steps:

1. Coring rock samples;

2. Measurement of anelastic strains as soon as the rock sample is retrieved from downhole. Although the ASR test is able to provide the rock strains in six directions (ε_{xx}, ε_{aa}, ε_{yy}, ε_{bb}, ε_{cc}, and ε_{zz}), as shown in Figure 5.1a, only ε_{xx}, ε_{aa} and ε_{yy}, are needed for the 2-D solution (Figure 5.1b);

3. Computation of the principal strains in the horizontal plane, ε_{11} and ε_{22}, for each time interval, according to (Goodman, 1980):

$$\begin{cases} \varepsilon_{11} = \dfrac{\varepsilon_{xx} + \varepsilon_{yy}}{2} + \sqrt{\varepsilon_{xy}^2 + \left[\dfrac{\varepsilon_{xx} - \varepsilon_{yy}}{2}\right]^2} \\ \varepsilon_{22} = \dfrac{\varepsilon_{xx} + \varepsilon_{yy}}{2} - \sqrt{\varepsilon_{xy}^2 + \left[\dfrac{\varepsilon_{xx} - \varepsilon_{yy}}{2}\right]^2} \end{cases} \tag{5.3}$$

where,

$$\varepsilon_{xy} = \frac{\varepsilon_{xx} - 2\varepsilon_{aa} + \varepsilon_{yy}}{2} \tag{5.4}$$

4. Determination of the hydrostatic and deviatoric anelastic strains, ε_{PP} and ε_{DD}, using:

$$\begin{cases} \varepsilon_{PP} = \dfrac{\varepsilon_{11} + \varepsilon_{22}}{2} \\ \varepsilon_{DD} = \dfrac{\varepsilon_{11} - \varepsilon_{22}}{2} \end{cases} \tag{5.5}$$

5. Determination of the hydrostatic and deviatoric stresses, P_0 and S_0, from ε_{PP} and ε_{DD}, via an inversion method, as described in the next section;

6. Computation of σ_{HMAX} and $\sigma_{h\,\min}$ from Equation 5.2;

7. Comparison of the obtained stresses with other field data as well as regional geological trends.

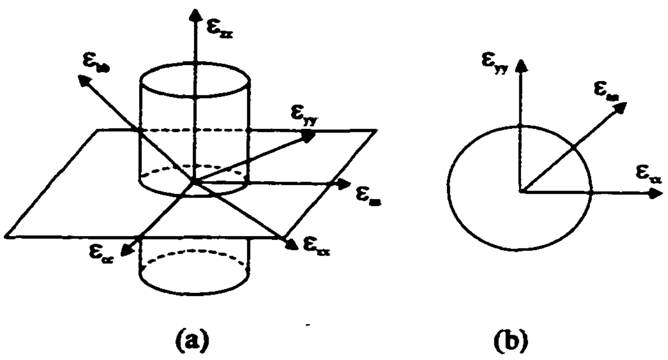

Figure 5.1: (a) ASR measuring orientations; (b) directions considered for the horizontal stresses calculation, based on the model plane strain assumption.

5.1 The Inverse Problem

The theory of inverse modeling (also known as back-analysis) allows inferring causing actions and initial conditions by matching a model to experimental observations. The determination of the hydrostatic and deviatoric in-situ stresses from the hydrostatic and deviatoric anelastic strains is a typical inverse problem. Figure 5.2 presents a scheme that helps understanding the concept of an inverse problem.

Several methods were tested for computing the horizontal in-situ stresses with the poroviscoelastic model, in order to define the most valid technique. If the rock radial strain could be transformed into the Laplace domain, then, computing in-situ stresses from the stress relief data would be done by simply applying Equation (3.66). A large effort was made in this direction: the radial strain from ASR data were curve-fitted by polynomial functions and transformed into the Laplace domain for calculating the initial stresses. This approach had a major drawback, since it

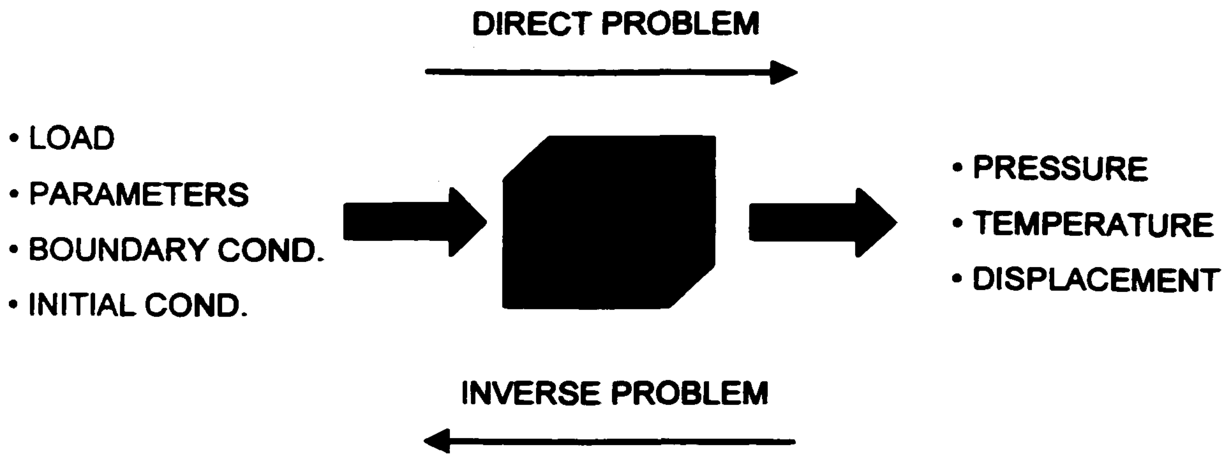

Figure 5.2: Schematic representation of direct and inverse problems.

needed the complete core deformation as input, i.e., the whole strain history since coring, while the ASR test can only provide the strain occurring after the core is retrieved and instrumented at the rig surface. In order to make the strains computed by the model and the ASR field data comparable, the displacements in Equation (3.66) were considered as (Figure 5.3):

$$\tilde{u}_r(s) = \tilde{u}_{r_{ASR}} - \tilde{u}_r(s^*) \tag{5.6}$$

where s is the Laplace variable and s^* corresponds to t^*, the starting time for the ASR test. Nevertheless, s^* cannot be computed for a single point, t^*, since the Laplace transform is a mapping function; and, therefore, the procedure was abandoned.

Other procedures were then analyzed aiming at the hydrostatic and deviatoric stresses that would produce the best curve-fittings for the strains generated by the model and the ones observed in the ASR test, i.e., minimizing the error (err) given by:

$$err = \mid \varepsilon_{r_{ASR}} - \varepsilon_{r_{MODEL}} \mid \tag{5.7}$$

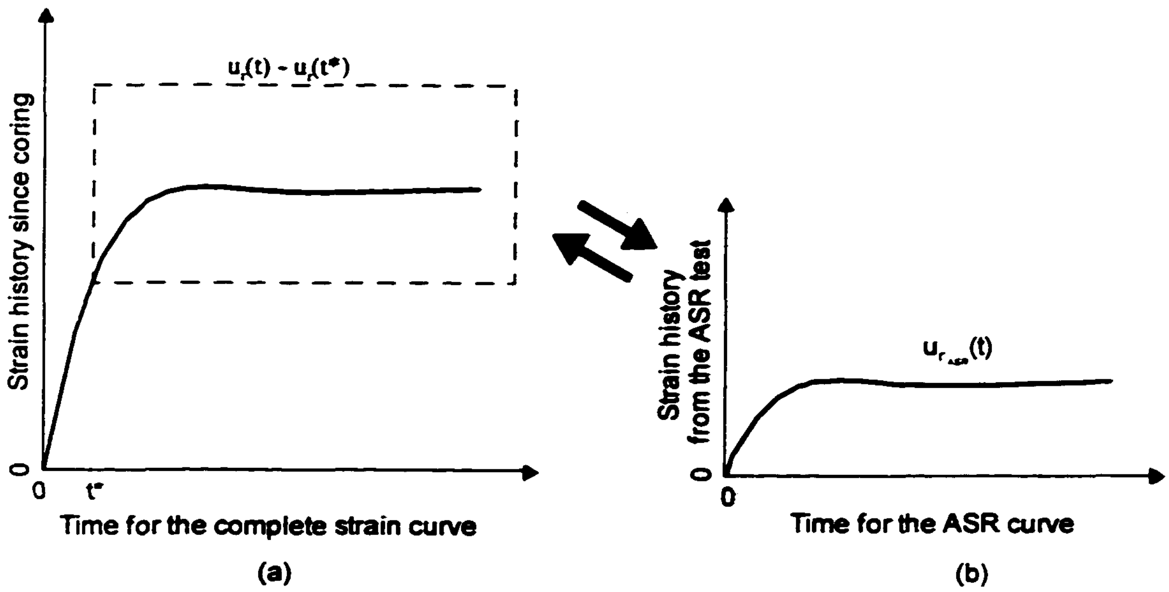

Figure 5.3: Strain history :(a) since coring (t* = time instant when the ASR test starts); and (b) strain measured by the ASR test.

Assuming the possibility of reaching $err = 0$, and using root finding algorithms such as the Newton Raphson method (Press, 1992), produced poor curve-fitting results and stress values which were unrealistic. This was attributed to divergence of the root-finding algorithm and inaccuracy of the experimentally determined rock parameters.

The Levenberg-Marquardt method (Finsterle, 1999) was attempted next, considering the lab-derived rock properties as initial guesses and allowing the method to modify them in order to give more flexibility to the stress computation. The idea is that whenever changes in the lab-derived rock parameter lead to a better curve-fitting, it can be assumed as a valid correction to experimental errors. The computed stresses were more realistic in this case, but the curve-fitting was still unsatisfactory, and a third method was chosen: the simplex minimization algorithm (Caceci and Cacheris, 1984). This approach has been proven to be always convergent and is indicated for multidimensional minimization problems, which is exactly the inverse problem under analysis, if one consider the rock properties as fitting parameters, together with the in-situ stresses. According to Shah and Hoek's (1992) application to the Hoek-Brown failure criterion, the simplex algorithm is also appropriate for fitting non-linear curves, like the ones derived from ASR tests and the poroviscoelastic model.

This method can be visualized as a geometric figure consisting of $n+1$ vertices in the n-dimensional space (Figure 5.4), i.e., each vertex has n-coordinates, constituted by the initial guesses of each variable. The figure shape changes as the method searches for the minimum error defined in Equation (5.7), expanding or contracting, as well as reflecting the vertices while moving in the n-dimensional space (Figure 5.5).

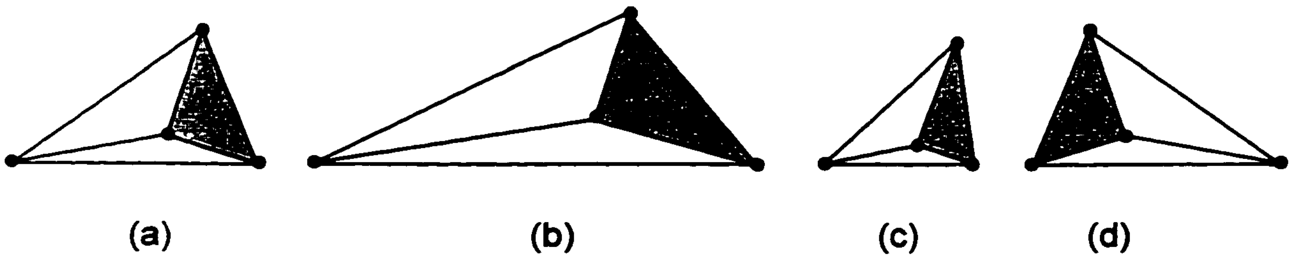

Figure 5.4: (a) a 3D (four vertices) simplex figure at the beginning of a step; (b) after an expansion; (c) contraction; and (d) reflection.

5.1.1 Synthetic Example

A synthetic example has been used in order to validate the application of the simplex method for computing the original stresses using the poroviscoelastic model. The theoretical strains in both hydrostatic and deviatoric loading were generated by the poroviscoelastic model assuming the rock parameters mentioned in Table 5.1, simulating an ASR curve to be fitted by the simplex code. A sensitivity analysis of the inversion process was also performed by varying:

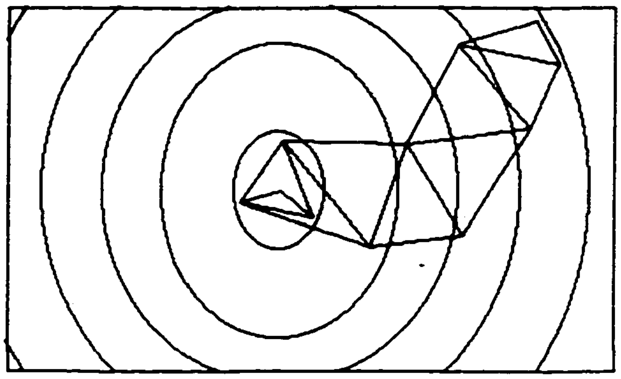

Figure 5.5: An example of the simplex moving in the response surface's contour plot, after Caceci and Cacheris (1984).

- the space dimension (number of rock parameters considered to be variable);
- the rock parameters; and,
- the initial guess for each rock parameter.

The input rock data were chosen within the seven rock parameters needed for fully describing the poroviscoelastic problem (E_1, E_2, μ_E, K, K_s, K_u, k), plus the hydrostatic or deviatoric stress (P_0 or S_0). In other words, the simplex geometric figure in the synthetic example had a maximum of nine vertices with eight coordinates each. The objective function was defined as the total error, err_{TOT}, given by:

$$err_{TOT} = \sum_{i=1}^{n} \mid \varepsilon_{r_{SYN}} - \varepsilon_{r_{MODEL}} \mid \tag{5.8}$$

where,

$$\begin{cases} n \text{ is the total number of adjusted points;} \\ \varepsilon_{r_{SYN}} \text{is the radial strain calculated by the synthetic example; and,} \\ \varepsilon_{r_{MODEL}} \text{is the radial strain generated by the inversion method} \end{cases}$$

Table 5.1: Input data for the synthetic example.

z (ft)	σ_{HMAX} (psi)	$\sigma_{h\,\min}$ (psi)	p_0 (psi)	p_{dri} (psi)	t_{rec} (sec)	t_{pre} (sec)	t_{test} (h)
3,000	2,400	1,800	1,300	1,500	10,000	0.0	27
E_1 (GPa)	E_2 (GPa)	μ_E (10^5GPa.sec)	K (GPa)	K_s (GPa)	K_u (GPa)	k (md)	μ_f (Pa.sec)
2.65	46.0	6.21	5.7	171.2	40.0	3.1	20E-3
$P_0 = \frac{(\sigma_H + \sigma_h)}{2} = 14.48$ MPa							
$S_0 = \frac{(\sigma_H - \sigma_h)}{2} = 2.07$ MPa							

z = coring depth;
σ_{HMAX} = maximum in-situ horizontal stress;
$\sigma_{h\,\min}$ = minimum in-situ horizontal stress;
p_0 = reservoir static pressure;
p_{dri} = drilling fluid pressure;
t_{rec} = recovery time;
t_{pre} = time for sample preparation before the ASR test;
t_{test} = duration of the synthetic ASR test;
P_0 = hydrostatic stress component;
S_0 = deviatoric stress component.
Core diameter: $D = 0.1$ m

Determination of the Synthetic Hydrostatic Stress from Back-analysis

A total of 15 data files with different initial guesses for the rock parameters (presented in Appendix B) were used for testing the program limitations when reproducing the synthetic hydrostatic stress. Table 5.2 shows the computed stresses and the total errors, according to Equation 5.8, for each input data set. The obtained curve-fittings are shown in Figures 5.6 and 5.7.

Analysis of the Results

The back-analysis was able to perfectly fit the synthetic hydrostatic strain curve for most of the chosen adjusting parameters, as shown in Figures 5.6 and 5.7. For some cases the fit was not so good, but the inaccuracies were never higher than 0.056%, which is perfectly acceptable. In fact, the hydrostatic stress computed by the inversion method was always very close (most of times identical) to the stress

Table 5.2: Hydrostatic stress computed for the synthetic example with the simplex code.

Input data file	Variable rock parameter	Computed stress (MPa)	Iterations	Total error ($\mu\varepsilon$)
guess-P1	$*$	14.48	0	44.04 x 10^{-13}
guess-P2	$**$	14.48	463	22.06 x 10^{-6}
guess-P3	$***$	14.48	472	48.02 x 10^{-6}
guess-P4	E_1	14.48	748	24.09 x 10^{-6}
guess-P5	E_1, E_2	14.61	737	104.5 x 10^{-2}
guess-P6	E_1, μ_E	14.55	709	109.1 x 10^{-2}
guess-P7	E_2	14.48	303	29.98 x 10^{-1}
guess-P8	μ_E	14.48	726	24.06 x 10^{-6}
guess-P9	E_2, μ_E	14.48	713	65.08 x 10^{-2}
guess-P10	E_1, E_2, μ_E	14.32	313	53.98 x 10^{-1}
guess-P11	K	19.80	278	29.20 x 10^{-1}
guess-P12	K_s	14.53	361	96.50 x 10^{-2}
guess-P13	K_u	14.48	441	166.3 x 10^{-5}
guess-P14	k	14.48	444	70.82 x 10^{-5}
guess-P15	E_1, E_2, μ_E K, K_s, K_u, k	14.13	346	54.52 x 10^{-1}

$*$ constant rock parameters and hydrostatic stress (original values).
$**$ only the stress is adjusted.
$***$ only the stress is adjusted from mostly negative initial values.

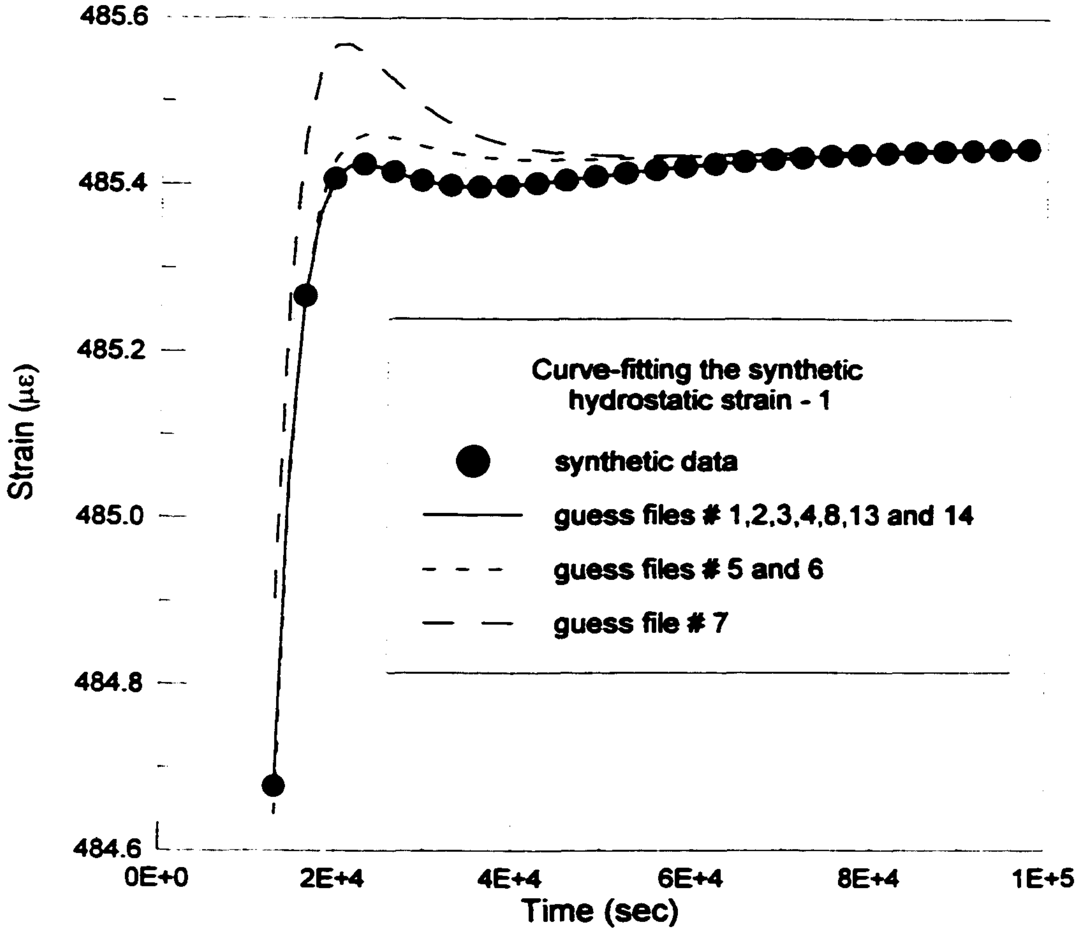

Figure 5.6: Curve-fittings for the synthetic hydrostatic strain (the plots have been splitted in two figures, for clarity purpose).

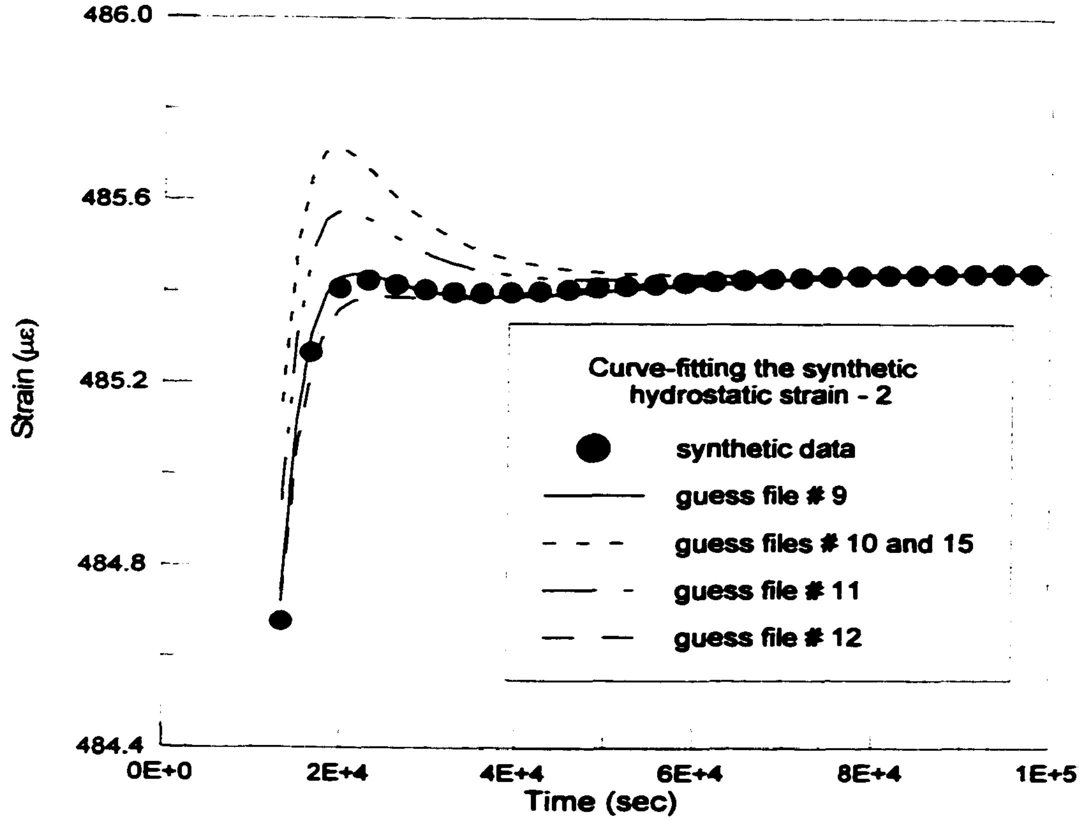

Figure 5.7: Curve-fittings for the synthetic hydrostatic strain (remaining curves).

predefined in the synthetic example, even when the initial guesses were far from the expected value, proving the method reliability.

Two observations deserved further investigations:

1) the final average values for the adjusted rock properties, presented in Table 5.3, were slightly different from the synthetic ones shown in Table 5.1. Although this could be expected whenever fitting experimental data, it was a surprise in the synthetic example;

2) the computed stress using the bulk modulus, K, as the only adjusting variable (input data file guess-P11), was far from the synthetic stress, as shown in Table 5.2.

Table 5.3: Computed average parameters in each run.

Input data file	E_1 (GPa)	E_2 (GPa)	μ_E (10^5GPa)	K (GPa)	K_s (GPa)	K_u (GPa)	k (md)
Synthetic	2.65	46.00	6.21	5.7	171.2	40.0	3.1
guess-P4	2.65						
guess-P5	3.76	62.07					
guess-P6	3.28		4.65				
guess-P7		60.84					
guess-P8			6.21				
guess-P9		60.84	9.30				
guess-P10	1.16	59.22	4.33				
guess-P11				11.51			
guess-P12					204.9		
guess-P13						54.80	
guess-P14							2.68
guess-P15	1.03	57.36	4.12	5.51	171.2	39.13	2.91

Both observations were verified throughout a second sensitivity analysis, performed in the following way (Velloso, 1999): the objective function was evaluated for only two variables at a time, one of them was always the hydrostatic stress, while the other was chosen among the rock parameters. Figure 5.8 shows a typical contour plot, obtained for all the rock parameters, excepting the bulk modulus. This figure indicates that the analyzed inversion problem is ill-posed for the input data:

the objective function could be minimized for the correct stress value by any value of the rock parameters, within $\pm 10\%$ of the correct one. In other words, the rock parameters adopted as input data are strongly correlated, and several combinations of them can lead to the correct stress and produce a good curve-fitting, explaining observation (1).

The contour plot for the rock bulk modulus, shown in Figure 5.9, indicates that wrong initial stresses can be obtained depending on the bulk modulus, even though properly minimizing the objective function. Therefore, there is not a unique solution when the bulk modulus is the only adjusting rock parameter, explaining observation (2).

Handling observation (2) is simple: the bulk modulus should not be used as one of the adjusting parameters in the back-analysis. Fixing observation (1), however, is a little more complex: Eisenhamer (1996), Finsterle (1999) and Press *et al.* (1999) pointed out that establishing a termination criteria is not a simple task in multidimensional minimization routines, since the variables cannot be treated independently. Because of this, one cannot expect to have simultaneous convergence in all the adjusting parameters.

Actually, depending on the analyzed problem, the simplex method may only find a local minimum, instead of the global one. In order to check on the existence of local minima in the in-situ stress back-analysis, the simplex code was modified from its original version: after reaching convergence with the intrinsic formulation, new coefficients were automatically defined for carrying on the expansion, contraction and reflection processes further on, allowing the algorithm to escape from local minima. The final solution, however, had no change at all, meaning the absence of local minima problems.

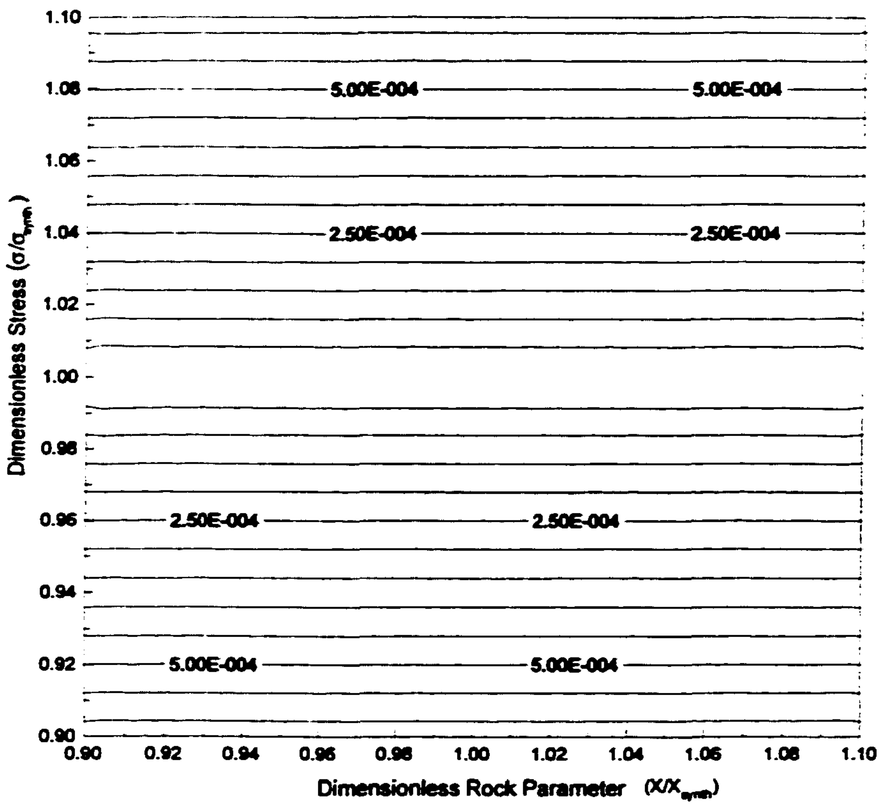

Figure 5.8: Typical contour plots for the objective function having the dimensionless hydrostatic stress and any dimensionless rock parameter as adjusting variables (exception for the bulk modulus).

Summarizing the analysis, the computed stresses and the curve-fittings were very reasonable, even though the rock parameters were not exactly the same at the end of the calculations. In order to preserve the physical meaning of the rock parameters penalty functions (which will be presented in section 5.2) must be used whenever applying the method to field or experimental data, when the variations in the parameters could be larger. The stresses computed in the field applications should be checked using geological data and other field tests, like microhydraulic fracturing and leakoff tests, in order to increase the reliability.

Deviatoric Stress

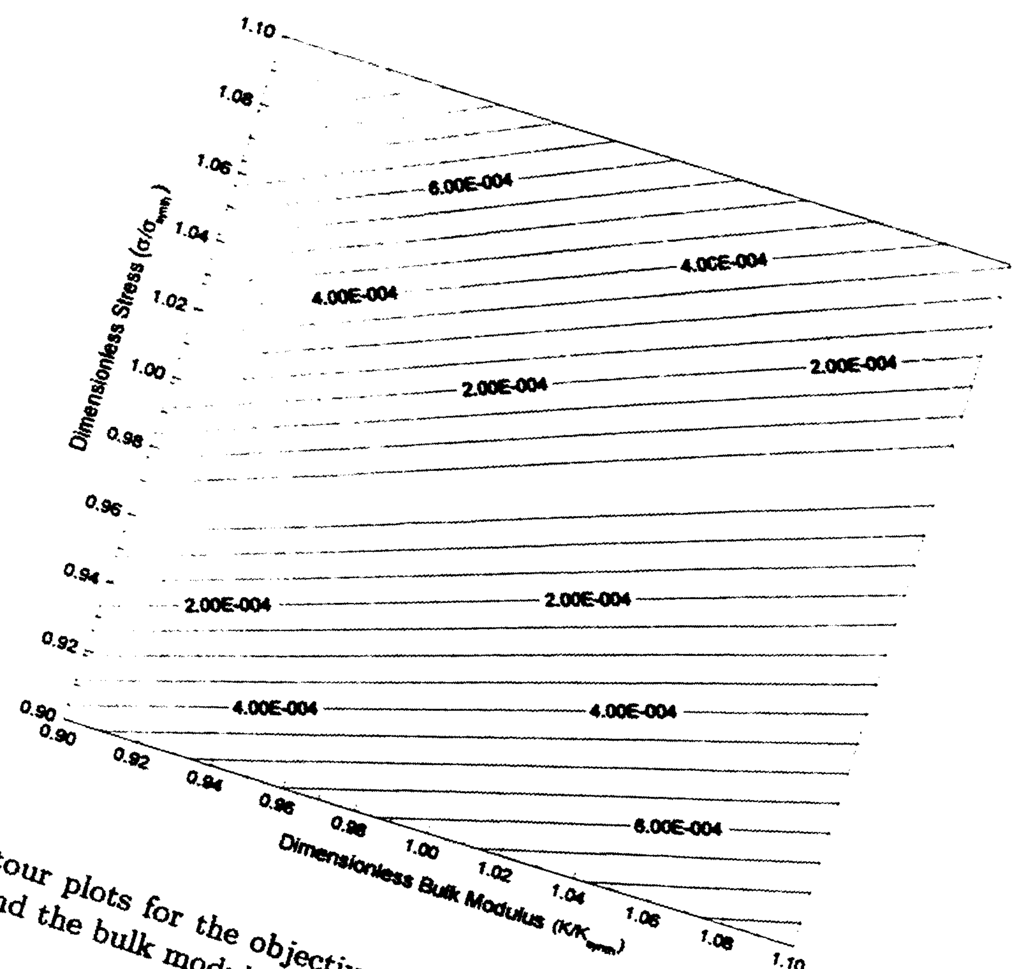

Figure 5.9: Contour plots for the objective function having the dimensionless hydrostatic stress and the bulk modulus as the adjusting variables.

The parameters considered as initial guesses for computing the deviatoric stress were not the same ones used in the hydrostatic problem. This is because Mode III is purely elastic and, therefore, there is no sense in using parameters like grain bulk modulus, undrained bulk modulus and permeability, which only refer to the rock poroelastic behavior. The code ability for reproducing the theoretical deviatoric stress was tested with 6 initial guess data sets, presented in Appendix B. Table 5.4 shows the computed stresses, while Figure 5.10 presents the curve-fittings for the synthetic deviatoric strain. The results are very good, probably because the stress-strain relationship under this loading mode do not include poroelastic effects, being thus, much simpler.

Table 5.4: Deviatoric stress calculated by the simplex code.

Input data file	Variable rock parameter	Deviatoric stress (MPa)	Iterations	Error ($\mu\varepsilon$)
guess-S1	*	2.07	0	36.60 x 10^{-13}
guess-S2	**	2.07	396	32.40 x 10^{-4}
guess-S3	* * *	2.07	443	30.40 x 10^{-4}
guess-S4	E_1	2.07	555	30.80 x 10^{-4}
guess-S5	E_2	2.07	900	24.20 x 10^{-4}
guess-S6	E_1, E_2, μ_E	2.07	558	26.40 x 10^{-4}

* constant rock parameters and deviatoric stress (original values).
** only the stress is adjusted.
* * * only the stress is adjusted from guess values far from the correct one.

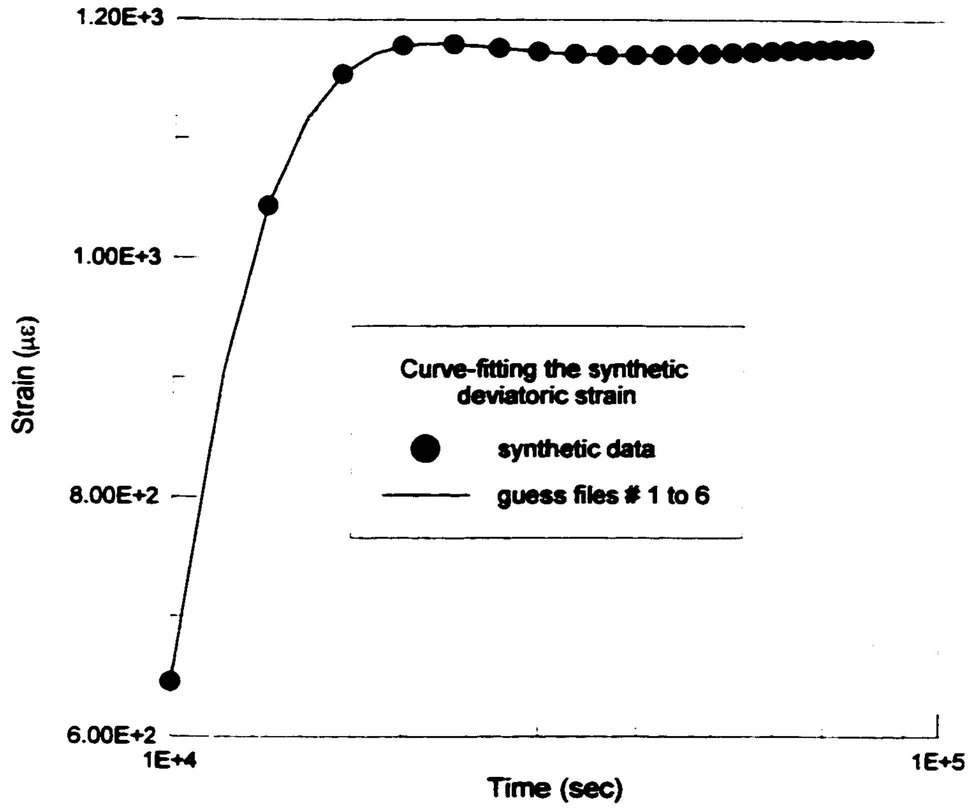

Figure 5.10: Curve-fitting for the synthetic deviatoric strain.

5.2 Field Cases

The poroviscoelastic model and the inversion algorithm were both applied to Petrobras' ASR data. The field tests were carried out between 1995 and 1997 (Siqueira *et al.*, 1996a; 1996b; 1997a; 1997b; and, 1997c), in the Potiguar and Sergipe-Alagoas Basins, depicted in Figure 5.11, gathering only the in-situ stress orientations, at that time. The stress magnitudes were not computed due to the lack of understanding of why the rock contracted, which occurred in most tests.

The observed rock shrinkage was a surprise mainly because most samples were sandstones with good permeability. DRX tests analyzed by Anjos and Silva (1998) detected a high percentage of interstitial clays, which could be held responsible for a slow fluid diffusion process, leading to such sample contractions.

The strain curves from the ASR tests are presented in Appendix C. The rock properties needed as input data for the model were experimentally obtained from lab compression tests, presented in Chapter 6, and used as initial guesses to fit the ASR experimental curves, with the simplex algorithm.

As discussed in the synthetic example, a few penalty functions were included in the inversion algorithm for curve-fitting purposes, in order to ensure the physical meaning of the rock properties, modified in the adjusting process. The use of penalty functions when curve-fitting experimental data through back-analysis is quite common (Shah and Hoek, 1991; Nascimento, 1998), assuring an acceptable range for the variables in each iteration. The way they work is quite simple: whenever a simplex iteration computes a value out of a prescribed range, a large dimensionless error (10^{30}) is attributed to the current iteration, obliging the code to go on interacting, until reaching convergence within the variables' prescribed ranges. Three restrictions were defined according to the rock mechanics constitutive relationships, presented in Chapter 3:

- Restriction # 1:

$$3K - E > 0 \tag{5.9}$$

where K is the bulk modulus and E is Young's modulus. This equation guarantees positive real values for Poisson's ratio and shear modulus;

- Restriction # 2:

$$K_s - K > 0 \tag{5.10}$$

where K_s is the grain bulk modulus. Equation 5.10 assures a positive Biot's coefficient; and,

- Restriction # 3:

$$0.5 > \nu_u > \nu \tag{5.11}$$

where ν_u and ν are the undrained and drained Poisson's ratio.

The initial guesses for the variable rock parameters in the input datafile were defined within ±10% of the lab-derived values, according to Eisenhamer (1996) recommendation. The initial guesses for the hydrostatic and deviatoric stresses were randomly taken as ±10% of the following reference values:

$$\begin{cases} dP_0/dz = 0.7 \text{ psi/ft;} \\ dS_0/dz = 0.1 \text{ psi/ft} \end{cases} \tag{5.12}$$

which, in turn, were based on the following estimates:

$$\begin{cases} d\sigma_v/dz = 1.0 \text{ psi/ft;} \\ d\sigma_{HMAX}/dz = 0.8 \text{ psi/ft;} \\ d\sigma_{h\,\min}/dz = 0.6 \text{ psi/ft.} \end{cases} \tag{5.13}$$

Figure 5.11: Location of the Potiguar and Sergipe-Alagoas Basins in Brazil.

5.2.1 Computing the In-Situ Horizontal Stresses for Wells A and B

The motivation for the ASR tests in wells A and B was the perspective of drilling horizontal wells in the field, aiming at the reservoir portion underneath the Açu River, in order to improve the drainage (Figure 5.12). The stress field was thus necessary for defining the optimum orientation of the horizontal wells.

The ASR measurements for well A (Figures C.2 and C.3 from Appendix C) show an initial rock expansion, followed by contraction, without stabilization during approximately 12 hours. The strain behavior for well B presented large rock contractions (Figures C.4 and C.5 from Appendix C), with a slight tendency for stabilization at the end of the 36 hours testing period. The combination of a com-

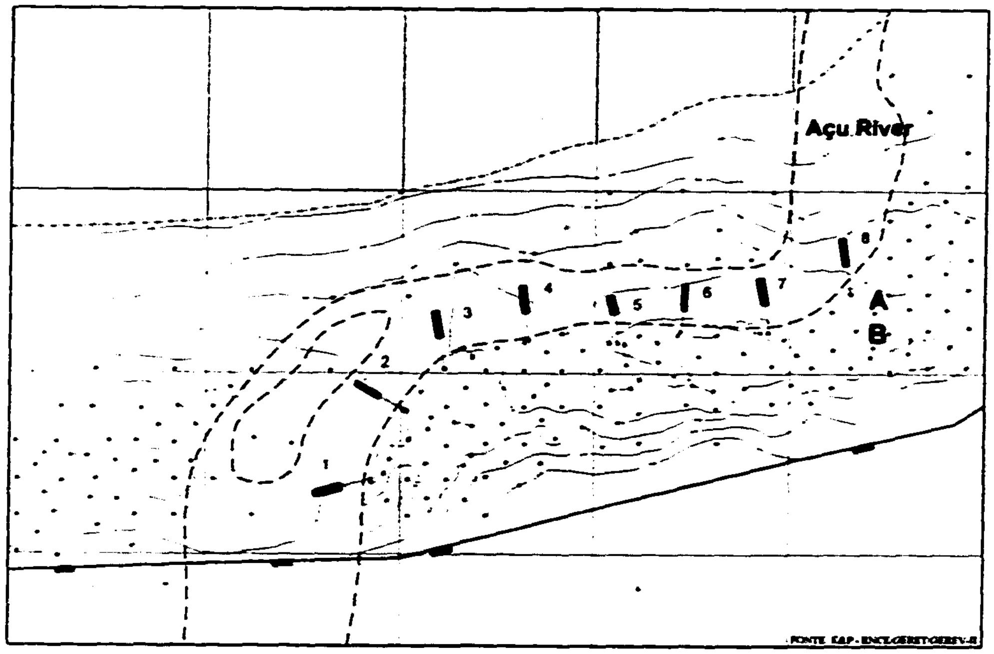

Figure 5.12: Field location of wells A and B, showing also horizontal wells already drilled (wells # 1, 3, 5 and 7), and to be drilled (wells # 2, 4, 6 and 8).

plex strain behavior, rock shrinkage and incomplete field testing (without the final strain stabilization) was an exception to the smooth expansion predicted by conventional viscoelastic modelling (Blanton, 1983; Blanton and Teufel, 1983; Teufel, 1983b).

The field conditions and the rock input data for the back-analyses of the two wells are shown in Tables 5.5 and 5.6. Two sandstone samples were tested for each well, resulting in the horizontal stresses shown in Table 5.7. The curve-fitting obtained for both the hydrostatic and deviatoric anelastic strains for each sample are presented in Figures 5.13 to 5.16.

Analyses of the Results from Wells A and B

As expected by the shallow coring depths (185.1 m for well A and 193.2 m for well B), the computed horizontal stresses indicate an almost hydrostatic stress field. It

Table 5.5: Input data for well A (from Chapter 6).

z (m)	σ_V (MPa)	D (m)	p_0 (MPa)	p_{dri} (MPa)	t_{rec} (hour)	t_{pre} (hour)	t_{test} (hour)
185.1	4.06	0.1	1.26	2.1	7.3	5.0	12.2
E_1 (GPa)	E_2 (GPa)	μ_E (10^5GPa.sec)	K (GPa)	K_s (GPa)	K_u (GPa)	k (md)	μ_f (Pa.sec)
1.23	4.73	11.24	9.4	185.5	16.55	15.4	900

Table 5.6: Input data for well B (from Chapter 6).

z (m)	σ_V (MPa)	D (m)	p_0 (MPa)	p_{dri} (MPa)	t_{rec} (hour)	t_{pre} (hour)	t_{test} (hour)
193.2	4.24	0.1	1.31	2.1	16.2	2.0	35.0
E_1 (GPa)	E_2 (GPa)	μ_E (10^5GPa.sec)	K (GPa)	K_s (GPa)	K_u (GPa)	k (md)	μ_f (Pa.sec)
1.08	2.48	9.88	2.0	156.9	63.45	8.9	900

Table 5.7: Horizontal stresses computed for wells A and B.

Sample	Hydrostatic Stress (MPa)	Deviatoric Stress (MPa)	σ_{HMAX} (MPa)	$\sigma_{h\min}$ (MPa)
A-1	3.55	0.88	4.43	2.67
A-2	4.19	0.62	4.81	3.57
Average - A	3.87	0.75	4.62	3.12
B-1	3.63	2.1E-8	3.63	3.63
B-2	4.43	0.07	4.50	4.36
Average - B	4.03	0.035	4.06	3.99

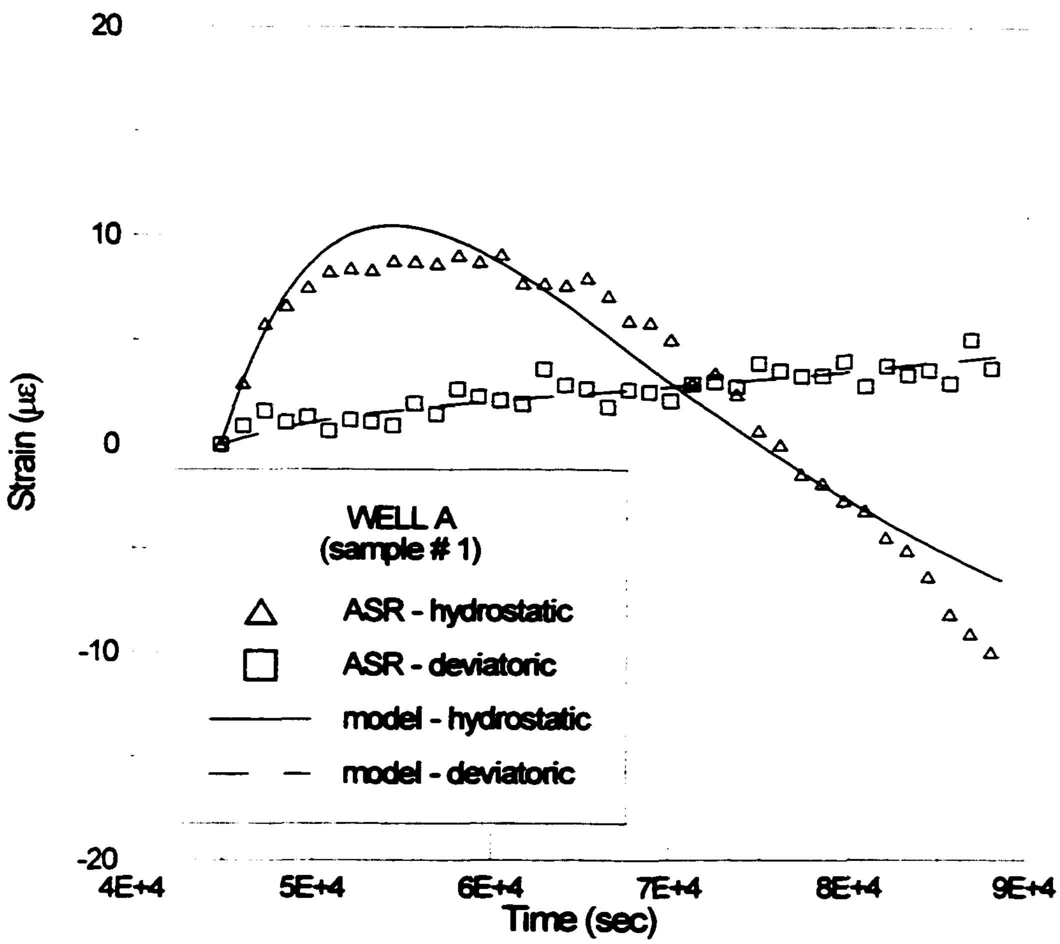

Figure 5.13: Curve-fitting for the hydrostatic and deviatoric strains from well A, sample # 1.

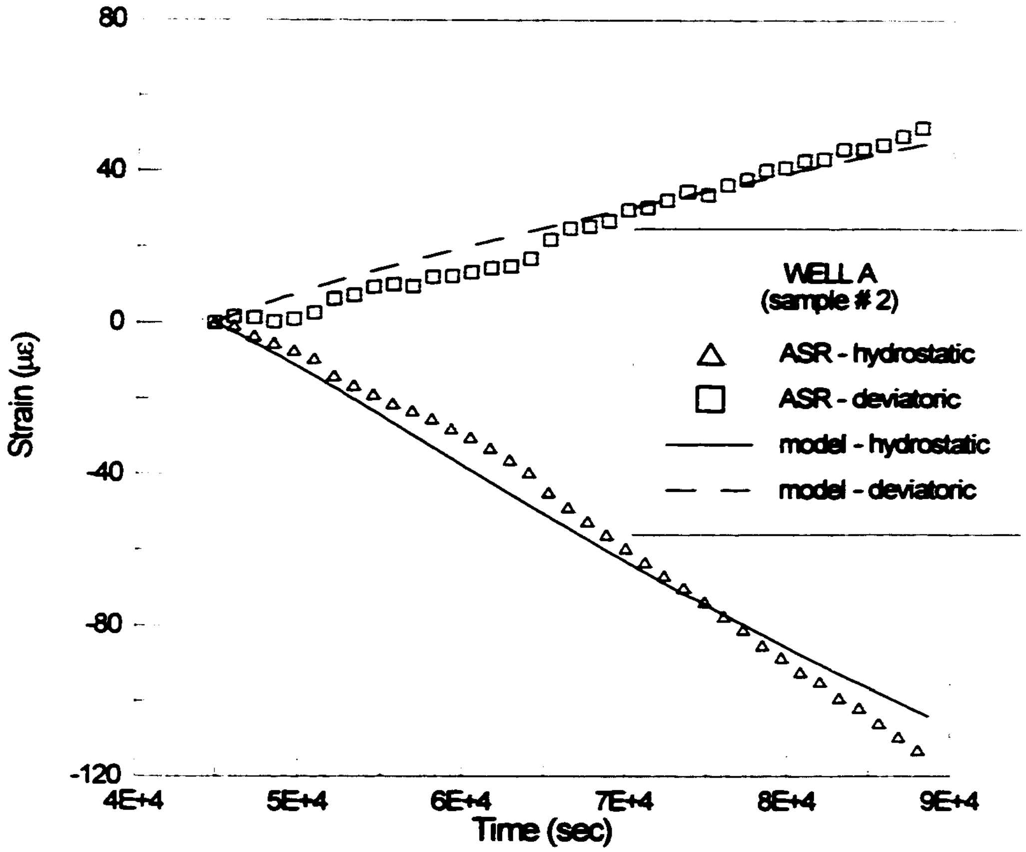

Figure 5.14: Curve-fitting for the hydrostatic and deviatoric strains from well A, sample # 2.

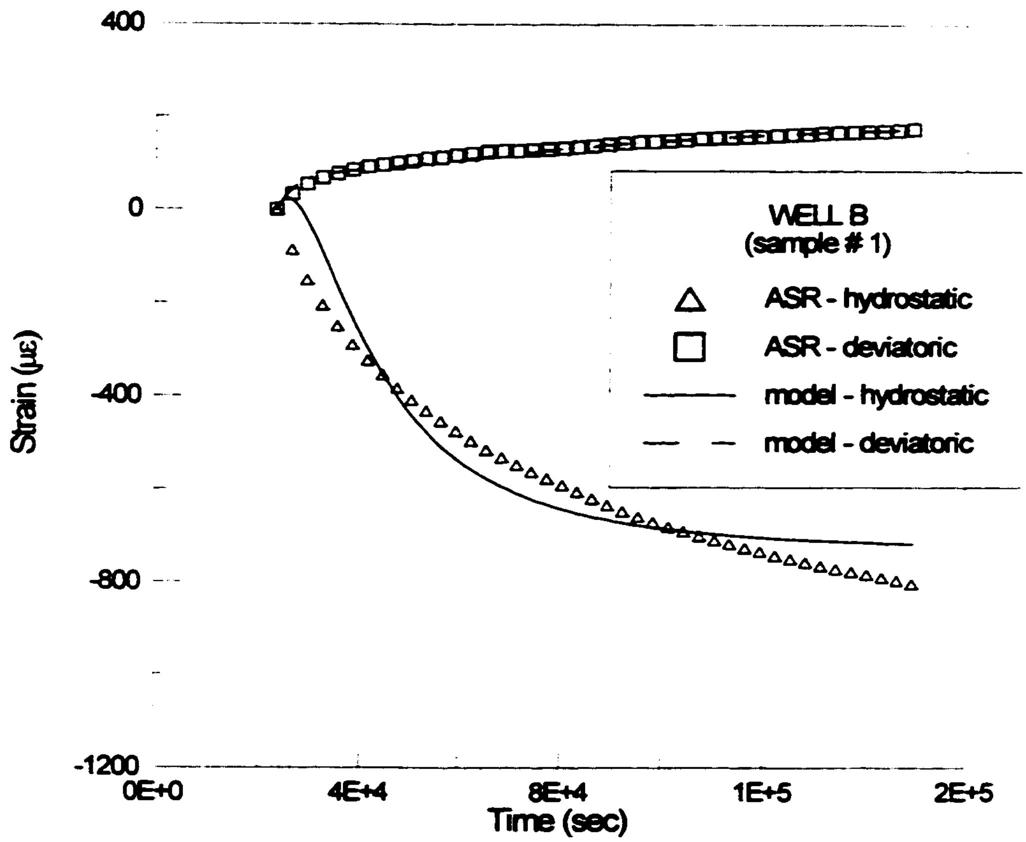

Figure 5.15: Curve-fitting for the hydrostatic and deviatoric strains from well B, sample # 1.

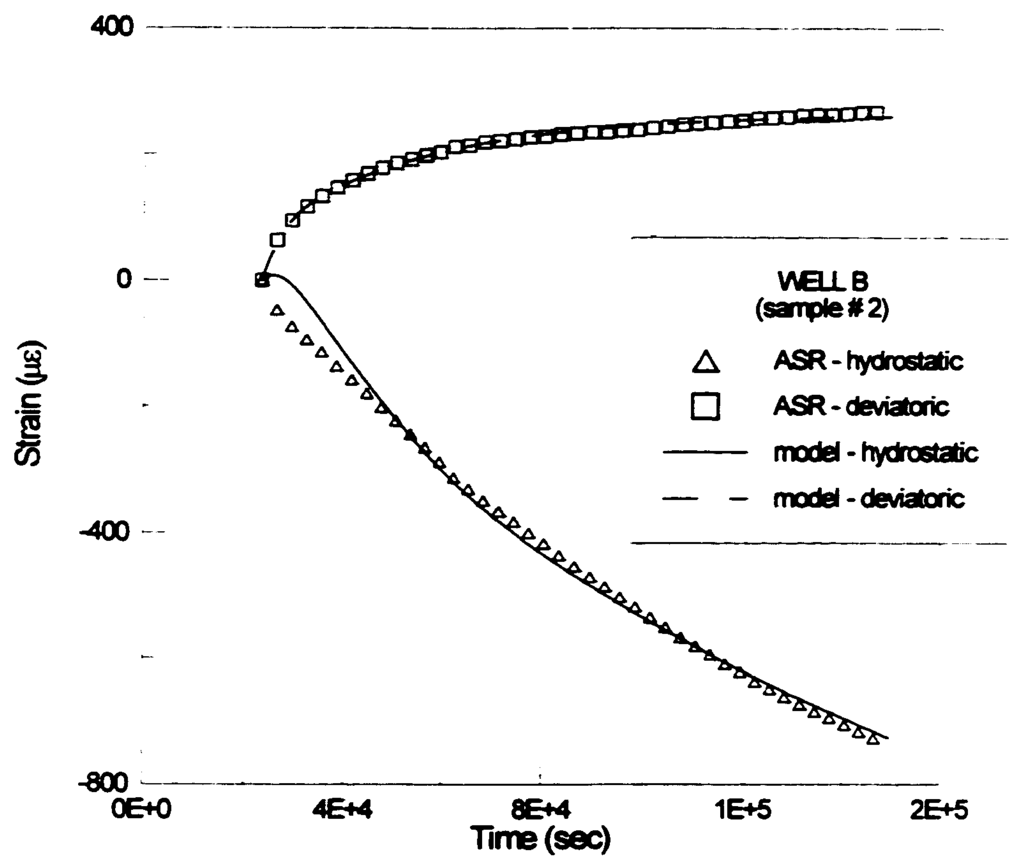

Figure 5.16: Curve-fitting for the hydrostatic and deviatoric strains from well B, sample # 2.

is not a surprise either that the maximum horizontal stress in well A is even higher than the vertical one, which would reflect the partial unloading of the overburden due to erosion, as pointed out by Roegiers and Vandamme (1999). and is also typical of shallow depths.

The qualitative aspect of the obtained results is further corroborated by Lima Neto's (1997) observations, who based himself on a detailed analysis of shallow seismic events in the region stating that the regional stress field follows the $\sigma_{HMAX} > \sigma_v > \sigma_{h\,\min}$, conditions.

The variation in the in-situ stresses computed for each well are larger than expected (from 8% to 25%), considering the samples good visual homogeneity (Figures D.1 to D.4 from Appendix D). This stress variation can only be attributed to inherent minor heterogeneities. The average hydrostatic stresses computed for wells A and B are within 12.1%, while the relative difference between the average deviatoric stresses is 21.8%. These differences are also high, but easier to explain, since according to a Petrobras' database (SIGEO, 1999), well A was practically vertical, while well B had an inclination of 23.12° at the coring depth. Considering then the plane strain assumption in the poroviscoelastic model, the stresses computed for well A are in a plane which is 23.12° from the stress plane in well B, and under these circumstances, one cannot expect more than similar values when comparing the stresses calculated for wells A and B.

Four horizontal wells have already been successfully drilled (wells # 1, 3, 5 and 7 in Figure 5.12), assuming a quasi-hydrostatic in-situ stress field in this particular field, and four more will be drilled (wells # 2, 4, 6 and 8 in Figure 5.12) in the near future.

5.2.2 Computing the In-Situ Horizontal Stresses for Well C

The sandstones cored from well C presented a strain recovery pattern which is close to conventional predictions (Figure C.6 and C.7 from Appendix C): sample C-1 expanded in all directions while sample C-2 had a short initial contraction followed by expansion in the vertical and inclined directions, and a small strain variation in the horizontal directions.

The input data used for computing the in-situ stresses in well C are shown in Table 5.8. Table 5.9 presents the calculated stresses while Figures 5.17 and 5.18 show the obtained curve-fittings. The horizontal stresses computed for this well were compared with the results of 8 hydrofrac tests realized nearby (Lima Neto, 1998), which provided an average maximum and minimum horizontal stresses of $\sigma_{HMAX} = 13.26 \pm 3.10$ MPa and $\sigma_{h\,\min} = 8.53 \pm 1.91$ MPa. These values fully encompass the stresses computed from samples C-1 and C-2. The relatively better comparison among the average stress from microfrac tests and the stresses computed for sample C-1 is corroborated by the good curve-fitting for both hydrostatic and deviatoric strains shown in Figure 5.17. The curve-fitting is also good for the deviatoric strain in sample C-2 (Figure 5.18), but the same is not true for the hydrostatic strain curve. This can be explained by the non-homogeneous anelastic strain behavior in the ASR tests (Figure C.7 from Appendix C), generating a weird deviatoric strain curve, which the model is unable to fit.

Table 5.8: Input data for well C (from Chapter 6).

z (m)	σ_V (MPa)	D (m)	p_0 (MPa)	p_{dri} (MPa)	t_{rec} (hour)	t_{pre} (hour)	t_{ASR} (hour)
480.1	10.86	0.1	4.70	5.4	14.0	1.8	25.2
E_1 (GPa)	E_2 (GPa)	μ_E (10^5GPa.sec)	K (GPa)	K_s (GPa)	K_u (GPa)	k (md)	μ_f (Pa.sec)
2.65	46.0	6.21	5.7	171.2	40.0	3.1	20.0

Table 5.9: Horizontal stresses computed for well C.

Sample	Hydrostatic Stress (MPa)	Deviatoric Stress (MPa)	σ_{HMAX} (MPa)	$\sigma_{h\min}$ (MPa)
C-1	9.4	0.55	9.95	8.95
C-2	10.3	0.64	10.94	9.66

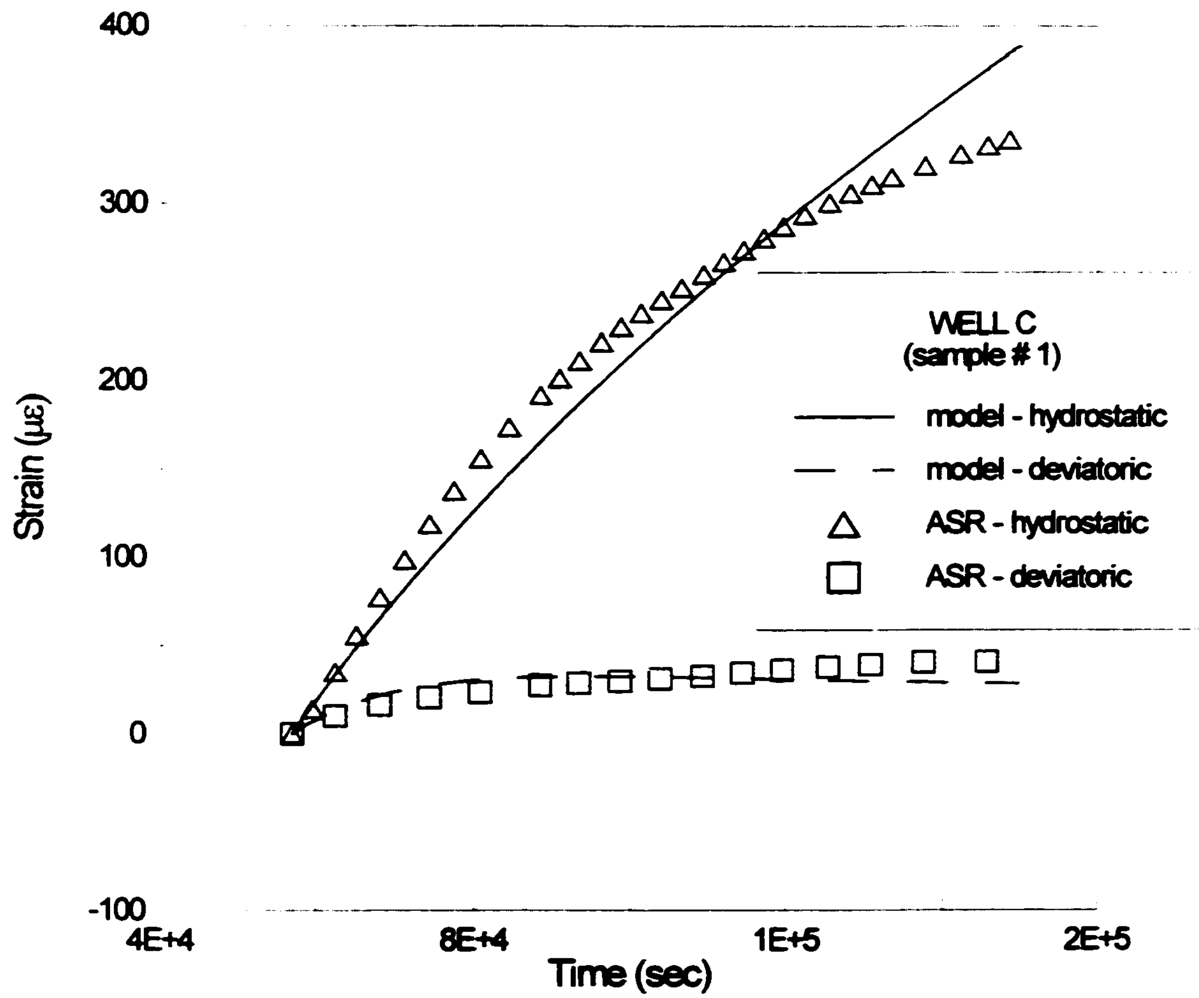

Figure 5.17: Curve-fitting for the hydrostatic and deviatoric strains from well C, sample # 1.

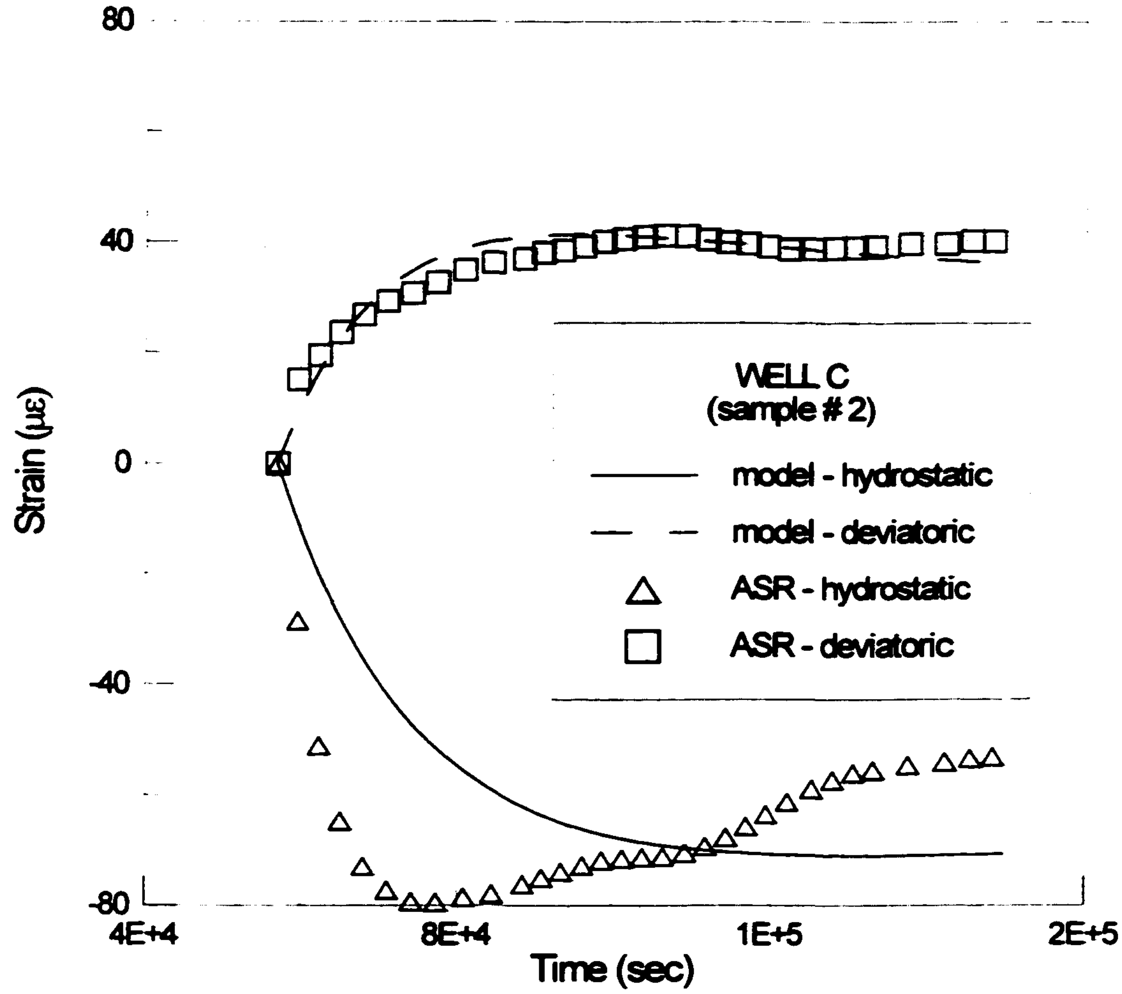

Figure 5.18: Curve-fitting for the hydrostatic and deviatoric strain from well C, sample # 2.

5.2.3 Computing the In-Situ Horizontal Stresses for Well D

Wells D and E are located in the Sergipe-Alagoas basin (Figure 5.19), which is characterized by several families of fractures, making it difficult to compare the calculated stresses, since different tectonic components could be present. Two distinct ASR tests have been run for the sandstones cored from well D: one with samples D-1 and D-2, from an average coring depth of 512.6 m, and another one with samples D-3 and D-4, cored at approximately 537.0 m. Figures C.8 to C.11, from Appendix C, show the complete strain curves for the ASR tests. The input parameters for the back-analyses are presented in Table 5.10, while the stress results are shown in Table 5.11.

The curve-fittings for the ASR tests with samples D-1 and D-2 (Figures 5.20 and 5.21) are very reasonable, but the same is not true for samples D-3 and D-4, mainly for the deviatoric strain fitting (Figures 5.22 and 5.23). In order to analyze the adjusting difficulties, the strain curves for the horizontal directions in all the four samples were amplified (Figures 5.24 to 5.27), highlighting an oscillating behavior in the strain curves for samples D-3 and D-4, in contrast to the strain pattern observed for samples D-1 and D-2. This strain oscillation cannot be a function of any monotonic diffusion process, mechanical malfunction of the testing apparatus, or even rock heterogeneity, and was attributed to temperature oscillations inside the testing chamber. It should be noted that in spite of the strain oscillations and the considerable rock heterogeneities, identified by visual inspection of the tested samples (Figures D.5 and D.6 in Appendix D), the model was still able to provide an average fitting, which corresponded to reasonable stresses.

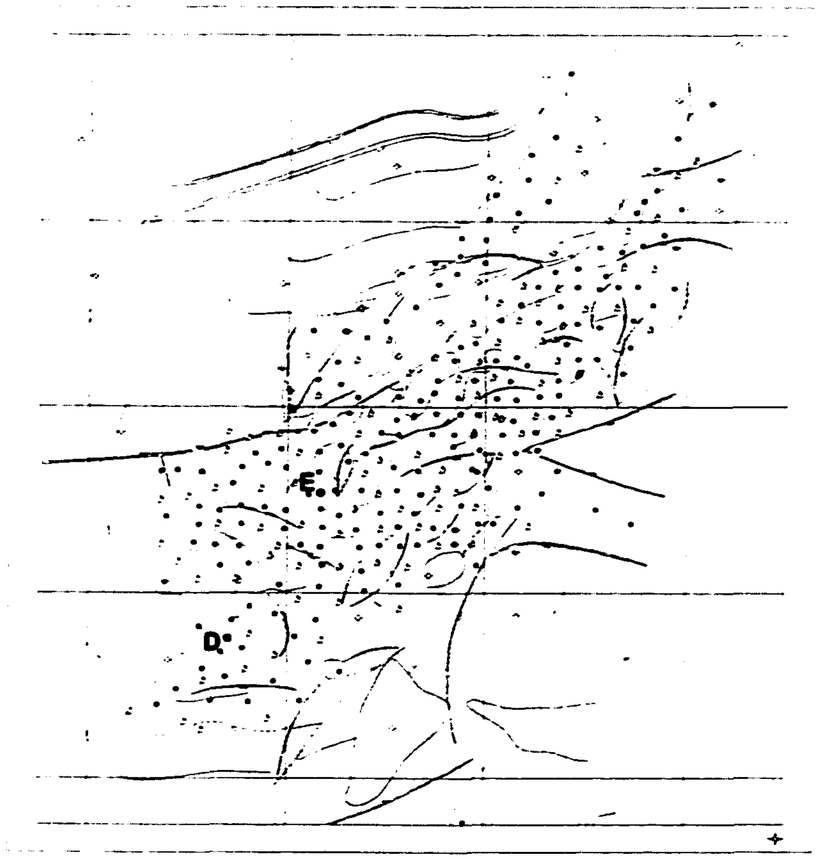

Figure 5.19: Location of wells D and E.

Table 5.10: Input data for well D (from Chapter 6).

Samples	z (m)	σ_V (MPa)	D (m)	p_0 (MPa)	p_{dri} (MPa)	t_{rec} (hour)	t_{pre} (hour)	t_{ASR} (hour)
D1, D2	512.6	11.7	0.1	3.5	4.9	6.5	2.3	35.5
D3, D4	537.0	11.8	0.1	3.7	5.1	5.8	2.2	56.7
	E (GPa)	K_1 (GPa)	μ_K (10^5GPa.sec)	K_2 (GPa)	K_s (GPa)	K_u (GPa)	k (md)	μ_f (Pa.sec)
	0.23	10.21	2.09	31.76	106.9	0.14	9.1	10.0

Table 5.11: Horizontal stresses computed for well D.

Sample	Hydrostatic Stress (MPa)	Deviatoric Stress (MPa)	σ_{HMAX} (MPa)	$\sigma_{h\min}$ (MPa)
D-1	10.62	9.3E-6	10.62	10.62
D-2	10.84	3.92	14.76	6.92
D-3	8.07	0.058	8.65	8.01
D-4	8.32	0.066	8.38	8.28

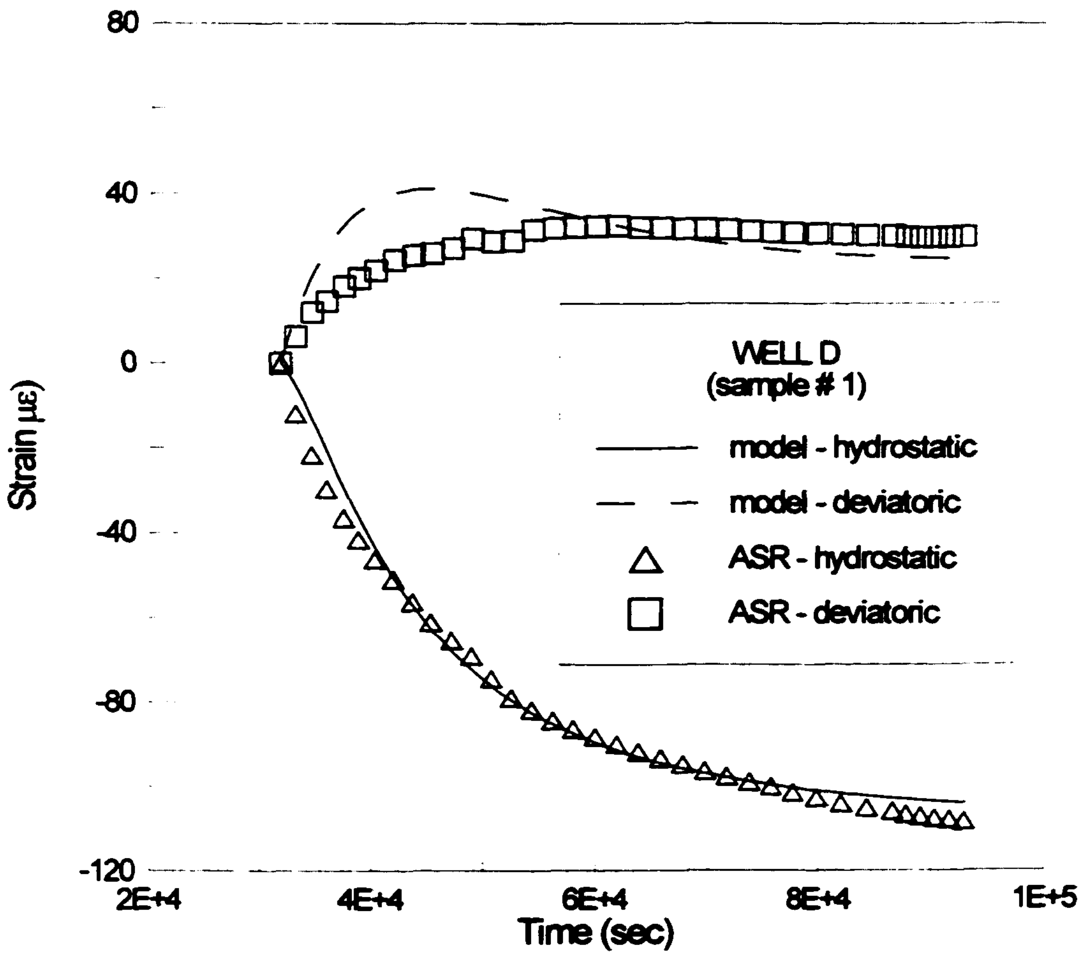

Figure 5.20: Curve-fitting for the hydrostatic and deviatoric strain from well D, sample # 1

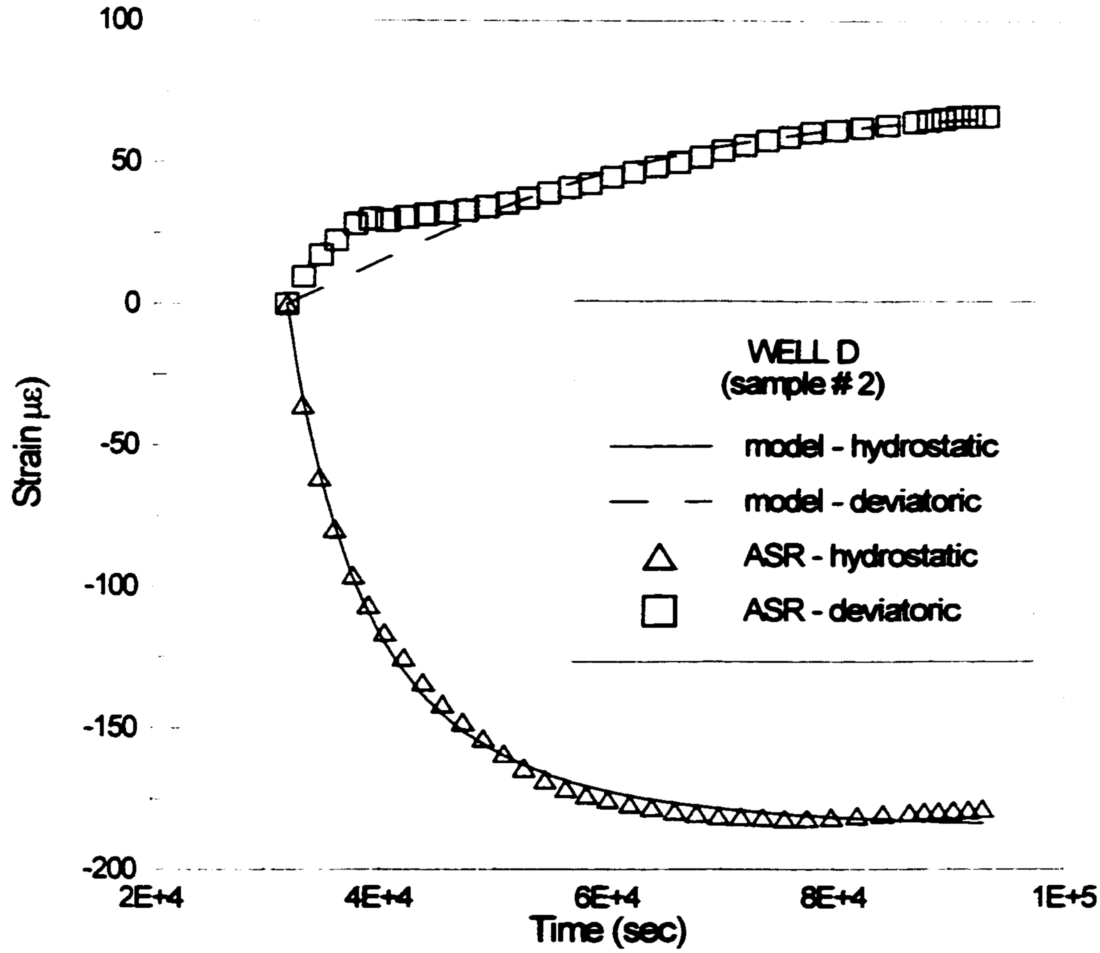

Figure 5.21: Curve-fitting for the hydrostatic and deviatoric strains from well D, sample # 2.

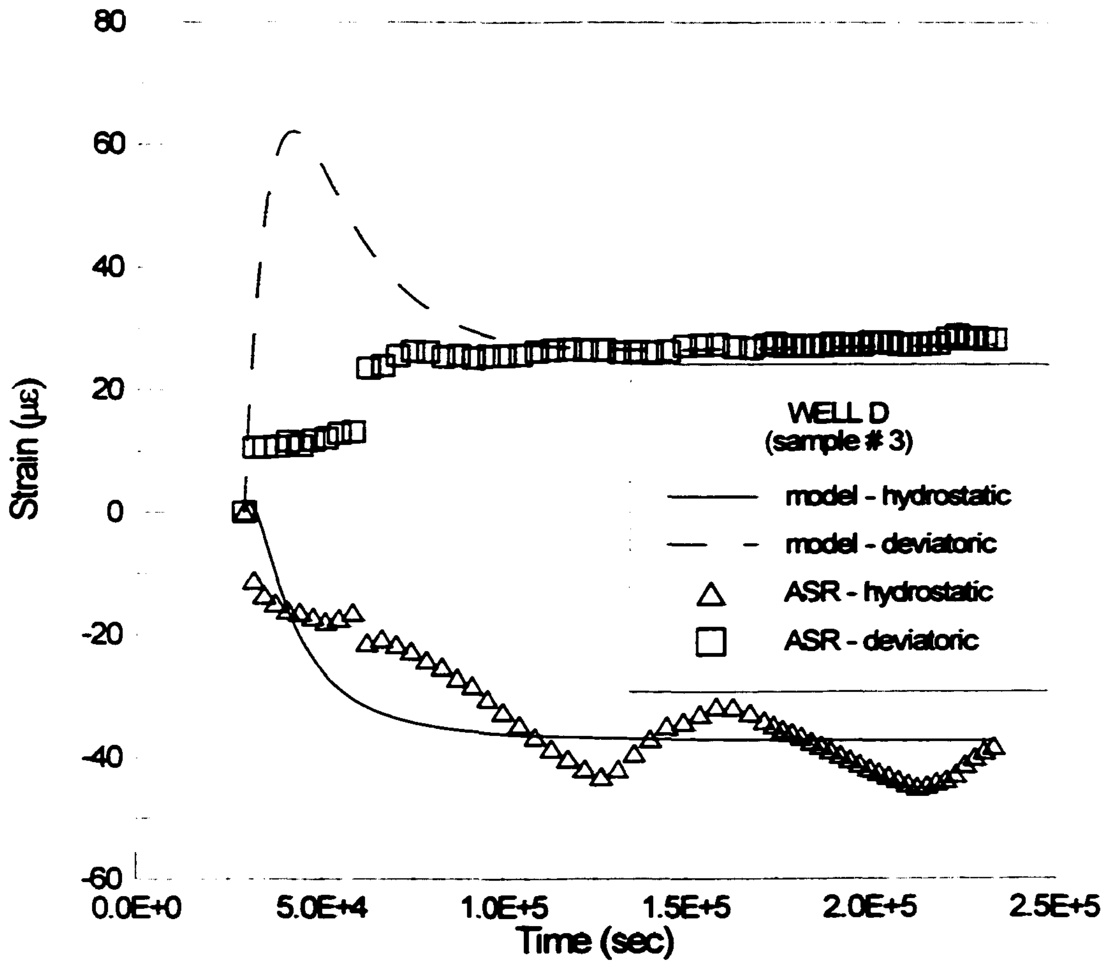

Figure 5.22: Curve-fitting for the hydrostatic and deviatoric strain from well D, sample # 3.

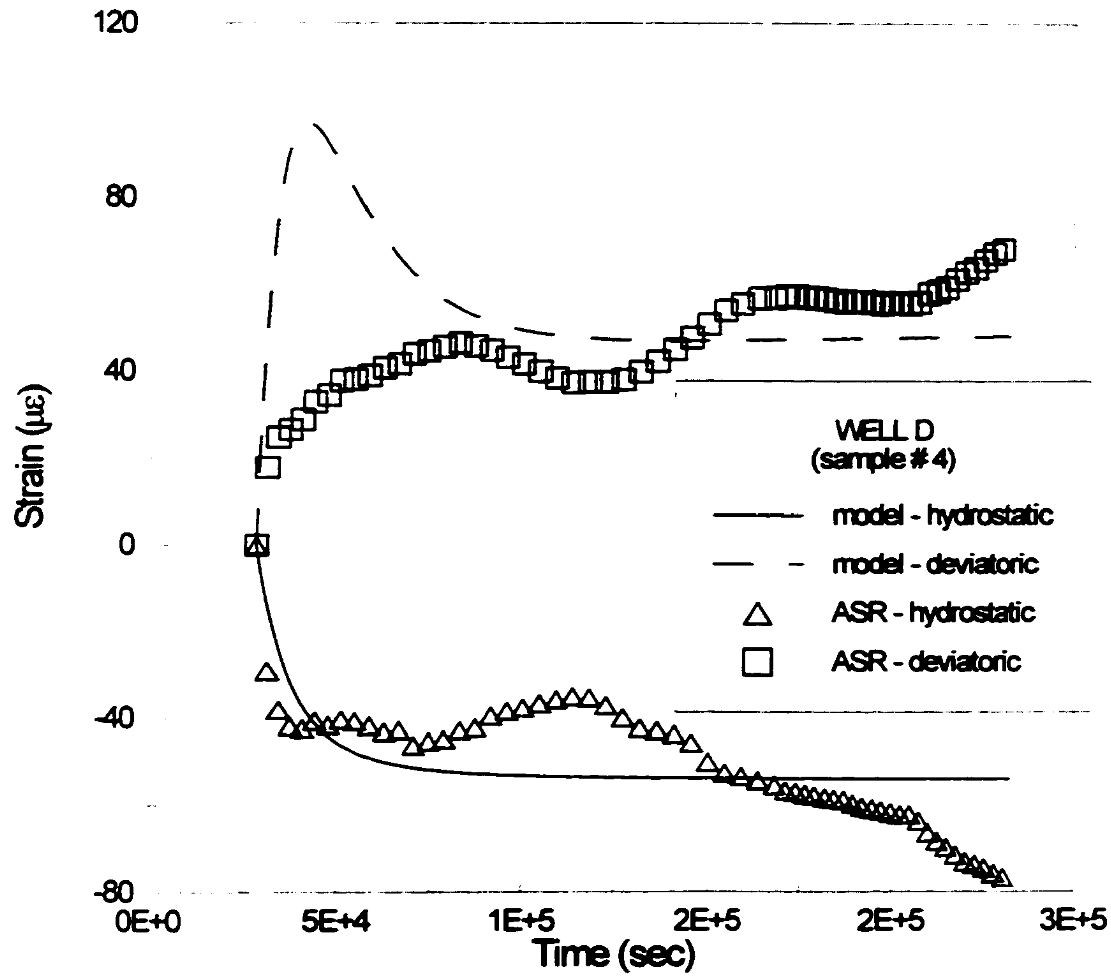

Figure 5.23: Curve-fitting for the hydrostatic and deviatoric strains from well D, sample # 4.

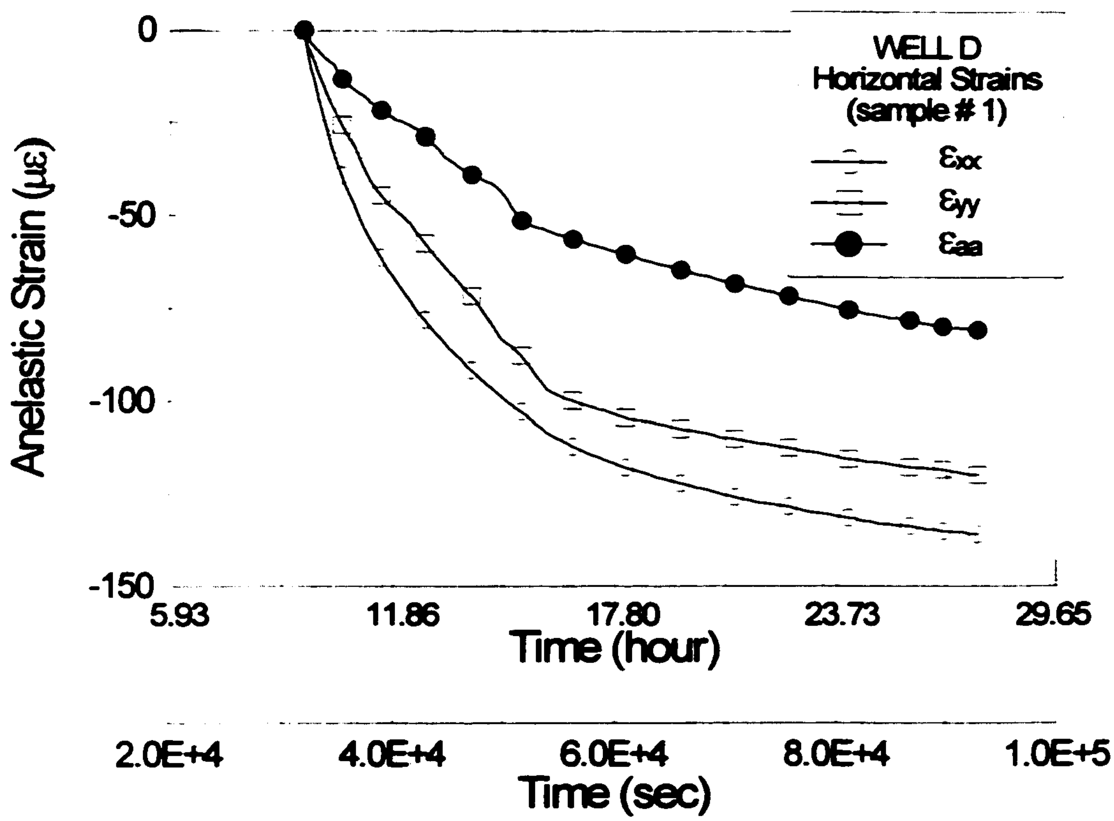

Figure 5.24: Anelastic horizontal strain measured by the ASR for well D, sample # 1.

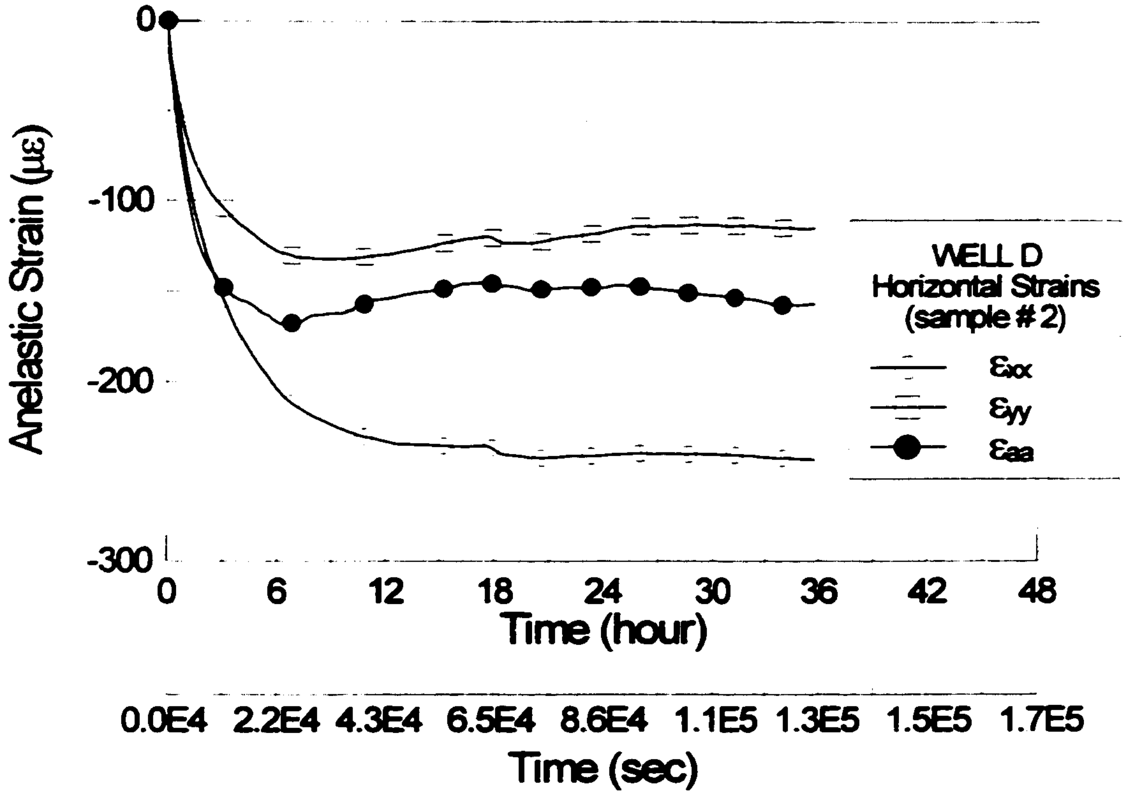

Figure 5.25: Anelastic horizontal strain measured by the ASR for well D, sample # 2.

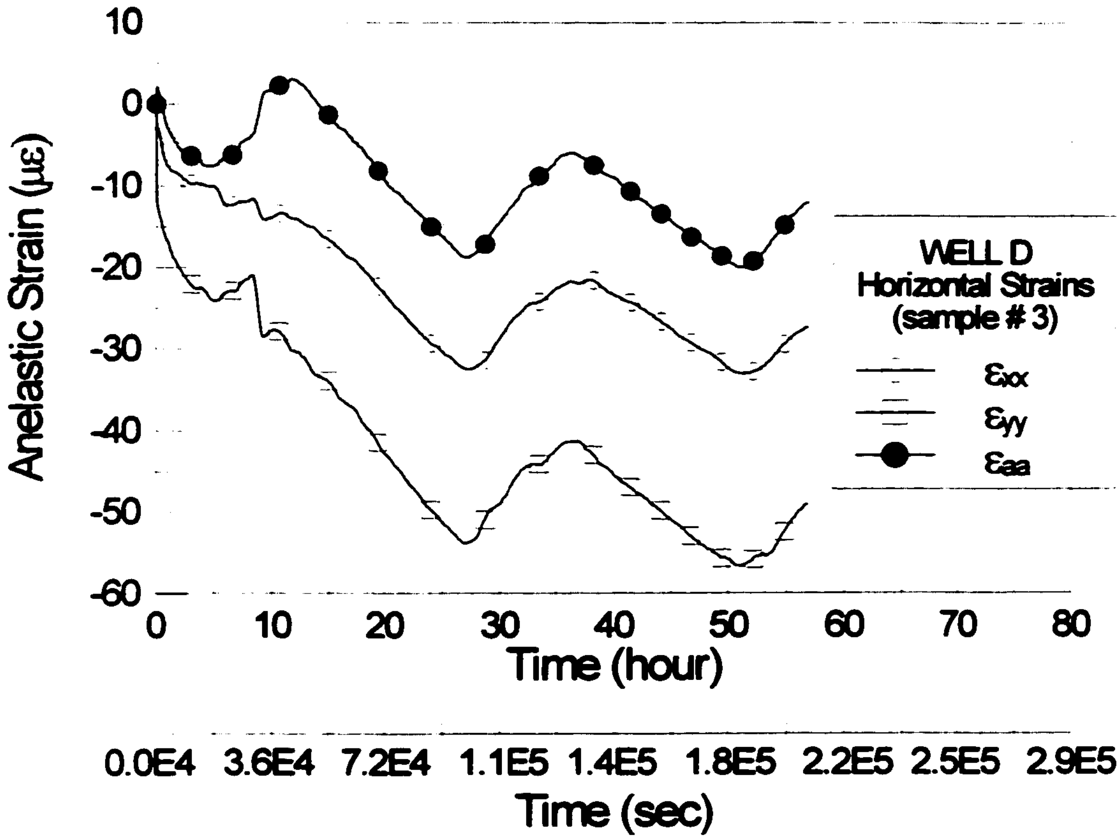

Figure 5.26: Anelastic horizontal strain measured by the ASR for well D, sample # 3.

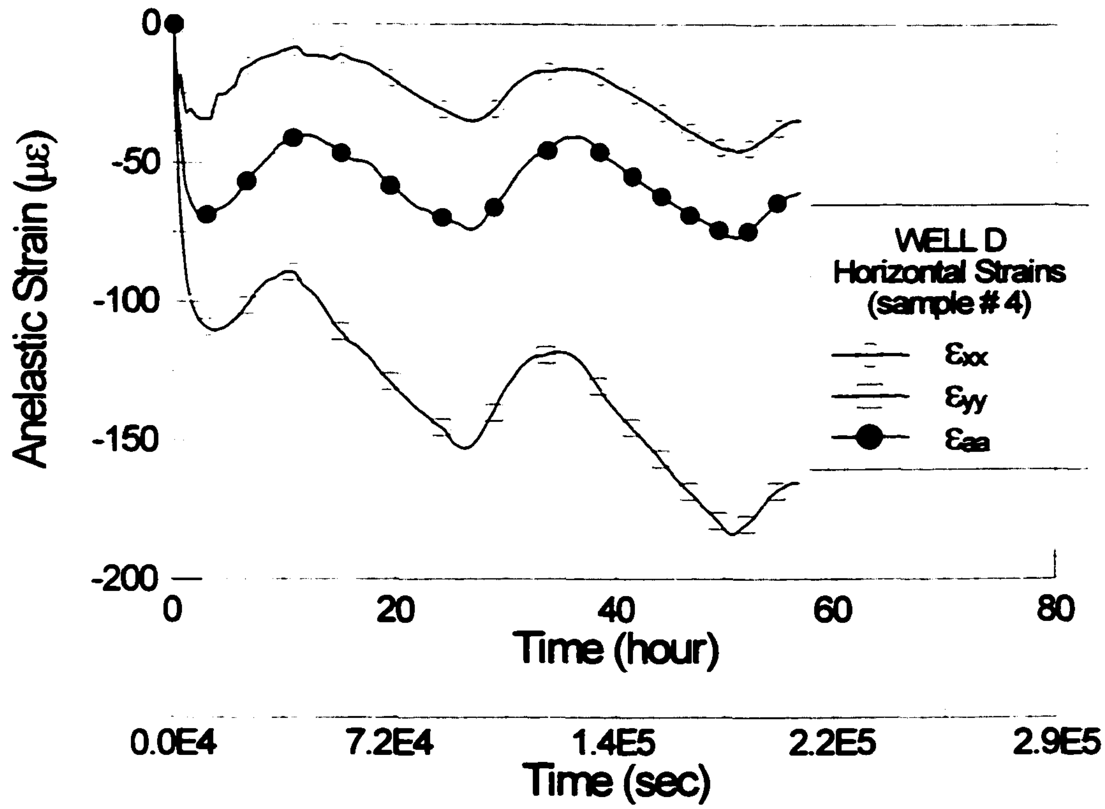

Figure 5.27: Anelastic horizontal strain measured by the ASR for well D, sample # 4.

5.2.4 Computing the In-Situ Horizontal Stresses for Well E

The ASR tests in well E were requested for helping defining the preferential orientation of hydraulic fracturing propagation in the field, with the final goal of designing a system of injection wells. Two conglomerate samples from this well (see Figure 5.28), have been tested: the ASR's in all the six directions are shown in Figures C.12 and C.13 from Appendix C. The input data for the back-analysis is shown in Table 5.12; the obtained stresses are shown in Table 5.13, and the curve-fittings are presented in Figures 5.29 and 5.30.

Once again thermal effects could be noticed during the ASR tests (Figures 5.31 and 5.32), associated with the low overall deformation of sample E1. The computed hydrostatic stresses are within a reasonable range (5%), but the same is not true for the deviatoric stresses, which are considerably different in each sample. The visual observation of the tested samples (Figures D.9 and D.10 from Appendix D) confirmed that the cores from well E were not of the adequate type for ASR tests: they were very heterogeneous, with a high probability of strong anisotropic strain behavior, due to different grain sizes and compositions. This can certainly explain the difference in the computed horizontal stresses for the two samples.

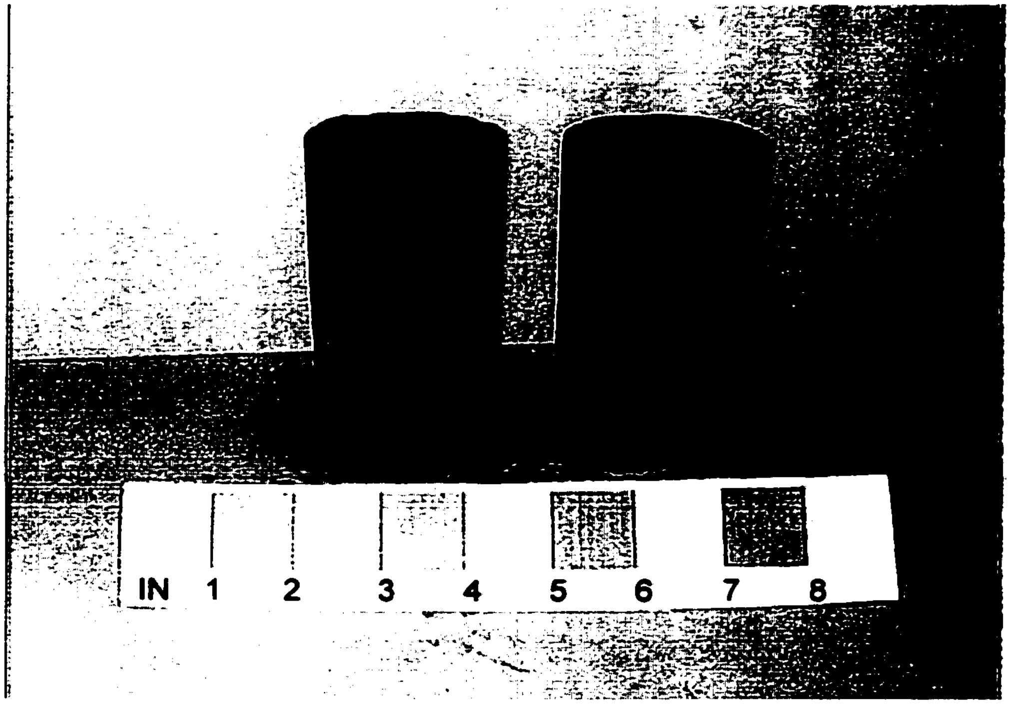

Figure 5.28: Conglomerate samples tested for well E.

Table 5.12: Input data for well E (from Chapter 6).

z (m)	σ_V (MPa)	D (m)	p_0 (MPa)	p_{dri} (MPa)	t_{rec} (hour)	t_{pre} (hour)	t_{ASR} (hour)
505.3	11.43	0.1	3.43	4.81	4.7	2.0	60.9
E_1 (GPa)	E_2 (GPa)	μ_E (10^5GPa.sec)	K (GPa)	K_s (GPa)	K_u (GPa)	k (md)	μ_f (Pa.sec)
11.23	4.73	11.24	9.4	185.5	16.55	15.4	900.0

Table 5.13: Horizontal stresses computed for well E.

Sample	Hydrostatic Stress (MPa)	Deviatoric Stress (MPa)	σ_{HMAX} (MPa)	$\sigma_{h\min}$ (MPa)
E-1	11.41	0.073	11.47	11.34
E-2	11.99	3.92	14.76	6.92

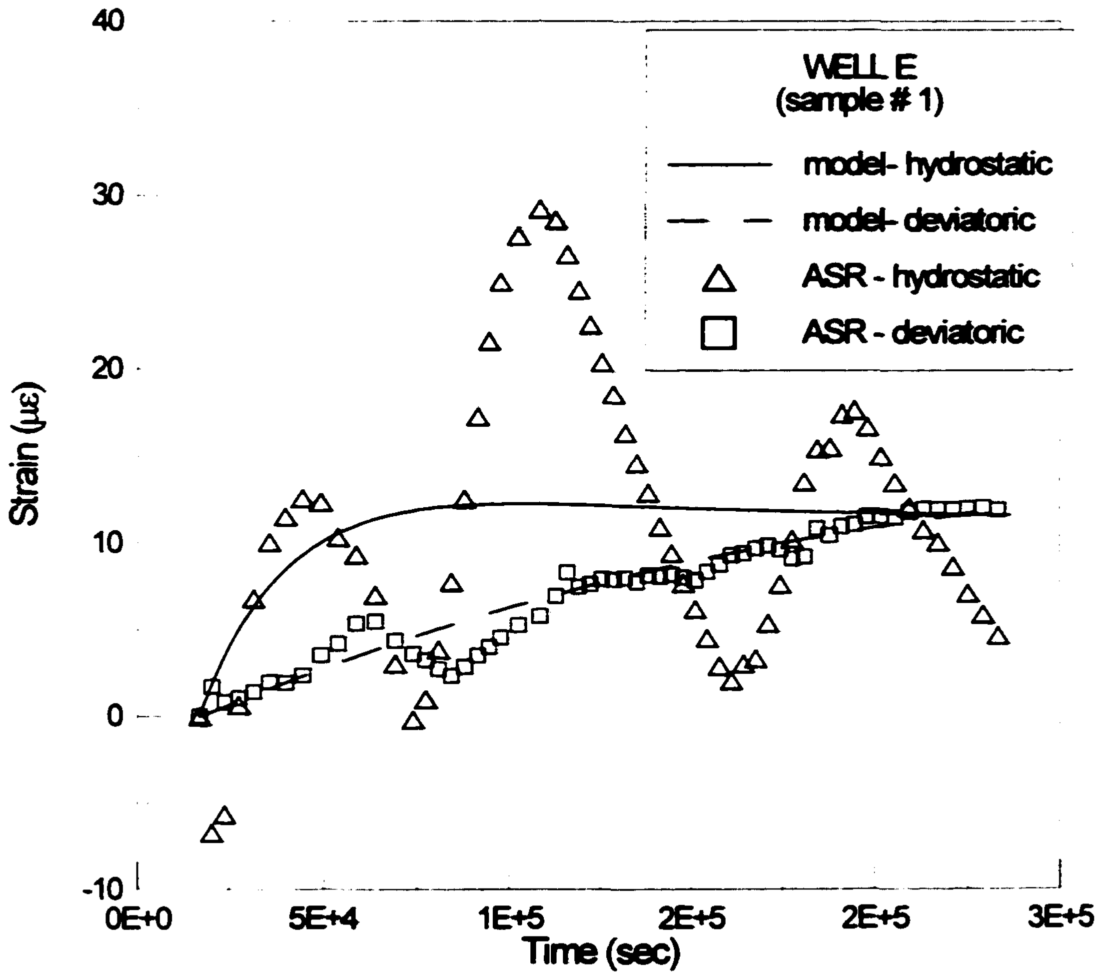

Figure 5.29: Curve-fitting for the hydrostatic and deviatoric strain from well E, sample # 1.

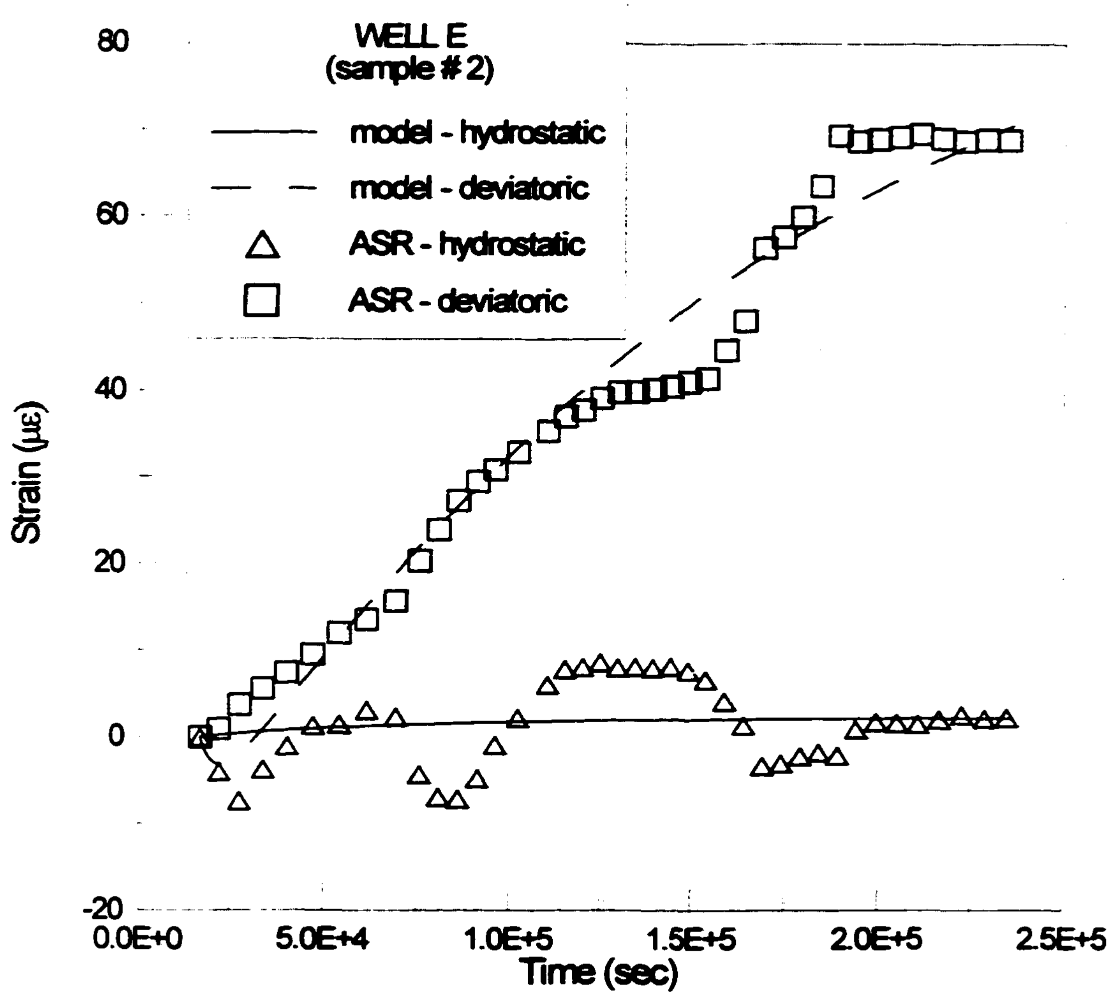

Figure 5.30: Curve-fitting for the hydrostatic and deviatoric strain from well E, sample # 2.

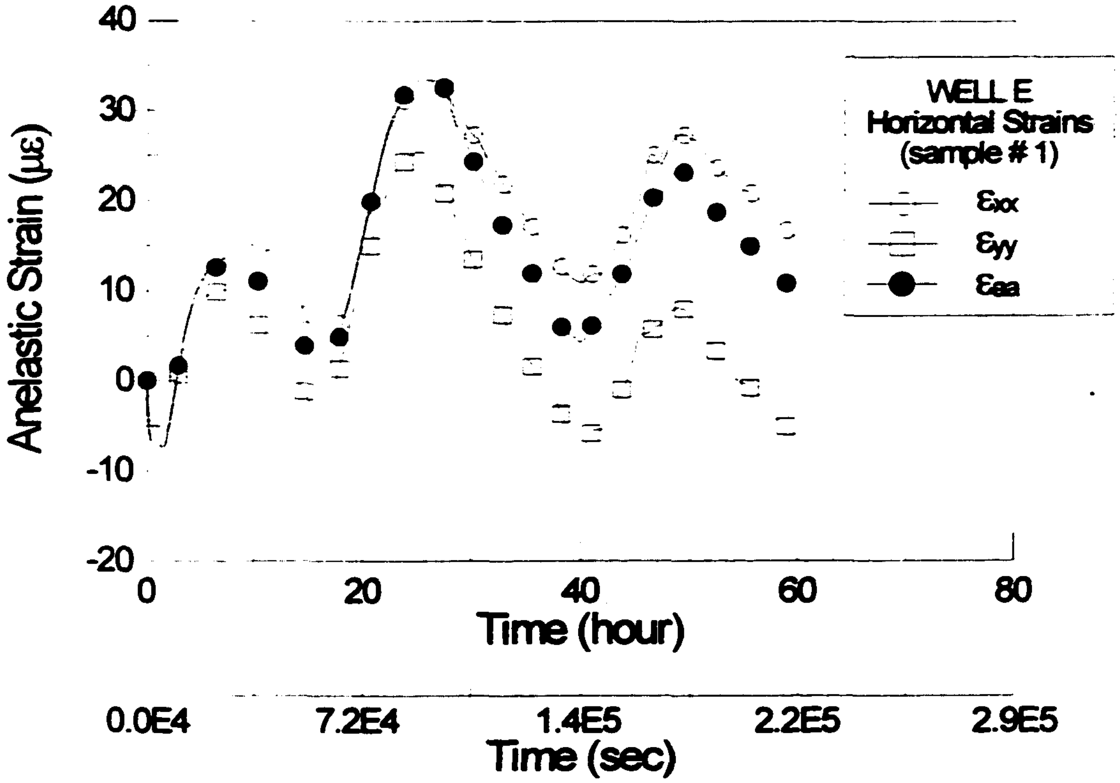

Figure 5.31: Anelastic horizontal strain measured by the ASR for well E, sample # 1.

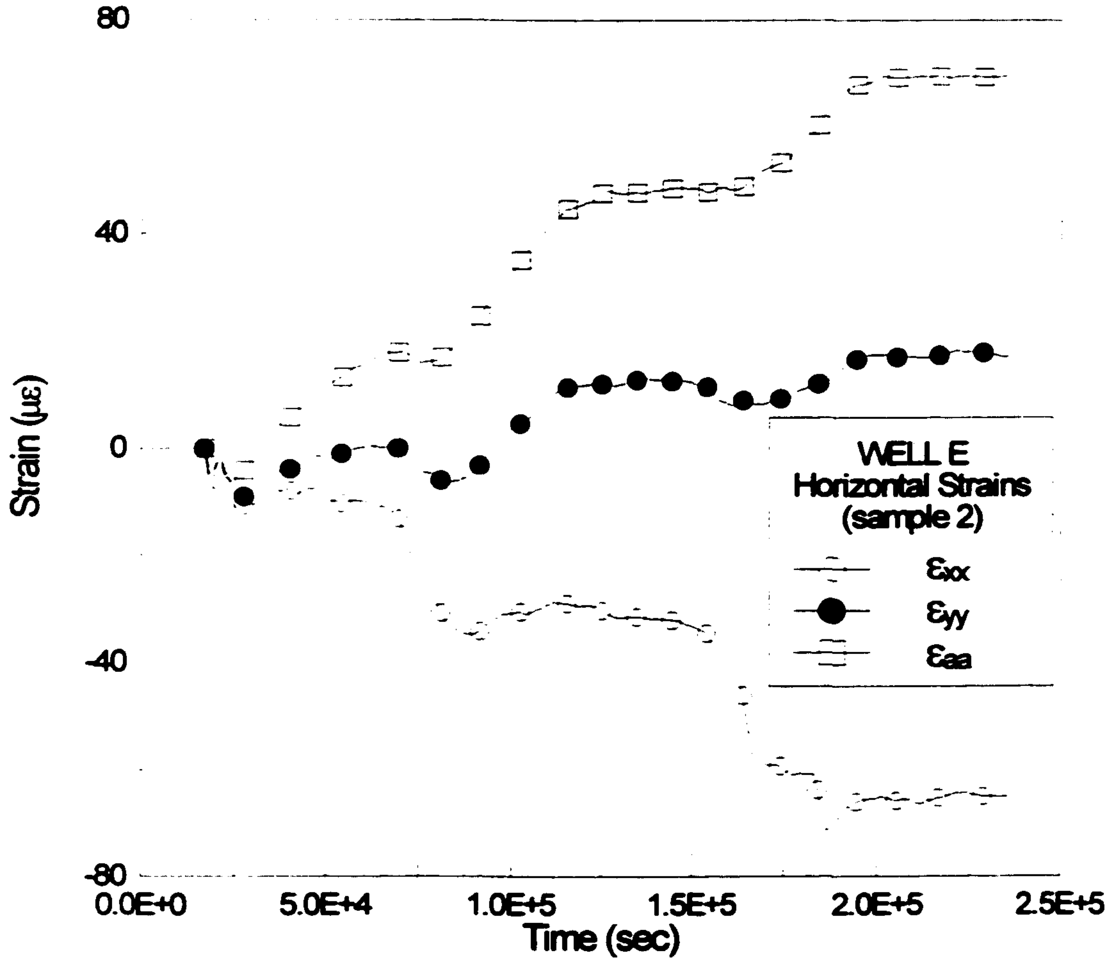

Figure 5.32: Anelastic horizontal strain measured by the ASR for well E, sample # 2.

5.3 Conclusions

1. Very good results were obtained from back-analyzing the hydrostatic synthetic stress case: the average computed stress was within 0.1 % of the original value while the standard deviation was 0.8 %. The original deviatoric stress was perfectly matched by the inversion process.

2. The analyzed inverse problem is somewhat ill-posed, since the correct stress value can be achieved for different sets of input data. Therefore, penalty functions were defined in order to keep the rock properties in an acceptable range of variation, according to the experimental data.

3. The horizontal stresses computed for the case histories were confirmed by other sources (shallow seismic events and microfracturing), whenever available.

4. Even with samples which were not appropriate for ASR tests (showing pre-existing fractures and large heterogeneities), and also problematic ASR tests (temperature fluctuation), the method was still able to provide reasonable strains and stresses.

5. The developed Fortran code (presented in Appendix E) is very efficient, taking less than 5 minutes for running most of the cases discussed in this chapter.

Chapter 6

Laboratory Results

A laboratory testing program was carried out in order to determine the mechanical properties of the rocks previously tested for the ASR, providing thus, the required input data for the stress computation (Chapter 5).

The tests were defined by taking into account that four independent constitutive constants (Young's modulus, E, bulk modulus, K, undrained Poisson's ratio, ν, and grain compressibility, K_s) plus the rock permeability, are sufficient for deriving all the relevant parameters for an isotropic poroelastic analysis. Including time-dependent properties for two of the basic constants (E and K), required four more parameters (E_2, μ_E, K_2, μ_K), according to the three-parameter solid model, totalizing eight rock constants to be obtained from the lab tests.

Table 6.1 summarizes the tests which were carried out and the parameters obtained on each one of them. Some extra rock data (Poisson's ratio, ν, undrained bulk modulus, K_u, and undrained Young's modulus, E_u) were generated from the laboratory tests, providing more than the minimum number of needed parameters. The rock petrophysical characteristics are shown in Table 6.2. They were provided by Petrobras' Research Center — CENPES.

Table 6.1: Test schedule and respective parameters.

Test Condition	Uniaxial Compression	Hydrostatic Compression	Triaxial Compression	Creep Test
Unconfined	E, ν			E_2, μ_E
Drained		K		K_2, μ_K
Undrained		K_u	E_u, ν_u	
Unjacketed		K_s		

s = solid constituent (grain); u = undrained

Table 6.2: Porosity and permeability of the tested samples.

Well #	Sample #	ϕ (%)	k (md)
A	1 & 2	17.8	15.4
B	3 & 4	19.1	8.9
C	5	17.1	3.1
D	6 & 7	13.5	9.3
E	8 & 9	11.0	71.2

6.1 Testing Procedure

A total of 9 samples were available, representing 5 different wells. The number of samples per well was extremely low (maximum of two); hence, a careful experimental procedure was elaborated for using the same samples in more than one test, without letting the rock mechanical properties being affected by the previous test. The main concern was to avoid plastic deformations that could change the rock characteristics, and make the subsequent tests not representative: the axial stress in unconfined compression tests, was always kept under the elastic limit, saving the sample for further testing; and, the maximum stress in confined compression tests was lower in the first tests, gradually increasing in the following ones. The test sequence is shown in Table 6.3.

Table 6.3: Test sequence.

Well #	Sample #	Test Sequence 1st	2nd	3rd	4th	5th
A	1	K	K_u	E_u, ν_u	K_s	E, ν
	2	E, ν	K_s	K_s	-	-
B	3	E, ν	K	K_u	E_u, ν_u	K_s
	4	E, ν	K_s	-	-	
C	5	E, ν	-	-	-	-
D	6	E, ν	-	-	-	-
	7	E_u, ν_u	K_s	K	K_2, μ	-
E	8	E, ν	K_u	E_u, ν_u	K_s	-
	9	E, ν	-	-	-	-

The tests were performed on right cylindrical samples, 2 inches in diameter and approximately 4 inches long. The samples were surface-grinded to assure that top and bottom were perfectly plane, parallel to each other and perpendicular to the longitudinal axis; oven-dried for 4 hours at 150° F, for cleaning the pores from the original pore fluid; and, finally, saturated with mineral oil. Table 6.4 shows the samples' geometrical characteristics, while Figure 6.1 summarizes the sample preparation procedures.

Table 6.4: Geometrical characteristics of the tested samples.

Well #	Sample #	Depth (m)	Rock Type	Diameter (mm)	Length (mm)
A	1	185.07	sandstone	50.29	98.04
	2	185.19	sandstone	50.29	97.79
B	3	193.06	sandstone	50.55	111.00
	4	193.09	sandstone	50.04	108.97
C	5	480.10	sandstone	50.55	108.97
D	6	510.78	sandstone	50.55	108.97
	7	536.39	sandstone	50.55	116.08
E	8	505.30	conglomerate	50.55	118.36
	9	505.38	conglomerate	50.55	114.81

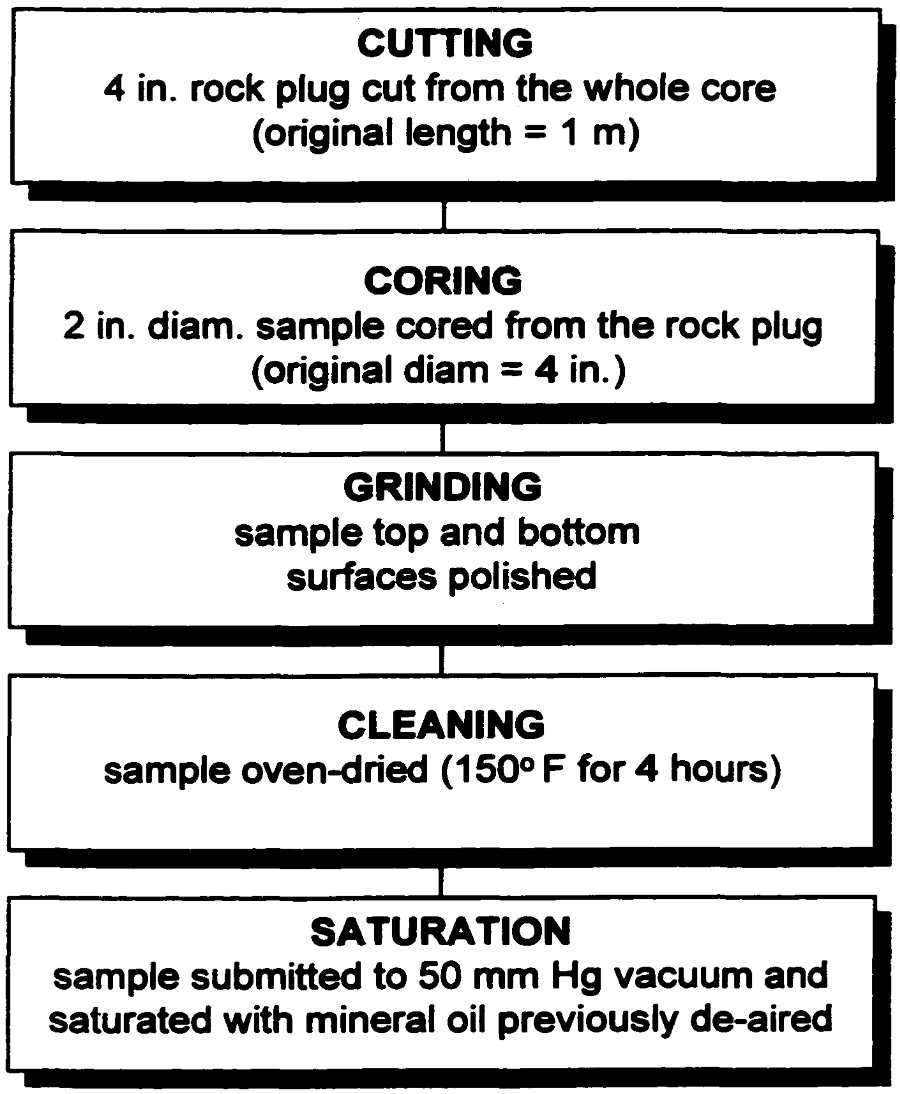

Figure 6.1: Procedures for sample preparation.

6.1.1 Uniaxial Compression Tests

The uniaxial compression tests were performed on a 319.25A/T MTS testing frame with capacity for applying up to 55 kip in compression. The samples were placed on top of the actuator and then compressed against the crossbar under constant displacement rate. Figure 6.2 shows the loading frame.

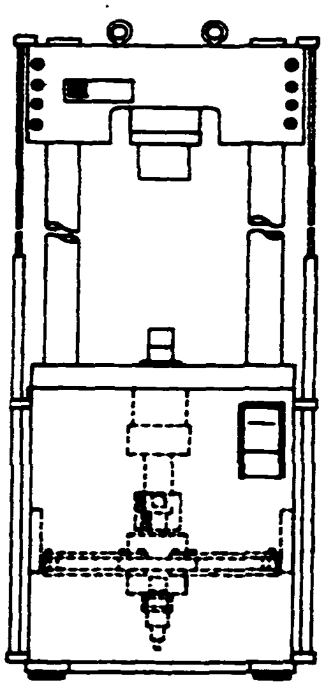

Figure 6.2: Loading frame MTS 319.025A/T, used for the uniaxial compression tests.

The goal of the uniaxial compression test was to determine Young's modulus and Poisson's ratio for each well. These two parameters are the most fundamental ones for describing the rock elastic behavior, being traditionally computed at 50% of the maximum stress attained in the test, for comparison purposes (ISRM, 1979).

Whenever possible, the tests were performed within the rock elastic limit. The rock behavior was monitored by plotting and carefully observing the curve axial load *versus* displacement; as soon as a linear trend was clearly defined,[1] the test was interrupted, saving the sample for further tests.

The rock axial strain was computed by:

$$\varepsilon_{ax}(\%) = \frac{\Delta\ell_{corr}}{\ell} \times 100 \tag{6.1}$$

where:

$$\begin{cases} \varepsilon_{ax}(\%) \text{ is the axial strain in percentage;} \\ \Delta\ell_{corr} \text{ is the actuator displacement (in inches),calibrated via an aluminum} \\ \quad \text{standard sample (the calibration procedure is shown in AppendixG); and,} \\ \ell \text{ is the sample axial length (also in inches).} \end{cases}$$

The rock lateral displacement was computed with the following expression:

$$\varepsilon_{lat}(\%) = \frac{\Delta\ell_{per}}{\pi D} \times 100 \tag{6.2}$$

where:

$$\begin{cases} \varepsilon_{lat}(\%) \text{ is the lateral strain in percentage;} \\ \Delta\ell_{per} \text{ is the change in the perimeter dimension (ininches); and,} \\ D \text{ is the sample diameter (in inches).} \end{cases}$$

The changes in the sample lateral perimeter, $\Delta\ell_{per}$, due to the compression load, were measured with a special chain-type lateral extensometer, depicted in Figure 6.3. The calibration of the lateral extensometer is also shown in Appendix G.

[1]Typical stress-strain curves for compression of porous materials always present an initial non-linear region (slightly convex upwards), due to the closure of microcracks, followed by a linear region, in which the stress-strain behavior is considered to be linear elastic. Immediately after the linear region the sample develop plastic irreversible deformations.

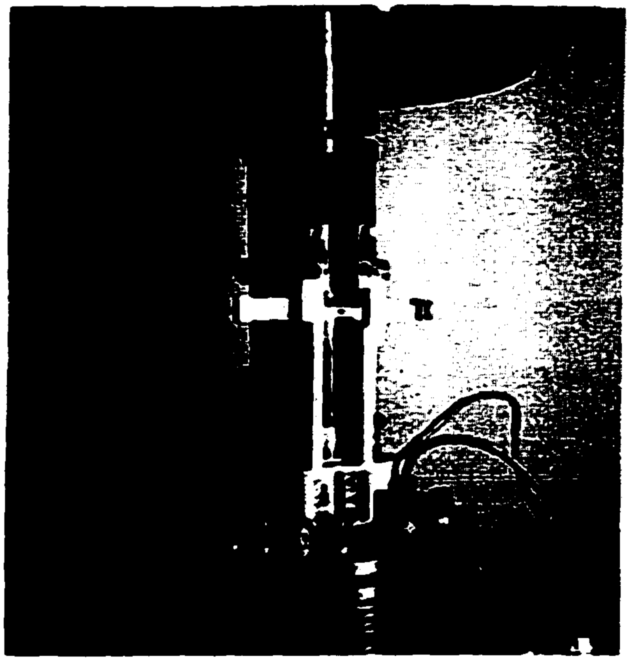

Figure 6.3: Rock sample instrumented for the uniaxial test.

The modulus of elasticity, or Young's modulus, E, was computed tangent to the stress-strain curve in the linear region (Jaeger and Cook, 1979):

$$E = \frac{d\sigma}{d\varepsilon_{ax}} \tag{6.3}$$

where:

$$\begin{cases} d\sigma \text{ is the change in the axial stress; and,} \\ d\varepsilon_{ax} \text{ is the correspondent change in the axial strain.} \end{cases}$$

Poisson's ratio, ν, was computed by:

$$\nu = \frac{\Delta\varepsilon_{lat}}{\Delta\varepsilon_{ax}} \tag{6.4}$$

Figure 6.4 shows schematically how the stress and strain intervals are related for computing E and ν.

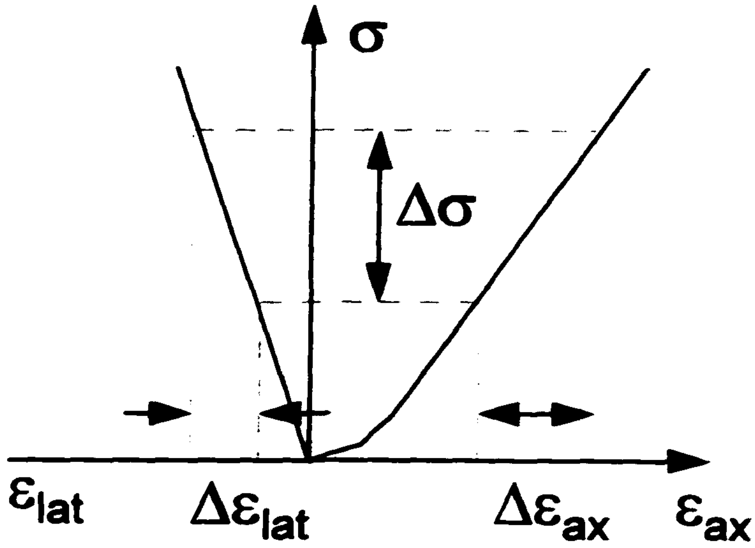

Figure 6.4: Gathering the stress and strain values for computing the elastic parameters from uniaxial tests.

6.1.2 Hydrostatic Compression Tests

Hydrostatic compression tests were run in a triaxial cell, with a capacity of 68 MPa confining pressure. The cell was installed in the 315.02 MTS loading frame (Figure 6.5), which is capable of applying up to 270 tons in axial compression. The parameters determined by this test were the drained and undrained rock bulk moduli. Hydrostatic unjacketed tests were also run for gathering the grain bulk modulus.

The procedure for the hydrostatic compression tests consisted in measuring the sample radial and axial deformations under increasing confining pressure. For the drained test, a valve connecting the sample pore fluid to the atmospheric pressure was left open; while for undrained tests it was closed.

The sample preparation for the confined tests consisted of the following steps:

1) A thermoshrinkable teflon membrane was adjusted around the rock sample

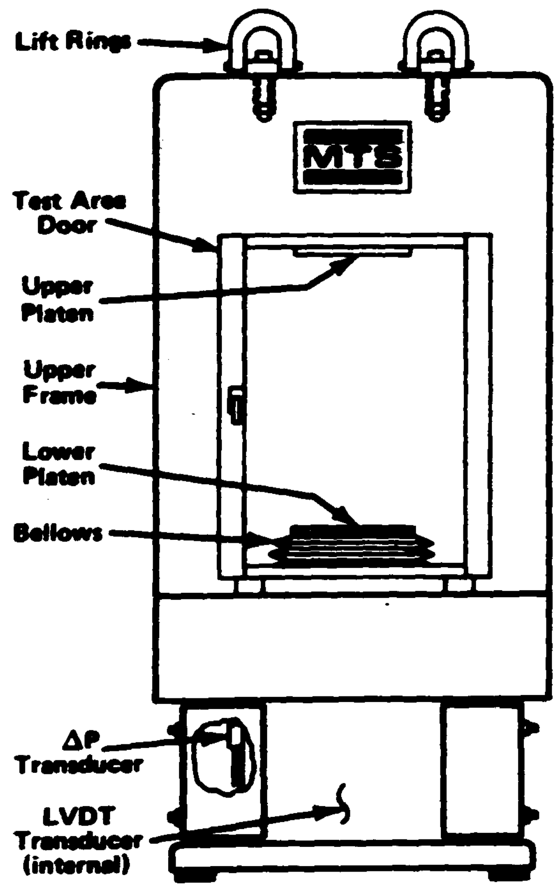

Figure 6.5: Loading frame MTS 315.02 utilized in the triaxial compression tests.

for isolating the rock pore fluid from the confining fluid. Before this, a special rubber was wrapped around the top and bottom part of the 2" sample, to ensure a smooth transition from the top and lower $2\frac{1}{8}$" steel caps, and avoid puncturing the membrane in sharp corners, when applying the confining pressure;

2) Two steel wires were firmly tightened to the top and lower caps to secure the membrane in place, and prevent confining fluid leaks to the pore fluid line;

3) Next, the two LVDTs and the lateral extensometer were installed for measuring the axial and lateral strains.

4) The instrumented sample, shown in Figure 6.6, was finally placed inside the triaxial cell, immersed in the confining fluid, and installed in the testing frame.

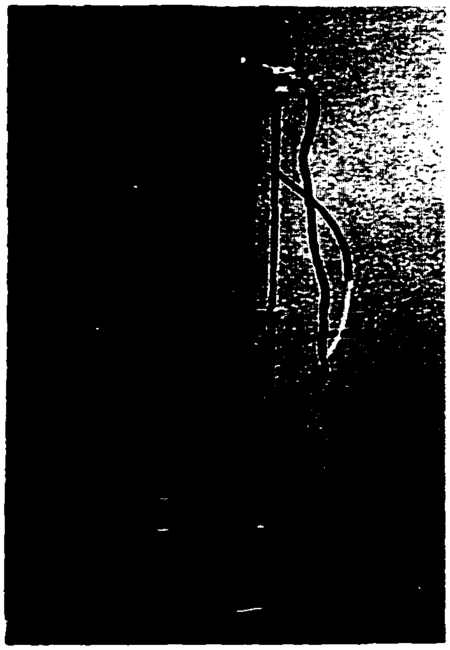

Figure 6.6: Sample instrumented for the hydrostatic and triaxial tests

The axial strain was computed by averaging the two LVDT's outputs (the LVDTs calibration is also shown in Appendix G).

The rock bulk moduli (drained, undrained and unjacketed) were computed by:

$$K = \left.\frac{dP_c}{d\varepsilon}\right|_{drained} \tag{6.5}$$

$$K_u = \left.\frac{dP_c}{d\varepsilon}\right|_{undrained} \tag{6.6}$$

$$K_s = \left.\frac{dP_c}{d\varepsilon}\right|_{unjacketed} \tag{6.7}$$

where:

$$\begin{cases} dP_c \text{ is the variation in the confining pressure;} \\ \varepsilon \text{ is the volumetric strain, computed as:} \end{cases}$$

$$\varepsilon = \varepsilon_{ax} + 2\,\varepsilon_{lat} \tag{6.8}$$

It is worth noting that there is a difference in the terminology about unjacketed tests: some authors (Abousleiman and Cheng, 1992) assume that since the confining fluid is free to flow into the rock pores, the test should be considered drained, while some others call it undrained (Zimmerman, 1991). In this work it is assumed that a drained test is a test where the pore pressure increment is zero throughout the whole test. Since the pore pressure increment in the unjacketed test is not null, but equal to the confining pressure increment, the test was considered to be undrained.

6.1.3 Triaxial Compression Tests

The triaxial compression tests were performed in accordance to the suggestions from the International Society of Rock Mechanics (ISRM, 1983). The tests had two distinct stages: 1 - application of a hydrostatic confining pressure until reaching the confining pressure specified for the test; and, 2 - additional axial loading. The procedure for the first stage was described in the previous section. The application of the axial load, also called deviatoric load, leads to stress-strain curves similar to the ones obtained in the uniaxial tests; allowing thus, for the computation of Young's modulus and Poisson's ratio under confined conditions. The tests were run under drained and undrained conditions, allowing the determination of the undrained Poisson's ratio, chosen as an initial parameter for the poroviscoelastic approach. Once more the tests were kept within the elastic region, monitored by checking in real-time the linearity of the curves axial displacement *versus* load and lateral displacement *versus* load.

6.1.4 Creep Compression Tests

The creep tests were run under both unconfined and confined (drained) conditions, aiming at the parameters for the viscoelastic model (E_2, μ_E and K_2, μ_K). Creep tests were also performed on unjacketed samples, for checking on the creep behavior for the solid grain. The samples tested under creep were not utilized for any further test, since the rock mechanical and physical characteristics were definitively modified by the plasticity induced during the tests.

The unconfined creep tests were run immediately after the uniaxial compression tests. The samples were left under uniaxial constant load and the axial strain was monitored with time until stabilization (around 17 hours). The procedure for the confined creep test was to raise the confining pressure to approximately the overburden stress and keep it constant for a period of time long enough for detecting a constant volumetric strain. The parameters necessary for the poroviscoelasticity governing equations were obtained by curve-fitting the experimental data points (Chapter 3).

6.2 Discussion of the Experimental Results

The analysis of the experimental data focuses on four items:

1) the values obtained for the mechanical parameters;

2) the procedure for computing the mechanical parameters;

3) the testing procedure; and,

4) the shape of the stress-strain curves.

6.2.1 Uniaxial Compression Tests

The results of the uniaxial compression tests are summarized in Table 6.5. Figures F.1 to F.9 from Appendix F show the experimental stress-strain curves.

Table 6.5: Elastic constants from uniaxial compression tests.

Well #	Sample #	Young's Modulus (MPa)	Poisson's Ratio
A	1	1.04	0.17
	2	1.42	0.11
B	3	1.01	0.07
	4	1.16	0.49
C	5	0.34	0.30
D	6	0.34	0.27
	7	0.12	0.00
E	8	10.40	0.25
	9	12.06	0.04

1) *Analysis of the calculated elastic parameters*

The values obtained for Young's modulus (Table 6.5) are relatively coherent within samples of the same well; the largest difference being 27% for well A. The results for Poisson's ratio, nevertheless, present a much larger variation. In order to confirm the measured values, the tests on samples 1, 2, 4, and 7 were repeated. Figures 6.7 to 6.10 show that the angular coefficient of the stress-strain curves obtained from different tests are practically identical, indicating a good reproducibility for the elastic parameters. The dispersed results were then totally attributed to the sample characteristics.

2) *Analysis of the procedure for computing the elastic parameters*

The standard way for determining Young's modulus and Poisson's ratio is by plotting a tangent to each of the stress-strain curves at 50% of the rupture load and then computing the angular coefficient (ISRM, 1979). This procedure, nevertheless, was not entirely applied, since the same sample was going to be used in other tests, and the loading was interrupted before the sample rupture. Both E and ν were still computed in the linear region, which was well defined in most of the plots.

3) *Analysis of the testing procedure*

With the exception for sample 01, all the uniaxial compression tests were carried out before any other test, as shown in Table 6.3. This excluded the possibility of having a distortion in the elastic constants. The elastic parameters were very reasonable even for sample 01, in the sense that they are similar to the ones computed for sample 02, from the same well.

4) *Analysis of the shape of the stress-strain curves*

The classical upward concavity in the first part of the stress *versus* axial strain curves was always present. This curvature is due to the closure of the internal microcracks in the initial loading stage (Lama and Vutukuri, 1978b), and is especially pronounced in samples 02, 03 and 04 (Figures F.2, F.3 and F.4).

The conglomerate samples (samples 08 and 09) are much stiffer than the other tested rocks, as indicated by the high Young's modulus shown in Table 6.5. The contribution of the testing equipment compressibility to the total measured strain is much higher; in this case the correction in the stress *versus* axial strain curve is larger than in the other tests, as seen in Figures F.8 and F.9.

In spite of the special attention for keeping the uniaxial compression tests within the samples elastic limit, it can be seen from the downward concavity on the stress *versus* lateral strain of Figure F.6, that this sample was tested beyond the linear elastic zone, having a sudden rupture shortly after 750 psi of axial stress.

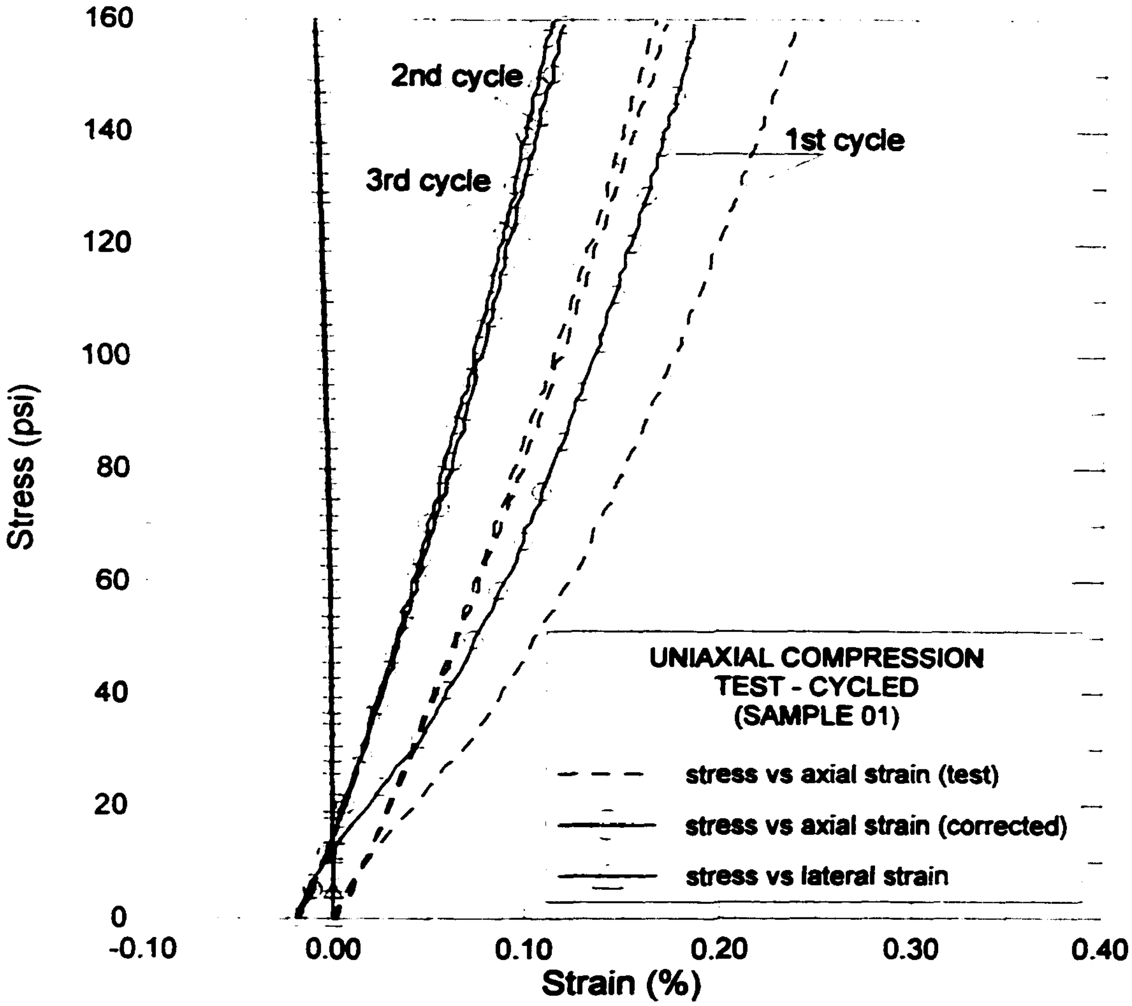

Figure 6.7: Cycled uniaxial compression test on sample 01.

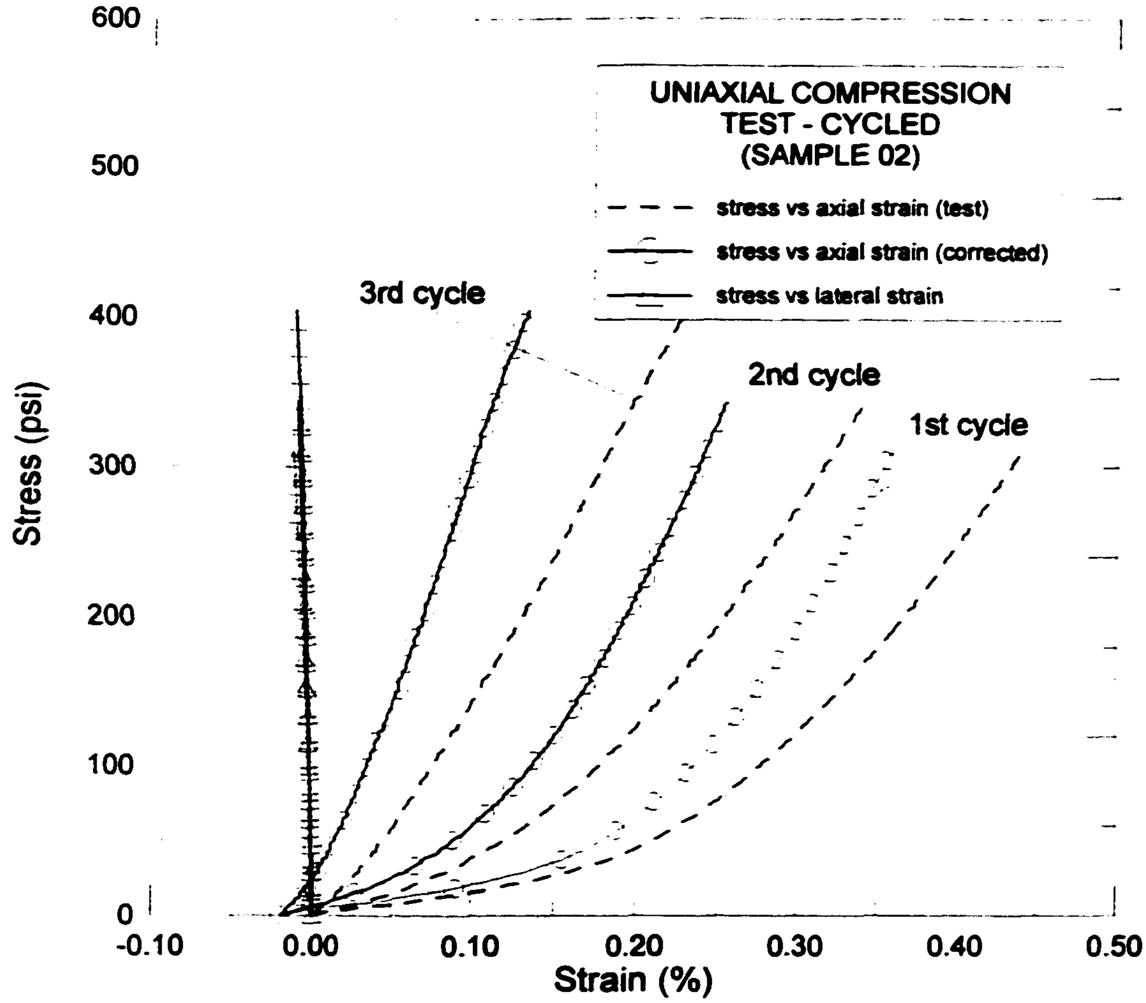

Figure 6.8: Cycled uniaxial compression test on sample 02.

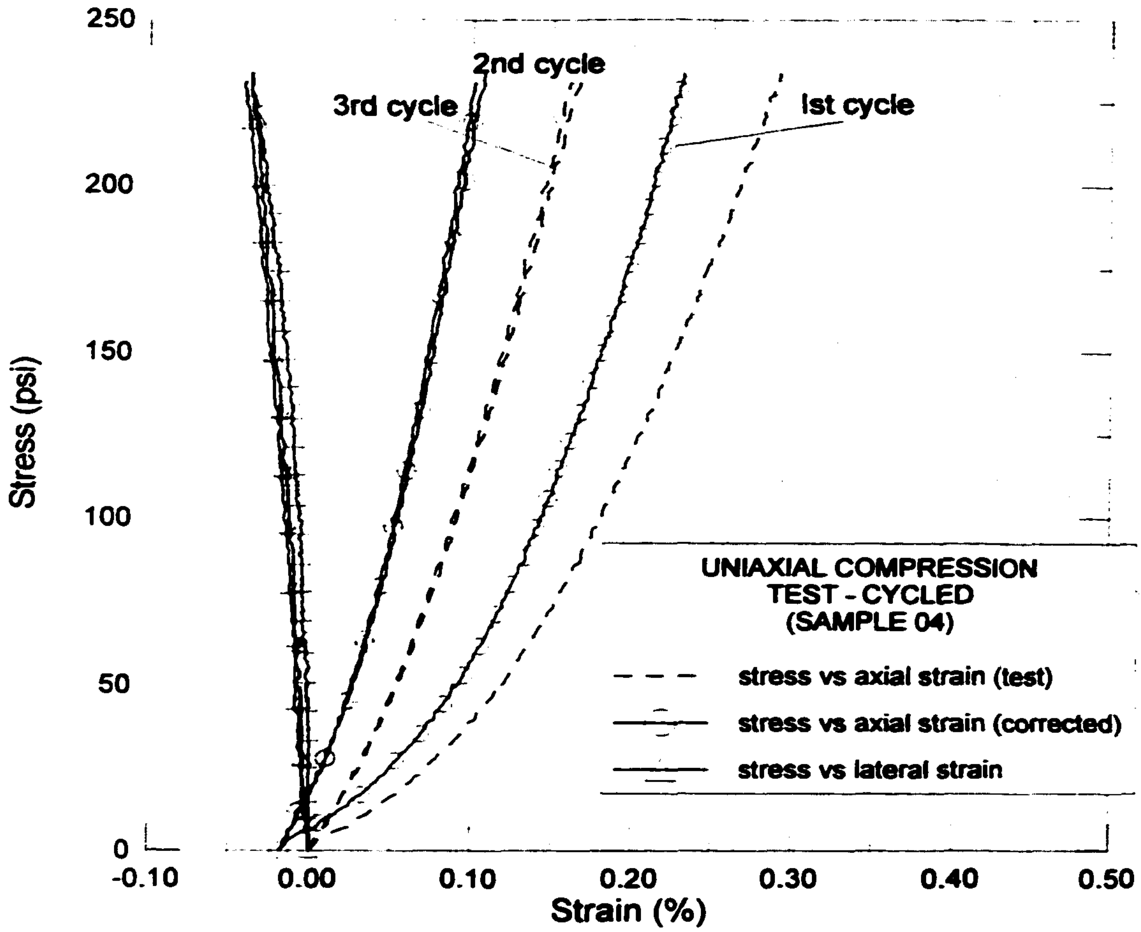

Figure 6.9: Cycled uniaxial compression test on sample 04.

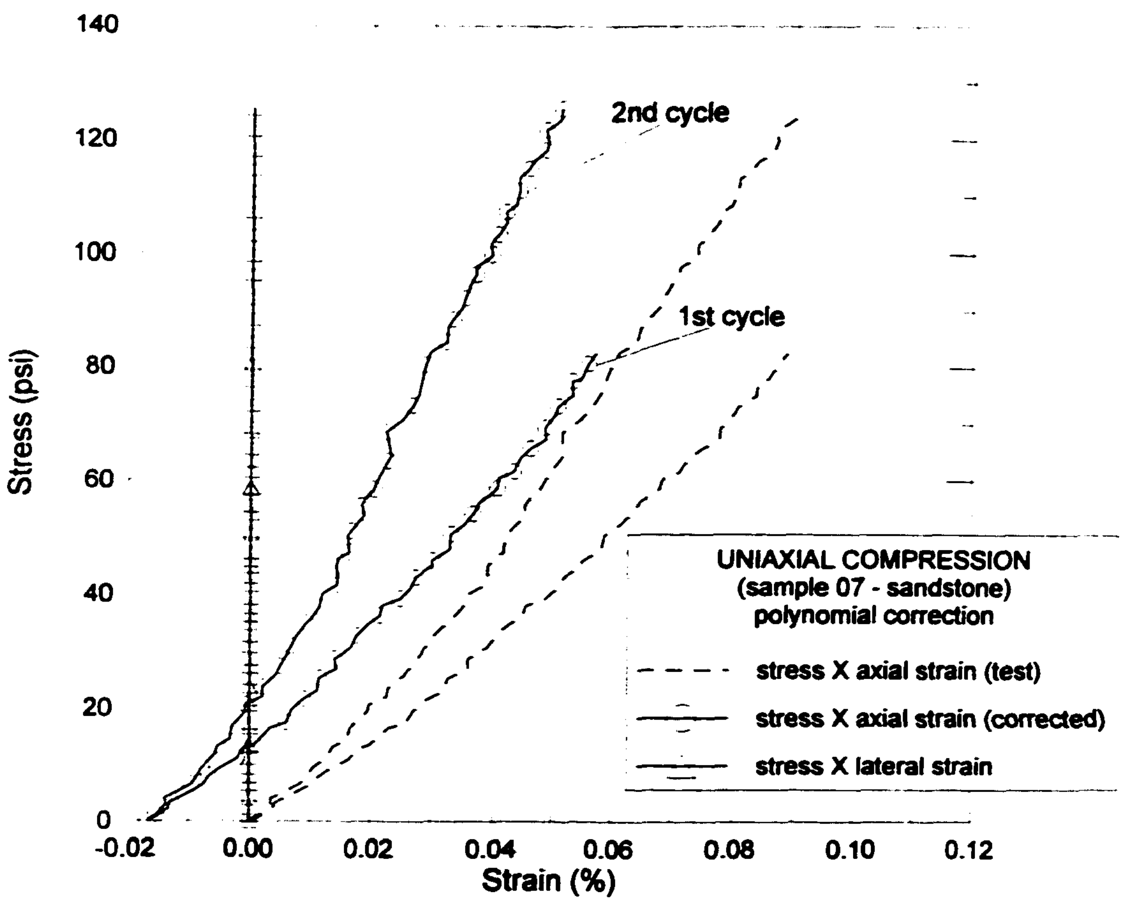

Figure 6.10: Cycled uniaxial compression test on sample 07.

6.2.2 Hydrostatic Compression Tests

The bulk moduli computed from the hydrostatic compression tests are shown in Table 6.6. Figures F.10 to F.23 show the curves confining pressure *versus* volumetric strain for each test.

Table 6.6: Bulk modulus from hydrostatic compression tests.

Well #	Sample #	Confining Pressure (MPa)$^{(1)}$ Drained	Confining Pressure (MPa)$^{(1)}$ Undr.	Drained Bulk Modulus (GPa)	Undr. Bulk Modulus (GPa)	Grain Bulk Modulus (GPa)
	1	27.59		3.93		
			67.59		16.55	
A			42.07			275.86
	2	55.17		14.90		
			62.07			95.55
	3	33.10		2.00		
			38.62		63.45	
B			54.48			111.72
	4		40.69			202.07
D	7		62.07			106.90
		82.76		6.41		
	8		68.96		24.14	
E			41.38			245.52
	9		62.07			266.21

(1) this is the maximum confining pressure attained during the test.

1) *Analysis of the calculated elastic parameters*

The hydrostatic tests determined three rock bulk moduli: drained, undrained and the grain bulk. The results shown in Table 6.6 agree very well with the expected relationship:

$$K < K_u < K_s \tag{6.9}$$

The first inequality in Equation (6.9) can be understood by considering that the pore fluid trapped in the rock pores, in the undrained conditions, will increase the pore pressure as a function of the confining pressure. This pore pressure build up will then contribute to decrease the compressibility of the overall rock-fluid system, i.e.: $K < K_u$. The other relationship, $K_u < K_s$, was mathematically proved by Zimmerman (1991), analyzing the strain induced in the rock bulk and pore volume for the undrained case.

2) *Analysis of the procedure for computing the elastic parameters*

The three bulk moduli were computed in the linear portion of the confining pressure *versus* volumetric strain curve, using Equations (6.5), (6.6) and (6.7). According to Zimmerman (1991) drained and undrained tests in sandstones have a linear region of the confining pressure *versus* volumetric strain curve located between 6.000 to 12.000 psi. However, the lower limit predicted by Zimmerman (1991) is not clear from the experimental results. The linear region was already established before 6.000 psi for several of the tested sandstones, indicating that this limit may have been affected by some other factors, like the testing condition and the sample preservation.

3) *Analysis of the testing procedure*

The hydrostatic compression tests were generally run after the uniaxial compression tests, with the exception of sample 01. This procedure does not seems to have affected the final results, since the stress-strain behavior was typical for the test under analysis. In other words, the uniaxial compression tests did not leave plastic deformations.

4) *Analysis of the shape of the stress-strain curves*

A small upward concavity can be seen in the initial part of the stress-strain plots for the drained and undrained tests. This non-linear region, nevertheless, is much less evident than in the uniaxial tests, as expected, because of the stiffening effect of the confining pressure.

The good linearity obtained in the stress-strain plots for the unjacketed test was already expected due to the samples relatively high permeability, as shown in Table

6.2. Since in this test the confining fluid is able to penetrate in the rock pore volume, any increment in the confining pressure will be transmitted to the pore fluid, leading to an uniform isotropic dilation directly proportional to the pressure increment. In other words, the grain bulk modulus should be constant in the unjacketed test, although small non-linearity can be seen in the beginning of the tests (Figures F.17 to F.23). These are attributed to the existence of microcracks in the rock matrix.

6.2.3 Triaxial Compression Tests

The undrained elastic parameters are shown in Table 6.7. The stress-strain curves are shown from Figure F.24 to F.27.

Table 6.7: Undrained elastic constants from triaxial compression tests.

Well #	Sample #	Confining Pressure (MPa)	E_u (GPa)	ν_u
A	1	27.59	3.86	0.11
B	3	0.44	3.17	0.13
D	7	6.90	23.72	0.21
E	8	68.96	30.90	0.27

1) *Analysis of the calculated elastic parameters*

The undrained elastic constants, computed from the triaxial compression tests, are presented again in Table 6.8 together with the elastic constants computed from the uniaxial compression tests. It can be seen that undrained Young's moduli are always higher than the unconfined ones, while Poisson's ratio are smaller in the confined tests. Theoretically speaking, both undrained constants were expected to be higher than the unconfined ones. One possible explanation for the low Poisson's ratio is the combining effect of the lateral confining pressure (tendency to reduce Poisson's ratio by restraining the rock lateral deformation) and the possibility of not having the sample 100 % saturated. Air inside the pores may have allowed larger axial deformations. Whatever the reason, the decreasing of Poisson's ratio as a function of the confining pressure have been reported before by Bloch (1993) in undrained tests on sandstones, for confining pressures between 300 and 6,000 psi.

Table 6.8: Comparison between the elastic parameter from drained uniaxial compression and undrained triaxial compression tests.

Well #	Young's Modulus (GPa)		Poisson's Ratio	
	Unconfined[1]	Confined	Unconfined[1]	Confined
A	1.23	3.86	0.14	0.11
B	1.08	3.17	0.28	0.13
D	0.34[2]	23.72	0.27[2]	0.21
E	11.86	30.90	0.14	0.27

[1] average of two samples.
[2] sample 06 only.

2) *Analysis of the procedure for computing the elastic parameters*

The elastic parameters were computed in the same way as in the uniaxial compression tests (Figure 6.4): a linear region was visually defined in the stress-strain curves and Equations (6.3) and (6.4) were applied according to Figure 6.4.

3) *Analysis of the testing procedure*

After computing low Poisson's ratio for some of the tests, the samples were resaturated and the tests repeated. The results, nevertheless, were exactly the same, meaning either that the sample saturation was not responsible for the low values of Poisson's ratio or that the saturation process was unable to reach 100%. The explanation for a saturation lower than 100% may then be attributed to the lack of a better cleaning process, that would have allowed the saturation fluid to penetrate in all the pore volume.

4) *Analysis of the shape of the stress-strain curves*

Since the triaxial tests were run after an initial hydrostatic pressurization, most of the microcracks in the rock were already closed since the beginning of the deviatoric loading phase, as shown in Figures F.24 to F.27. A downward concavity can be seen in the stress *versus* axial strain curves for samples 01 (Figure F.24) and 08 (Figure F.27) meaning that the rock is departing from the linear region, but not necessarily from the elastic region.

6.2.4 Creep Compression Tests

Generally speaking, creep tests (Lama and Vutukuri, 1978a) are characterized by an exponential behavior: the linear increase in the deformation during the first stage of the test (when the sample is submitted to an initial constant loading rate), is replaced by a gradual approach to an asymptotic value, as soon as the load is kept constant. The creep constants, presented in Table 6.9, were computed by curve-fitting the experimental data and by applying the methodology described in Chapter 3.

Table 6.9: Creep constants for the three-parameter solid model.

Sample #	Test Type #	Young's Modulus (GPa)		Bulk Modulus (GPa)		Viscosity (10^5GPa.sec)
		E_1	E_2	K_1	K_2	μ
5	unconfined	2.65	46.00	-	-	6.21
9	"	12.06	13.98	-	-	11.24
7	confined	-	-	10.21	31.76	2.09

Unconfined creep compression tests:

The difference between the creep behavior shown in Figures F.28 and F.29 is certainly due to the material properties: sample 09 is a conglomerate, with a much higher Young's modulus (E =12.06 MPa) than sample 05, (E = 0.34 MPa): thus, sample 05 is expected to be much more ductile than sample 09, explaining the larger strain variation. Another interesting aspect of these two plots is the homogeneous behavior of the sandstone deformation, as compared to the quasi-erratic behavior of the conglomerate. This can be attributed to the large variation of the conglomerate grain size, generating a more irregular pattern of slippage in the grain boundaries.

Confined Creep Compression Tests:

The creep test under drained hydrostatic compression (Figure F.30) produced a very homogeneous volumetric strain *versus* time plot, perhaps because the micro-cracks were previously closed by the confining pressure in the earlier stages of the test.

Unjacketed Creep Compression Tests:

The results of the hydrostatic creep compression tests with the unjacketed samples, nevertheless, are very atypical, suggesting that the solid mineral grain does not present creep behavior. As a matter of fact, a small decrease in the deformation can be seen under constant loading (Figures F.31 to F.33), meaning that the samples had somehow 'recovered' with time some of the strain imposed in the initial loading. This behavior can only be attributed to the uniformization of the pore pressure in a partly saturated sample: the initial reduction in the sample bulk volume is slowly recovered as the air spaces are filled in by the confining oil, increasing the pore pressure and generating a certain amount of dilation.

Chapter 7

Conclusions and Recommendations

1. Inferring the in-situ stresses is a difficult task for the petroleum industry. Most of the operating and service companies use as many methods as possible in order to increase the interpretation reliability of field and laboratory tests. Determining the in-situ stress orientations is less complex than computing its magnitudes.

2. A few models have been developed in the past for analyzing the rock anelastic strain behavior after coring, achieving good results whenever the rock has expanded due to the stress relief. Rock contraction was also observed and properly attributed to pore pressure diffusion and thermal effects. Nevertheless, a model capable of computing the stress magnitudes whatever the strain pattern was still missing in the rock mechanics literature.

3. The theory of coupled poroelasticity has been associated to a viscoelastic model for representing the rock deformation process after coring. The formulation was able to simulate rock expansion, contraction and their combination.

4. Five independent rock elastic parameters: Young's modulus; drained bulk modulus; undrained bulk modulus; grain bulk modulus; plus the rock per-

meability were defined as input for the poroelastic approach. The chosen viscoelastic model required two more parameters for each rock property assumed to have a viscous characteristics, in order to fulfill the spring-dashpot scheme.

5. Several laboratory compression tests were carried out in order to provide the necessary input rock data. The rock viscous behavior was identified in the drained bulk modulus as well as in the Young's modulus through creep tests. No evidence of creep was detected in the grain bulk modulus.

6. Depending on the rock type and the initial stress conditions, the changes in the pore volume can be of the same order of magnitude as the expansion due to the stress relief; affecting thus, the rock overall deformation.

7. The probability of having noticeable poroelastic effects in the ASR test was higher for rocks with low permeability, because the fluid diffusion process is slow enough to affect the ASR test long after core retrieval.

8. An inversion method was defined combining the simplex algorithm and the poroviscoelastic model for computing the hydrostatic and deviatoric in-situ stresses from ASR data. The method was first validated with a synthetic example, showing that the correct stress values and good curve-fittings can be obtained in spite of small changes in the rock input parameters, which are adjusted in the multidimensional minimization process carried out by the algorithm. The Fortran code is shown in Appendix E.

9. Petrobras' field cases, which have been sitting aside, awaiting for a solution able to handle the complex rock strain behavior, were analyzed by the new formulation having the experimentally determined rock properties and ASR

measurements as input data. The results were validated by other field information as well as geological analyses of the tested samples, confirming the method applicability.

7.1 Achieved Goals

The main achievements presented in this dissertation can be summarized as follows:

- A model capable of reproducing any strain trajectory in the ASR process after coring has been developed in Fortran. The method is based on the rock properties; the initial stresses; the drilling fluid pressure at the coring depth; and, the ASR measuring data;
- A suitable set of rock properties has been defined for analyzing the rock anelastic strain behavior: from experimental observations its viscoelastic behavior was attributed to the drained bulk modulus and to the Young's modulus;
- The parametric study indicated the conditions in which poroviscoelastic effects should be taken into account: low rock permeabilities and small differences among the horizontal in-situ stresses and the pore fluid pressure;
- An inversion algorithm, also written in Fortran, was successfully applied together with the poroviscoelastic model for computing the horizontal in-situ stresses from ASR field measurements, working fine even for complex strain patterns, which could not be analyzed by conventional viscoelastic methods;

7.2 Model Limitations

Leaving the restrictions for analyzing ASR data aside, since they are not intrinsic to the presented work, the major limitations in the developed model can be listed as:

- Only radial fluid flow and, consequently, plane strain condition was included in the poroelastic formulation, not considering thus, the influence of the rock axial strain. Even though the axial in-situ stress can be very often assumed as the overburden stress, the rock horizontal and vertical strains are linked by Poisson's ratio, which should somehow affect the ASR process and thus, the computation of the horizontal in-situ stresses;

- Thermal effects were not included in the model, although temperature usually decreases from the underground to the surface and may, consequently, play some role in the shrinkage process;

7.3 Recommendations

1. Rock stresses inferred by the back-analysis presented in this dissertation should be compared to other sources of information in order to check on the results reliability. This procedure would help confirming the validity of the curve-fitting generated by the method, which may be reasonable even for unrealistic stress values, since the inverse analysis was identified as an ill-posed problem for the utilized input rock data.

2. Thermal effects may be very important as demonstrated by the strain oscillations presented in Chapter 5, which were caused by small temperature oscillations (± 1 °C). In some regions, the temperature gradient can be as much as 38 °C/km (Souza, 1988). Therefore, the strain caused by the rock cooling off during tripping out of the hole should be evaluated. A complete formulation would have to couple the temperature diffusion process to the rock anelastic strain due to the stress relief, and to the poroelastic effects. Furthermore, including the thermal effects would need experimental determination of the rock

thermal expansion coefficient, which would become, then, another adjusting parameter in the back-analysis.

3. Including the axial strain in the model is another recommendation even though difficult in a near future. This improvement means abandoning the plane strain assumption and the radial flow consideration, which would lead to a new poroelastic formulation, not yet developed.

4. New rock creep tests should be conducted with larger observation times to confirm the lack of viscous effects in the grain bulk modulus and also in the undrained bulk modulus.

5. The experimental determination of the rock elastic parameters should have been done at the in-situ estimated stresses, rather then in the elastic region, in order to be more representative. The final in-situ stress computation, nevertheless, was not affected, because of the adjusting process in the multidimensional back-analysis.

References

1. Abousleiman, Y., Cheng, A.H.-D., "Poroviscoelasticity Theory and Applications, Part I", Rock Mechanics Institute - The University of Oklahoma, Report RMC-92-01, 1992.

2. Abousleiman, Y., Cheng, A.H.-D., Roegiers, J.-C., "Poroviscoelastic Analysis of Borehole and Cylinder Problems", Acta Mechanica 119, pp. 199–219, Springer-Verlag, 1996.

3. Abousleiman, Y., Cui, L., "Poroelastic Solutions in Transversely Isotropic Media for Wellbore and Cylinder", International Journal of Solids and Structures, Vol. 35, No. 34-35, pp. 4905–4929, 1998.

4. Abramowitz, M., Stegun, I.A., *Handbook of Mathematical Functions*, Dover Publications, Inc., 9th Printing, New York, 1970.

5. Anjos, S.M.C., Silva, C.M.A., "Petrographical Analyses of Sandstone and Conglomerate Samples Previously Tested in the ASR", Petrobras/CENPES (in Portuguese), Technical Report DIGER - 01, 1998.

6. Bell, J.S., "The Stress Regime of the Scotian Shelf Offshore Eastern Canada to 6 kilometers Depth and Implications for rock Mechanics and Hydrocarbon Migration", Rock at Great Depth, pp. 1243-1265, Balkema, Rotterdam, 1990.

7. Bell, J.S., Babcock, E.A., "The Stress Regime of the Western Canadian Basin

and Implications for Hydrocarbon Production", Bulletin of Canadian Petroleum Geology, Vol. 34, No. 3, pp. 364-378, 1986.

8. Bell, J.S., Caillet, G., Adams, J., "Attempts to Detect Open Fractures and Non-Sealing Faults with Dipmeter Logs", Geological Applications of Well Logs II, Geological Society of London, 1991.

9. Bell, J.S., Caillet, G., Le Marrec, A., "The Present-Day of the Southwestern Part of the Aquitaine Basin, France, as Indicated by Oil Well Data", Journal of Structural Geology, Vol. 14, No. 8/9 pp. 1019–1032, 1992.

10. Ben Naceur, K., Toubul, E., "Mechanisms Controlling Fracture Height Growth in Layered Media", paper SPE 16433, prepared for presentation at the SPE/DOE Low Permeability Symposium held in Denver, Colorado, 1987.

11. Biot, M.A., "General Theory of Three Dimensional Consolidation", Journal of Applied Physics, Vol. 12, pp. 155–164, February, 1941.

12. Blanton, T.L., "The Relation Between Recovery Deformation and In-Situ Stress Magnitudes", paper SPE 11624, presented at the SPE/DOE Symposium on Low Permeability, Denver, Colorado, 1983.

13. Blanton, T.L., Teufel, L.W., "A Field Test of the Strain Recovery Method of Stress Determination in Devonian Shale", paper SPE 12304, presented at the SPE Eastern Regional Meeting, Champion, Pennsylvania, 1983.

14. Blanton, T.L., Teufel, L.W., "A Critical Evaluation of Recovery Deformation Measurements as a Mean of In-Situ Stress Determination", paper SPE 15217, prepared for presentation at the 1986 SPE Unconventional Gas Technology Symposium held in Louisville, Kentucky, 1986.

15. Blanton, T.L., "Discussion of a Viscoelastic Constitutive Model for Determining In-Situ Stress Magnitudes from Anelastic Strain Recovery of Core", SPE Productin Engineering, pp. 281–287, 1989.

16. Bloch, M., "An Experimental Study of the Mechanical Properties of the Catu Sandstone", M.Sc. Thesis (in Portuguese), Pontificial Catholic University of Rio de Janeiro - PUC/RJ, Brazil, 1993.

17. Bloch, M., Siqueira, C.A.M., Ferreira, F.H., Conceição, J.C.J., "Techniques for Determining In-Situ Stress Direction and Magnitudes", paper SPE 39075, presented at the 5th Latin American and Caribbean Petroleum Engineering Conference and Exhibition — LACPEC, Rio de Janeiro, Brazil, August 3-7, 1997.

18. Boone, T.J., Detournay, E., "Response of a Vertical Hydraulic Fracture Intersecting a Poroelastic Formation Bounded by Semi-Infinite Impermeable Layers", International Journal of Rock Mechanics Mining Science and Geomechanical Abstracts, Vol. 27, No. 3, pp. 189–197, 1990.

19. Boone, T.J., Kry, P.R., Bharatha, S., Gronseth, J.M., "Poroelastic Effects Related to Stress Determination by Microfrac Tests in Permeable Rock", 32nd Rock Mechanics Symposium, pp. 25–34, Norman, Oklahoma, 1991a.

20. Boone, T.J., Ingraffea, A.R., Roegiers, J.-C., "Simulation of Hydraulic Propagation in Poroelastic Rock with Application to Stress Measurement techniques", International Journal of Rock Mechanics Mining Science and Geomechanical Abstracts, Vol. 28, No. 1, pp. 1–14, 1991b.

21. Brady, B.H.G., Brown, E.T., *Rock Mechanics for Underground Mining*, George Allen & Unwin Ltd., 1985.

22. Breretron. N.R., Chroston, P.N., Evans, C.J., "Pore Pressure as an Explanation of Complex Anelastic Strain Recovery Results", Rock Mechanics and Rock Engineering, Vol. 28, pp. 59–66, Springer–Verlag, 1995.

23. Bruce, S., "A Mechanical Stability Log", paper IADC/SPE 19942, prepared for presentation at the IADC/SPE Drilling Conference, Houston, Texas, 1990.

24. Brumley. J., Christiansem, C., Jorgenson, L.N., Khulman, H.A., Abass, H., "In-Situ Stress Field Determination and Formation Characterization - Offshore Qatar Case History", paper SPE 28143, prepared for presentation at the SPE/ISRM Rock Mechanics in Petroleum Engineering Conference held in Delft, The Netherlands, 1994.

25. Butterworth, S., Chroston, P.N., Davenport, C.A., Breretron, N.R., Evans, C.J., "Anelastic Strain Recovery of Rock Core from the English Midlands", 32nd Rock Mechanics Symposium, pp. 55–62, Norman, Oklahoma, 1991.

26. Caceci. M.S., Cacheris, P., "Fitting Curves to Data — The Simplex Algorithm is the Answer", Byte Magazine, No. 5, Green Publishing Inc., May 1984.

27. Chen, W., Salleb, F., *Constitutive Equations for Engineering Materials*, Vol. I. John Wiley and Sons, New York, 1982.

28. Cheng, A.H.-D.,"Material Coefficients of Anisotropic Poroelasticity", International Journal of Rock Mechanics Mining Science and Geomechanical Abstracts, Vol. 54, No. 2, pp. 199–205, 1997.

29. Coates, G.R., Denoo, S.A., "Mechanical Properties Program Using Borehole Analysis and Mohr's Circle", Society of Profissionals Well Log Analysts, SPWLA 22nd Annual Logging Symposium, 1981.

30. Cook, J.M., Bradford, I.D.R., Plumb, R.A., "A Study of Physical Mechanisms of Sanding and Application to Sand Prediction", paper SPE 28852, prepared for presentation at the European Petroleum Conference held in London, October 1994.

31. Cornet, F.H., Valete, B., "In-Situ Stress Determination from Hydraulic Injection Test Data", Journal of Geophysical Research, Vol. 89, No. B13, pp. 11,257-11,537, 1984.

32. Cui, L., Abousleiman, "The Axisymetric Mandel-Type Problem", Poromechanics, pp. 397-402, Balkema, Rotterdam, 1998.

33. Cui, L., Cheng, A.H.-D., Kaliakin, V.N., Abousleiman, Y., Roegiers, J.-C., "Finite Element Analyses of Anisotropic Poroelasticity: A Generalized Mandel's Problem and Inclined Borehole Problem", International Journal for Numerical and Analytical Methods in Geomechanics, Vol. 20, pp. 381-401, 1996.

34. Daneshy, A.A., Slusher, G.L., Chisholm, P.T., Magee, D.A., "In-Situ Stress Measurements During Drilling", Journal of Petroleum Technology, August 1986.

35. De Bree, P., Walters, J.V., "Micro/Minifrac Test Procedures and Interpretation for In-Situ Stress Determination", International Journal of Rock Mechanics Mining Science and Geomechanical Abstracts, Vol. 26, No. 6, pp. 515–521, 1989

36. Detournay, E., Cheng, A.H.-D., Roegiers, J.-C., McLennan, J.D., "Poroelasticity Considerations in In-Situ Stress Determination by Hydraulic Fracturing", International Journal of Rock Mechanics Mining Science and Geomechanical Abstracts, Vol. 26, No. 6, pp. 507–513, 1989.

37. Detournay, E., Cheng, A.H.-D., "Fundamentals of Poroelasticity", Comprehensive Rock Engineering Principles, Practices and Projects, Vol. II, Pergamon Press, 1993.

38. Detournay, E., Roegiers, J.-C., "Comment on Wellbore Breakouts and In-Situ Stress by Mark Zoback, Daniel Moos, Larry Mastin and Roger N. Anderson", Journal of Geophysical Research, Vol. 91, No. B14, pp. 14,161-14,162, 1986.

39. Economides, M.J., Nolte, K.,G., *Reservoir Stimulation*, Prentice Hall, 2nd Edition, 1989.

40. Eisenhamer, J.D., Hulbert, S., Zoltan, G.L., Shaw, R.A., "Aspec — User's Guide, Reference Manual and Installation Guide", 1996.

41. El Rabaa, A.W.M., "Determination of Hydraulic Fracture Direction in Deviated Wells", paper SPE 17482, presented at the poster session of the 58th SPE California Regional Meeting in Long Beach, California, March 23–25, 1988.

42. El Rabaa, A.W.M., Meadows, D.L., "Laboratory and Field Application of the Strain Relaxation Method", paper SPE 15072, prepared for presentation at the 56th SPE California Regional Meeting in Oakland, California, April 2–4, 1986.

43. Fejerskov, M., Bratli, R., "Can Dipmeter Logs be Used to Identify In-Situ Stress Directions in the North Sea?", paper SPE/ISRM 47237 prepared for presentation at the SPE/ISRM Eurock' 98, Trondheim, Norway, 1998.

44. Fjær, E., Holt, R., Per Hosrud, R., Risnes, A.M., *Petroleum Related Rock Mechanics*, Elsevier, 1992.

45. Ferreira, F.H., "A Numerical Solution for Poroelasticity Problems", M.Sc.

Thesis (in Portuguese), Pontificial Catholic University of Rio de Janeiro - PUC/RJ, 1996.

46. Finsterle, S., "iTough2 User's Guide", Earth Science Division, Lawrence Berkeley National Laboratory, University of California, Berkeley, 1999.

47. Flügge, W., *Viscoelasticity*, Second Edition, Springer-Verlag, 1975.

48. Fung, R.L., Vijayakumar, S., Cormack, D.E., "Calculation of Vertical Fracture Containment in Layered Formations", SPE Formation Evaluation, pp. 518-522, December 1987.

49. Germanovich, L.N., Roegiers, J.-C., Dyskin, A.V., "A Model for Breakouts in Brittle Rocks", Eurock' 94, Balkema, Rotterdam, 1994.

50. Goodman, R.E., *Introduction to Rock Mechanics*, 2nd Edition, John Wiley & Sons, 1980.

51. Gough, D.I., Bell, S.S., "Stress Orientations from Borehole Wall Fractures with Examples from Colorado, East Texas and Northern Canada", Canadian Journal of Earth Sciences, Vol. 19, pp. 1358-1370, 1982.

52. Graves, R.,personal communication, 1995.

53. Guenot, A., Santarelli, F.J., "Borehole Stability: a New Challenge for an Old Problem", Proceedings of the 29th U.S. Symposium on Rock Mechanics, Balkema Rotterdam, 453-460, 1988.

54. Haimson, B.C., "The Hydrofracturing Stress Measuring Method and Recent Field Results", International Journal of Rock Mechanics Mining Science and Geomechanicsl Abstracts, Vol. 15, pp. 167-178, 1978.

55. Haimson, B.C., "Status of In-Situ Stress Determination Methods", Key Questions in Rock Mechanics, Balkema, Rotterdam, 1988.

56. Haimson , B.C., Herrick, C.G., "Borehole Breakouts and In-Situ Stress", XI Drilling Symposium, Houston, Texas, 1989.

57. Haimson , B.C., Huang, X., "Hydraulic Fraturing Breakdown Pressure and In-Situ Stress at Great Depth", Rock at Great Depth, Balkema, Rotterdam, 1990.

58. Haimson, B.C., Song, I., "A New Borehole Failure Criterion for Estimating In-Situ Stress from Breakout Span", Proceedings of the 8th International Congress on Rock Mechanics, pp. 341-346, Tokyo, Japan, 1995.

59. Hayman, A.J., Parent, P., Cheung, P., Verges. P., "Improved Borehole Imaging by Ultrasonics", paper SPE 28440, prepared for presentation at the 69th SPE Annual Technical Conference and Exhibition, Los Angeles, California, 25–28 September, 1994.

60. Hill, R.E., Peterson, R.E., Warpinski, N.R., Lorenz, J.C., Teufel, L.W., Aslakson, J.K, "Techniques for Determining Subsurface Stress Direction and Assessing Fracture Azimuth", paper SPE 29192, prepared for presentation at the SPE Eastern Regional Conference and Exhibition held in Charleson, West Virginia, November 8–10, 1994.

61. Hubbert, M.K., Willis, D.G., "Mechanics of Hydraulic Fracturing", Petroleum Transactions of AIME, Vol. 210, pp. 110-123, 1957.

62. International Society for Rock Mechanics – ISRM, "Commission on Standardization of Laboratory and Field Tests: Suggested Methods for Determining

the Uniaxial Compressive Strength and Deformability of Rock Materials", International Journal of Rock Mechanics Mining Science and Geomechanical Abstracts, Vol. 20, pp. 135–140, 1979.

63. International Society for Rock Mechanics – ISRM, "Commission on Standardization of Laboratory and Field Tests: Suggested Methods for Determining the Strength of Rock Materials in Triaxial Compression", International Journal of Rock Mechanics Mining Science and Geomechanical Abstracts, Vol. 16, No. 6, pp. 285–290, 1983.

64. Jaeger, J.C. & Cook, N.G.W., *Fundamentals of Rock Mechanics*, 3rd Edition, Chapman & Hall, 1979.

65. Khulman, R.D., "Microfrac tests Optimize Frac Jobs", Oil & Gas Journal, pp. 45–49, January, 1990.

66. Khulman, R.D., Perez, J.I., Clairborne, E.B., "Microfracture Stress Tests, Anelastic Strain Recovery, and Differential Strain Analysis Assist in Bakken Shale Horizontal Drilling Program", paper SPE 24379, prepared for presentation at the SPE Rocky Mountain Regional Meeting held in Casper, Wyoming, May 18–21, 1992.

67. Kreyszig, E., *Advanced Engineering Mathematics*, 7th Edition, John Wiley and Sons,1993.

68. Lacy, L.L., "Comparison of Hydraulic Fracture Orientation Techniques", paper SPE 13225, presented at the 59th SPE Annual Technical Conference and Exhibition, Houston, Texas, 16–19 September, 1984.

69. Lama, R.D., Vutukuri, V.S., *Handbook on Mechanical Properties of Rocks*, Trans Tech Publications, Vol. 2, 1978a.

70. Lama, R.D., Vutukuri, V.S., *Handbook on Mechanical Properties of Rocks*, Trans Tech Publications, Vol. 3, 1978b.

71. Lessi, J.,Perreau, P., Kocher, M., "In-Situ Strain Measurements: Core Relaxation Method", *Revue de L 'Institut Français du Pétrole* (in French), Vol. 43, Jan-Feb, 1988.

72. Lima Neto, F.F., "An example of the Interference of a Weak Interface in the Regional Tectonic Stress Distribution: The Stress Field in the Potiguar Basin (Northeast of Brazil)", M.Sc. Thesis (in Portuguese), Federal University of Ouro Preto — UFOP/MG, Brazil, 1998.

73. Martin, C.D., Martino, J.B., Dzik, E.J., "Comparison of Borehole Breakouts from Laboratory and Field Tests", paper SPE 28050, prepared for presentation at the SPE/ISRM Rock Mechanics in Petroleum Engineering Conference held in Delft, The Netherlands, 1994.

74. Matseuki, K., Takeuchi, "Three-Dimensional In-Situ Stress Determination by Anelastic Strain Recovery of a Rock Core", 34th U.S. Rock Symposium, 1990.

75. Matseuki, K., Takeuchi, "Three-Dimensional In-Situ Stress Determination by Anelastic Strain Recovery of a Rock Core", International Congress on Rock Mechanics, Aachen, germany, 1991.

76. Meehan, N.D., "Rock Mechanics Issues in Petroleum Engineering", Rock Mechanics, pp. 3-17, Balkema, Rotterdam, 1994.

77. Morales, R., Frangachán E., Prado, E., "Production Optimization by an Artificial Control of Fracture Height Growth", paper SPE 38150, prepared for presentation at the SPE European Formation Damage Conference, Hague, The Netherlands, June 2-3, 1997.

78. Morita, N.,Whitfill, D.L., Fede, O.P., Lovik, T.H., "Parametric Study of Sand Production Prediction: Analytical approach", paper SPE 16990, prepared for presentation at the 62nd SPE Annual Technical Conference and Exhibition, Dallas, Texas, 1987.

79. Morrison, R., Thibodaux, J., "The Six-Arm Dipmeter, a New Concept by Geosource", Society of Profissionals Well Log Analysts, SPWLA, 25th Annual Logging Symposium, June 10–13, 1984.

80. Mukherjee, H., Morales, R.H., Denoo, S.A., "Influence of the Rock Heterogeneities on Fracture Geometry in the Green River Basin", SPE Production Engineering, pp. 267-274, August 1992.

81. Mullen, M.E., Norman, W.D, Wine, J.D., Stewart, B.R., "Investigation of Height Growth in Frac Pack Completions", paper SPE 36458, prepared for presentation at the SPE Annual Technical Conference and Exhibition, Denver, Colorado, October 6–9, 1996.

82. Nascimento, E.A., "Mathematical Modelling of Underground Water Flow", Ph.D. Dissertation (in Portuguese), Federal University of Rio de Janeiro — UFRJ/RJ, Brazil, 1998.

83. Nolte, K.G., "Fracture Design Considerations Based in Pressure Analysis", presented at the SPE Cottom Valley Symposium held in Tyler, Texas, 1982.

84. Nolte, K.G., "Fracturing Pressure Analysis", in *Recents Advances in Hydraulic Fracturing*, SPE Monograph, Vol. 12, 1989.

85. Ong, S.H., Roegiers, J.-C., "Fracture Initiation from Inclined Boreholes in Anisotropic Formations", Journal of Petroleum Technology, 1996.

86. Owen, L.B., Toronto, T.W., Peterson, R.E., " Reliability of Anelastic Strain Recovery Estimates for Stress Orientation in the Travis Peak Formation, Harrison County, Texas", paper SPE 18165, prepared for presentation at the 63rd SPE Annual Technical Conference and Exhibition held in Houston, Texas, October 2–5, 1988.

87. Paillet, L.F., Kim, K., "Character and Distribution of Borehole Breakouts and theur Relationship to In-Situ Stresses in Deep Columbia River Basalts", Journal of Geophysical Research, Vol. 92, No. B7, pp. 6223-6234, 1987.

88. Pennington, W.D., Edwards, D.P., "Integrating Well Log Data and Laboratory Data for the Determination of Maximum Drawdown Limits in the Presence of Weak Sands", paper SPE 28453, prepared for presentation at the SPE Annual Technical Conference and Exhibition, New Orleans, 1994.

89. Pereira, M.J., Macedo, J.M., "Santos Basin: The Outlook for a New Petroleum Province on the Southeastern Brazilian Continental Shelf", Petrobras' Geoscience Bulletin (in Portuguese), Vol. 4, No. 1, pp. 3-11, Jan-March, 1990.

90. Perreau, P.J., Heugas, O., Santarelli, F.J., "Tests of ASR, DSCA, and Core Discing Analyses to Evaluate In-Situ Stresses", paper SPE 17960, prepared for presentation at the SPE Middle East Oil Technical Conference and Exhibition held in Manama, Bahrain, March 11–14, 1989.

91. Petroleum Review, "New Production to Come from Ever Deeper Water", Petroleum Review, Vol. 52, No. 615, pp. 16-19, April, 1998.

92. Podrouzek, A.J., Bell, J.S., "Stress Orientation from Wellbore Breakouts on the Scotian Shelf, Eastern Canada", Geological Survey of Canada, paper 85–1B, pp. 59–62, 1985.

93. Press, W.H., Teukolsky, S.A., Vetterling, W.T., Flannery, B.P., *Numerical Receipes in FORTRAN, the Art of Scientific Computing*, 2nd Edition Cambridge University Press, Cambridge, 1992.

94. Ramos, G., Katahara, K., Keck, R., Baztle, M., "In-Situ Predictions and Measurements in an Unconsolidated Sandstone Formation, the Lower Frio, East Texas", Rock Mechanics in Petroleum Engineering Conference held in Delft, The Netherlands, pp. 361-368, August 29–31, 1994.

95. Ramos, G.G., Rathmell, J.J., "Effects of Mechanical Anisotropy on Core Strain Measurements for In-Situ Stress Measurements", paper SPE 19593, prepared for presentation at the 64th SPE Annual Technical Conference and Exhibition held in San Antonio, Texas, October 8–11, 1989.

96. Ren, N.-K., Roegiers, J.-C., "Differential Strain Curve Analysis — A New Method for Determining the Pre-Existing Stress State from Rock Core Measurements", prepared to be presented at the 5th Congress of the International Society of Rock Mechanics, Melbourne, Australia, April, 1983.

97. Rice, J.R., Cleary, M.P., "Some Basic Stress Diffusion Solutions for Fluid-Saturated Elastic Porous Media with Compressible Constituents", Reviews of geophysics and Space Physics, Vol. 14, No. 2, May 1976.

98. Roegiers, J.-C., personal communication, 1999.

99. Roegiers, J.-C., Ishijima, Y., "Coupled Fracturing Model and its Application to Hydraulic Fracturing", paper SPE 12311, presented at the SPE Eastern Regional Meeting held in Champion, Pennsylvania, 1983.

100. Roegiers, J.-C., Vandamme, L., *Rock Mechanics for the Petroleum Engineer*, unpublished, 1999.

101. Schmitt, D.R., Zoback, M.D., "Poroelastic Effects in the Determination of the Maximum Horizontal Principal Stress in Hydraulic Fracturing Tests — A Proposed Breakdown Equation Employing a Modified Effective Stress Relation for Tensile Failure", International Journal of Rock Mechanics Mining Science and Geomechanical Abstracts, Vol. 26, No. 6, pp. 499–506, 1989.

102. Seiler, D., King, G., Eubanks, D., "Field Test Results of a Six Arm Microresistivity Borehole Imaging Tool", Society of Profissionals Well Log Analysts, SPWLA 35th Annual Logging Symposium, 1994.

103. Shah, S., Hoek, E., "Simplex Reflection Analysis of Laboratory Strength Data", Canadian Geotechnical Journal, Vol. 29, 1992.

104. SIGEO — Integrated System for Geology and Geophysics, Petrobras Database, 1999.

105. Siqueira, C.A.M., Soares, A.C., Freitas, S.M.S., "Determination of the In-Situ Stress Field for Well 7-ET-670-RN with the ASR-3D Equipment", Petrobras/CENPES (in Portuguese), 1996a.

106. Siqueira, C.A.M., Soares, A.C., Martins, J.A.S., Freitas, S.M.S., "Determination of the In-Situ Stress Field for Well 7-ET-706-RN with the ASR-3D Equipment", Petrobras/CENPES (in Portuguese), 1996b.

107. Siqueira, C.A.M., Soares, A.C., Martins, J.A.S., Freitas, S.M.S., "Determination of the In-Situ Stress Field for Well 7-AP-278-RN with the ASR-3D Equipment", Petrobras/CENPES (in Portuguese), 1997a.

108. Siqueira, C.A.M., Soares, A.C., Martins, J.A.S., Freitas, S.M.S., "Determination of the In-Situ Stress Field for Well 8-SZ-362-SE with the ASR-3D Equipment", Petrobras/CENPES (in Portuguese), 1997b.

109. Siqueira, C.A.M., Soares, A.C., Martins, J.A.S., Freitas, S.M.S., "Determination of the In-Situ Stress Field for Well 8-SZ-364-SE with the ASR-3D Equipment", Petrobras/CENPES (in Portuguese), 1997c.

110. Smith, M.B., "Effect of the Fracture Azimuth on Production with Application to the Wattenberg Gas Field", paper SPE 8298, presented at the 54th SPE Annual Fall Technical Conference and Exhibition held in Las Vegas, Nevada, September, 23-26, 1979.

111. Souza, M.S., "Quality Controlling Diagenetic Factors for the Reservoirs in the Açu Formation, Estreito and Rio Panon Fields, Potiguar Basin - Rio Grande do Norte, Brazil", M.Sc. Thesis (in Portuguese), Federal University of Ouro Preto - UFOP/MG, Brazil, 1988.

112. Stehfest, H., "Numerical inversion of Laplace Transforms", Comm. ACM., Vol. 13, No. 1, pp. 47-49, January 1970a.

113. Stehfest, H., "Remark on Numerical inversion of Laplace Transforms", Comm. ACM., Vol. 13, No. 10, pp. 624, October 1970b.

114. Strickland, G., Ren, N-K., "Predicting the In-Situ Stress for Deep Wells Using Differential Strain Curve Analysis", paper SPE/DOE 8954, presented at the SPE-DOE Symposium on Unconventional Gas Recovery, Pittsburg, Pennsylvania, 1980.

115. Taylor, T.J., "Interpretation and Application of Borehole an Borehole Televiewer Surveys", Society of Profissionals Well Log Analysts, SPWLA, 24th Annual Logging Symposium , June 27–30, 1983.

116. Terratek, Inc. "Anelastic Strain Recovery - ASR 3D Operations Manual", March, 1995.

117. Teufel, L.W., "Prediction of Hydraulic Fracture Azimuth from Anelastic Strain Recovery of Oriented Core", Proceedings of the 23rd Symposium on Rock Mechanics, New York, 1982.

118. Teufel, L.W., "Determination of the Principal Horizontal In-Situ Stress Directions from Anelastic Strain Recovery Measurements of Oriented Cores from Deep Wells: Application to the Cottom Valley Formation of East Texas", Geomechanics 57, 1983a.

119. Teufel , L.W., "Determination of In-Situ Stress from Anelastic Strain Recovery Measurements of Oriented Core", paper SPE 11649, presented at the 1983 SPE/DOE Symposium on Low Permeability, Denver, Colorado, March 14–16, 1983b.

120. Teufel, L.W., "Determination of Hydraulic Fracture Azimuth by Geophysical, Geological, and Oriented-Core Methods at the Multiwell Experiment Site, Rifle, Colorado", paper SPE 13226, presented at the 59th SPE Annual Technical Conference and Exhibition held in Houston, Texas, September 16–19, 1984.

121. Teufel, L.W., "In-Situ Stress State in the Mounds Test Well as Determined by the Anelastic Strain Recovery Method", paper SPE 13896, presented at the SPE/DOE Symposium on Low Permeability held in Denver, May 19–22, 1985a.

122. Teufel, L.W., "In-Situ Stress Measurements in Inclined Holes in the North Sea: Application to Water Flooding and Enhanced Oil Recovery", SPE 13986/1, 1985b.

123. Vandamme, L., Jeffrey, R.G., Curran, J.H., "Effects of three-Dimensionalization on a Hydraulic Fracture Pressure Profile", Rock Mechanics, Key to Energy

Production, 1987.

124. Velloso, R.Q., "Inferring Hydraulic Parameters in Partially Saturated Soils", M.Sc. Thesis (in Portuguese), Pontificial Catholic University of Rio de Janeiro - PUC/RJ, 1999.

125. Wang, D.F., Yassir, N., Enever, J., Davies, P., "Laboratory Investigation of Core-Based Stress Measurement Using Synthetic Sandstone", International Journal of Rock Mechanics and Mining Science, Vol. 34, No. 3–4, pp. 345–353, 1997.

126. Warpinski, N.R., "Detemining the Minimum In-Situ Stress from Hydraulic Fracturing through Perforations", International Journal of Rock Mechanics Mining Science and Geomechanical Abstracts, Vol. 26, No. 6, pp. 523-531, 1989.

127. Warpinski, N.R., Clark, J.A., Schmidt, R.A., Huddle, C.W., "Laboratory Investigation on the Effect of In-Situ Stress on Hydraulic Fracture Containment", Society of Petroleum Engineers Journal, Vol. 22, No. 3, pp. 333-340, 1982a.

128. Warpinski, N.R., Schmidt, R.A., Northrop, D.A., "In-Situ Stresses: the Predominant Influence on Hydraulic Fracture Containment", Journal of Petroleum Technology, pp. 653-663, 1982b.

129. Warpinski, N.R., Teufel, L.W.,"A Viscoelastic Constitutive Model for Determining In-Situ Stress Magnitudes from Anelastic Strain Recovery of Core", paper SPE 15368, prepared for presentation at the 61st SPE Annual Technical Conference and Exhibition held in New Orleans, Lousiania, October 5–8, 1986.

130. Warpinski, N.R., Smith, M.B., "Rock Mecahnics and Fracture Geometry", in *Recent Advances in Hydraulic Fracturing*, SPE Monograph V. 12, 1989.

131. Warpinski, N.R., Teufel, L.W., "Author's Reply to Discussion of a Viscoelastic Constitutive Model for Determining In-Situ Stress Magnitudes from Anelastic Strain Recovery of Core", SPE Production Engineering, pp. 287–289, August, 1989.

132. Warpinski, N.R., Teufel, L.W., "In-Situ Stress Measurement at Rainier Mesa, Nevada Test Site – Influence of Topography and Lithology on the Stress State in Tuff", International Journal of Rock Mechanics Mining Science and Geomechanical Abstracts, Vol. 28, No. 2/3, pp. 143-161, 1991.

133. Yale, D.P., Ryan, T.C., "In-Situ Stress and Hydraulic Fracture Orientation in the Mid-Continent Area, US", Rock Mechanics, Balkema, Rotterdam, 1994.

134. Yale, D.P., Strubhar, M.K., El Rabaa, A.W., "A Field Comparison of Techniques for Determining the Direction of Hydraulic Fractures", Rock Mechanics, Balkema, Rotterdam, 1992.

135. Yew, C.H., Chiou, Y.J., "The Effects of In-Situ Stresses and Layer Properties on the Containment of a Hydraulic Fracture", SPE paper 12332, Unsolicited, 1983.

136. Zheng, Z., personal communication, 1999.

137. Zheng, Z., Cook, N.G.W., Myer, L.R., "Borehole Breakout and Stress Measurements", Key Questions in Rock Mechanics, Balkema, Rotterdam, 1988.

138. Zimmerman, R.W., *Compressibility of Sandstones*, Elsevier Science Publishers, New York, 1991.

139. Zoback, M., Moos, D., Mastin L., Anderson, R.N. , "Wellbore Breakouts and In-Situ Stress", Journal of Geophysical Research, Vol. 90, pp. 5523-5530, 1985.

140. Zoback, M., Peska, P., "In-Situ Stress and Rock Strength in the GBRN/DOE Pathfinfder Well, South Eugene Island, Gulf of Mexico", Journal of Petroleum Technology, July 1995.

Appendix A

Long Term Solution

Once the excess pore pressure is allowed to drain for larger periods of time, the rock samples achieve a final equilibrium state with the external load. The radial displacements computed from the poroelastic approach should then reproduce the elastic solution with the same boundary conditions.

The linear elasticity constitutive equation presented in Chapter 3 (Equation 3.6) can be rewritten in terms of strain as:

$$2G\varepsilon_{ij} = \sigma_{ij} - \frac{\nu}{1+\nu}\sigma_{kk}\delta_{ij} + \alpha\frac{1-2\nu}{1+\nu}p\delta_{ij}, \tag{A.1}$$

which for the radial direction becomes:

$$\varepsilon_r = \frac{1}{2G}\left[\sigma_r - \frac{\nu}{1+\nu}(\sigma_z + \sigma_\theta + \sigma_r) + \alpha\frac{1-2\nu}{1+\nu}p\right]. \tag{A.2}$$

The radial displacement, u_r, is then computed by:

$$u_r = \int \varepsilon_r dr, \tag{A.3}$$

giving the radial displacement of the lateral surface at $r = R$:

$$u_r = \frac{R}{2G}\left[\sigma_r - \frac{\nu}{1+\nu}(\sigma_z + \sigma_\theta + \sigma_r) + \alpha\frac{1-2\nu}{1+\nu}p\right]. \tag{A.4}$$

Considering now the axial strain given by:

$$\varepsilon_z = \frac{1}{2G}\left[\sigma_z - \frac{\nu}{1+\nu}(\sigma_z + \sigma_\theta + \sigma_r) + \alpha\frac{1-2\nu}{1+\nu}p\right], \tag{A.5}$$

and assuming plane strain and hydrostatic conditions; i.e.:

$$\varepsilon_z = 0; \text{ and,} \tag{A.6}$$

$$\sigma_r = \sigma_\theta = -P(t) \tag{A.7}$$

the axial stress can be computed as:

$$\sigma_z = 2\nu\sigma_r + \alpha p \tag{A.8}$$

For Mode I loading, the pore pressure increment is null:

$$p = 0, \tag{A.9}$$

and the radial displacement can be finally computed by replacing Equations (A.9), (A.8) and (A.7) into Equation (A.4):

$$u_r = \frac{-PR}{2G}(1-2\nu) \tag{A.10}$$

For Mode II loading, the radial and the tangential stresses are null:

$$\sigma_r = \sigma_\theta = 0, \tag{A.11}$$

and the pore pressure total increment, $p = p(t)$, generates only radial displacements and axial stress. The axial stresses is computed by replacing Equations (A.6) and (A.11), into (A.5), giving:

$$\sigma_z = -(1-2\nu)\,\alpha p, \tag{A.12}$$

The radial displacement for Mode II is finally computed by replacing Equations (A.12) and (A.11) into (A.4):

$$u_r = \frac{pR}{2G}(1-2\nu)\,\alpha \tag{A.13}$$

The long term radial displacement in both modes I and II was verified by adding Equations (A.10) and (A.13):

$$u_r = (\alpha p - P)\frac{R}{2G}(1-2\nu) \tag{A.14}$$

It should be noted that compression was assumed to be negative in Equation (A.14), according to the convention used for deriving the poroviscoelastic model. The radial load P and the pore pressure p can assumed constant or time-dependent.

The viscoelastic solution, for comparing with the poroviscoelastic approach, can be obtained by simply replacing the elastic parameters in Equation (A.14) — α, G and ν — by their correspondent ones: $\bar{\alpha}$, $\bar{G}$ and $\bar{\nu}$.

Appendix B

Initial Guesses for the Synthetic Example

B.1 Initial Guesses for computing the Hydrostatic Synthetic Stresses

Table B.1: Guess file P1.

E_1 (GPa)	E_2 (GPa)	μ_E (10^5GPa.sec)	K (GPa)	K_s (GPa)	K_u (GPa)	k (md)	*Stress* (Pa)
2.65	46.0	6.21	5.7	171.2	40.0	3.1	14.48

Table B.2: Guess file P2.

E_1 (GPa)	E_2 (GPa)	μ_E (10^5GPa.sec)	K (GPa)	K_s (GPa)	K_u (GPa)	k (md)	*Stress* (Pa)
2.65	46.0	6.21	5.7	171.2	40.0	3.1	10.0
2.65	46.0	6.21	5.7	171.2	40.0	3.1	11.0
2.65	46.0	6.21	5.7	171.2	40.0	3.1	12.0
2.65	46.0	6.21	5.7	171.2	40.0	3.1	13.0
2.65	46.0	6.21	5.7	171.2	40.0	3.1	14.0
2.65	46.0	6.21	5.7	171.2	40.0	3.1	15.0
2.65	46.0	6.21	5.7	171.2	40.0	3.1	16.0
2.65	46.0	6.21	5.7	171.2	40.0	3.1	17.0
2.65	46.0	6.21	5.7	171.2	40.0	3.1	18.0

Table B.3: Guess file P3.

E_1 (GPa)	E_2 (GPa)	μ_E (10^5GPa.sec)	K (GPa)	K_s (GPa)	K_u (GPa)	k (md)	$Stress$ (Pa)
2.65	46.0	6.21	5.7	171.2	40.0	3.1	-10.0
2.65	46.0	6.21	5.7	171.2	40.0	3.1	11.0
2.65	46.0	6.21	5.7	171.2	40.0	3.1	-12.0
2.65	46.0	6.21	5.7	171.2	40.0	3.1	13.0
2.65	46.0	6.21	5.7	171.2	40.0	3.1	-14.0
2.65	46.0	6.21	5.7	171.2	40.0	3.1	15.0
2.65	46.0	6.21	5.7	171.2	40.0	3.1	-16.0
2.65	46.0	6.21	5.7	171.2	40.0	3.1	17.0
2.65	46.0	6.21	5.7	171.2	40.0	3.1	-18.0

Table B.4: Guess file P4.

E_1 (GPa)	E_2 (GPa)	μ_E (10^5GPa.sec)	K (GPa)	K_s (GPa)	K_u (GPa)	k (md)	$Stress$ (Pa)
0.2	46.0	6.21	5.7	171.2	40.0	3.1	10.0
0.4	46.0	6.21	5.7	171.2	40.0	3.1	11.0
0.6	46.0	6.21	5.7	171.2	40.0	3.1	12.0
0.8	46.0	6.21	5.7	171.2	40.0	3.1	13.0
1.0	46.0	6.21	5.7	171.2	40.0	3.1	14.0
1.0	46.0	6.21	5.7	171.2	40.0	3.1	15.0
1.5	46.0	6.21	5.7	171.2	40.0	3.1	16.0
2.0	46.0	6.21	5.7	171.2	40.0	3.1	17.0
2.5	46.0	6.21	5.7	171.2	40.0	3.1	18.0

Table B.5: Guess file P5.

E_1 (GPa)	E_2 (GPa)	μ_E (10^5GPa.sec)	K (GPa)	K_s (GPa)	K_u (GPa)	k (md)	$Stress$ (Pa)
0.2	16.0	6.21	5.7	171.2	40.0	3.1	10.0
0.4	26.0	6.21	5.7	171.2	40.0	3.1	11.0
0.6	36.0	6.21	5.7	171.2	40.0	3.1	12.0
0.8	46.0	6.21	5.7	171.2	40.0	3.1	13.0
1.0	56.0	6.21	5.7	171.2	40.0	3.1	14.0
1.0	66.0	6.21	5.7	171.2	40.0	3.1	15.0
1.5	76.0	6.21	5.7	171.2	40.0	3.1	16.0
2.0	86.0	6.21	5.7	171.2	40.0	3.1	17.0
2.5	96.0	6.21	5.7	171.2	40.0	3.1	18.0

Table B.6: Guess file P6.

E_1 (GPa)	E_2 (GPa)	μ_E (10^5GPa.sec)	K (GPa)	K_s (GPa)	K_u (GPa)	k (md)	*Stress* (Pa)
0.2	46.0	0.5	5.7	171.2	40.0	3.1	10.0
0.4	46.0	1.0	5.7	171.2	40.0	3.1	11.0
0.6	46.0	2.0	5.7	171.2	40.0	3.1	12.0
0.8	46.0	3.0	5.7	171.2	40.0	3.1	13.0
1.0	46.0	4.0	5.7	171.2	40.0	3.1	14.0
1.0	46.0	5.0	5.7	171.2	40.0	3.1	15.0
1.5	46.0	6.0	5.7	171.2	40.0	3.1	16.0
2.0	46.0	7.0	5.7	171.2	40.0	3.1	17.0
2.5	46.0	8.0	5.7	171.2	40.0	3.1	18.0

Table B.7: Guess file P7.

E_1 (GPa)	E_2 (GPa)	μ_E (10^5GPa.sec)	K (GPa)	K_s (GPa)	K_u (GPa)	k (md)	*Stress* (Pa)
2.65	16.0	6.21	5.7	171.2	40.0	3.1	10.0
2.65	26.0	6.21	5.7	171.2	40.0	3.1	11.0
2.65	36.0	6.21	5.7	171.2	40.0	3.1	12.0
2.65	46.0	6.21	5.7	171.2	40.0	3.1	13.0
2.65	56.0	6.21	5.7	171.2	40.0	3.1	14.0
2.65	66.0	6.21	5.7	171.2	40.0	3.1	15.0
2.65	76.0	6.21	5.7	171.2	40.0	3.1	16.0
2.65	86.0	6.21	5.7	171.2	40.0	3.1	17.0
2.65	96.0	6.21	5.7	171.2	40.0	3.1	18.0

Table B.8: Guess file P8.

E_1 (GPa)	E_2 (GPa)	μ_E (10^5GPa.sec)	K (GPa)	K_s (GPa)	K_u (GPa)	k (md)	*Stress* (Pa)
2.65	46.0	0.5	5.7	171.2	40.0	3.1	10.0
2.65	46.0	1.0	5.7	171.2	40.0	3.1	11.0
2.65	46.0	2.0	5.7	171.2	40.0	3.1	12.0
2.65	46.0	3.0	5.7	171.2	40.0	3.1	13.0
2.65	46.0	4.0	5.7	171.2	40.0	3.1	14.0
2.65	46.0	5.0	5.7	171.2	40.0	3.1	15.0
2.65	46.0	6.0	5.7	171.2	40.0	3.1	16.0
2.65	46.0	7.0	5.7	171.2	40.0	3.1	17.0
2.65	46.0	8.0	5.7	171.2	40.0	3.1	18.0

Table B.9: Guess file P9.

E_1 (GPa)	E_2 (GPa)	μ_E (10^5GPa.sec)	K (GPa)	K_s (GPa)	K_u (GPa)	k (md)	*Stress* (Pa)
2.65	16.0	0.5	5.7	171.2	40.0	3.1	10.0
2.65	26.0	1.0	5.7	171.2	40.0	3.1	11.0
2.65	36.0	2.0	5.7	171.2	40.0	3.1	12.0
2.65	46.0	3.0	5.7	171.2	40.0	3.1	13.0
2.65	56.0	4.0	5.7	171.2	40.0	3.1	14.0
2.65	66.0	5.0	5.7	171.2	40.0	3.1	15.0
2.65	76.0	6.0	5.7	171.2	40.0	3.1	16.0
2.65	86.0	7.0	5.7	171.2	40.0	3.1	17.0
2.65	96.0	8.0	5.7	171.2	40.0	3.1	18.0

Table B.10: Guess file P10.

E_1 (GPa)	E_2 (GPa)	μ_E (10^5GPa.sec)	K (GPa)	K_s (GPa)	K_u (GPa)	k (md)	*Stress* (Pa)
0.2	16.0	0.5	5.7	171.2	40.0	3.1	10.0
0.4	26.0	1.0	5.7	171.2	40.0	3.1	11.0
0.6	36.0	2.0	5.7	171.2	40.0	3.1	12.0
0.8	46.0	3.0	5.7	171.2	40.0	3.1	13.0
1.0	56.0	4.0	5.7	171.2	40.0	3.1	14.0
1.0	66.0	5.0	5.7	171.2	40.0	3.1	15.0
1.5	76.0	6.0	5.7	171.2	40.0	3.1	16.0
2.0	86.0	7.0	5.7	171.2	40.0	3.1	17.0
2.5	96.0	8.0	5.7	171.2	40.0	3.1	18.0

Table B.11: Guess file P11.

E_1 (GPa)	E_2 (GPa)	μ_E (10^5GPa.sec)	K (GPa)	K_s (GPa)	K_u (GPa)	k (md)	*Stress* (Pa)
2.65	46.0	6.21	1.7	171.2	40.0	3.1	10.0
2.65	46.0	6.21	3.7	171.2	40.0	3.1	11.0
2.65	46.0	6.21	5.7	171.2	40.0	3.1	12.0
2.65	46.0	6.21	7.7	171.2	40.0	3.1	13.0
2.65	46.0	6.21	9.7	171.2	40.0	3.1	14.0
2.65	46.0	6.21	2.7	171.2	40.0	3.1	15.0
2.65	46.0	6.21	4.7	171.2	40.0	3.1	16.0
2.65	46.0	6.21	6.7	171.2	40.0	3.1	17.0
2.65	46.0	6.21	8.7	171.2	40.0	3.1	18.0

Table B.12: Guess file P12.

E_1 (GPa)	E_2 (GPa)	μ_E (10^5GPa.sec)	K (GPa)	K_s (GPa)	K_u (GPa)	k (md)	$Stress$ (Pa)
2.65	46.0	6.21	5.7	100.0	40.0	3.1	10.0
2.65	46.0	6.21	5.7	180.0	40.0	3.1	11.0
2.65	46.0	6.21	5.7	200.0	40.0	3.1	12.0
2.65	46.0	6.21	5.7	220.0	40.0	3.1	13.0
2.65	46.0	6.21	5.7	280.0	40.0	3.1	14.0
2.65	46.0	6.21	5.7	150.0	40.0	3.1	15.0
2.65	46.0	6.21	5.7	190.0	40.0	3.1	16.0
2.65	46.0	6.21	5.7	210.0	40.0	3.1	17.0
2.65	46.0	6.21	5.7	250.0	40.0	3.1	18.0

Table B.13: Guess file P13.

E_1 (GPa)	E_2 (GPa)	μ_E (10^5GPa.sec)	K (GPa)	K_s (GPa)	K_u (GPa)	k (md)	$Stress$ (Pa)
2.65	46.0	6.21	5.7	171.2	10.0	3.1	10.0
2.65	46.0	6.21	5.7	171.2	30.0	3.1	11.0
2.65	46.0	6.21	5.7	171.2	50.0	3.1	12.0
2.65	46.0	6.21	5.7	171.2	70.0	3.1	13.0
2.65	46.0	6.21	5.7	171.2	90.0	3.1	14.0
2.65	46.0	6.21	5.7	171.2	20.0	3.1	15.0
2.65	46.0	6.21	5.7	171.2	40.0	3.1	16.0
2.65	46.0	6.21	5.7	171.2	60.0	3.1	17.0
2.65	46.0	6.21	5.7	171.2	80.0	3.1	18.0

Table B.14: Guess file P14.

E_1 (GPa)	E_2 (GPa)	μ_E (10^5GPa.sec)	K (GPa)	K_s (GPa)	K_u (GPa)	k (md)	$Stress$ (Pa)
2.65	46.0	6.21	5.7	171.2	40.0	0.05	10.0
2.65	46.0	6.21	5.7	171.2	40.0	0.5	11.0
2.65	46.0	6.21	5.7	171.2	40.0	2.0	12.0
2.65	46.0	6.21	5.7	171.2	40.0	4.0	13.0
2.65	46.0	6.21	5.7	171.2	40.0	6.0	14.0
2.65	46.0	6.21	5.7	171.2	40.0	0.1	15.0
2.65	46.0	6.21	5.7	171.2	40.0	1.0	16.0
2.65	46.0	6.21	5.7	171.2	40.0	3.0	17.0
2.65	46.0	6.21	5.7	171.2	40.0	5.0	18.0

Table B.15: Guess file P15.

E_1 (GPa)	E_2 (GPa)	μ_E (10^5GPa.sec)	K (GPa)	K_s (GPa)	K_u (GPa)	k (md)	*Stress* (Pa)
0.2	16.0	0.5	1.7	100.0	10.0	0.05	10.0
0.4	26.0	1.0	3.7	180.0	30.0	0.5	11.0
0.6	36.0	2.0	5.7	200.0	50.0	2.0	12.0
0.8	46.0	3.0	7.7	220.0	70.0	4.0	13.0
1.0	56.0	4.0	9.7	280.0	90.0	6.0	14.0
1.0	66.0	5.0	2.7	150.0	20.0	0.1	15.0
1.5	76.0	6.0	4.7	190.0	40.0	1.0	16.0
2.0	86.0	7.0	6.7	210.0	60.0	3.0	17.0
2.5	96.0	8.0	8.7	250.0	80.0	5.0	18.0

B.2 Initial Guesses for Computing the Deviatoric Synthetic Stresses

Table B.16: Guess file S1.

E_1 (GPa)	E_2 (GPa)	μ_E (10^5GPa.sec)	K (GPa)	K_s (GPa)	K_u (GPa)	k (md)	*Stress* (Pa)
2.65	46.0	6.21	5.7	171.2	40.0	3.1	2.07

Table B.17: Guess file S2.

E_1 (GPa)	E_2 (GPa)	μ_E (10^5GPa.sec)	K (GPa)	K_s (GPa)	K_u (GPa)	k (md)	*Stress* (Pa)
2.65	46.0	6.21	5.7	171.2	40.0	3.1	1.0
2.65	46.0	6.21	5.7	171.2	40.0	3.1	2.0
2.65	46.0	6.21	5.7	171.2	40.0	3.1	3.0
2.65	46.0	6.21	5.7	171.2	40.0	3.1	4.0
2.65	46.0	6.21	5.7	171.2	40.0	3.1	5.0
2.65	46.0	6.21	5.7	171.2	40.0	3.1	6.0
2.65	46.0	6.21	5.7	171.2	40.0	3.1	7.0
2.65	46.0	6.21	5.7	171.2	40.0	3.1	8.0
2.65	46.0	6.21	5.7	171.2	40.0	3.1	9.0

Table B.18: Guess file S3.

E_1 (GPa)	E_2 (GPa)	μ_E (10^5GPa.sec)	K (GPa)	K_s (GPa)	K_u (GPa)	k (md)	$Stress$ (Pa)
2.65	46.0	6.21	5.7	171.2	40.0	3.1	10.0
2.65	46.0	6.21	5.7	171.2	40.0	3.1	30.0
2.65	46.0	6.21	5.7	171.2	40.0	3.1	18.0
2.65	46.0	6.21	5.7	171.2	40.0	3.1	45.0
2.65	46.0	6.21	5.7	171.2	40.0	3.1	25.0
2.65	46.0	6.21	5.7	171.2	40.0	3.1	60.0
2.65	46.0	6.21	5.7	171.2	40.0	3.1	72.0
2.65	46.0	6.21	5.7	171.2	40.0	3.1	80.0
2.65	46.0	6.21	5.7	171.2	40.0	3.1	65.0

Table B.19: Guess file S4.

E_1 (GPa)	E_2 (GPa)	μ_E (10^5GPa.sec)	K (GPa)	K_s (GPa)	K_u (GPa)	k (md)	$Stress$ (Pa)
6.50	46.0	6.21	5.7	171.2	40.0	3.1	1.0
3.00	46.0	6.21	5.7	171.2	40.0	3.1	2.0
4.80	46.0	6.21	5.7	171.2	40.0	3.1	3.0
12.00	46.0	6.21	5.7	171.2	40.0	3.1	4.0
2.32	46.0	6.21	5.7	171.2	40.0	3.1	5.0
4.95	46.0	6.21	5.7	171.2	40.0	3.1	6.0
8.67	46.0	6.21	5.7	171.2	40.0	3.1	7.0
7.44	46.0	6.21	5.7	171.2	40.0	3.1	8.0
1.00	46.0	6.21	5.7	171.2	40.0	3.1	9.0

Table B.20: Guess file S5.

E_1 (GPa)	E_2 (GPa)	μ_E (10^5GPa.sec)	K (GPa)	K_s (GPa)	K_u (GPa)	k (md)	$Stress$ (Pa)
2.65	16.0	6.21	5.7	171.2	40.0	3.1	1.0
2.65	26.0	6.21	5.7	171.2	40.0	3.1	2.0
2.65	36.0	6.21	5.7	171.2	40.0	3.1	3.0
2.65	46.0	6.21	5.7	171.2	40.0	3.1	4.0
2.65	6.0	6.21	5.7	171.2	40.0	3.1	5.0
2.65	4.0	6.21	5.7	171.2	40.0	3.1	6.0
2.65	10.0	6.21	5.7	171.2	40.0	3.1	7.0
2.65	80.0	6.21	5.7	171.2	40.0	3.1	8.0
2.65	1.0	6.21	5.7	171.2	40.0	3.1	9.0

Table B.21: Guess file S6.

E_1 (GPa)	E_2 (GPa)	μ_E (10^5GPa.sec)	K (GPa)	K_s (GPa)	K_u (GPa)	k (md)	$Stress$ (Pa)
6.50	16.0	0.12	5.7	171.2	40.0	3.1	1.0
3.00	26.0	2.21	5.7	171.2	40.0	3.1	2.0
4.80	36.0	32.1	5.7	171.2	40.0	3.1	3.0
12.00	46.0	4.21	5.7	171.2	40.0	3.1	4.0
2.32	6.0	5.21	5.7	171.2	40.0	3.1	5.0
4.95	4.0	6.21	5.7	171.2	40.0	3.1	6.0
8.67	10.0	5.21	5.7	171.2	40.0	3.1	7.0
7.44	80.0	6.89	5.7	171.2	40.0	3.1	8.0
1.00	1.0	8.12	5.7	171.2	40.0	3.1	9.0

Appendix C

Field Results

This Appendix presents the complete plots of ASR tests made by Petrobras in the Potiguar and Sergipe-Alagoas Basins. The horizontal strains from these plots were used as input data in the back-analyses discussed in Chapter 5 for computing the in-situ horizontal stresses in the respective wells, at the cored depths. Two samples were tested for each well, with the exception of well D, where a total of four samples have been tested at different depths. The plots show the rough strain data in six directions:

- vertical (ε_{zz});
- horizontal (ε_{xx}, ε_{aa}, ε_{yy}); and,
- inclined (ε_{bb}, ε_{cc}).

which were computed with the help of a steel frame supporting a total of 12 LVDTs, two in each direction, as shown in Figure C.1.

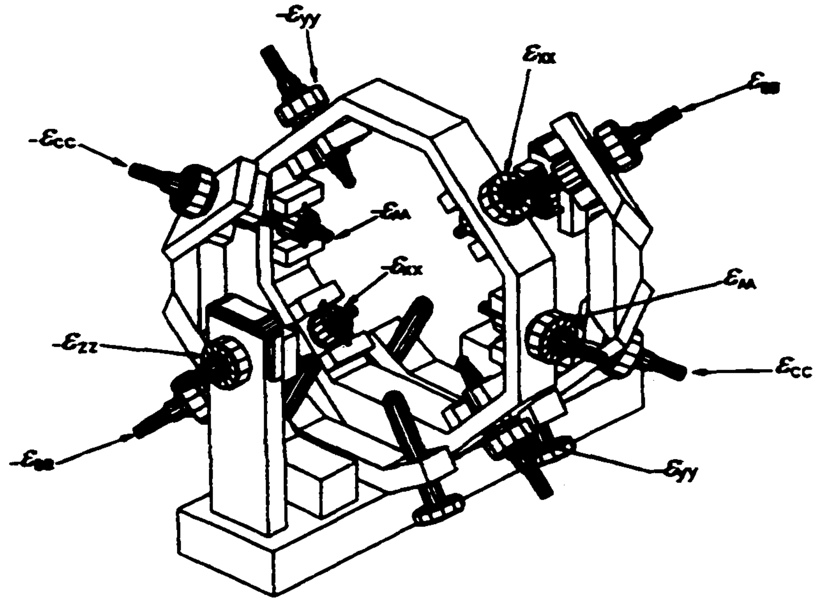

Figure C.1: Sample support for measuring the strains in the ASR test.

ASR curves for the samples from well A:

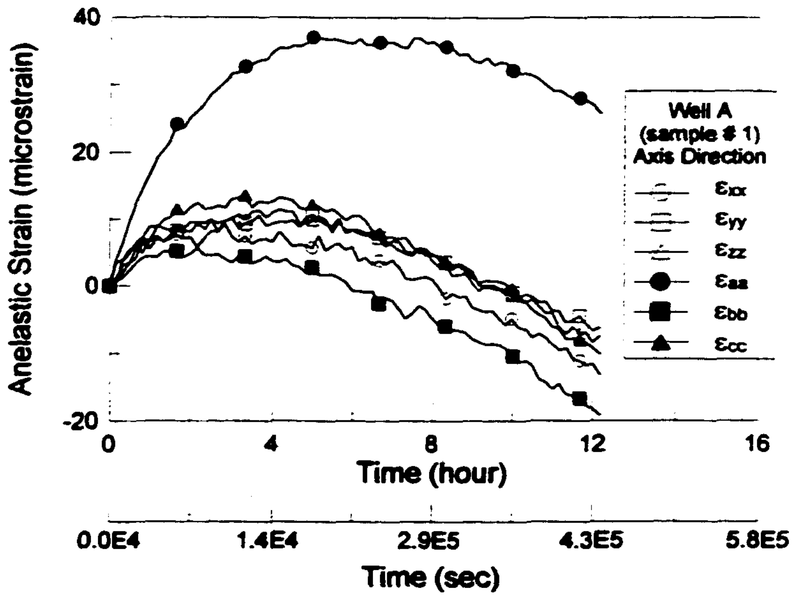

Figure C.2: Anelastic Strain Recovery for well A, sample # 1.

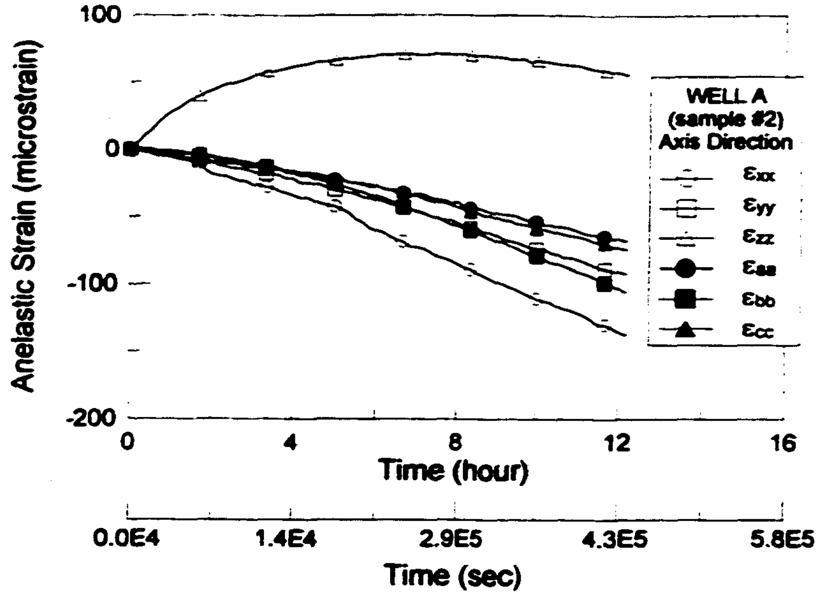

Figure C.3: Anelastic Strain Recovery for well A, sample # 2.

ASR curves for the samples from well B:

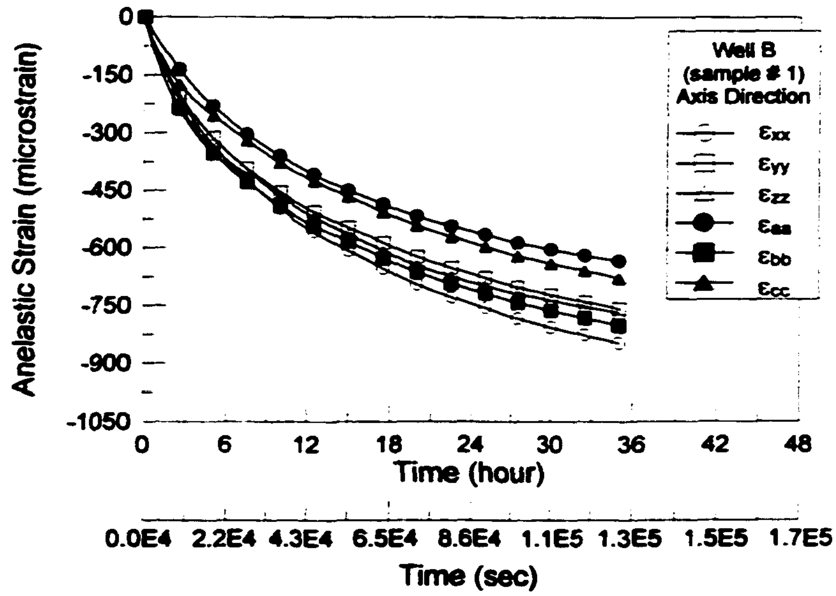

Figure C.4: Anelastic Strain Recovery for well B, sample # 1.

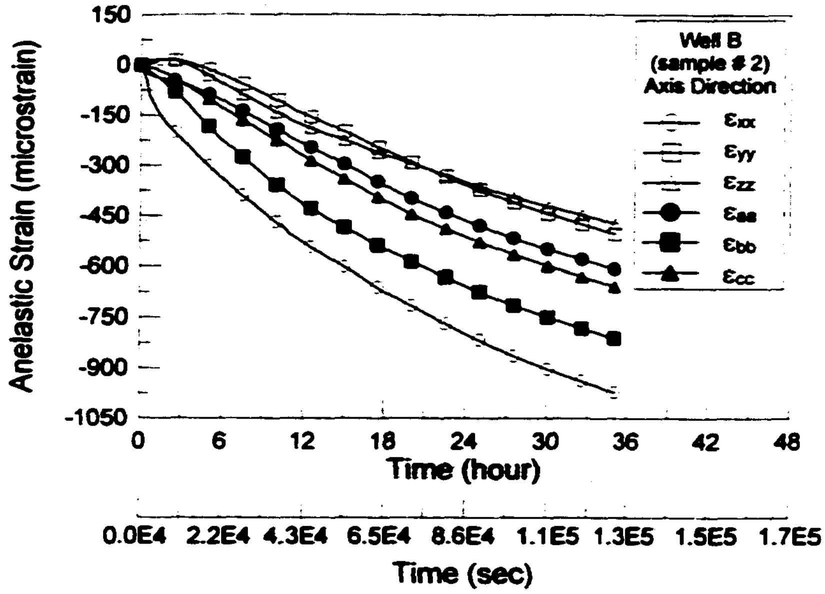

Figure C.5: Anelastic Strain Recovery for well B, sample # 2.

ASR curves for the samples from well C:

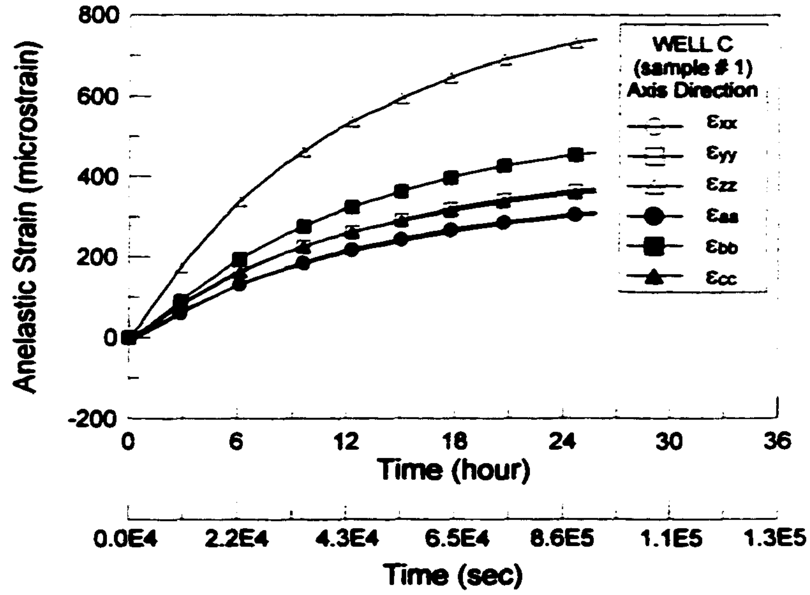

Figure C.6: Anelastic Strain Recovery for well C, sample # 1.

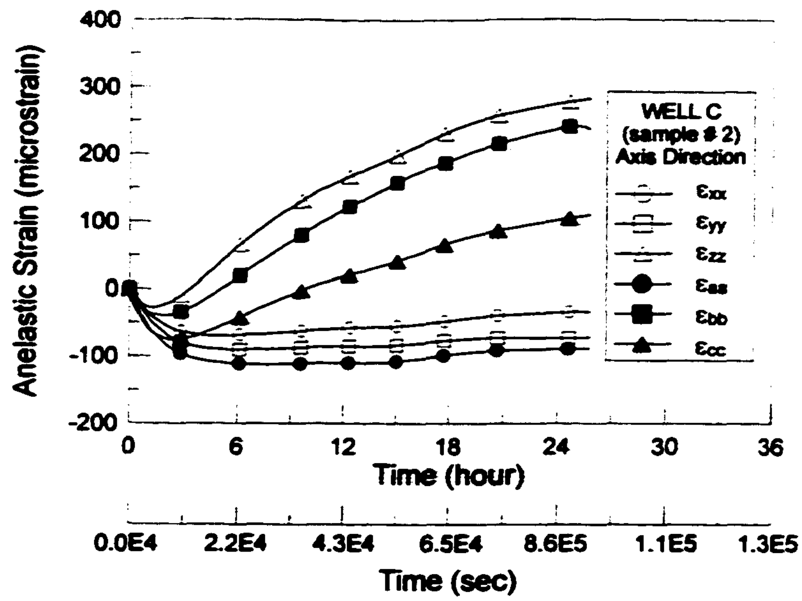

Figure C.7: Anelastic Strain Recovery for well C, sample # 2.

ASR curves for the samples from well D:

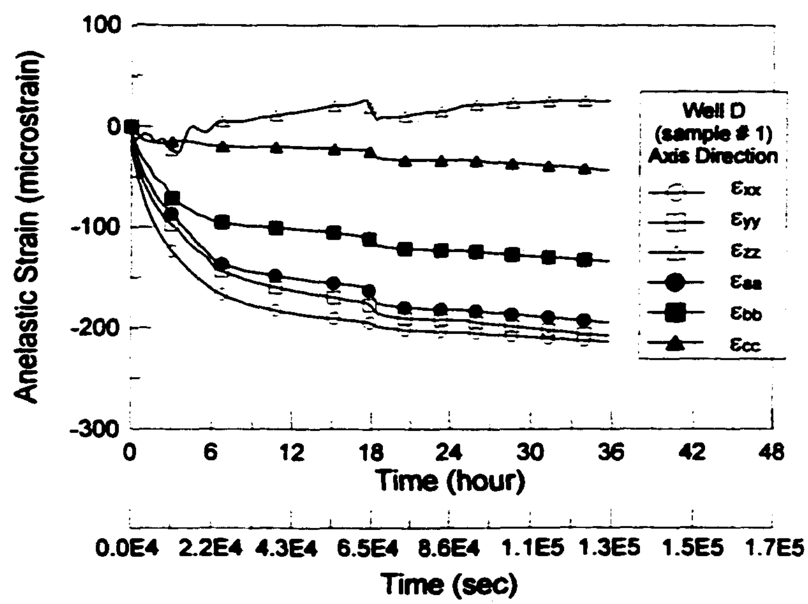

Figure C.8: Anelastic Strain Recovery for well D, sample # 1.

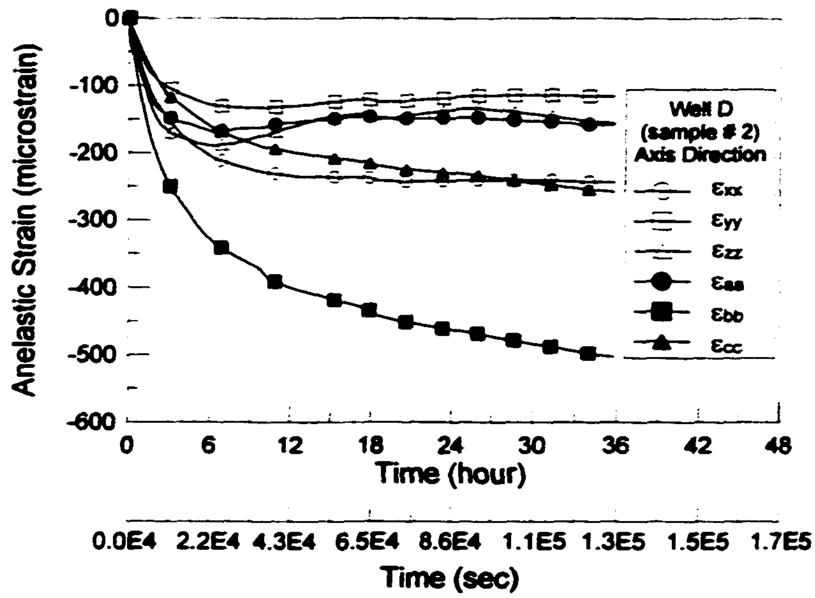

Figure C.9: Anelastic Strain Recovery for well D, sample # 2.

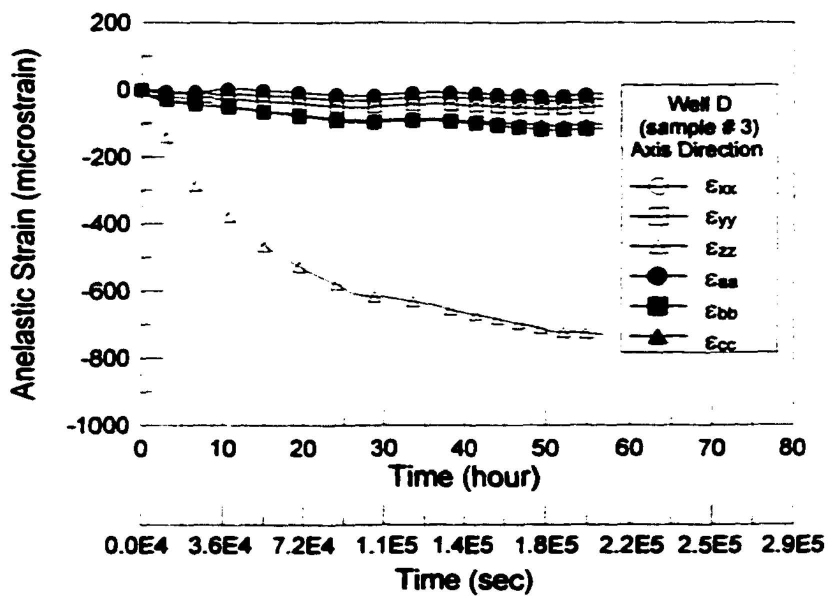

Figure C.10: Anelastic Strain Recovery for well D, sample # 3.

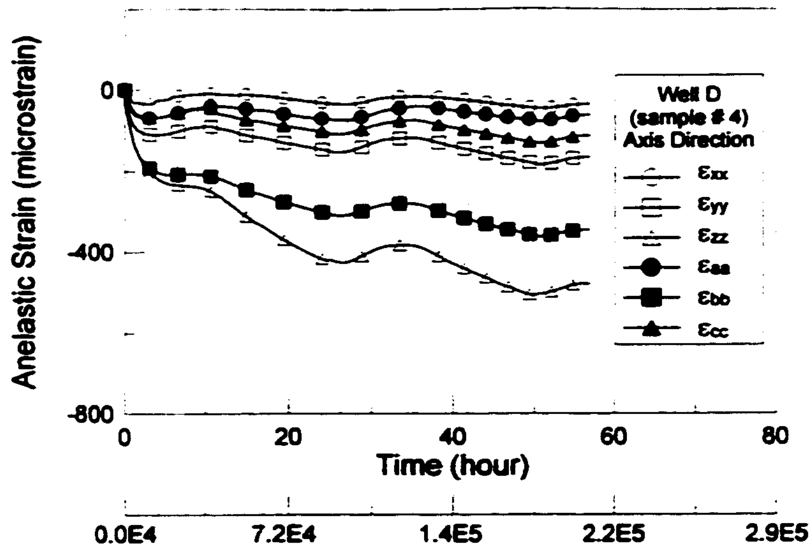

Figure C.11: Anelastic Strain Recovery for well D, sample # 4.

ASR curves for the samples from well E:

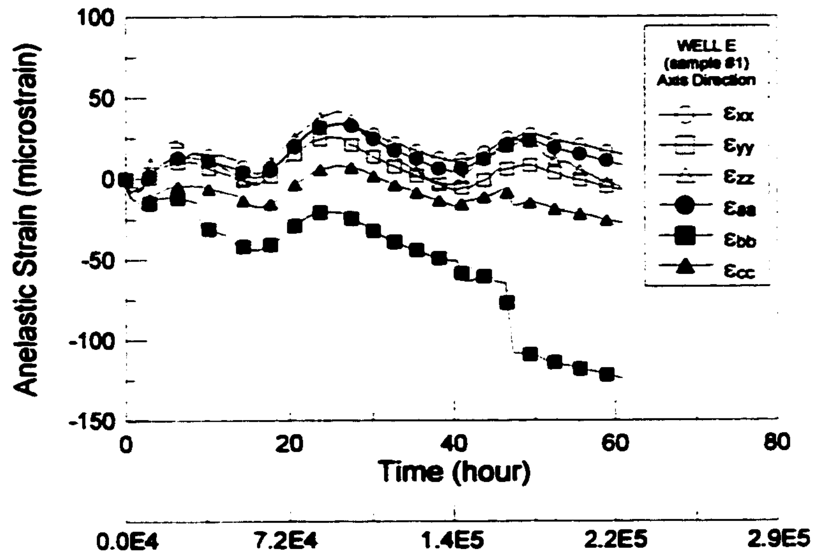

Figure C.12: Anelastic Strain Recovery for well E, sample # 1.

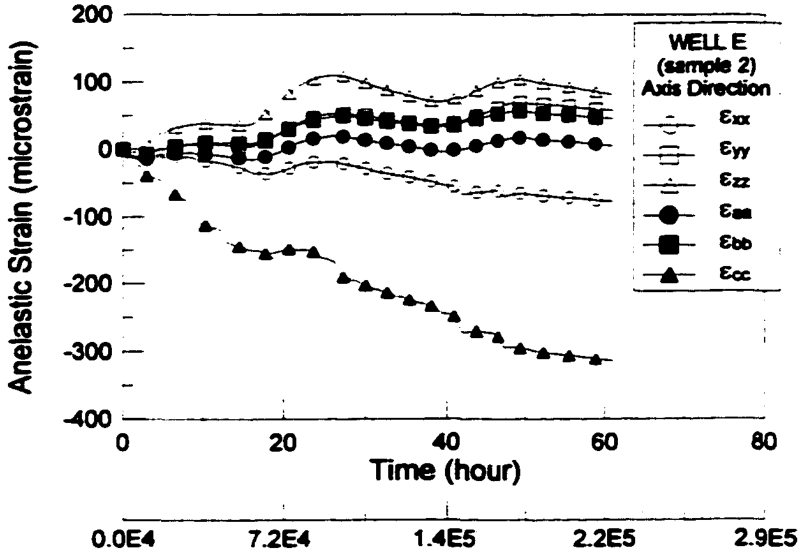

Figure C.13: Anelastic Strain Recovery for well E, sample # 2.

Appendix D

Brief Description of the Tested Samples

Macroscopic analyses were sufficient for checking on the sample's characteristics: the rock heterogeneity was clear for samples from wells D and E, while the others were considered homogeneous (Figures D.1 to D.10). This observation helped understand the differences in the stresses computed for samples cored just a few centimeters apart, in the same well.

The sandstones from wells A and B presented quartz, K-feldspars, clay minerals, calcite, dolomite and small amounts of plagioclase, pyrite and halite. The clay minerals detected by the DRX analysis were: smectite, irregular mixed-layers of illite-smectite (I/S) and caulinite. Petrographically speaking, the sandstones from these wells are medium-grained, well-sorted and without rock fragments, as shown from Figures D.1 to D.4. The main issue detected in the petrographical analyses was the high amount of interstitial clay, covering the grains or filling the intergranular spaces, which could be responsible for the rock contraction observed in the ASR tests.

The samples from wells D and E presented a fine-to-coarse grained sandstone with shale layers and conglomerates, showing also metamorphic rocks (Figures D.5 to D.10). The DRX test detected: quartz, clay minerals, plagioclasts, K-feldspars, dolomite and some pyrite, calcite and halite. A great amount of rock fragments (quartzite, gnaisse and mica-schist) were also found, indicating a highly heterogeneous rock type and explaining why the computed stresses were quite different in the samples from the same well, in these two cases.

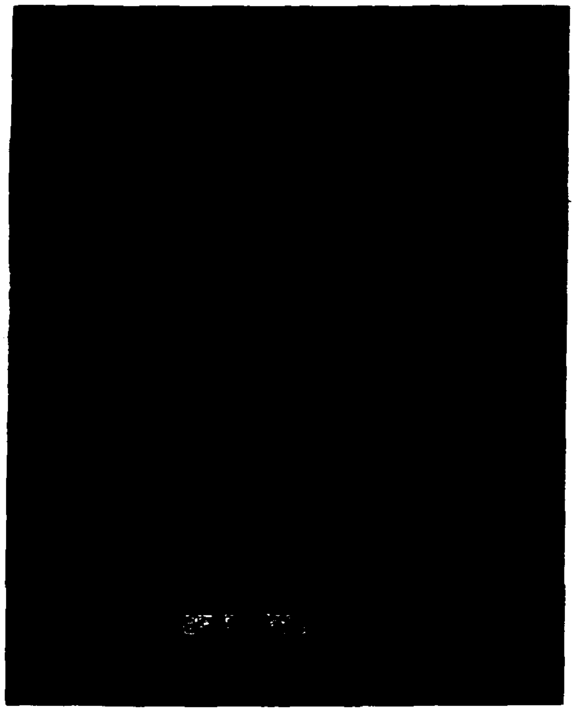

Figure D.1: Well A, sample # 1: gray sandstone, medium-grained, well-sorted.

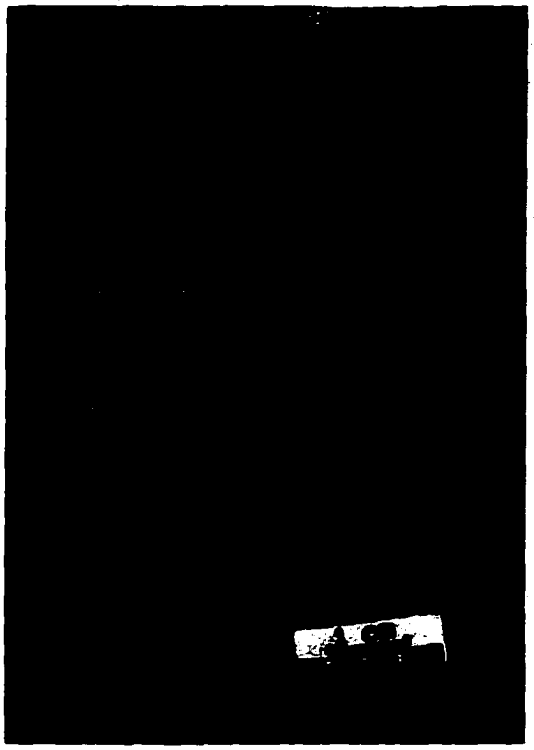

Figure D.2: Well A, sample # 2: once again a gray sandstone, medium-grained, well-sorted.

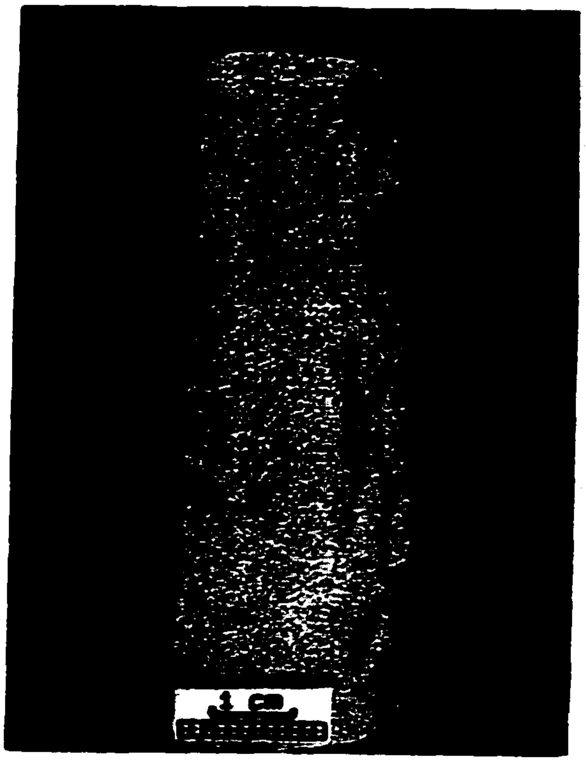

Figure D.3: Well B, sample # 1: also in this well the samples were classified as a gray sandstone, medium-grained, well-sorted.

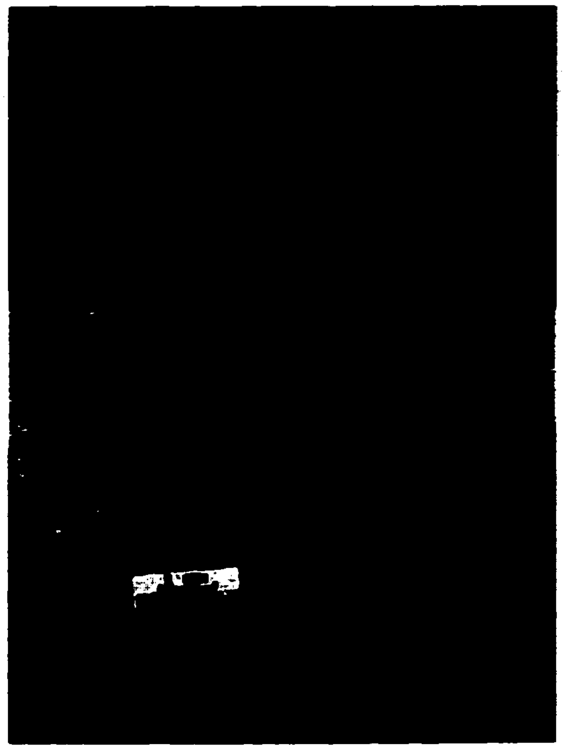

Figure D.4: Well B, sample # 2: once more a gray sandstone, medium-grained, well-sorted.

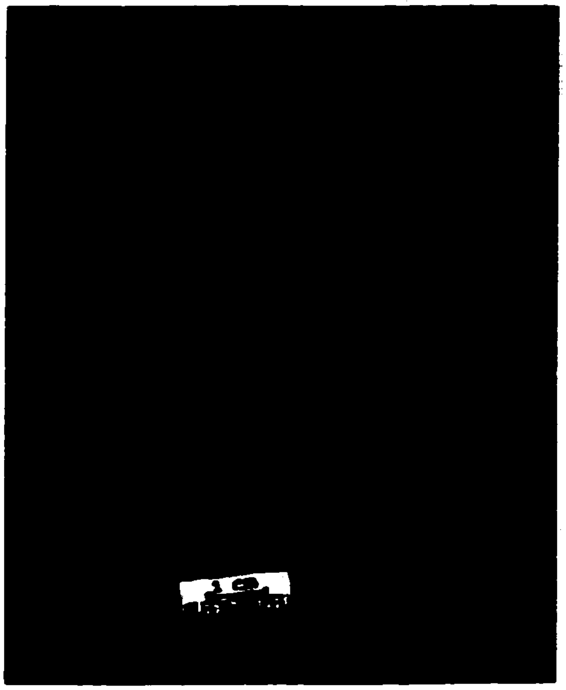

Figure D.5: Well D, sample # 1: a brownish sandstone, fine-grained, moderately well-sorted, rich in pelitic fragments.

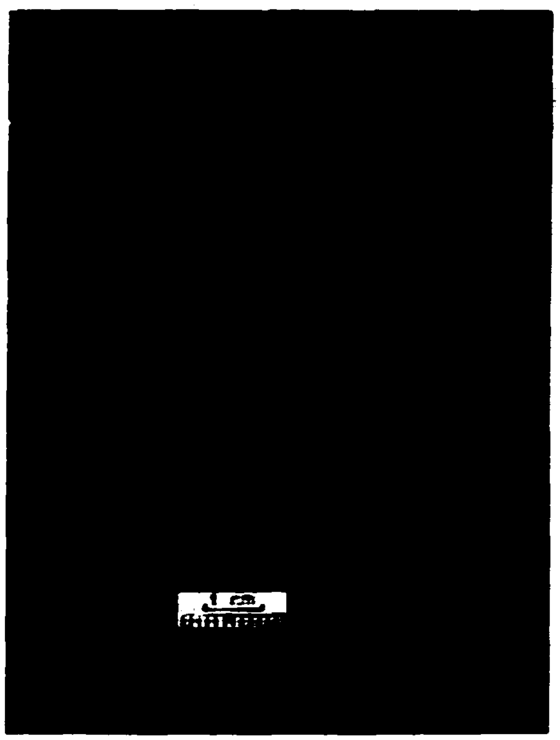

Figure D.6: Well D, sample # 2: a brownish sandstone, fine-to-medium grained, with shaly interlaminations, rich in pelitic fragments coarse sized.

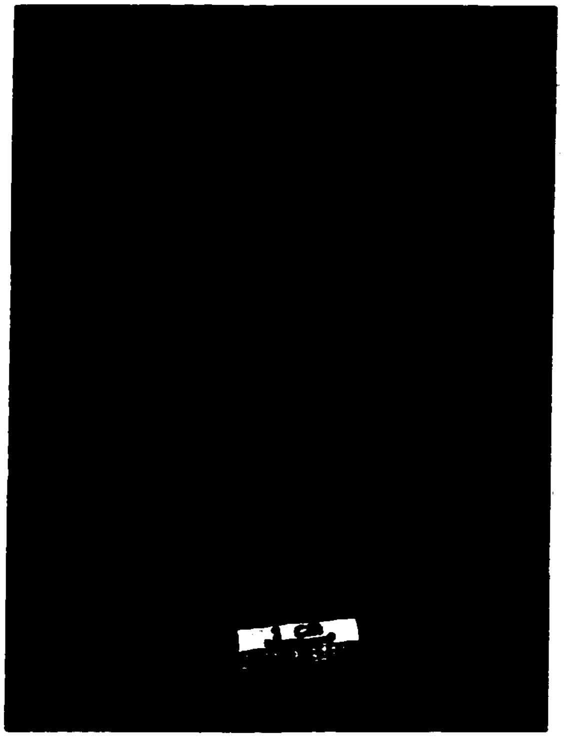

Figure D.7: Well D, sample # 3: a brownish sandstone, medium-to-fine grained with centimetric lens of pelitic fragments coarse sized.

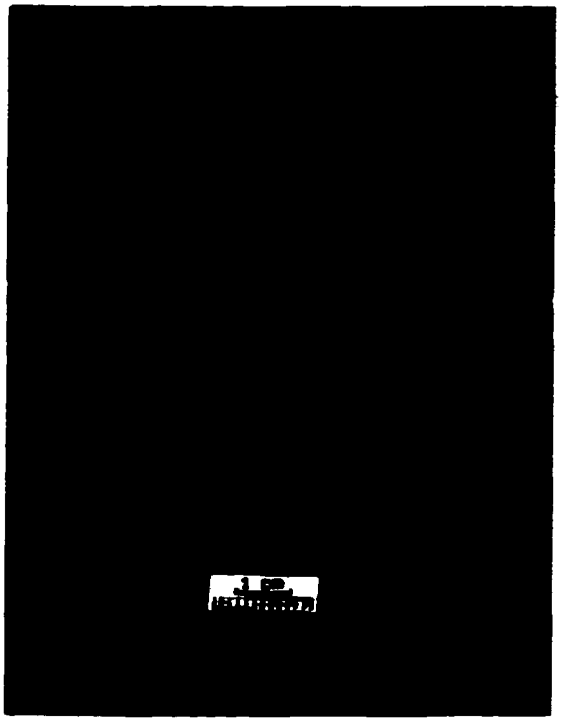

Figure D.8: Well D, sample # 4: this sample presents three different lithologies: A - shaly siltstone; B - fine grained sandstone with millimetric clay laminae; C - medium-grained sandstone with cross-beddings.

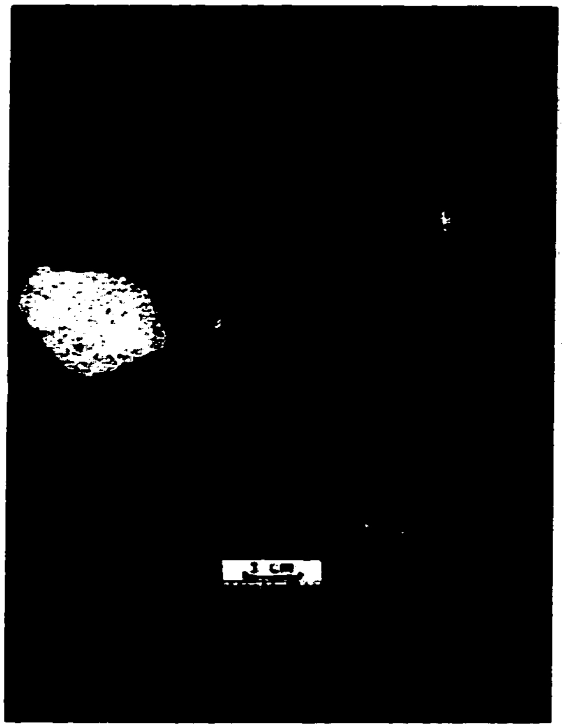

Figure D.9: Well E, sample # 1: a brownish conglomerate with 3 cm particles, fragments of metamorphic rocks, quartz, feldspar, mica and a coarse sand matrix .

Figure D.10: Well E, sample # 2: a brownish conglomerate with rounded particles (4.5 to 5 cm) partly cimented by dolomite, with fragments of metamorphic rocks, quartz, feldspar, mica and a coarse sand matrix .

Appendix E

Fortran Code

This appendix briefly shows how the Fortran code works. Basically, three independent horizontal anelastic strains (45^o apart), generated by ASR measurements, are input to the code (**ASR** file in the block diagram shown in Figure E.1). From these data, the principal horizontal strains are calculated (**PSTRASR**), as well as the hydrostatic and deviatoric strains (**STRASR**), fitted by a curve generated by the poroviscoelastic model (**EQUA** subfunction).

The input data for the model are the initial guesses (**GUESS**), and the rock constants including the field data (**CONST**). With the help of the simplex algorithm (**SIMPLEX** subroutine) the difference between the hydrostatic and deviatoric strains provided by the ASR, and the ones calculated by the model are minimized (**FUNK** subroutine). The results can be seen for each vertex of the simplex n-dimensional figure (**VERTC**), while the average value for each adjusted parameter is also available (**AVG**). The curve generated by the average values, i.e., the fitting curve, is stored in the file **DISPL**. Figure E.1 shows a scheme for the Fortran code.

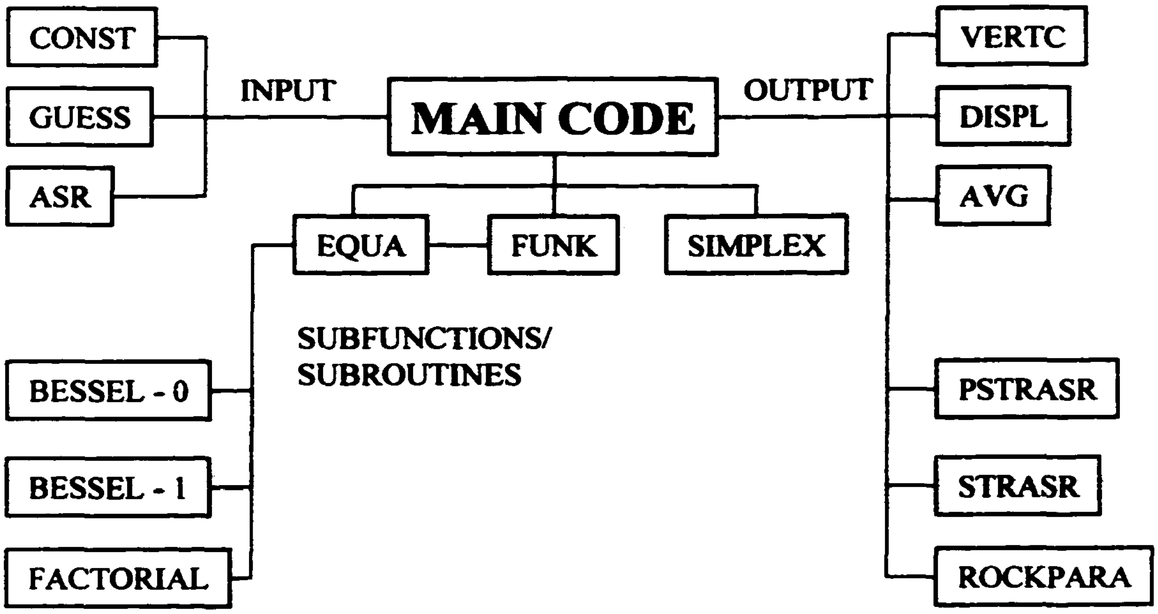

Figure E.1: Schematics for the Fortran code.

The input and output files can be detailed in the following way:

Input Files

ASR.DAT – This file inputs the horizontal strains measured in the field with the ASR device. The file is constituted by four columns and n-rows (where n is the number of time steps taken in the field test), having the time instant and the corresponding strains in three independent orientations (45^o apart): x, a and y, in the format shown in Table E.1.

Table E.1: Format for the ASR input data (3 first lines for sample # A-1 data).

time (*sec*)	ε_x ($\mu\varepsilon$)	ε_a ($\mu\varepsilon$)	ε_y ($\mu\varepsilon$)
44820.720	0.000E+00	0.000E+00	0.000E+00
45420.840	3.464E+00	1.178E+00	6.912E-001
46021.680	0.864E+00	3.060E+00	2.065E+000

CONST.DAT – The rock constants which are not taken as adjusting parameters are input in this file, together with the field conditions, as presented in Table

E.2.

Table E.2: CONST file for computing the synthetic hydrostatic example.

PARAMETER	DESCRIPTION	VALUE
PROBL	problem type (e.g., Mode I + II)	12
AK2	K_2	5.7 GPa
AMIK	μ_K	9.85E5 GPa
PZER	reservoir pressure, p_{res}	8.96 MPa
PDRI	drilling fluid pressure, p_{dri}	10.34 MPa
TREC	recovery time	10^4 sec
EXTR	core external radius	0.05 m
VISCO	fluid viscosity	20,000 Pa-sec
NLIN	number of lines in the original ASR file	100

GUESS.DAT – According to the desired number of adjusting parameters, n, this file has $n+1$ lines, e.g., the file corresponding to the synthetic example for the hydrostatic stress – guess file P10, (from Table B.10):

```
0.20 16. 0.5D5  5.7 171.2 40. 3.1 10.
0.40 26. 1.D5   5.7 171.2 40. 3.1 11.
0.60 36. 2.D5   5.7 171.2 40. 3.1 12.
0.80 46. 3.D5   5.7 171.2 40. 3.1 13.
1.00 56. 4.D5   5.7 171.2 40. 3.1 14.
1.00 66. 5.D5   5.7 171.2 40. 3.1 15.
1.50 76. 6.D5   5.7 171.2 40. 3.1 16.
2.00 86. 7.D5   5.7 171.2 40. 3.1 17.
2.50 96. 8.D5   5.7 171.2 40. 3.1 18.
```

Output Files

PSTRASR.DAT – Outputs the principal strains in the horizontal plane;

STRASR.DAT – Outputs the deviatoric and hydrostatic strains in the horizontal plane;

ROCKPARA.DAT - Outputs the input rock parameters as a check for the values read by the code;

VERTC.DAT – This file contains the final value for each adjusting rock parameter at each vertex of the n-dimensional Simplex figure at the moment the algorithm ends the iterative process (the global error becomes lower than the predefined tolerance), e.g., the file correspondent to the synthetic example P10[1]:

```
1.162          59.216    433643.058
5.700         171.200        40.000
3.100          14.321
2.698E-007                    313

1.162          59.216    433642.852
5.700         171.200        40.000
3.100          14.321
2.698E-007                    313

1.162          59.216    433643.495
5.700         171.200        40.000
3.100          14.321
2.698E-007                    313

1.162          59.216    433643.252
5.700         171.200        40.000
3.100          14.321
2.698E-007                    313

1.162          59.216    433643.517
5.700         171.200        40.000
3.100          14.321
2.698E-007                    313

1.162          59.216    433642.210
5.700         171.200        40.000
3.100          14.321
2.698E-007                    313

1.162          59.216    433644.416
5.700         171.200        40.000
3.100          14.321
2.698E-007                    313

1.162          59.216    433642.289
5.700         171.200        40.000
3.100          14.321
2.698E-007                    313

1.162          59.216    433643.187
5.700         171.200        40.000
3.100          14.321
2.698E-007                    313
```

[1]the data shown follows the exact output format from the Fortran code, corresponding to: E_1, E_2, μ_k, K, K_s, K_u, k, *error* and the number of iterations ($it = 313$). It should be noted that the error here is in *meters*, which converted to microstrains ($\mu\varepsilon$) is exactly 53.98 x 10^{-1}, as shown in Table 5.2.

AVG.DAT – The average values for the adjusted parameters in each vertex, the number of iterations and the global error are shown in this file, together with the computed in-situ stresses, e.g., the data for the P10 example, where the hydrostatic stress was computed as P = 14.32 MPa, after 313 iterations:

```
hydrostatic stress computation
     1.162          313
    59.216          313
433643.142          313
     5.700          313
   171.200          313
    40.000          313
     3.100          313
    14.321          313
     2.698E-007
```

DISPL – The instant time and the correspondent strain computed from the average adjusted parameters constitute this file, which will be used for plotting the fitting curve, e.g., the data used for plotting the curve for the P10-example (only the first 10 rows are shown below):

```
10000  482.582
11628  483.938
13256  484.677
14884  485.067
16512  485.266
18140  485.363
19768  485.406
21396  485.422
23024  485.424
24652  485.420
```

The main program is subdivided into 8 sections, all of them initiated by comments in the code, which are gathered by a few steps of the main routine, the subfunctions and subroutines, as shown below:

1 - INITIAL STEPS

1.1 - OPENING THE INPUT FILES

1.2 - OPENING THE OUTPUT FILES

1.2.1 - PRINCIPAL STRAINS, HYDROSTATIC AND DEVIATORIC STRAINS

4.4 - MODE III

5 - FACTORIAL COMPUTATION

6 - MODIFIED BESSEL FUNCTION OF THE FIRST KIND AND ORDER ZERO

7 - MODIFIED BESSEL FUNCTION OF THE FIRST KIND AND FIRST ORDER

8 - SIMPLEX SUBROUTINE

The complete Fortran code is shown below:

```
C      SIMPASR.FOR
C
       PROGRAM MAURO1
       IMPLICIT REAL *8(A-H,O-Z)
       DIMENSION T(1000),STX(1000),STA(1000),STY(1000),
      cSTXY(1000),ST1(1000),ST2(1000),str_P(1000),STR(1000),
      cstr_S(1000),X(9,8),C(9),X1(8),XA(9),XS(9),Y(9),
      cUFIN(1000),V(30)
       INTEGER I,K,B(30),J(30),N,M,IJ,NHLF
C
C      1 - INITIAL STEPS
C      1.1 - OPENING THE INPUT FILES
C
       OPEN (UNIT = 1,FILE='C:\CONST.DAT')
       OPEN (UNIT = 2,FILE='C:\GUESS.DAT')
       OPEN (UNIT = 11,FILE='C:\ASRDAT.DAT')
       READ (1,*)C(1),C(2),C(3),C(4),C(5),C(6),C(7),C(8),C(9)
       DO 1 I=1,9
       READ (2,*)X(I,1),X(I,2),X(I,3),
      c               X(I,4),X(I,5),X(I,6),X(I,7),X(I,8)
     1 CONTINUE
       TYPE=C(1)
C
C      1.1 - OPENING THE OUTPUT FILES
C      1.1.1 - PRINCIPAL STRAINS, HYDROSTATIC AND DEVIATORIC
C              STRAINS AND CHECK ON THE ROCK PARAMETERS
C
       OPEN (UNIT = 33,FILE='C:\ PSTRASR. DAT ')
       OPEN (UNIT = 44,FILE='C:\STRASR. DAT ')
       OPEN (UNIT = 55,FILE='C:\ ROCKPARA.DAT')
C
       WRITE (55,*)C(1),C(2),C(3),C(4),C(5),C(6),C(7),C(8),C(9)
       DO 12 I=1,9
       WRITE(55,*)X(I,1),X(I,2),X(I,3),
      c           X(I,4),X(I,5),X(I,6),X(I,7),X(I,8)
    12 CONTINUE
```

```
C
C     1.1.2 - RESULTS
C
      OPEN (UNIT = 6,FILE='C:\ VERTC.DAT')
      OPEN (UNIT = 7,FILE='C:\ DISPL.DAT')
      OPEN (UNIT = 8,FILE='C:\AVG.DAT')
C
C     1.2 - COMPUTING STRAINS FROM THE ASR
C           (INITIAL TIME T(1) = RECOVERY + PREPARATION)
C
      DO 2 I=1,C(9)
      READ (11,*)T(I),STX(I),STA(I),STY(I)
      STXY(I)=(STX(I)-2.*STA(I)+STY(I))/2.
      ST1(I)=(STX(I)+STY(I))/2.+SQRT(STXY(I)**2+
     c       ((STX(I)-STY(I))/2.)**2)
      ST2(I)=(STX(I)+STY(I))/2.-SQRT(STXY(I)**2+
     c       ((STX(I)-STY(I))/2.)**2)
      str_P(I)=((ST1(I)+ST2(I))/2.)
      str_S(I)=((ST1(I)-ST2(I))/2.)
      WRITE (33,*)T(I),ST1(I),ST2(I)
      WRITE (44,*)T(I),str_P(I),str_S(I)
      IF (TYPE.EQ.12.)THEN
      STR(I)=str_P(I)
      ELSE
      STR(I)=str_S(I)
      END IF
    2 CONTINUE
C
C     2 - APPLYING THE SIMPLEX METHOD
C         TO THE OBJECTIVE FUNCTION
C
      DO 4 I=1,9
      DO 3 J1=1,8
      X1(J1)=X(I,J1)
    3 CONTINUE
      Y(I)=FUNK(X1,C,STR,T)
    4 CONTINUE
      CALL simplex(X,Y,9,8,8,1.D-4,it,C,STR,T)
C
C     2.1 - PRINTING THE FINAL PARAMETERS
C           AND ERROR FOR THE CURVE-FITTING
C
      YS=0.0
      DO 15 I=1,9
      WRITE(6,*)X(I,1),X(I,2),X(I,3),X(I,4),X(I,5),
     c          X(I,6),X(I,7),X(I,8)
      WRITE(6,*)Y(I),it
      YS=YS+Y(I)
   15 CONTINUE
      IF (C(1).EQ.12.)THEN
      WRITE (*,*) ''hidrostatic stress computation''
      ELSE
```

```
      WRITE (*,*) ''deviatoric stress computation''
      END IF
      DO 17 JA=1,8
      XS(JA)=0.
      DO 16 I=1,9
      XS(JA)=X(I,JA)+XS(JA)
   16 CONTINUE
      XA(JA)=XS(JA)/9.
      WRITE (*,*) XA(JA),it
      WRITE (8,*) XA(JA),it
   17 CONTINUE
      WRITE (*,*) YS/9.
      WRITE (8,*) YS/9.
C
C     2.2 - PLOTTING THE CURVE FROM THE MODEL
C
      AE1    = XA(1)
      AE2    = XA(2)
      AMIE   = XA(3)
      AK1    = XA(4)
      AKS    = XA(5)
      AKU    = XA(6)
      PERM   = XA(7)
      PLOAD  = XA(8)
      PROBL  = C(1)
      AK2    = C(2)
      AMIK   = C(3)
      PZER   = C(4)
      PDRI   = C(5)
      TREC   = C(6)
      EXTR   = C(7)
      VISCO  = C(8)
      NLIN   = C(9)
      OGN=LOG(2.)
      N=8
      NHLF=N/2
      DO 19 I=1,N
      SOMA=0.0
      CREAL=(I+1)/2
      B(I)=AINT(CREAL)
      J(I)=MIN(I,NHLF)
      DO 18 K=B(I),J(I)
      SOMA=SOMA+(((K**NHLF)*FAC(2*K))/(FAC(NHLF-K)*FAC(K)*
     cFAC(K-1)*FAC(I-K)*FAC(2*K-I)))
   18 CONTINUE
      V(I)=(-1)**(I+NHLF)*SOMA
   19 CONTINUE
      DO 41 IJ=1,NLIN
      SOMAT=0.0
      TIN=T(IJ)
      DO 31 M=1,N
      VAR=M*(OGN/TIN)
```

```
      SOMAT=(V(M)*(EQUA(VAR,AE1,AK1,AKS,PERM,VISCO,EXTR,PROBL,
     c              PZER,TREC,PLOAD,PDRI,AK2,AMIK,AE2,AMIE,AKU))
     c        +SOMAT
   31 CONTINUE
      UFIN(IJ)=((OGN/TIN)*SOMAT)
      WRITE (7,*)TIN,UFIN(IJ)-UFIN(1)
   41 CONTINUE
      STOP
      END
C
C     3 - OBJECTIVE FUNCTION (GLOBAL ERROR COMPUTATION)
C
      DOUBLE PRECISION FUNCTION FUNK(VX,VC,VASR,T)
      IMPLICIT REAL *8(A-H,O-Z)
      DIMENSION VX(8),VC(9),VASR(1000),UMOD(1000),T(1000),V(30)
      INTEGER B(30),J(30)
      AE1    = VX(1)
      AE2    = VX(2)
      AMIE   = VX(3)
      AK1    = VX(4)
      AKS    = VX(5)
      AKU    = VX(6)
      PERM  = VX(7)
      PLOAD = VX(8)
      PROBL = VC(1)
      AK2    = VC(2)
      AMIK   = VC(3)
      PZER  = VC(4)
      PDRI  = VC(5)
      TREC  = VC(6)
      EXTR  = VC(7)
      VISCO = VC(8)
      NLIN  = VC(9)
      ERRO=0.
      OGN=LOG(2.)
      N=8
      NHLF=N/2
      DO 20 I=1,N
      SOMA=0.0
      CREAL=(I+1)/2
      B(I)=AINT(CREAL)
      J(I)=MIN(I,NHLF)
      DO 10 K=B(I),J(I)
      SOMA=SOMA+(((K**NHLF)*FAC(2*K))/(FAC(NHLF-K)*FAC(K)*
     cFAC(K-1)*FAC(I-K)*FAC(2*K-I)))
   10 CONTINUE
      V(I)=(-1)**(I+NHLF)*SOMA
   20 CONTINUE
      DO 40 IJ=1,NLIN
      SOMAT=0.0
      TIN=T(IJ)
      DO 30 M=1,N
```

```
         VAR=M*(OGN/TIN)
         SOMAT=(V(M)*(EQUA(VAR,AE1,AK1,AKS,PERM,VISCO,EXTR,PROBL,
        c            PZER,TREC,PLOAD,PDRI,AK2,AMIK,AE2,AMIE,AKU))
        c       +SOMAT
         IF (SOMAT .EQ. 0.0) THEN
         ERRO=1.E30
         GOTO 45
         END IF
      30 CONTINUE
         UMOD(IJ)=((OGN/TIN)*SOMAT)
         ERRO=ERRO+ABS(UMOD(IJ)-UMOD(1)-VASR(IJ))
      40 CONTINUE
      45 FUNK = ERRO
         END
C
C    4 - LAPLACE DOMAIN EQUATIONS - THE POROVISCOELASTIC MODEL
C
     DOUBLE PRECISION FUNCTION EQUA(S,Y1,BK1,BKG1,PE,VI,A,P,
    c                              PPIN,RECT,STIN,DRIP,BK2,
    c                              VISK,Y2,VISY,UK1)
     IMPLICIT REAL *8(A-H,O-Z)
C
C     4.1 - COMPUTATION OF THE POROELASTIC PARAMETERS
C
C     4.1.1 - TIME-DEPENDENT BULK MODULUS (BULK)
C
C     BULK=BK1*(1.+(VISK/BK2)*S)/((1.+BK1/BK2)+(VISK/BK2)*S)
      BULK=BK1
      IF (BULK.LE.0.0) THEN
      EQUA=0.0
      GOTO 5
      END IF
C
C     4.1.2 - TIME-DEPENDENT YOUNG'S MODULUS (Y)
C
      Y=Y1*(1.+(VISY/Y2)*S)/((1.+Y1/Y2)+(VISY/Y2)*S)
C     Y=Y1
      IF (Y1.LE.0.0) THEN
      EQUA=0.0
      GOTO 5
      END IF
      reKY  = 3.*BULK-Y
      IF (reKY .LE. 0.0) THEN
      EQUA=0.0
      GOTO 5
      END IF
C
C     4.1.3 - TIME-DEPENDENT GRAIN BULK MODULUS (BG)
C
C     BG=BKG1*(1.+(VIKG/BKG2)*S)/((1.+BKG1/BKG2)+(VIKG/BKG2)*S)
      BG=BKG1
      reKKS = BG - BULK
```

```
      IF (rekks .LE. 0.0) THEN
      EQUA=0.0
      GOTO 5
      END IF
C
C     4.1.4 - TIME-DEPENDENT UNDRAINED BULK MODULUS (UK)
C
C     UK=UK1*(1.+(VIUK/UK2)*S)/((1.+UK1/UK2)+(VIUK/UK2)*S)
      UK=UK1
      IF (UK1.LE.0.0) THEN
      EQUA=0.0
      GOTO 5
      END IF
C
C     4.1.5 - SHEAR MODULUS (G)
C
      G=(3.*BULK*Y)/(9.*BULK-Y)
      IF (G.LE.0.0) THEN
      EQUA=0.0
      GOTO 5
      END IF
C
C     4.1.6 - POISSON'S RATIO (PS)
C
      PS=(3.*BULK-Y)/(6.*BULK)
      IF (PS.LT.0.0) THEN
      EQUA=0.0
      GOTO 5
      END IF
      IF (PS.GT.0.5) THEN
      EQUA=0.0
      GOTO 5
      END IF
C
C     4.1.7 - BIOT'S COEFFICIENT (ALFA)
C
      ALFA=1.-(BULK/BG)
      IF (ALFA.LT.0.0) THEN
      EQUA=0.0
      GOTO 5
      END IF
C
C     4.1.8 - UNDRAINED POISSON RATIO (UP)
C
      UP=(3.*UK-2.*G)/(2.*(3.*UK+G))
      IF (UP .GT. 0.5 .or. UP .LE. PS) THEN
      EQUA=0.0
      GOTO 5
      END IF
C
C     4.1.9 - SKEMPTOM B-PARAMETER (SKEMB)
C
```

```
      SKEMB=(3.*(UP-PS))/(ALFA*(1.-2.*PS)*(1.+UP))
C
C     4.1.10 - POROELASTIC STRESS COEFFICIENT (E)
C
      E=(ALFA*(1.-2.*PS))/(2.*(1.-PS))
C
C     4.1.11 - BIOT'S MODULUS (BM)
C
      BM=2.*G*(UP-PS)/(ALFA**2*(1.-2.*UP)*(1.-2.*PS))
C
C     4.1.12 - DIFFUSIVITY COEFFICIENT (DIFC)
C              (PE is in md, VI is in PA.sec and G is in GPa)
C
      DIFC=(1.E-6*2.*(PE/VI)*G*(1.-PS)*(UP-PS))/
     c((ALFA**2)*((1.-2.*PS)**2)*(1.-UP))
      IF (DIFC.LE.0.0) THEN
      EQUA=0.0
      GOTO 5
      END IF
C
C     4.2 - TYPICAL ARGUMENTS
C
      QSI=A*SQRT(S/DIFC)
      BETA=QSI
      D3=((1.-PS)*BESSI0(BETA)-2.*(UP-PS)*BESSI1(BETA)/BETA)
      D4=((1.-2.*UP)*(1.-PS)*BESSI0(BETA))+
     c2.*((UP-PS)*(BESSI1(QSI)/QSI))
      D5=2.*E*(1.-PS)*(((1.-2.*UP)*BESSI1(BETA)/BETA)+
     c(BESSI1(QSI)/QSI))
C
C     4.3 - RADIAL DISPLACEMENT IN MODES I AND II COMBINED
C           (STIN, PPIN and DRIP are in MPa, G is in GPa
C            and since A is in m, EQUA is also in m)
C
      IF(P.eq.12.) THEN
      TFAC=(DRIP/S)*(((1.-EXP(-RECT*S))/(RECT*S))-1.)
      STIL=TFAC+STIN/S
      PTIL=TFAC+PPIN/S
C
C     EQUA FOR COMPUTING DISPLACEMENTS:
C
C     EQUA=(STIL*D4-PTIL*D5)*1.E-3*A/(2.*G*D3)
C
C     EQUA FOR COMPUTING MICROSTRAINS:
C            (delta A/A)*1E6
C
      EQUA=(STIL*D4-PTIL*D5)*(1.E+3)/(2.*G*D3)
      END IF
C
C     4.4 - Mode III
C
C
```

```
      IF(P.eq.3.) THEN
      TFAC=DRIP/S*(((1.-EXP(-RECT*S))/(RECT*S))-1.)
      STIL=TFAC+STIN/S
C
C     EQUA FOR COMPUTING DISPLACEMENTS:
C
C     EQUA=STIL*1.E-3*A/(2.*G)
C
C     EQUA FOR COMPUTING MICROSTRAINS:
C             (delta A/A)*1E6
C
      EQUA=STIL*(1.E+3)/(2.*G)
      END IF
5     END
C
C     5 - FACTORIAL COMPUTATION
C     DOUBLE PRECISION FUNCTION FAC(I)
      IMPLICIT REAL *8(A-H,O-Z)
      FAC=1.0
      IF(I.LE.1)RETURN
      DO 10 J=2,I
      FAC=FAC*J
10    CONTINUE
      END
C
C     6 - MODIFIED BESSEL FUNCTION OF
C         THE FIRST KIND AND ORDER ZERO
C
      DOUBLE PRECISION FUNCTION BESSI0(X)
      IMPLICIT REAL *8(A-H,O-Z)
      DATA P1,P2,P3,P4,P5,P6,P7/1.0D0,3.5156229D0,3.0899424D0,
     c1.2067492D0,0.2659732D0,0.360768D-1,0.45813D-2/
      DATA Q1,Q2,Q3,Q4,Q5,Q6,Q7,Q8,Q9/0.39894228D0,0.1328592D-1,
     c0.225319D-2,-0.157565D-2,0.916281D-2,-0.2057706D-1,
     c0.2635537D-1,-0.1647633D-1,0.392377D-2/
      IF (ABS(X).LT.3.75) THEN
      Y=(X/3.75)**2
      BESSI0=P1+Y*(P2+Y*(P3+Y*(P4+Y*(P5+Y*(P6+Y*P7)))))
      ELSE
      AX=ABS(X)
      Y=3.75/AX
      BESSI0=(EXP(AX)/SQRT(AX))*(Q1+Y*(Q2+Y*(Q3+Y*(Q4+Y*
     c(Q5+Y*(Q6+Y*(Q7+Y*(Q8+Y*Q9))))))))
      ENDIF
      END
C
C     7 - MODIFIED BESSEL FUNCTION OF
C         THE FIRST KIND AND FIRST ORDER
C
      DOUBLE PRECISION FUNCTION BESSI1(X)
      IMPLICIT REAL *8(A-H,O-Z)
      DATA P1,P2,P3,P4,P5,P6,P7/0.5D0,0.87890594D0,0.51498869D0,
```

```
     c0.15084934D0,0.2658733D-1,0.301532D-2,0.32411D-3/
      DATA Q1,Q2,Q3,Q4,Q5,Q6,Q7,Q8,Q9/0.39894228D0,-0.3988024D-1,
     c-0.362018D-2,0.163801D-2,-0.1031555D-1,0.2282967D-1,
     c-0.2895312D-1,0.1787654D-1,-0.420059D-2/
      IF (ABS(X).LT.3.75) THEN
      Y=(X/3.75)**2
      BESSI1=X*(P1+Y*(P2+Y*(P3+Y*(P4+Y*(P5+Y*(P6+Y*P7))))))
      ELSE
      AX=ABS(X)
      Y=3.75/AX
      BESSI1=(EXP(AX)/SQRT(AX))*(Q1+Y*(Q2+Y*(Q3+Y*(Q4+Y*
     c(Q5+Y*(Q6+Y*(Q7+Y*(Q8+Y*Q9))))))))
      IF (X.LT.0.)BESSI1=-BESSI1
      END IF
      END
C
C     8 - SIMPLEX SUBROUTINE
C
      SUBROUTINE simplex(p,y,mp,np,ndim,ftol,iter,vc,vasr,t)
      IMPLICIT REAL *8(A-H,O-Z)
      DOUBLE PRECISION funk,ftol,rtol,sum,swap,ysave,ytry,amotry
      INTEGER iter,mp,ndim,np,NMAX,ITMAX
      PARAMETER (NMAX=8,ITMAX=1000)
      DIMENSION p(mp,np),y(mp),vc(9),vasr(1000),t(1000),psum(NMAX),
     cpold(mp,np),yold(mp)
      INTEGER i,ihi,ilo,inhi,j,m,n
      pold = p
      yold = y
      ICONT=0
      A=1.0
      ERROn=1.E-6
      iter=0
    1 do 12 n=1,ndim
      sum=0.
      do 11 m=1,ndim+1
      sum=sum+p(m,n)
   11 continue
      psum(n)=sum
   12 continue
    2 ilo=1
      if (y(1).gt.y(2)) then
      ihi=1
      inhi=2
      else
      ihi=2
      inhi=1
      endif
      do 13 i=1,ndim+1
      if(y(i).le.y(ilo)) ilo=i
      if(y(i).gt.y(ihi)) then
      inhi=ihi
      ihi=i
```

```
      else if(y(i).gt.y(inhi)) then
      if(i.ne.ihi) inhi=i
      endif
   13 continue
      rtol=2.*abs(y(ihi)-y(ilo))/(abs(y(ihi))+abs(y(ilo)))
C     rtol=abs(y(ihi)-y(ilo))
C     rtol=abs(y(ihi))
      EMAX=y(ihi)
      if (rtol.lt.ERROn) then
      swap=y(1)
      y(1)=y(ilo)
      y(ilo)=swap
      do 14 n=1,ndim
      swap=p(1,n)
      p(1,n)=p(ilo,n)
      p(ilo,n)=swap
   14 continue
C
C     CHANGE IN THE SIMPLEX COEFFICIENTS
C     FOR ESCAPING LOCAL MINIMA PROBLEMS
C
C     if (EMAX.GT.ERROn) then
C     A=A*1.5
C     ICONT=ICONT+1
C     y=yold
C     p=pold
C     WRITE (*,*) 'ICONT,ITER =', ICONT, iter
C     WRITE (*,*) 'ERRO MAX,A     =              ', EMAX,A
C     iter=0
C     pause
C     else
C     return
C     endif
      endif
      if (iter.ge.ITMAX) then
      write(*,*) ''ITMAX exceeded in simplex''
      write(*,*) 'rtol=',rtol
      return
      end if
      iter=iter+2
      AA=-1.*A
      AB=2.*A
      AC=0.5/A
      ytry=amotry(p,y,psum,mp,np,ndim,ihi,AA,vc,vasr,t)
      if (ytry.le.y(ilo)) then
      ytry=amotry(p,y,psum,mp,np,ndim,ihi,AB,vc,vasr,t)
      else if (ytry.ge.y(inhi)) then
      ysave=y(ihi)
      ytry=amotry(p,y,psum,mp,np,ndim,ihi,AC,vc,vasr,t)
      if (ytry.ge.ysave) then
      do 16 i=1,ndim+1
      if(i.ne.ilo)then
```

```
      do 15 j=1,ndim
      psum(j)=0.5*(p(i,j)+p(ilo,j))
      p(i,j)=psum(j)
   15 continue
      y(i)=funk(psum,vc,vasr,t)
      endif
   16 continue
      iter=iter+ndim
      goto 1
      endif
      else
      iter=iter-1
      endif
      goto 2
      END
      DOUBLE PRECISION FUNCTION amotry(p,y,psum,mp,np,ndim,ihi,fac,
     cvc,vasr,t)
      IMPLICIT REAL *8(A-H,O-Z)
      INTEGER ihi,mp,ndim,np,NMAX
      DOUBLE PRECISION fac,funk,fac1,fac2,ytry
      PARAMETER (NMAX=8)
      DIMENSION p(mp,np),psum(np),y(mp),vc(9),vasr(1000),
     ct(1000),ptry(NMAX)
      INTEGER j
      fac1=(1.-fac)/ndim
      fac2=fac1-fac
      do 11 j=1,ndim
      ptry(j)=psum(j)*fac1-p(ihi,j)*fac2
   11 continue
      ytry=funk(ptry,vc,vasr,t)
      if (ytry.lt.y(ihi)) then
      y(ihi)=ytry
      do 12 j=1,ndim
      psum(j)=psum(j)-p(ihi,j)+ptry(j)
      p(ihi,j)=ptry(j)
   12 continue
      endif
      amotry=ytry
      return
      END
```

Appendix F

Experimental Results

F.1 Uniaxial Compression Tests

Figures F.1 to F.9 show the experimental and the corrected stress-strain curves. Since the displacement used for computing the axial strain was not measured directly on the rock sample, but on the actuator of the testing equipment, the measured values include the displacement of all the equipment parts involved the compression process. In order to isolate the rock axial strain from the total measured strain, the testing system was calibrated (the calibration method is shown in Appendix G), allowing the computation of the actual rock axial strain.

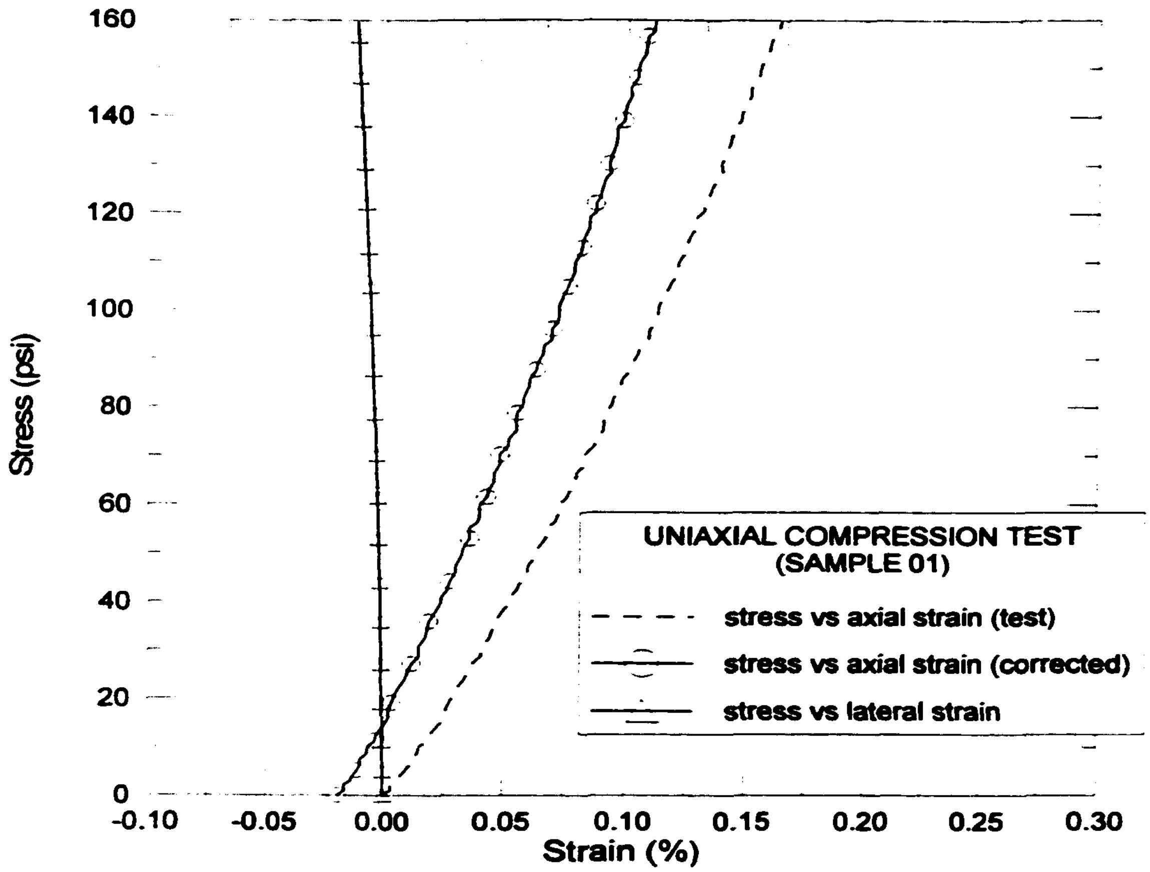

Figure F.1: Stress-strain curves for the uniaxial compression test of sample 01.

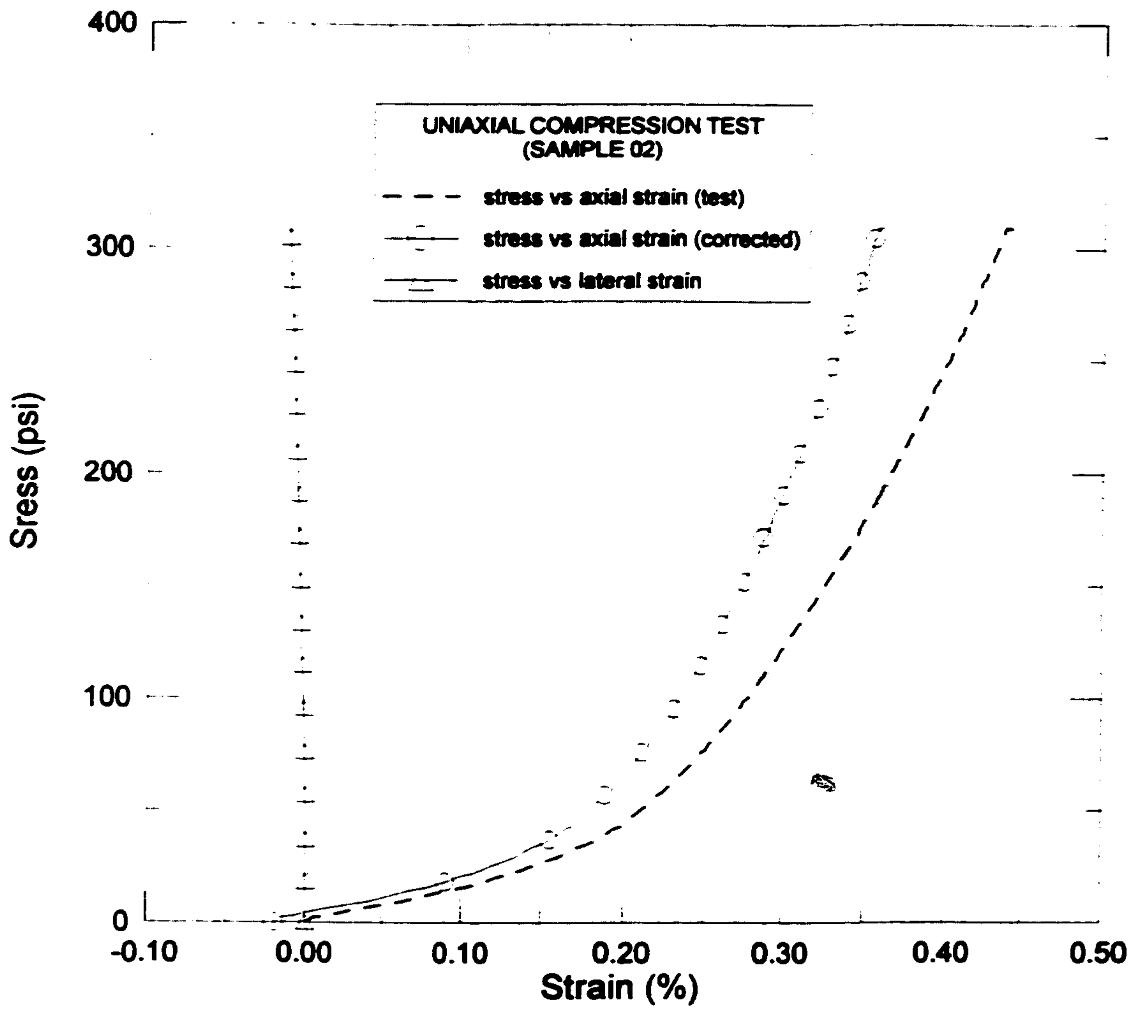

Figure F.2: Stress-strain curves for the uniaxial compression test of sample 02.

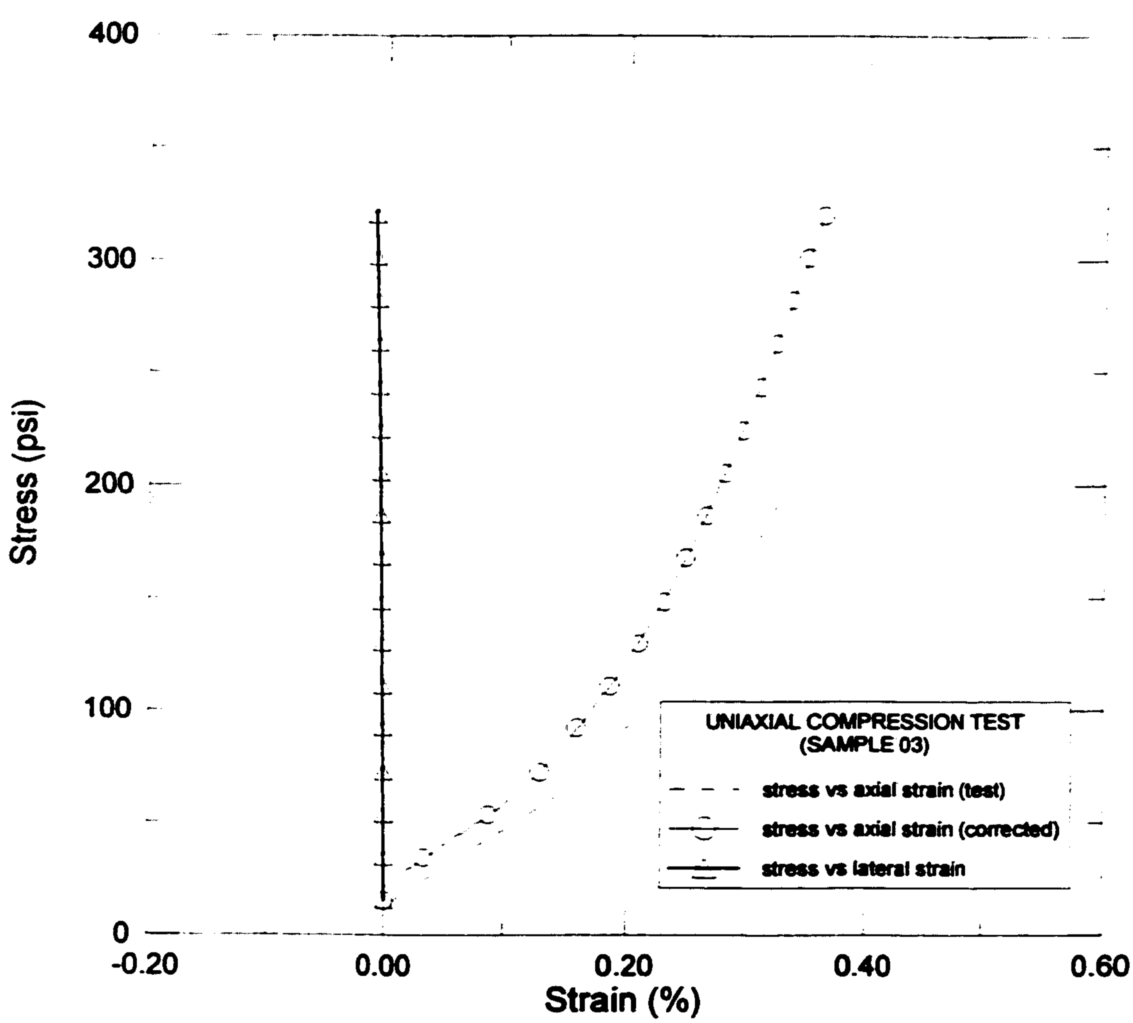

Figure F.3: Stress-strain curves for the uniaxial compression test of sample 03.

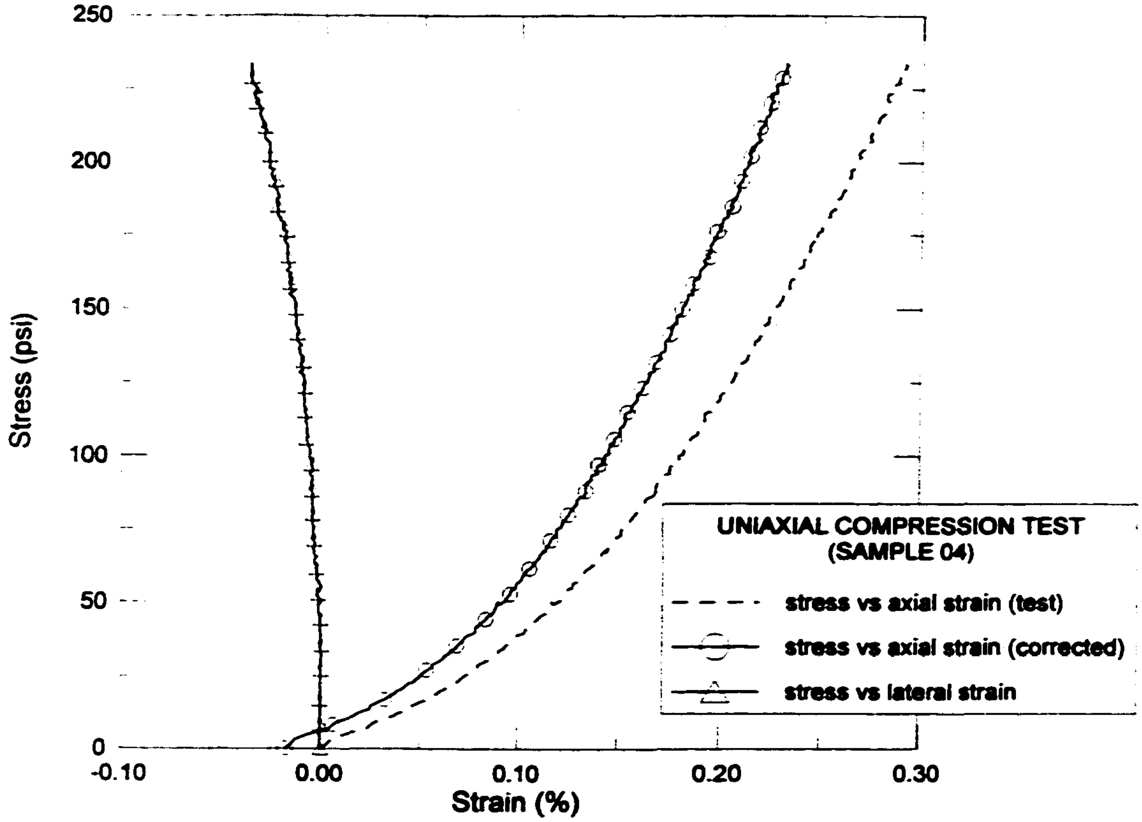

Figure F.4: Stress-strain curves for the uniaxial compression test of sample 04.

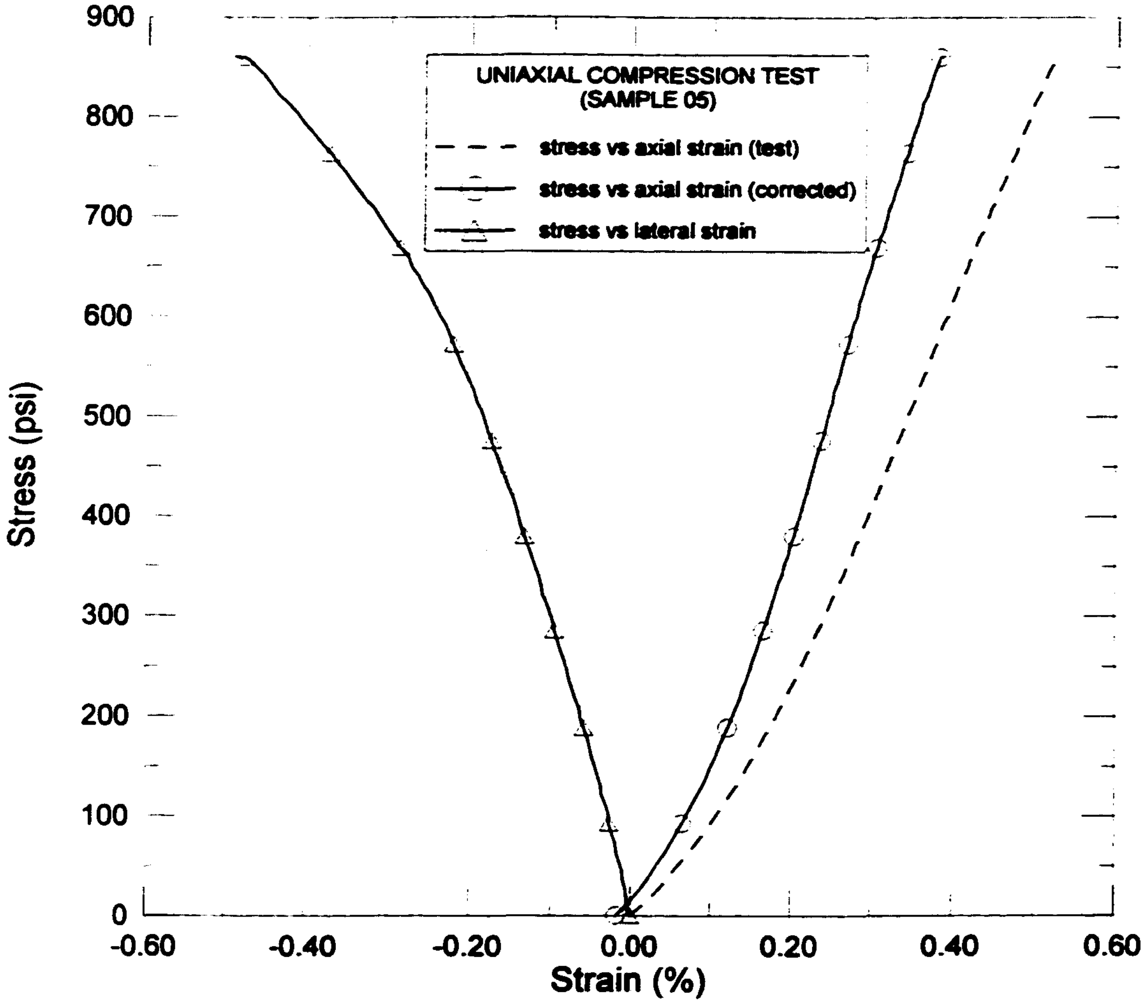

Figure F.5: Stress-strain curves for the uniaxial compression test of sample 05.

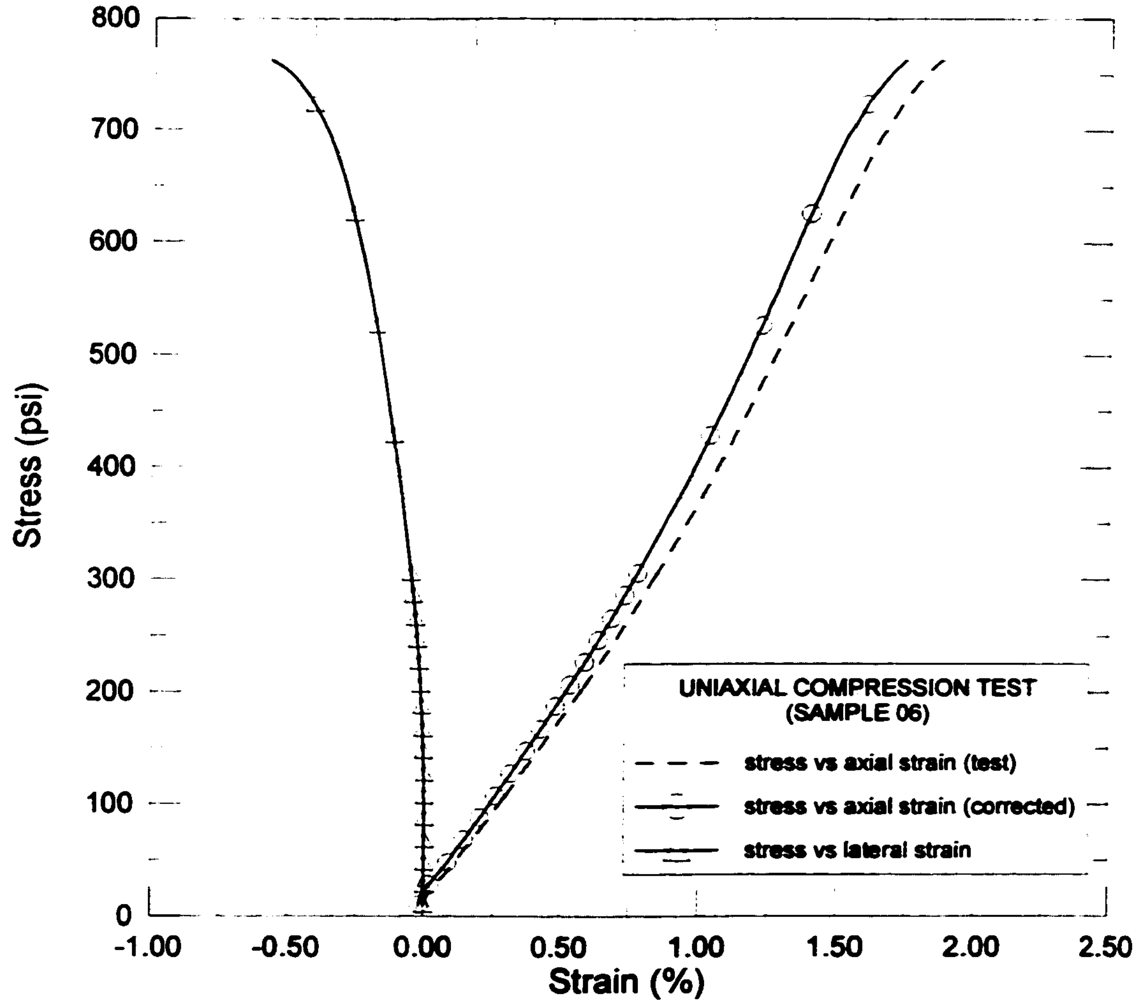

Figure F.6: Stress-strain curves for the uniaxial compression test of sample 06.

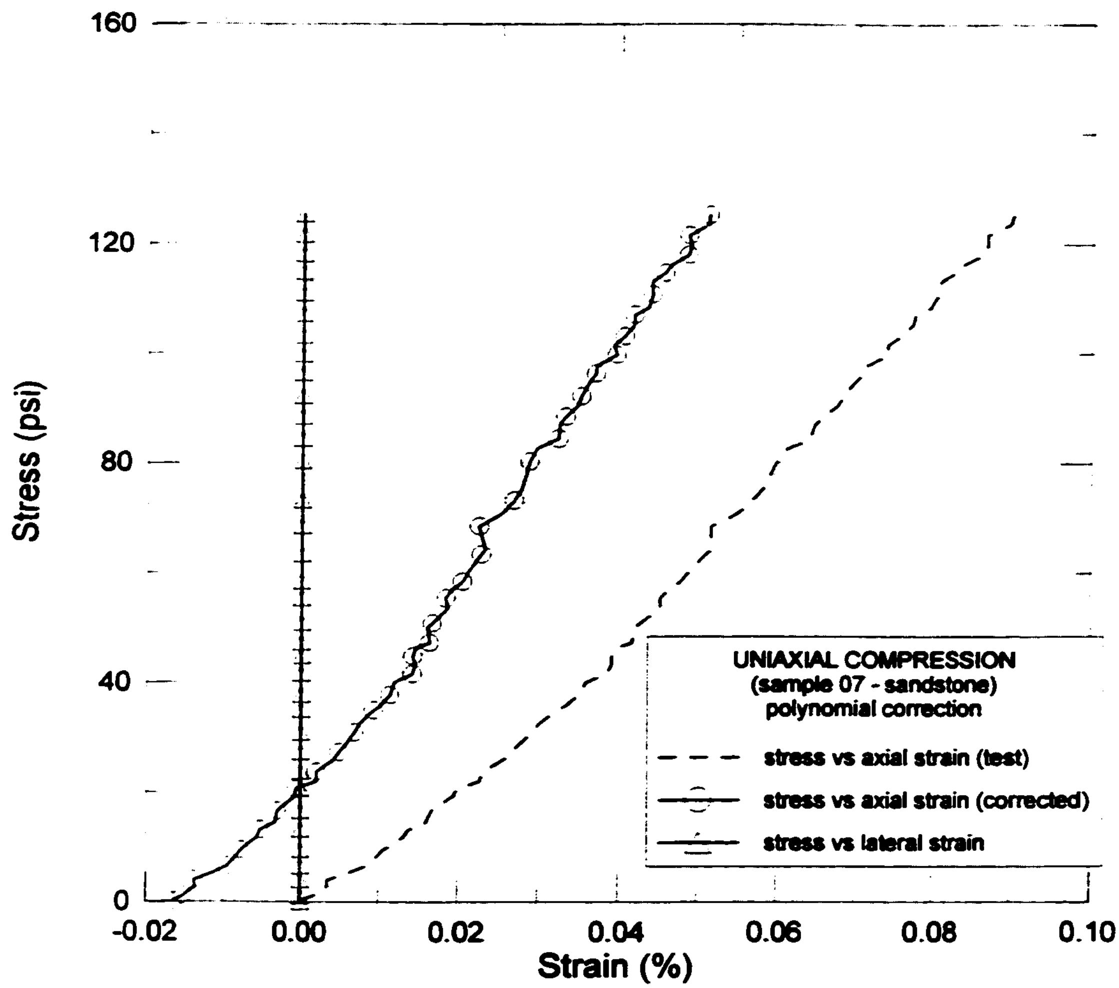

Figure F.7: Stress-strain curves for the uniaxial compression test of sample 07.

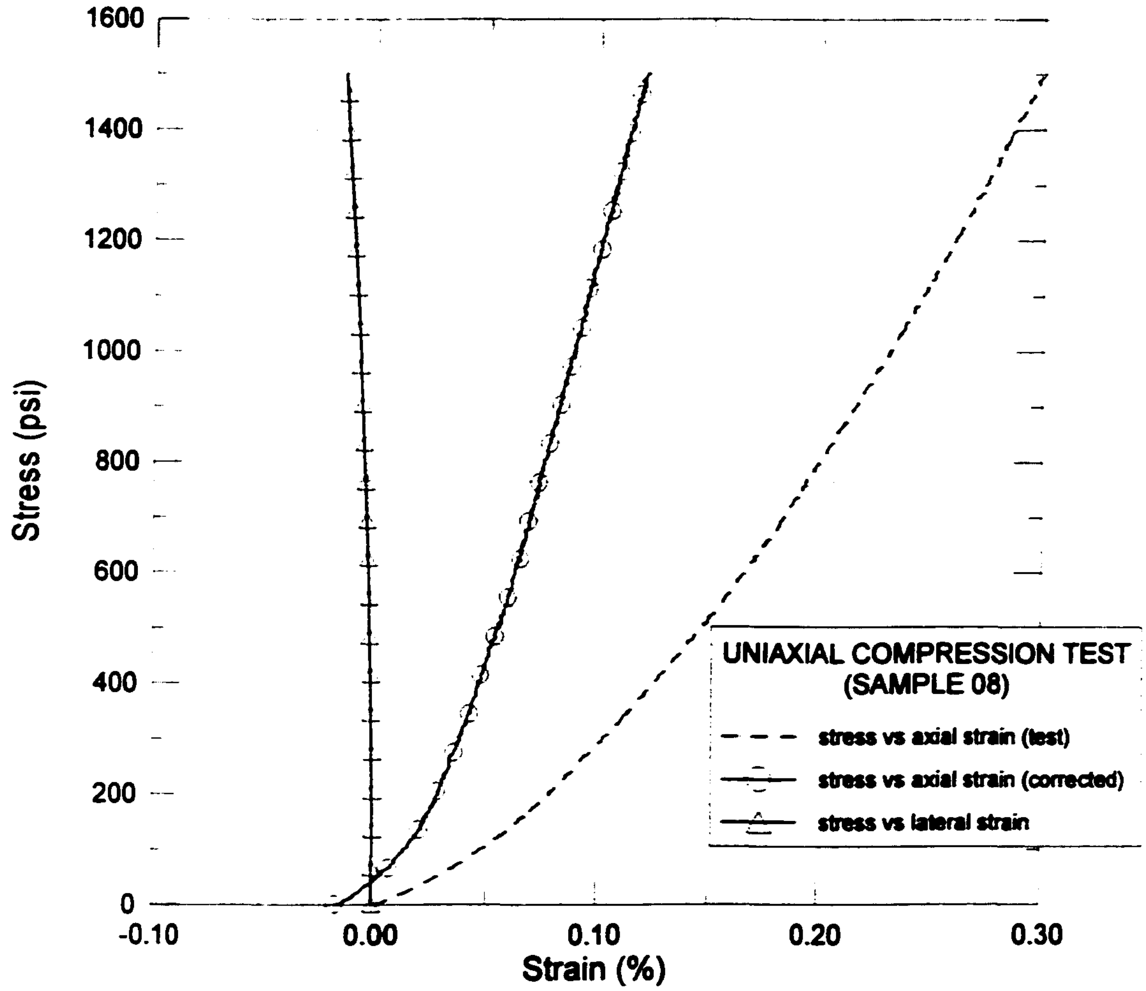

Figure F.8: Stress-strain curves for the uniaxial compression test of sample 08.

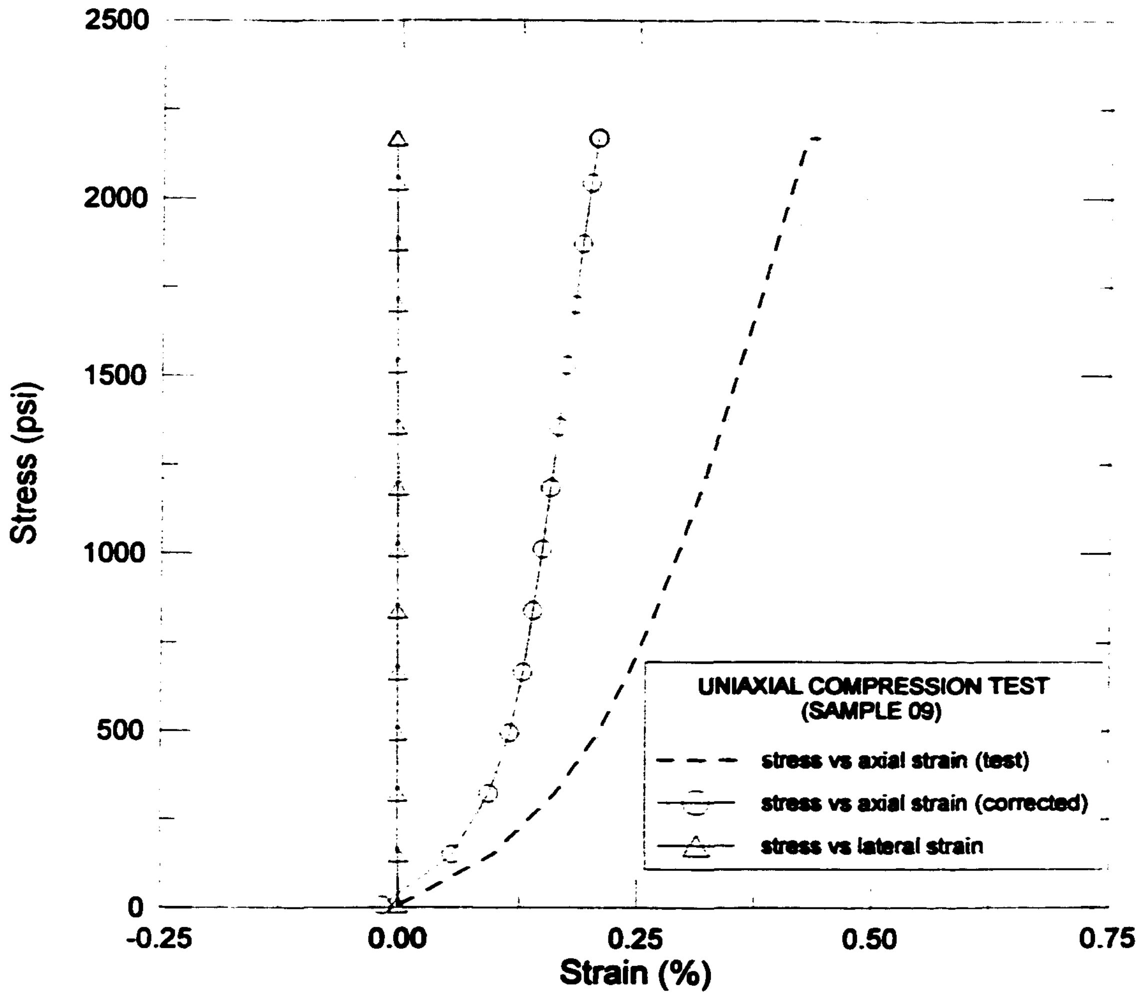

Figure F.9: Stress-strain curves for the uniaxial compression test of sample 09.

F.2 Hydrostatic Compression Tests

Figures F.10 to F.23 show the confining pressure *versus* volumetric strain curves for each hydrostatic compression test.

F.2.1 Drained Hydrostatic Compression

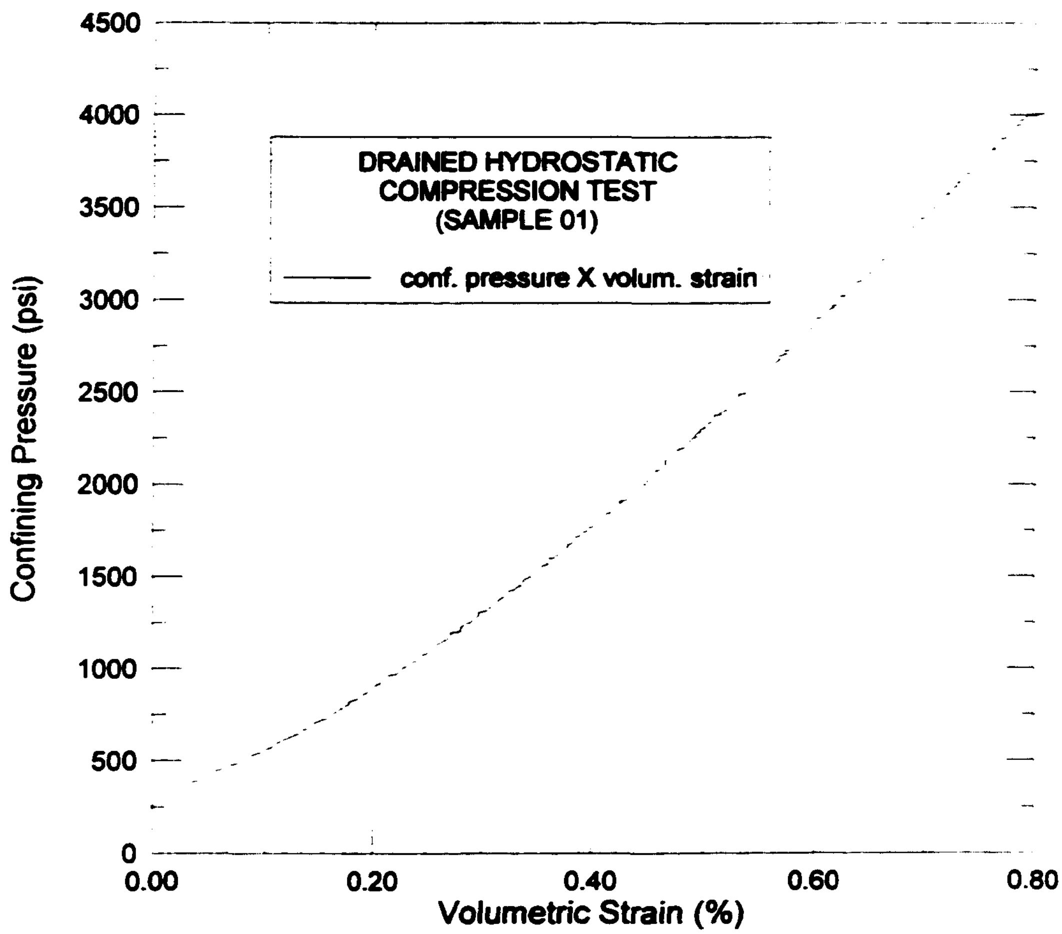

Figure F.10: Confining pressure versus volumetric strain for the drained hydrostatic compression test of sample 01.

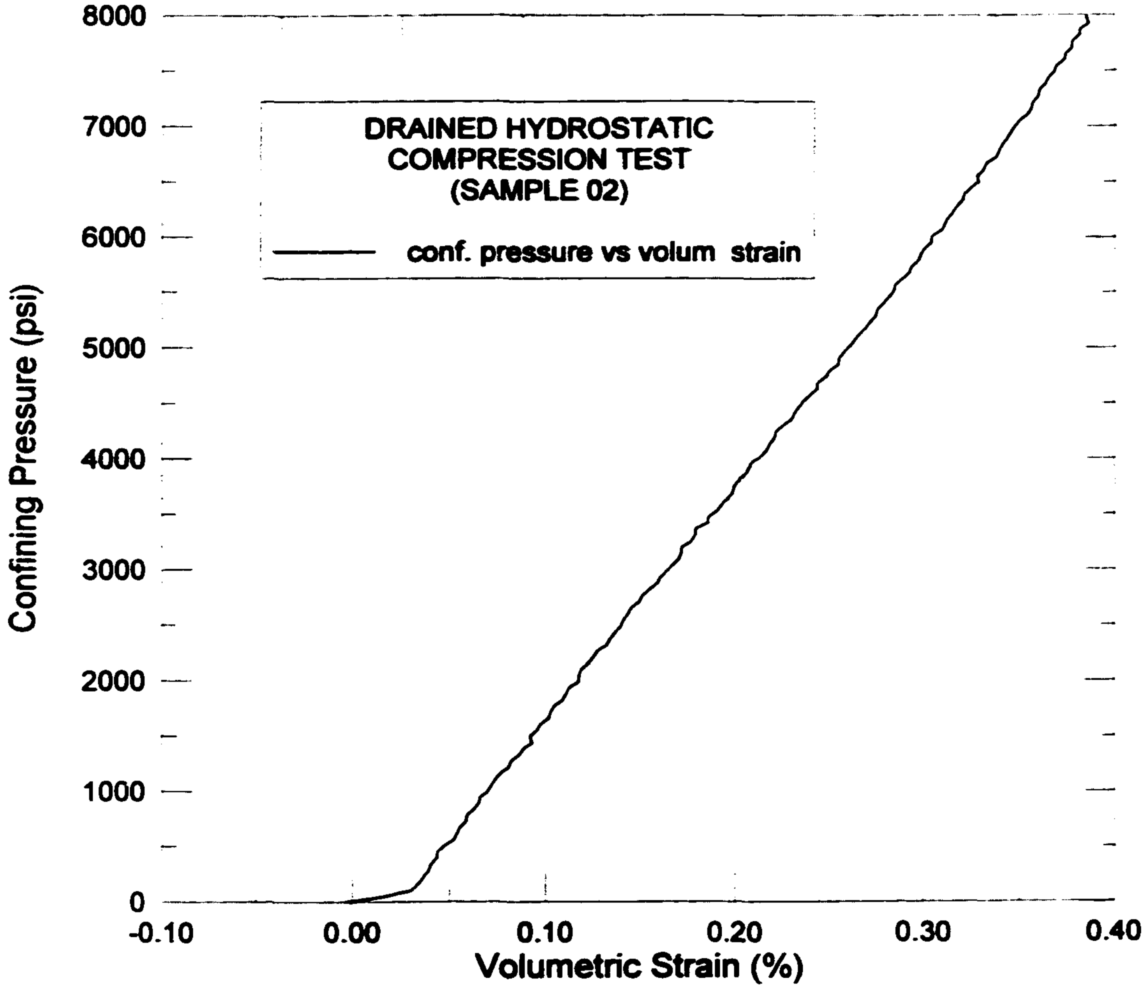

Figure F.11: Confining pressure versus volumetric strain for the drained hydrostatic compression test of sample 02.

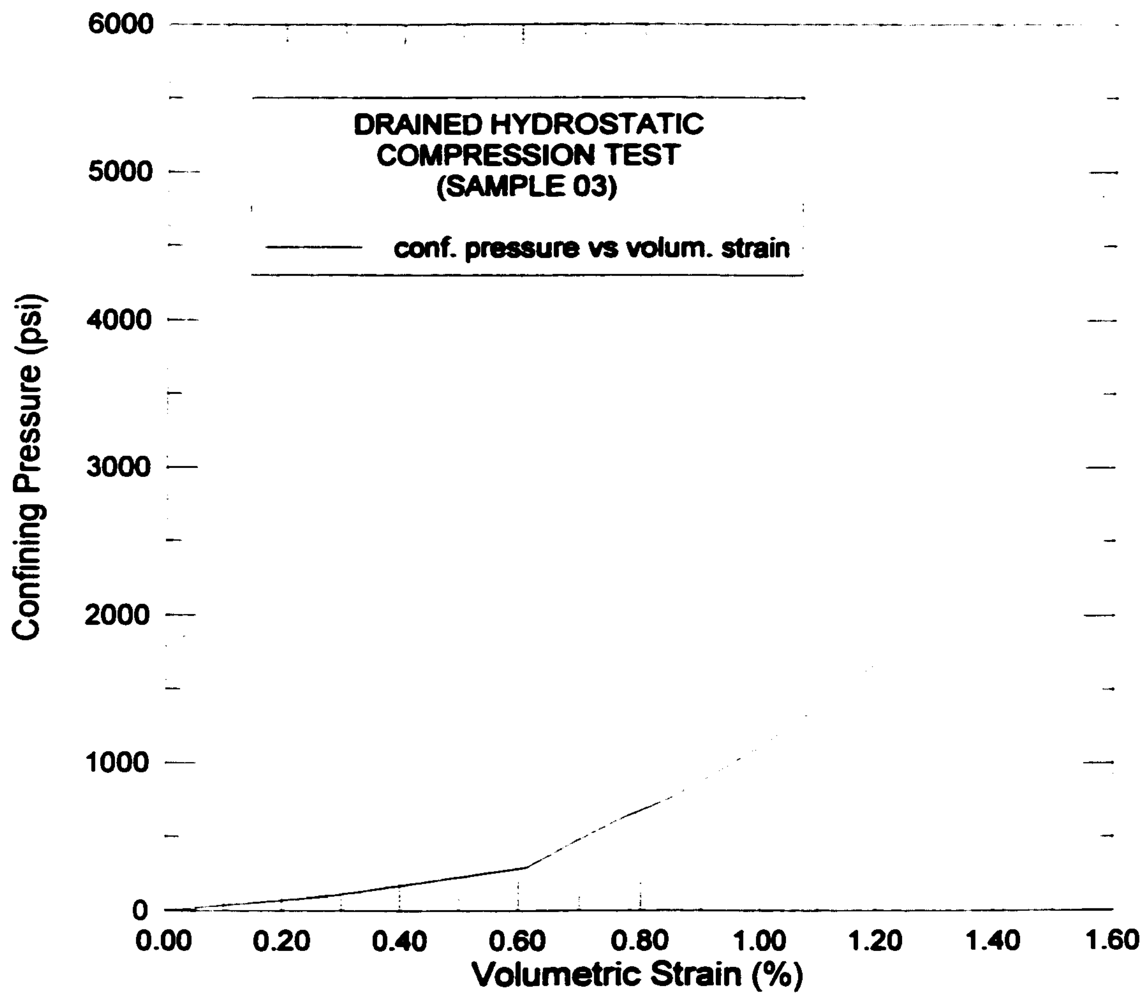

Figure F.12: Confining pressure versus volumetric strain for the drained hydrostatic compression test of sample 03.

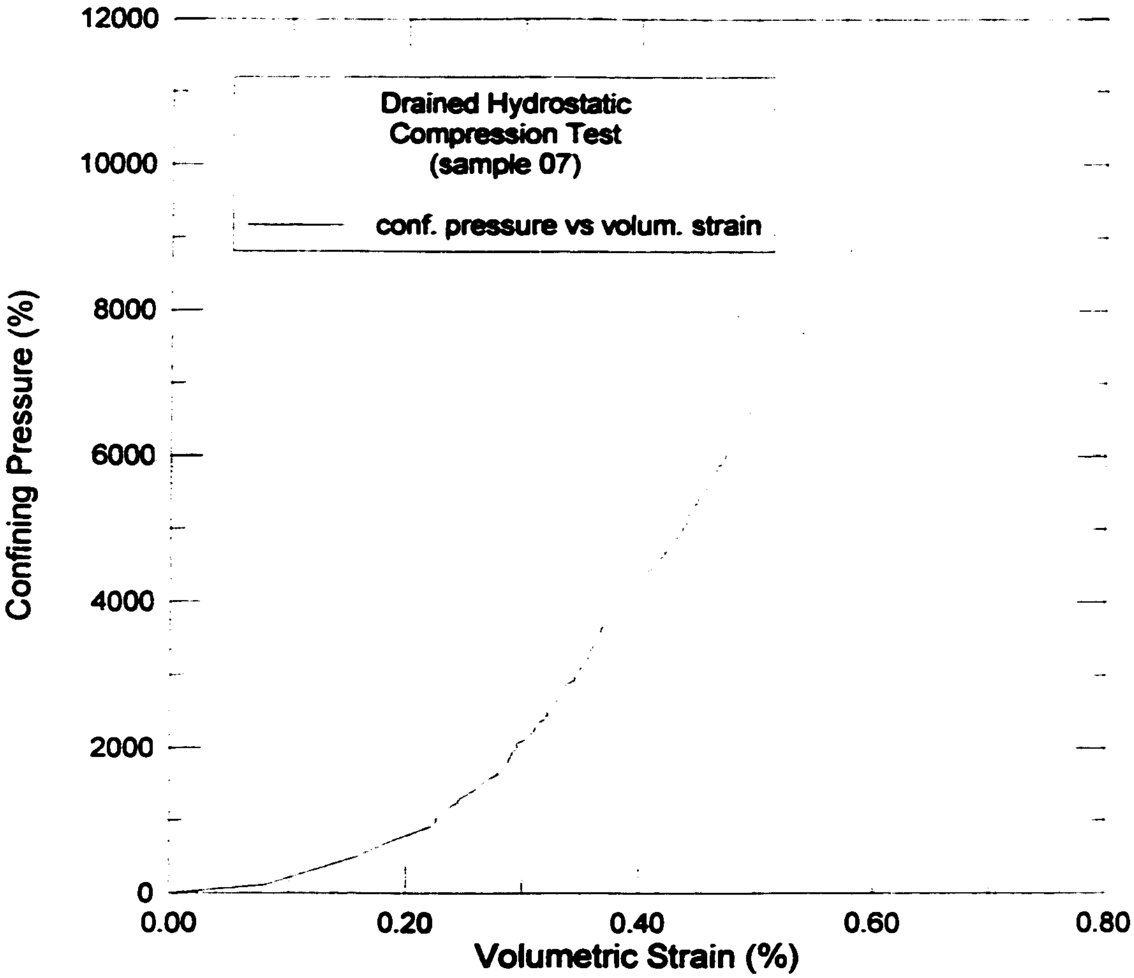

Figure F.13: Confining pressure versus volumetric strain for the drained hydrostatic compression test of sample 07.

F.2.2 Undrained Hydrostatic Compression

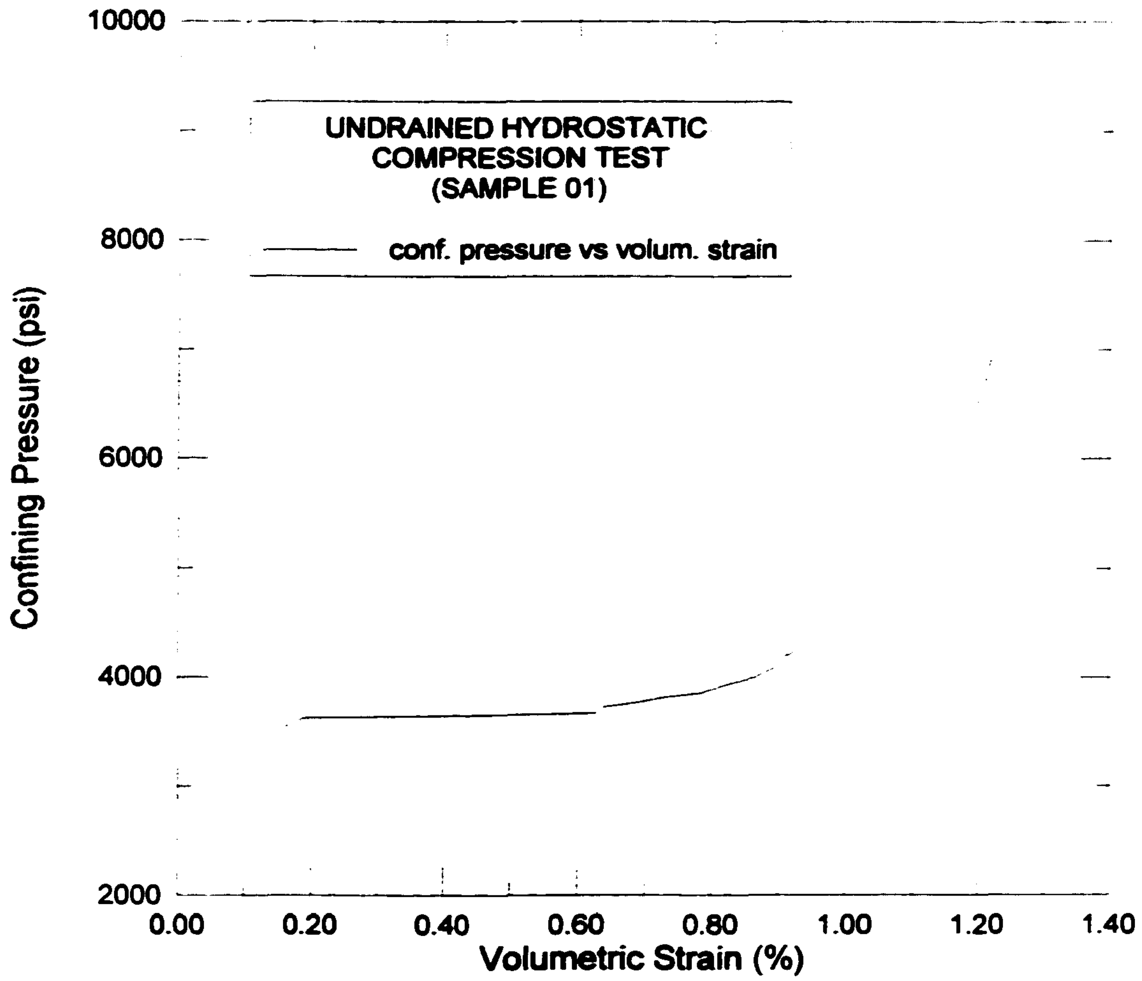

Figure F.14: Confining pressure versus volumetric strain for the undrained hydrostatic compression test of sample 01.

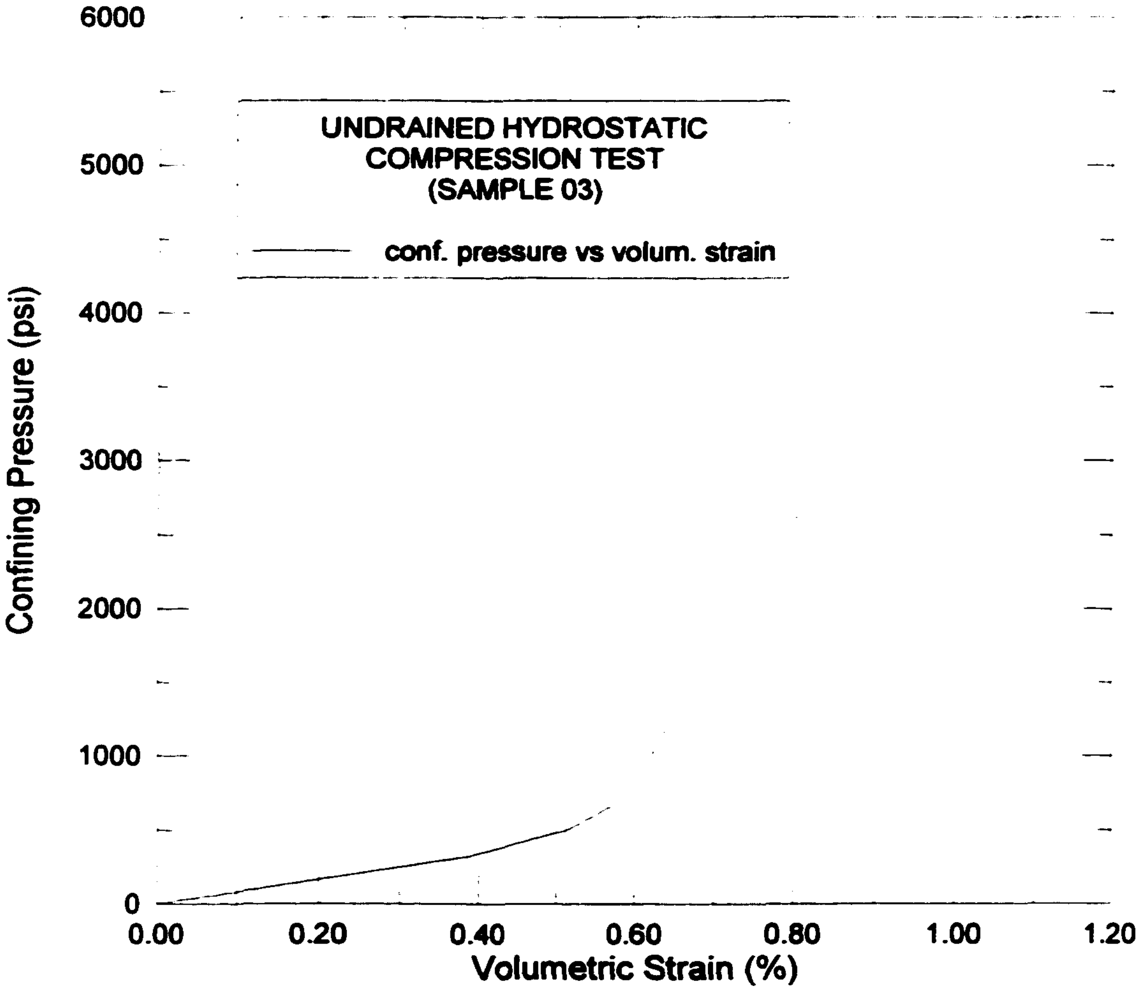

Figure F.15: Confining pressure versus volumetric strain for the undrained hydrostatic compression test of sample 03.

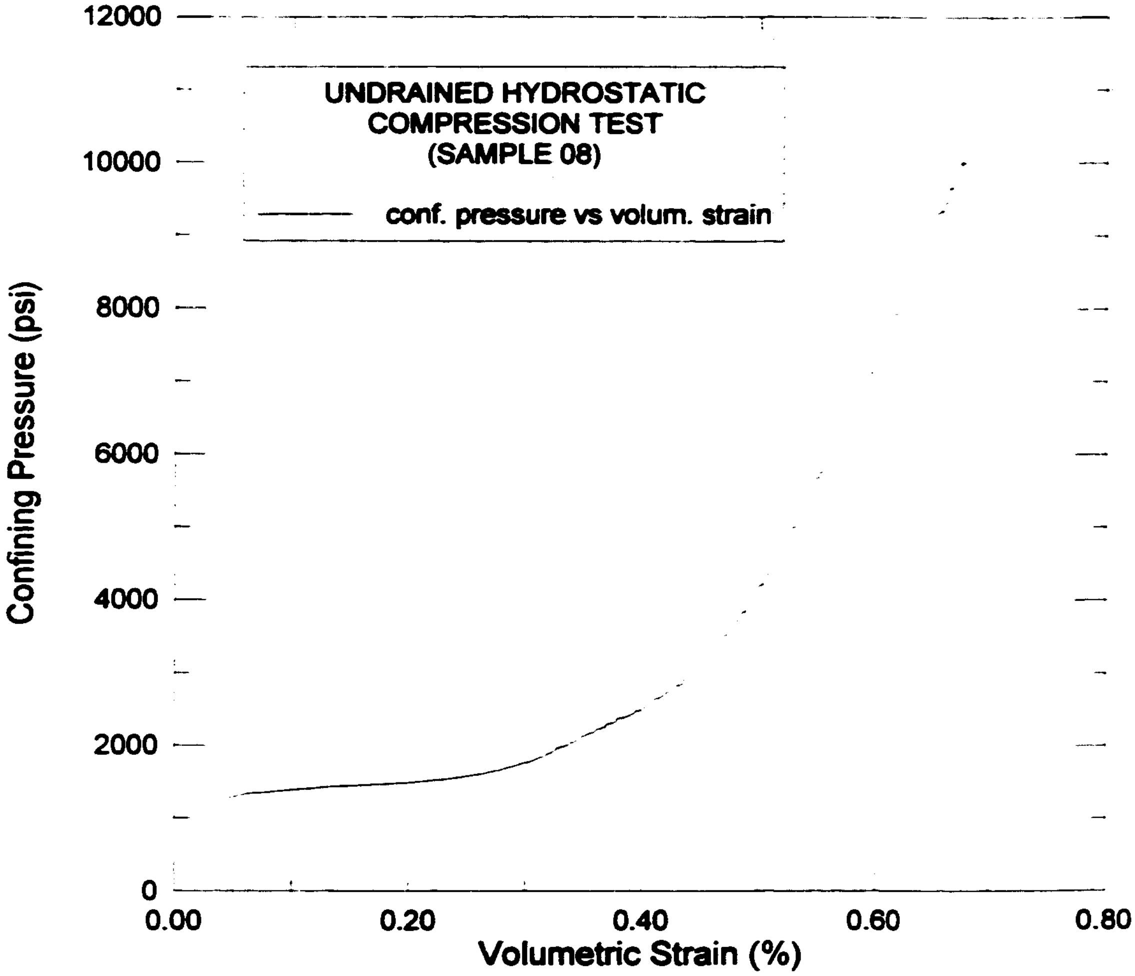

Figure F.16: Confining pressure versus volumetric strain for the undrained hydrostatic compression test of sample 08.

F.2.3 Unjacketed Hydrostatic Compression

The stress-strain curves used for computing the grain bulk modulus are shown from Figures (F.17) to (F.23).

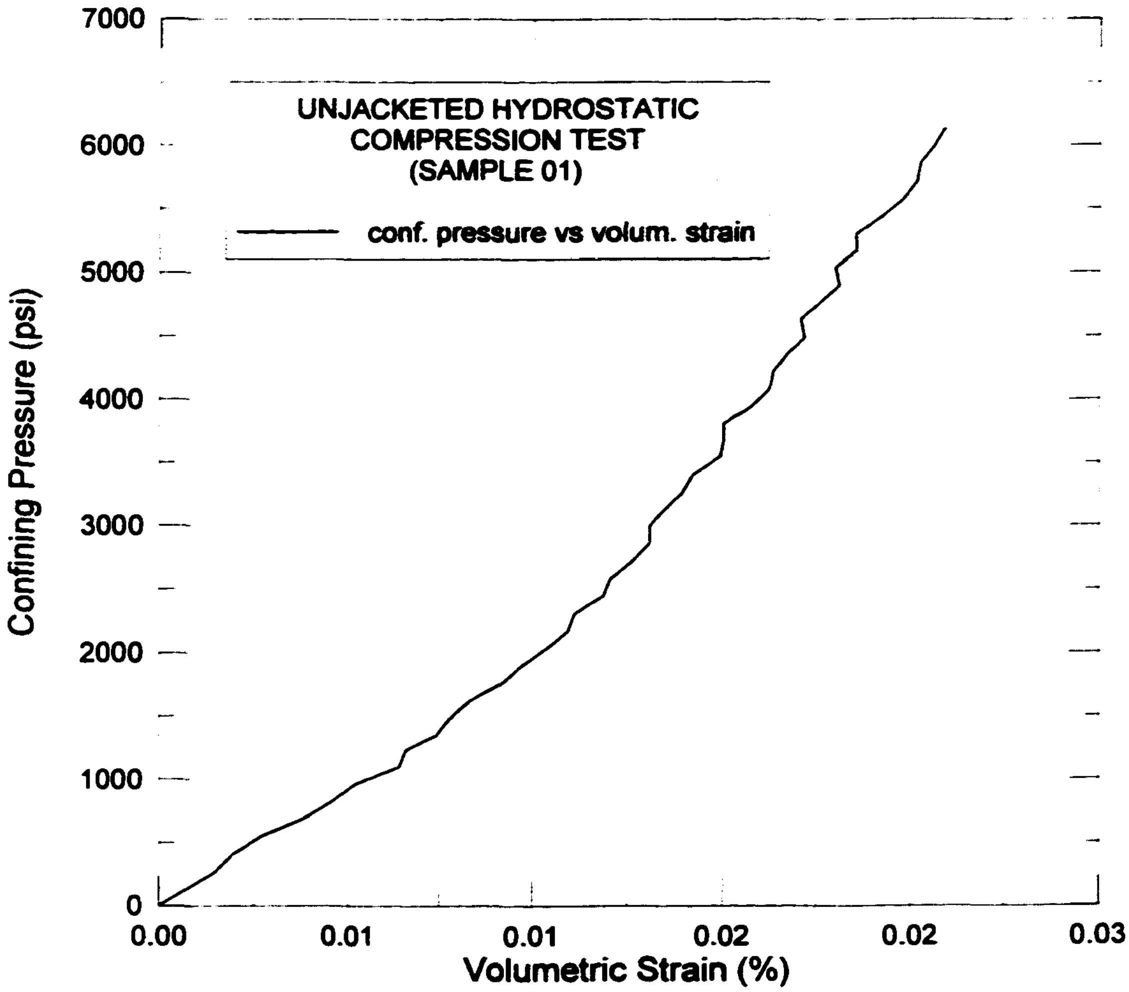

Figure F.17: Confining pressure versus volumetric strain for the unjacketed hydrostatic compression test of sample 01.

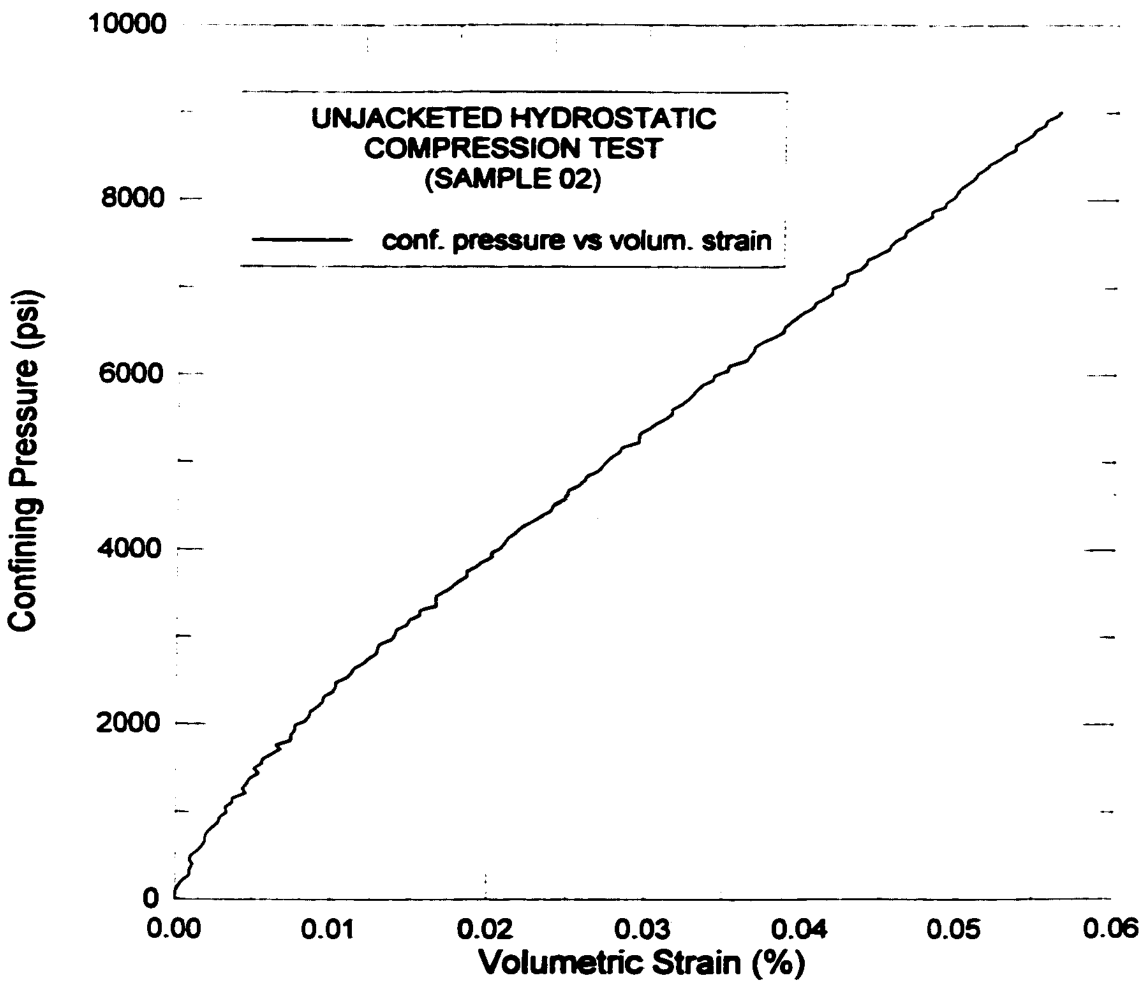

Figure F.18: Confining pressure versus volumetric strain for the unjacketed hydrostatic compression test of sample 02.

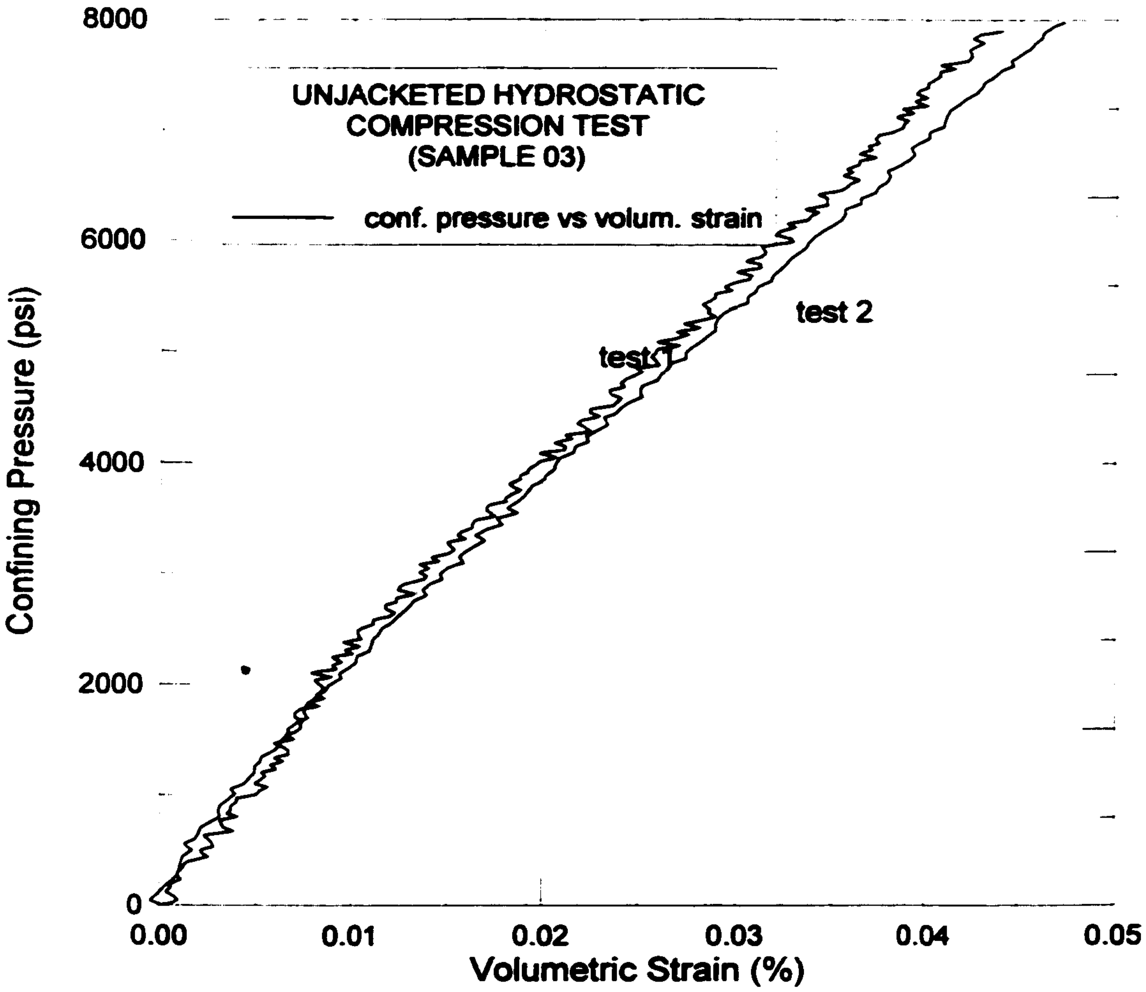

Figure F.19: Confining pressure versus volumetric strain for the unjacketed hydrostatic compression test of sample 03.

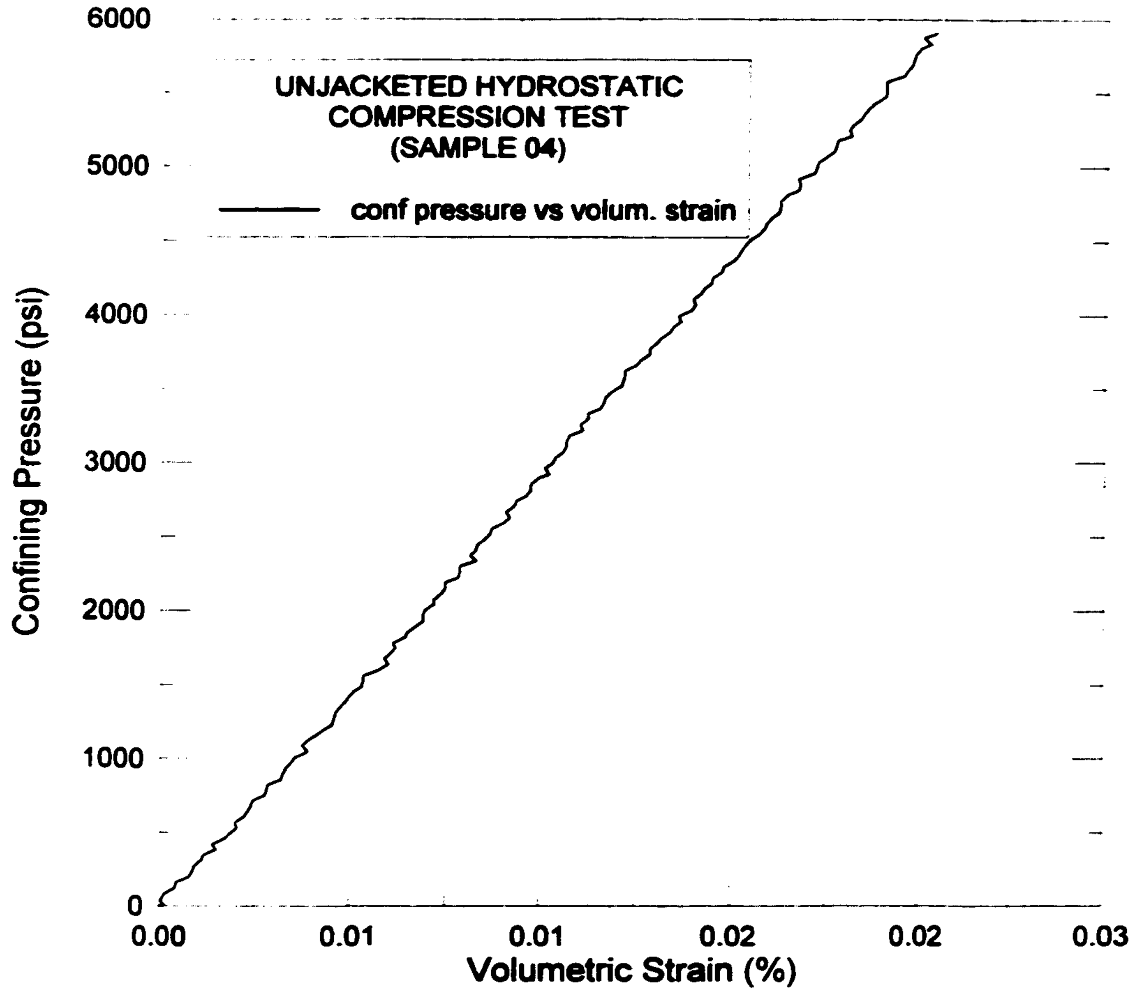

Figure F.20: Confining pressure versus volumetric strain for the unjacketed hydrostatic compression test of sample 04.

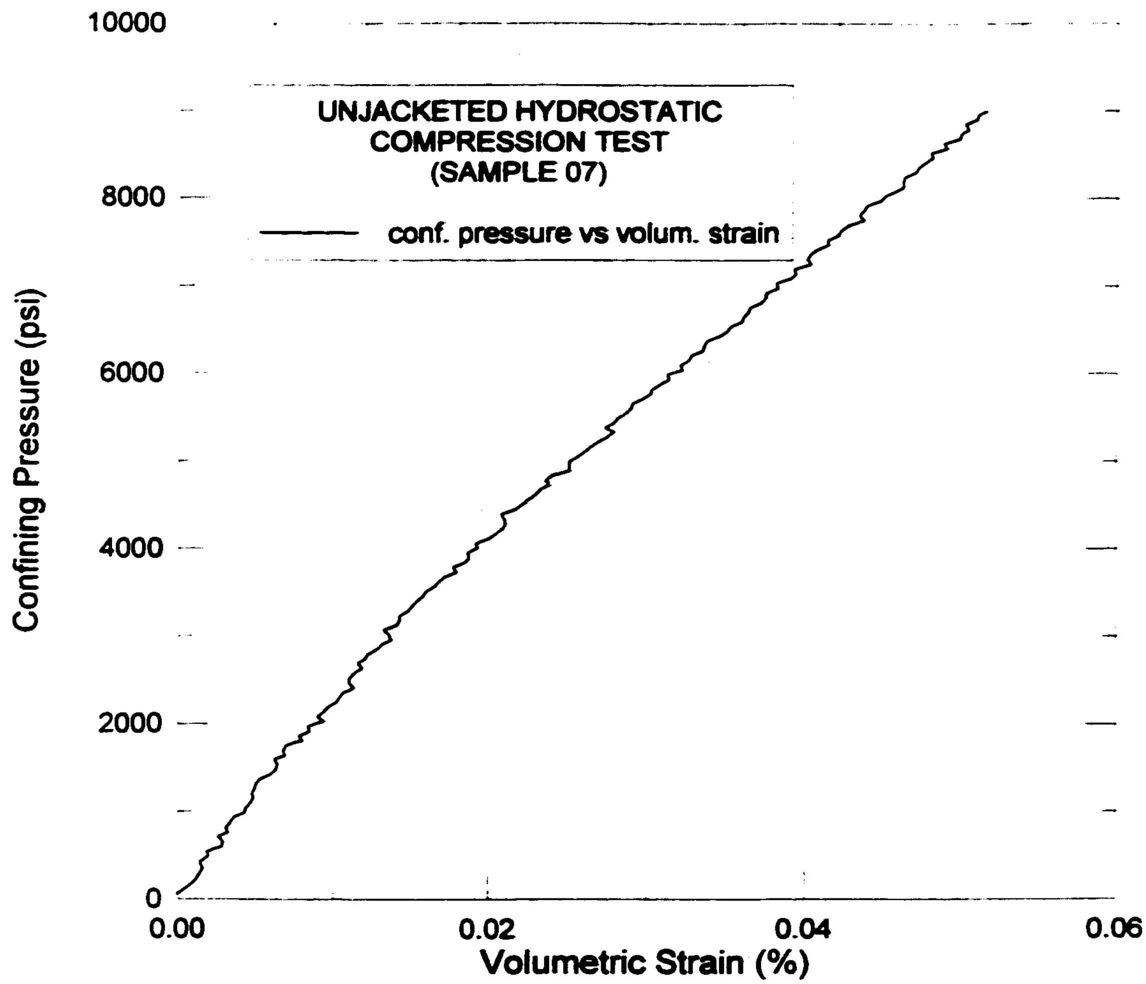

Figure F.21: Confining pressure versus volumetric strain for the unjacketed hydrostatic compression test of sample 07.

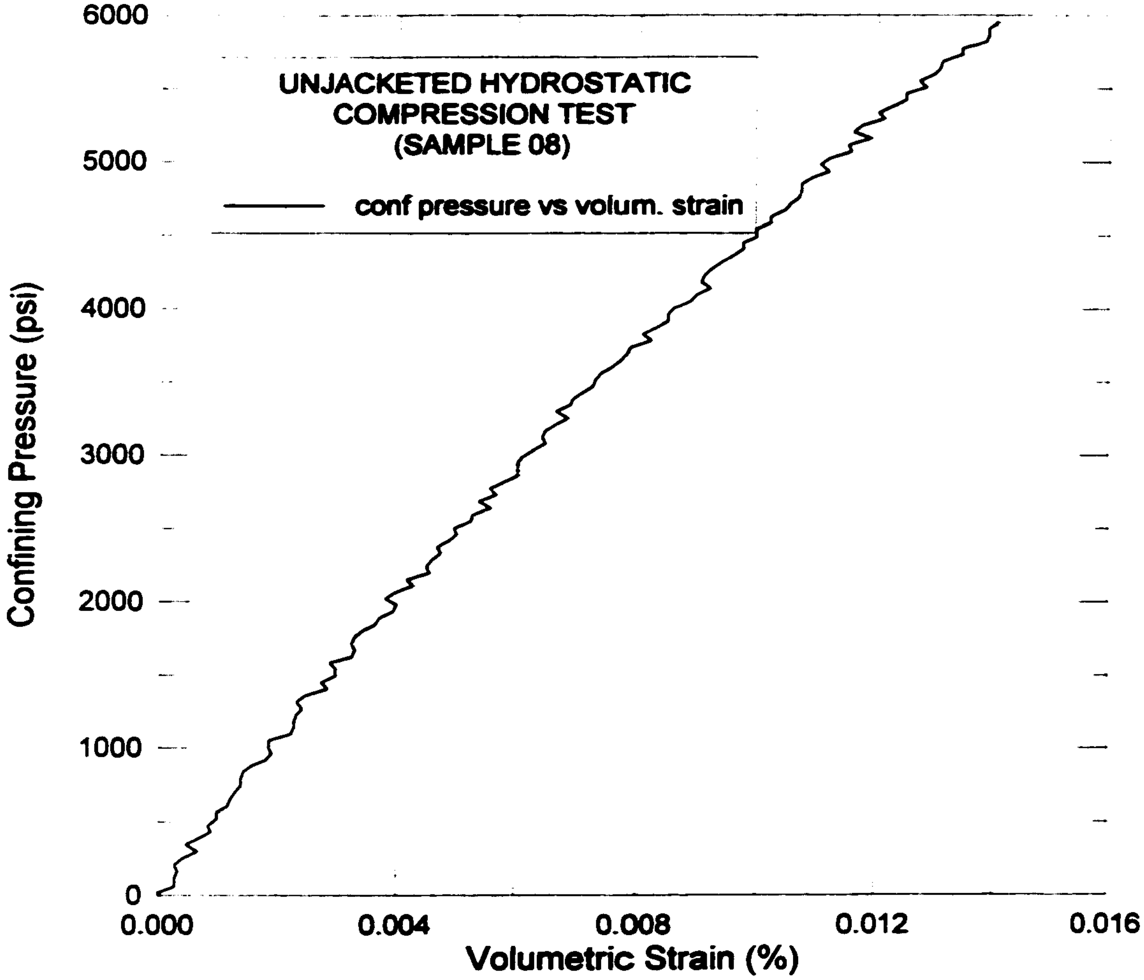

Figure F.22: Confining pressure versus volumetric strain for the unjacketed hydrostatic compression test of sample 08.

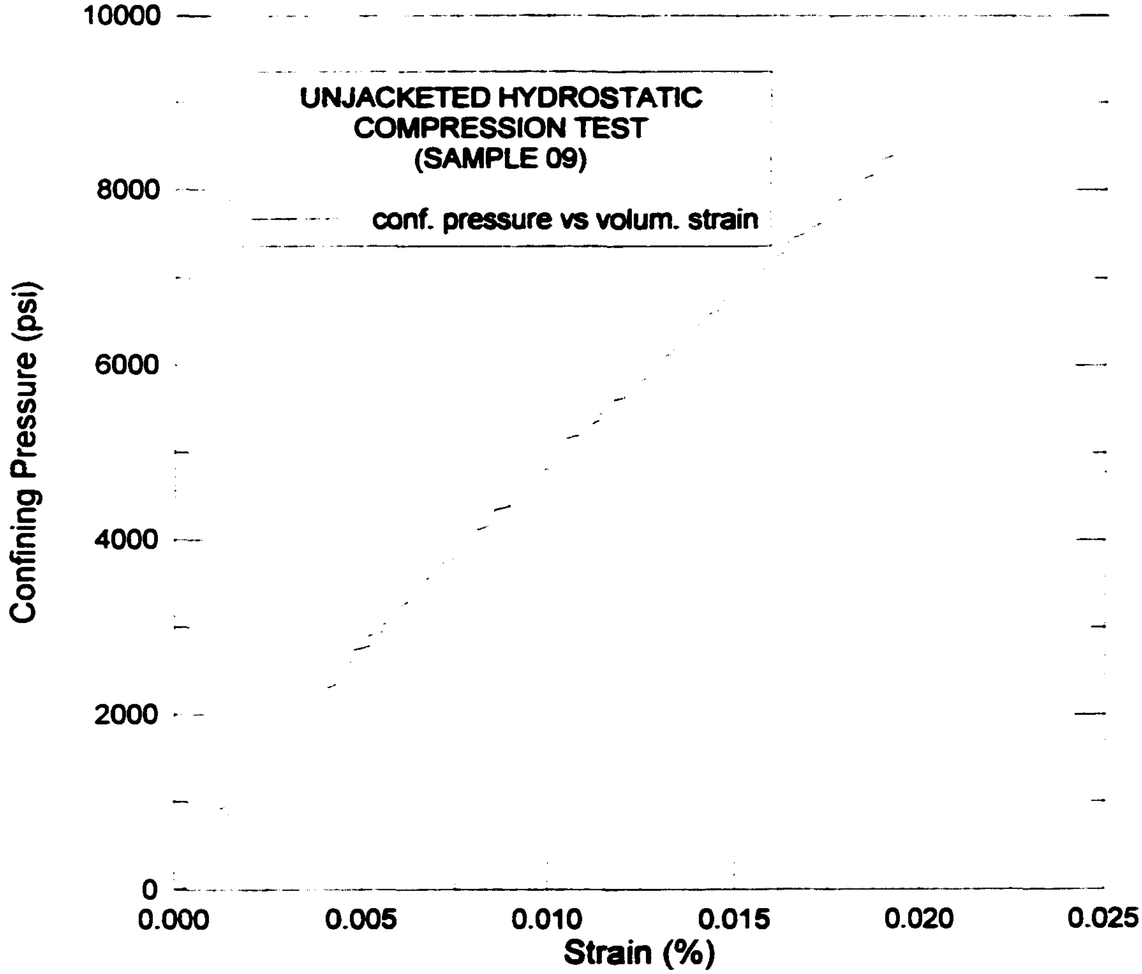

Figure F.23: Confining pressure versus volumetric strain for the unjacketed hydrostatic compression test of sample 09.

F.3 Triaxial Compression Tests

The stress-strain curves for the triaxial compression tests are shown from Figure F.24 to F.27.

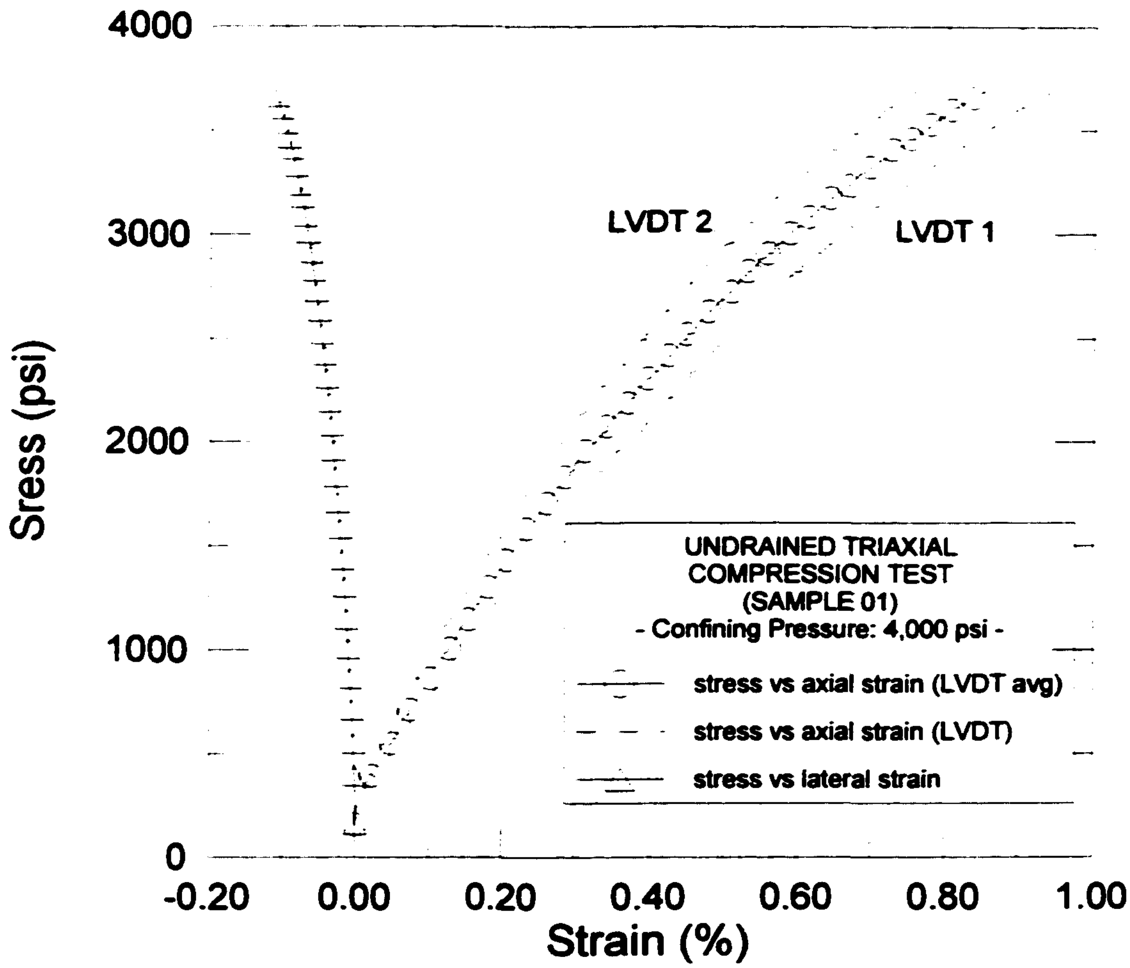

Figure F.24: Stress-strain curves for the undrained triaxial compression test - sample 01.

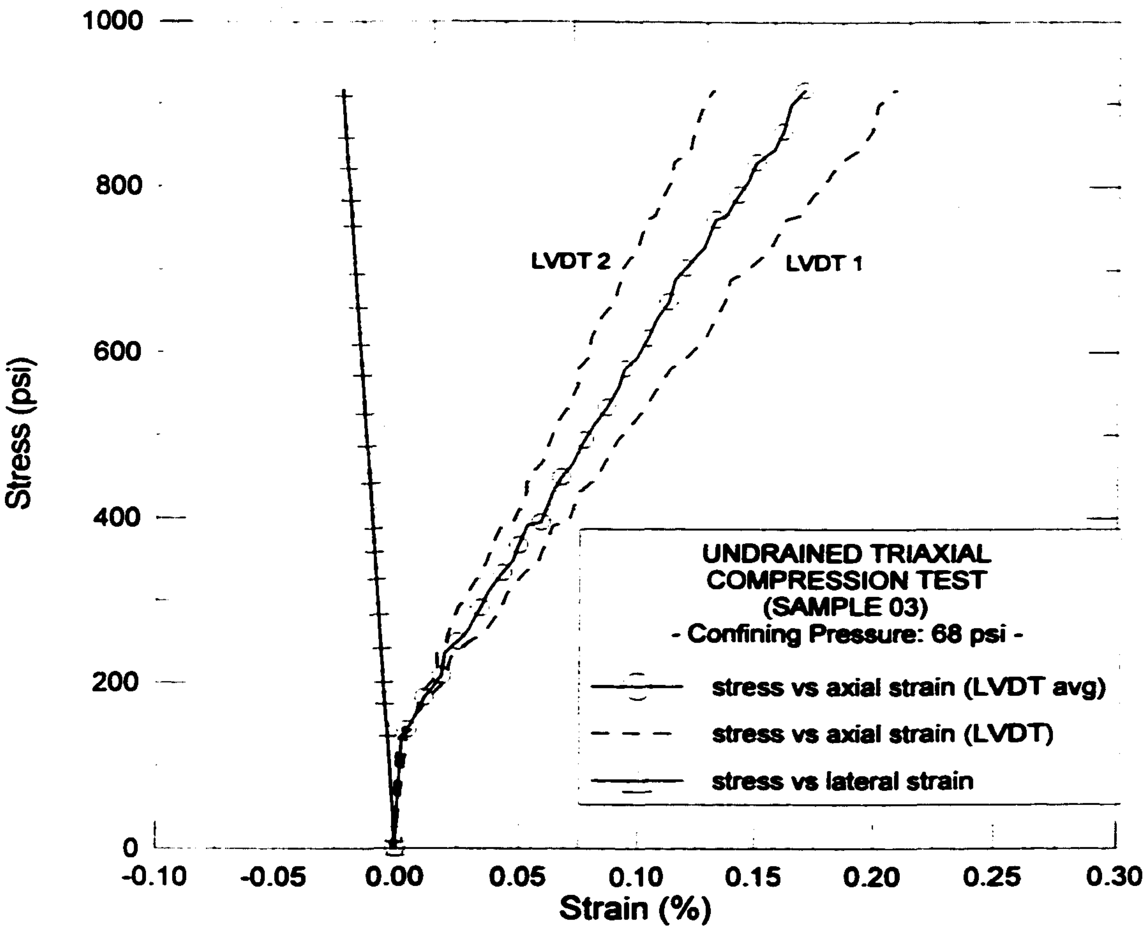

Figure F.25: Stress-strain curves for the undrained triaxial compression test - sample 03.

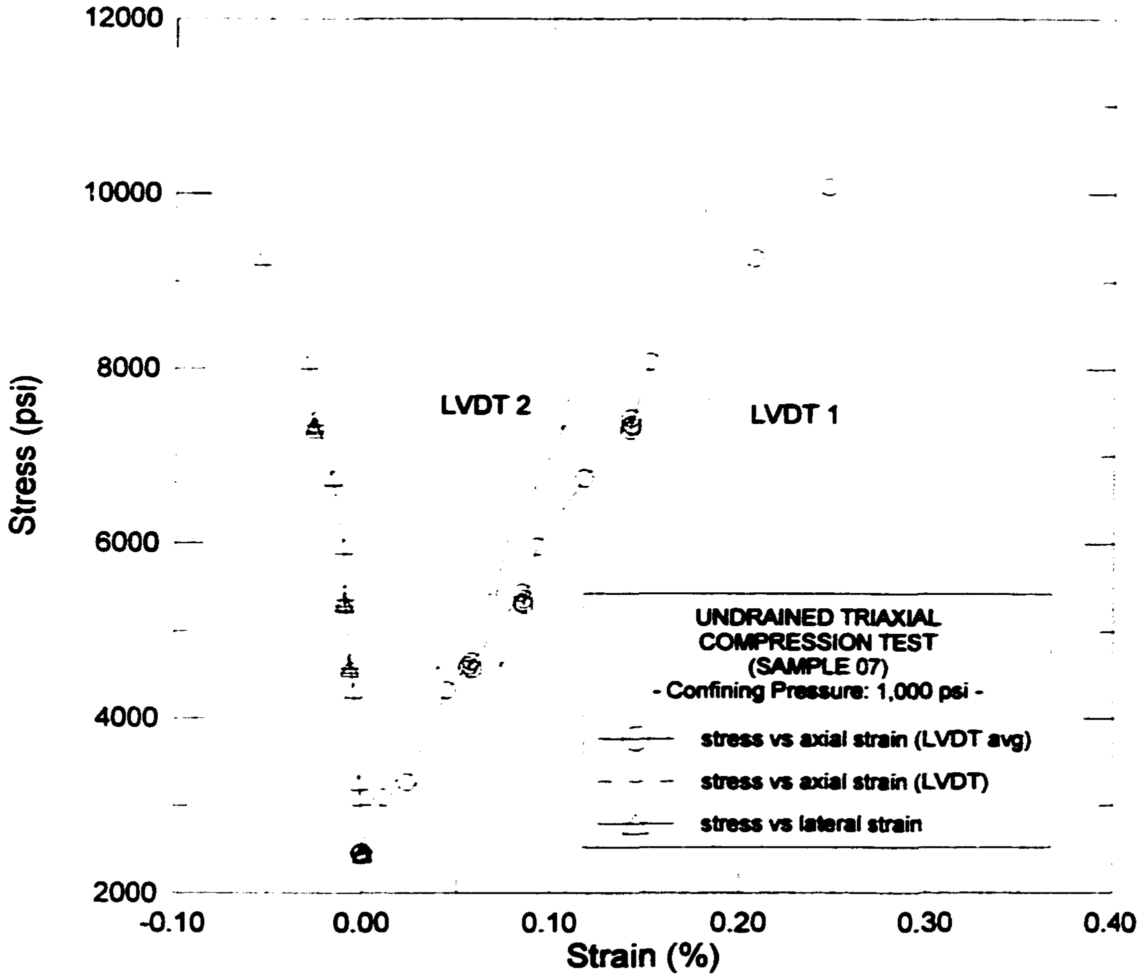

Figure F.26: Stress-strain curves for the undrained triaxial compression test - sample 07.

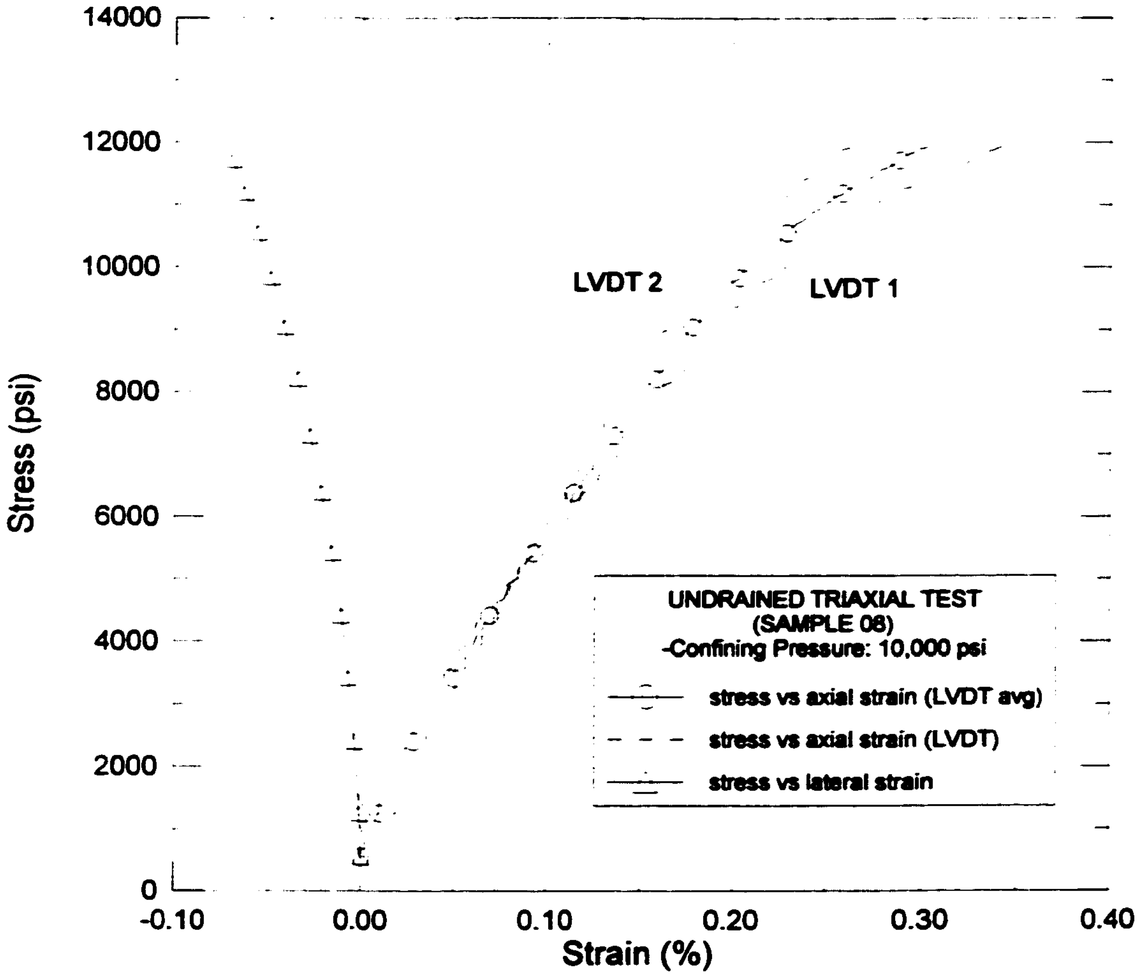

Figure F.27: Stress-strain curves for the undrained triaxial compression test - sample 08.

F.4 Creep Compression Tests

F.4.1 Creep Tests Under Unconfined Compression

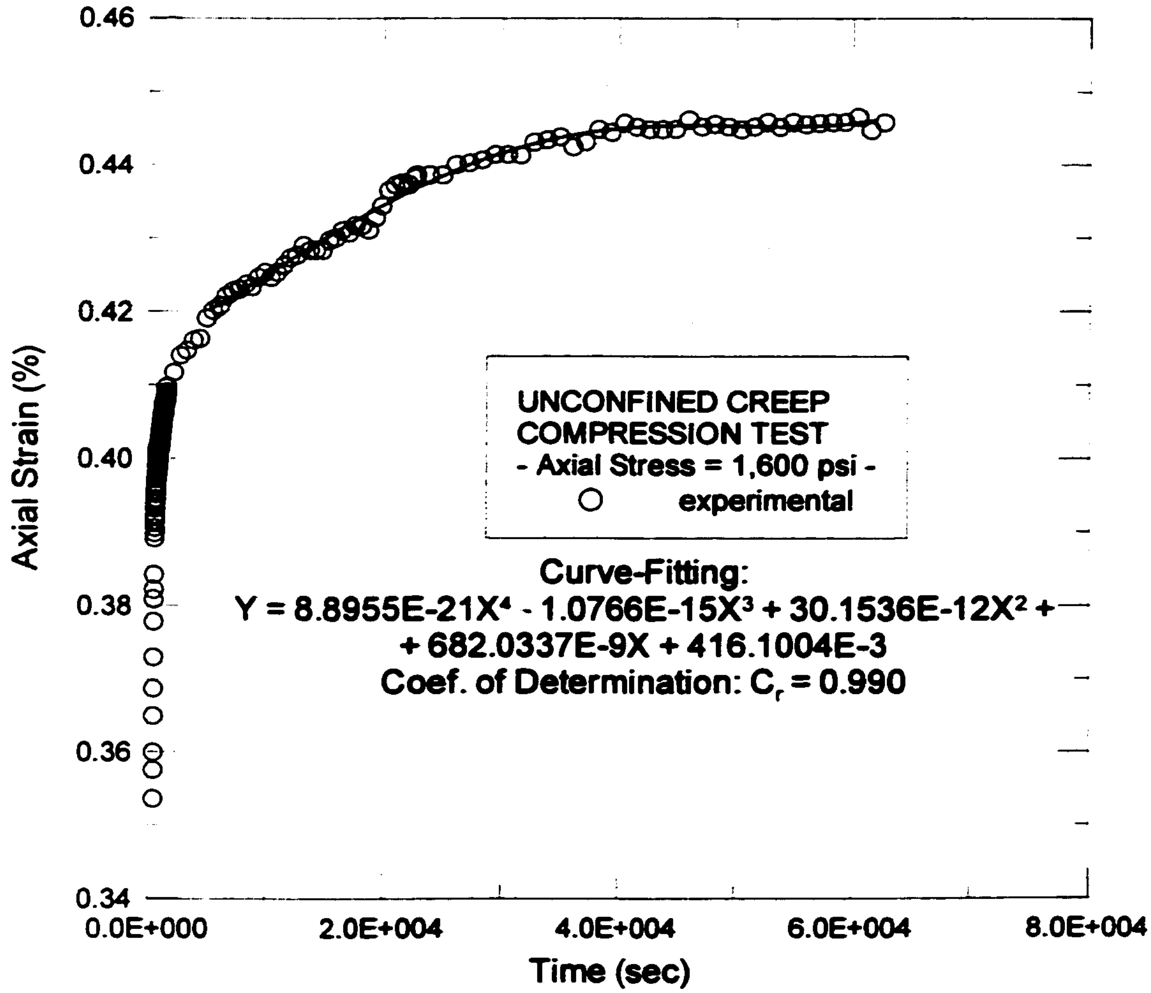

Figure F.28: Unconfined creep compression test for sample 05.

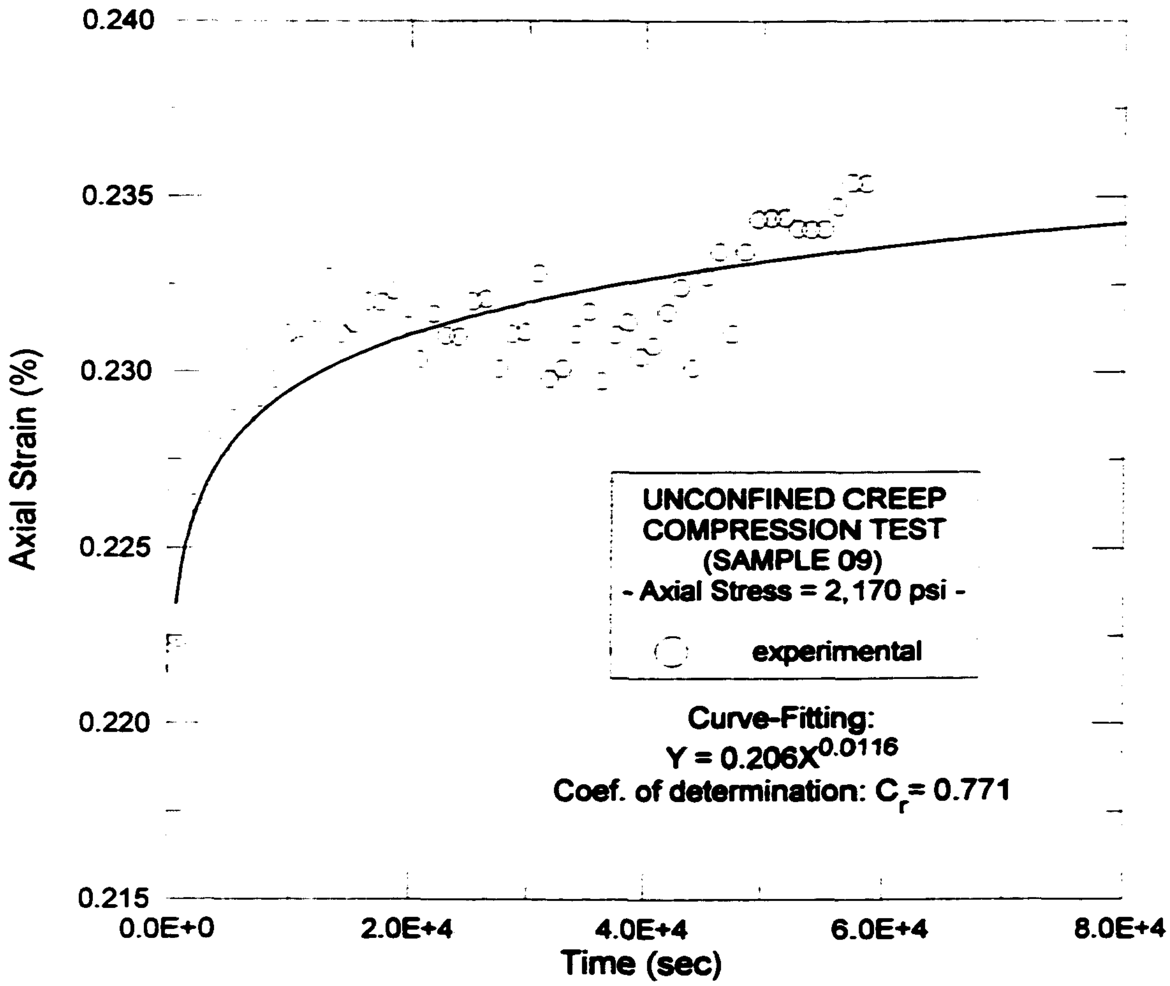

Figure F.29: Unconfined creep compression test for sample 09.

F.4.2 Creep Tests Under Drained Hydrostatic Compression

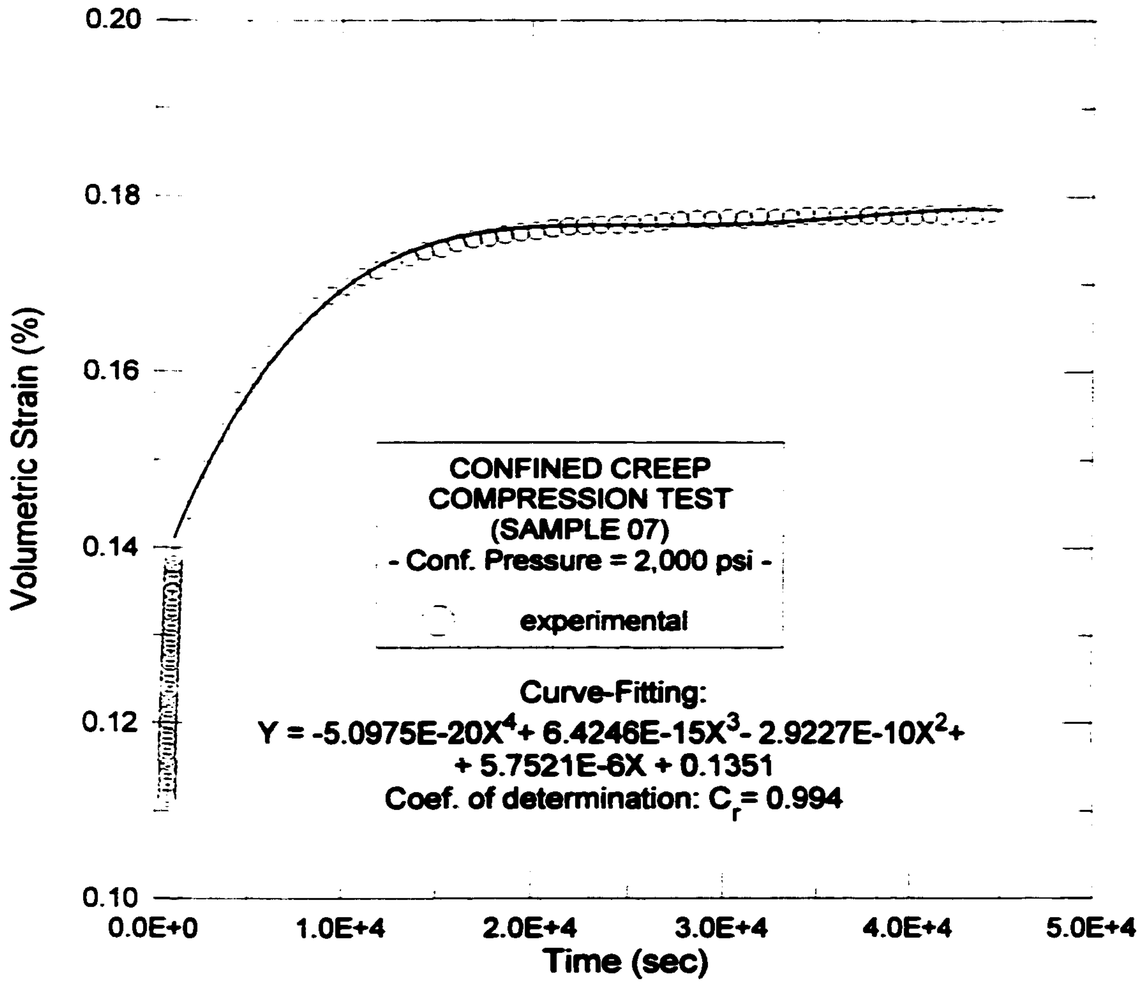

Figure F.30: Confined creep compression test for sample 07.

Creep Tests Under Unjacketed Hydrostatic Compression

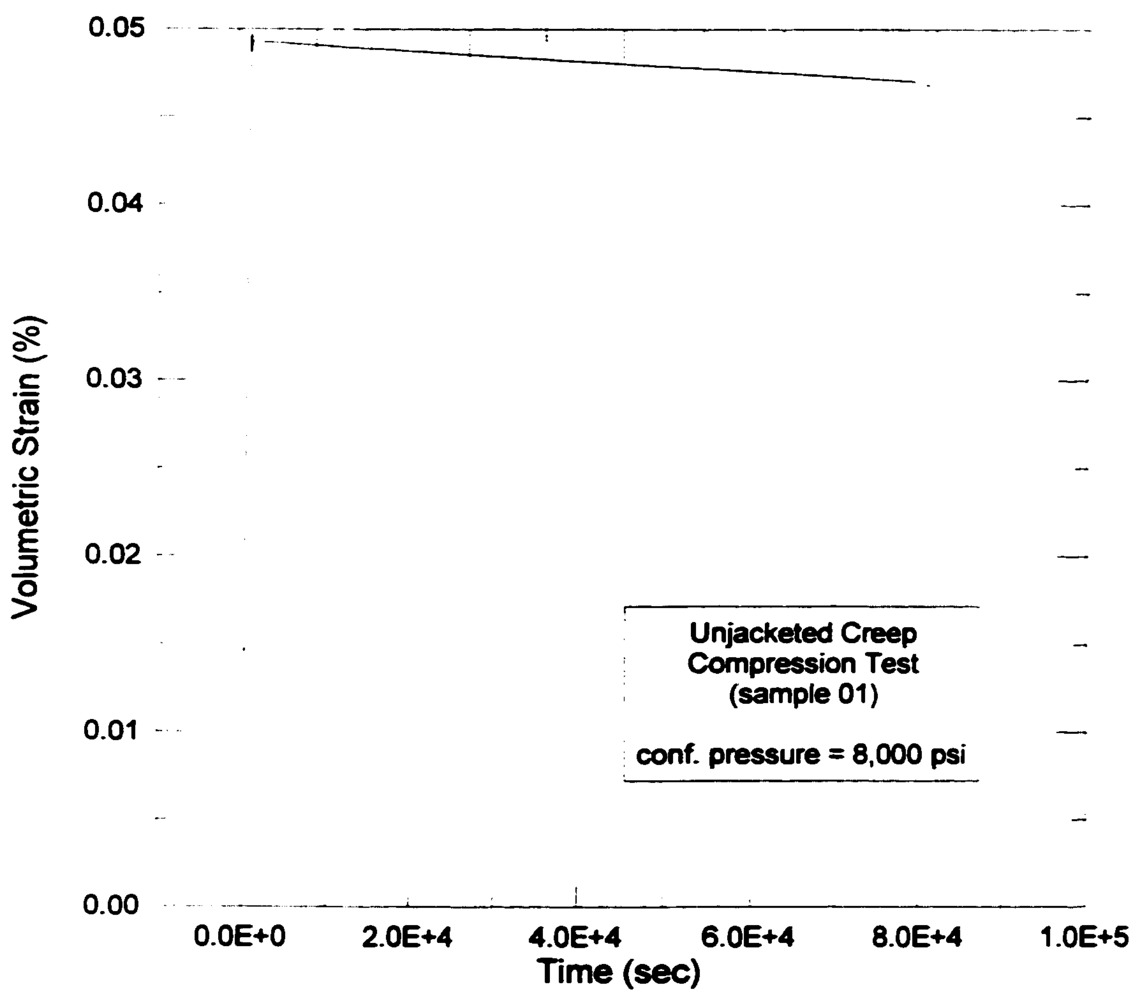

Figure F.31: Creep test for sample 01, unjacketed under hydrostatic compression.

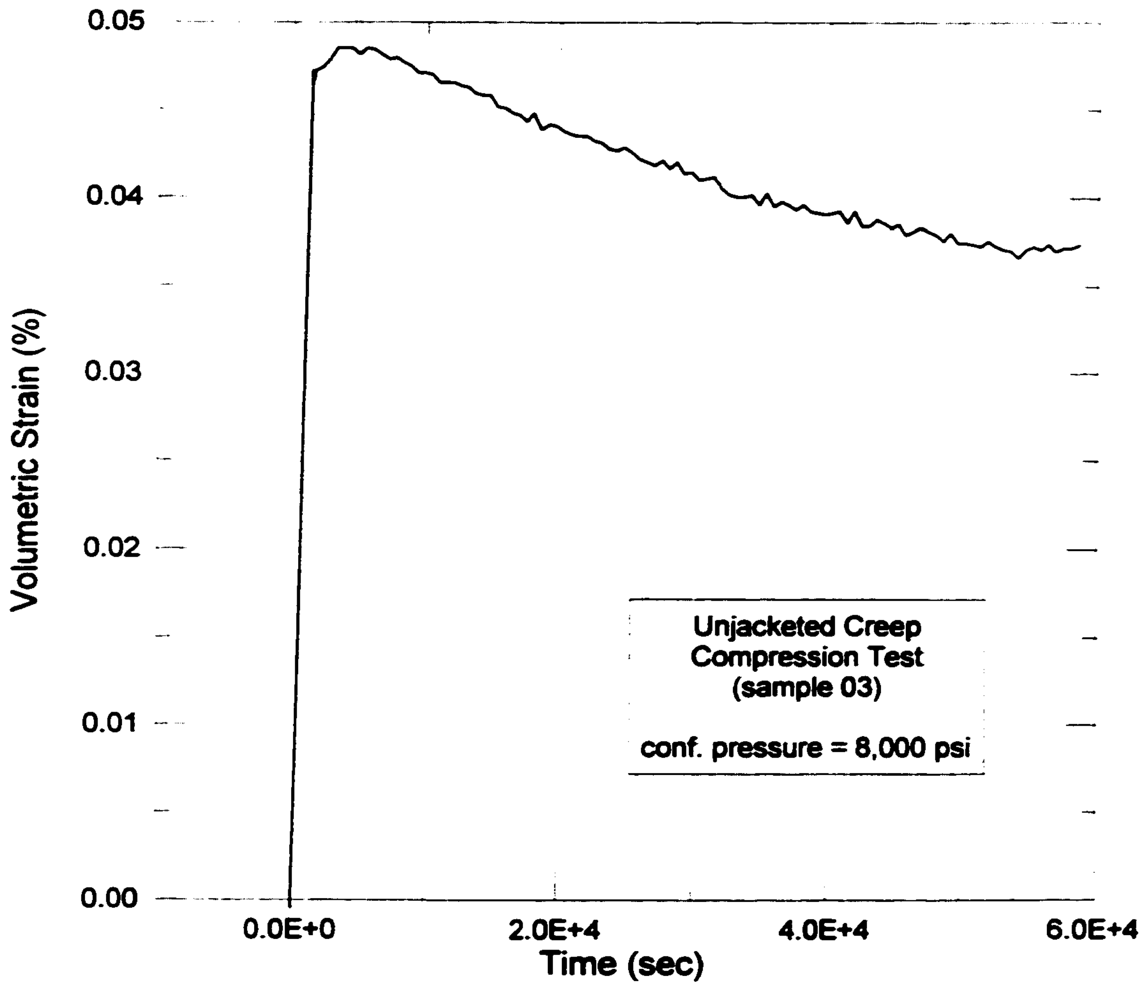

Figure F.32: Creep test for sample 03, unjacketed under hydrostatic compression.

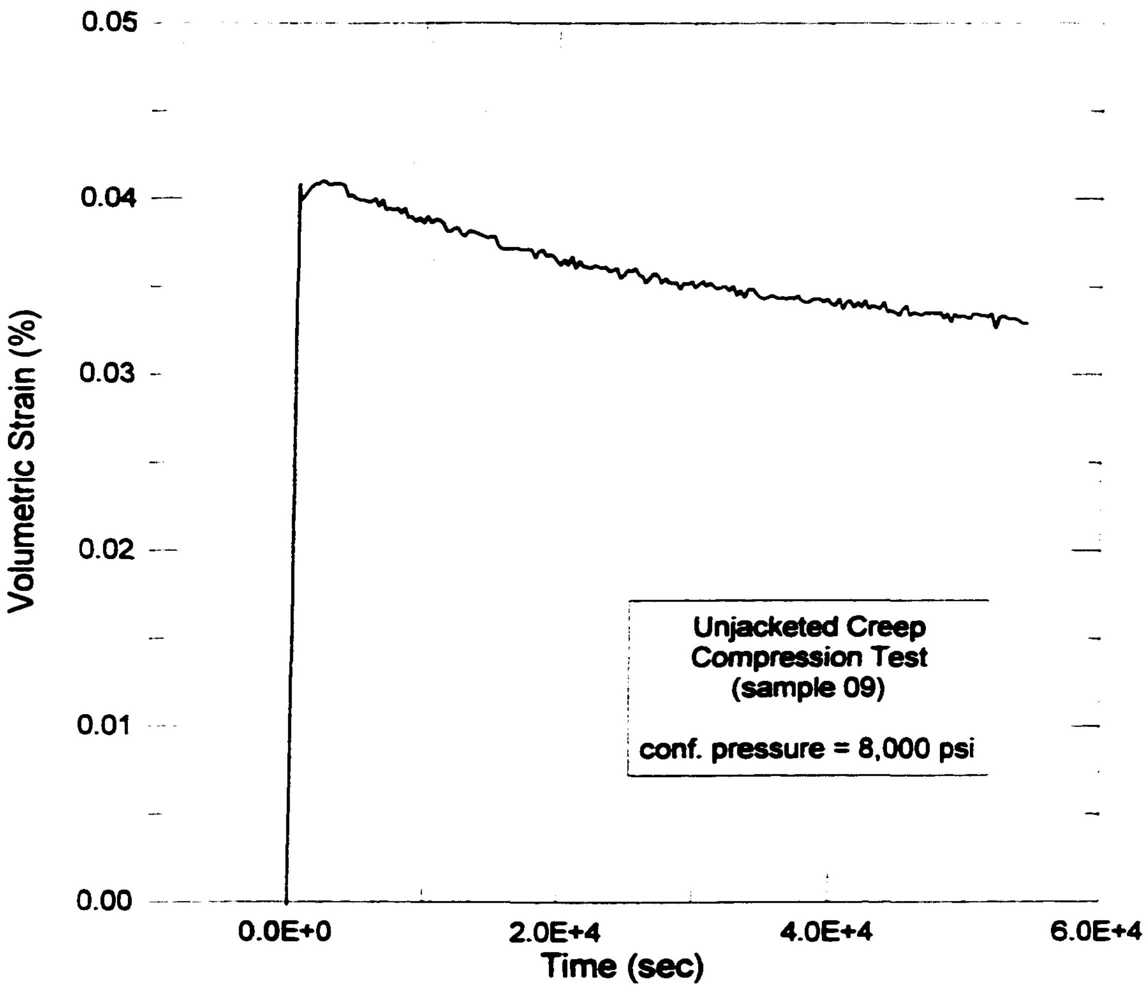

Figure F.33: Creep test for sample 09, unjacketed under hydrostatic compression.

Appendix G

System Calibration

Two loading frames have been used in the experimental testing program: an MTS 319, for uniaxial compression tests; and an MTS 815, for triaxial compression tests. The axial displacement was calibrated in both equipments with a standard aluminum sample, for which the elastic constants are known (provided by the manufacturer). The sample characteristics are shown in Table G.1.

Table G.1: Aluminum sample characteristics.

Length (in)	4.250
Diameter (in)	2.125
Young's modulus (psi)	10.4E06
Poisson's ratio	0.32

The calibration procedure was to simply run a compression test in the aluminum elastic region, using the uniaxial set up for calibrating the MTS 319, and the triaxial set up for the calibration of the MTS 815 system. The experimental load-displacement curve for the aluminum sample was then compared with the curve plotted according to the aluminum elastic parameters, and the excess of displacement was attributed to the accommodation of the testing system components.

G.1 Axial Displacement in the Uniaxial Compression Tests

In the tests with the MTS 319 loading frame, the rock axial strain was derived from the actuator total displacement. Between the actuator and the loading frame, nevertheless, there are several components, like spacers and caps, that reduce the system overall stiffness and contribute to the measured displacement. Although all these components are made of steel, the interface between them and also the interface with the testing sample itself will always increase the system compressibility. Figure G.1 shows the difference in the measured strain for the stress-strain curve based on the aluminum Young's modulus and the experimental result from testing the standard sample.

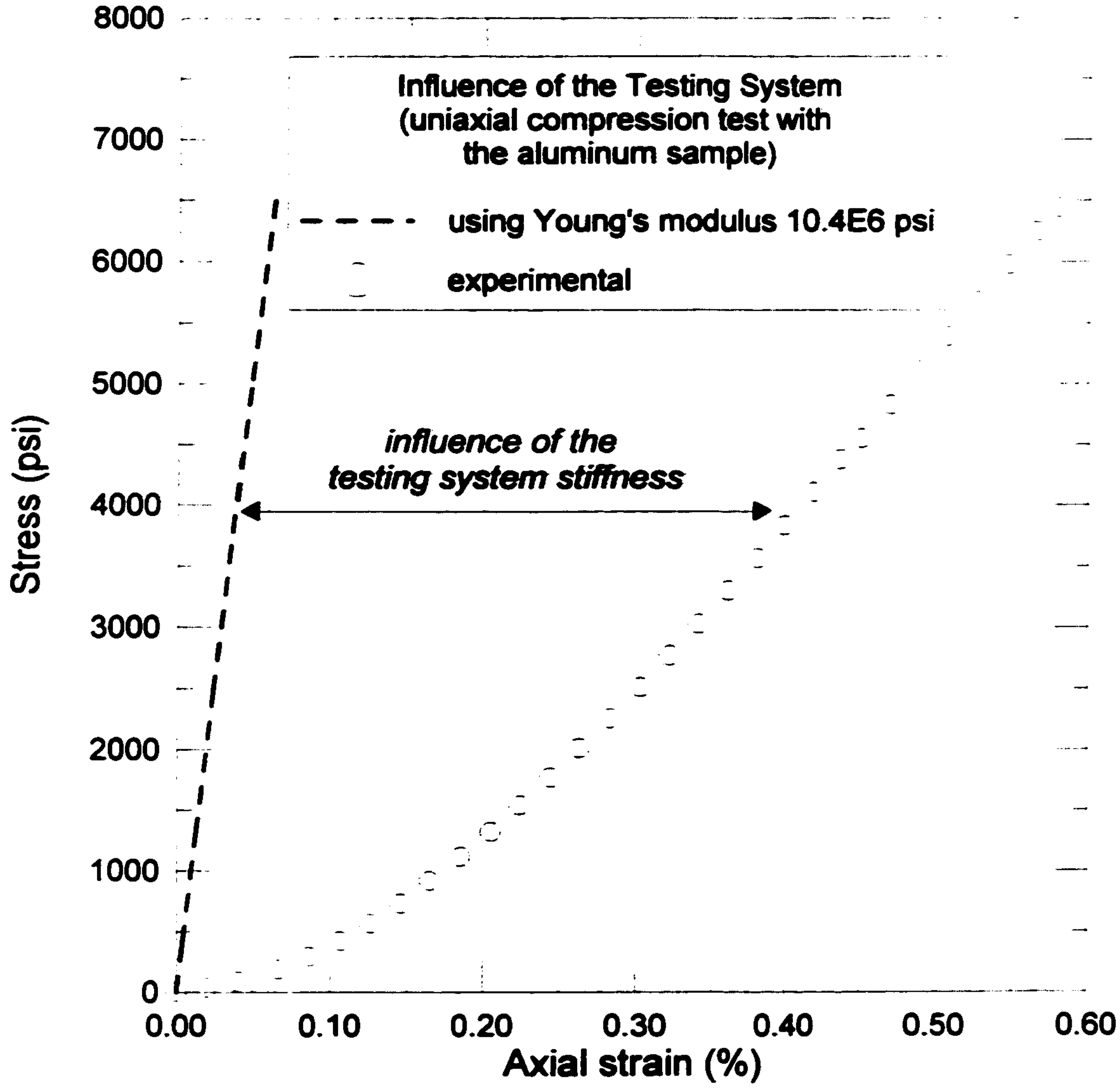

Figure G.1: Stress-strain curve for the uniaxial compression of the aluminum sample.

The calibration curve was calculated by subtracting the expected aluminum displacement from the total displacement obtained in the test, for each applied load, according to:

$$\Delta l_{cal} = \Delta l_{test} - \Delta l_{Al} \tag{G.1}$$

where:

$$\begin{cases} \Delta l_{cal} \text{ is the amount of displacement due to the system influence;} \\ \Delta l_{test} \text{ is the displacement measured in the aluminum test; and,} \\ \Delta l_{AL} \text{ is the displacement according to the aluminum properties.} \end{cases}$$

In order to have Δl_{cal} available for each rock test, a polynomial fit (5th-degree) was derived for expressing Δl_{cal} as a function of the applied load. The curve-fitting is shown in Figure G.2, and the resulting polynomial is:

$$\Delta l_{cal} = 7.591 \times 10^{-4} + 2.719 \times 10^{-6} L - 3.539 \times 10^{-10} L^2 +$$

$$+ 3.048 \times 10^{-14} L^3 - 1.237 \times 10^{-18} L^4 + 1.885 \times 10^{-23} L^5 \tag{G.2}$$

where L is the load corresponding to the measured displacement.

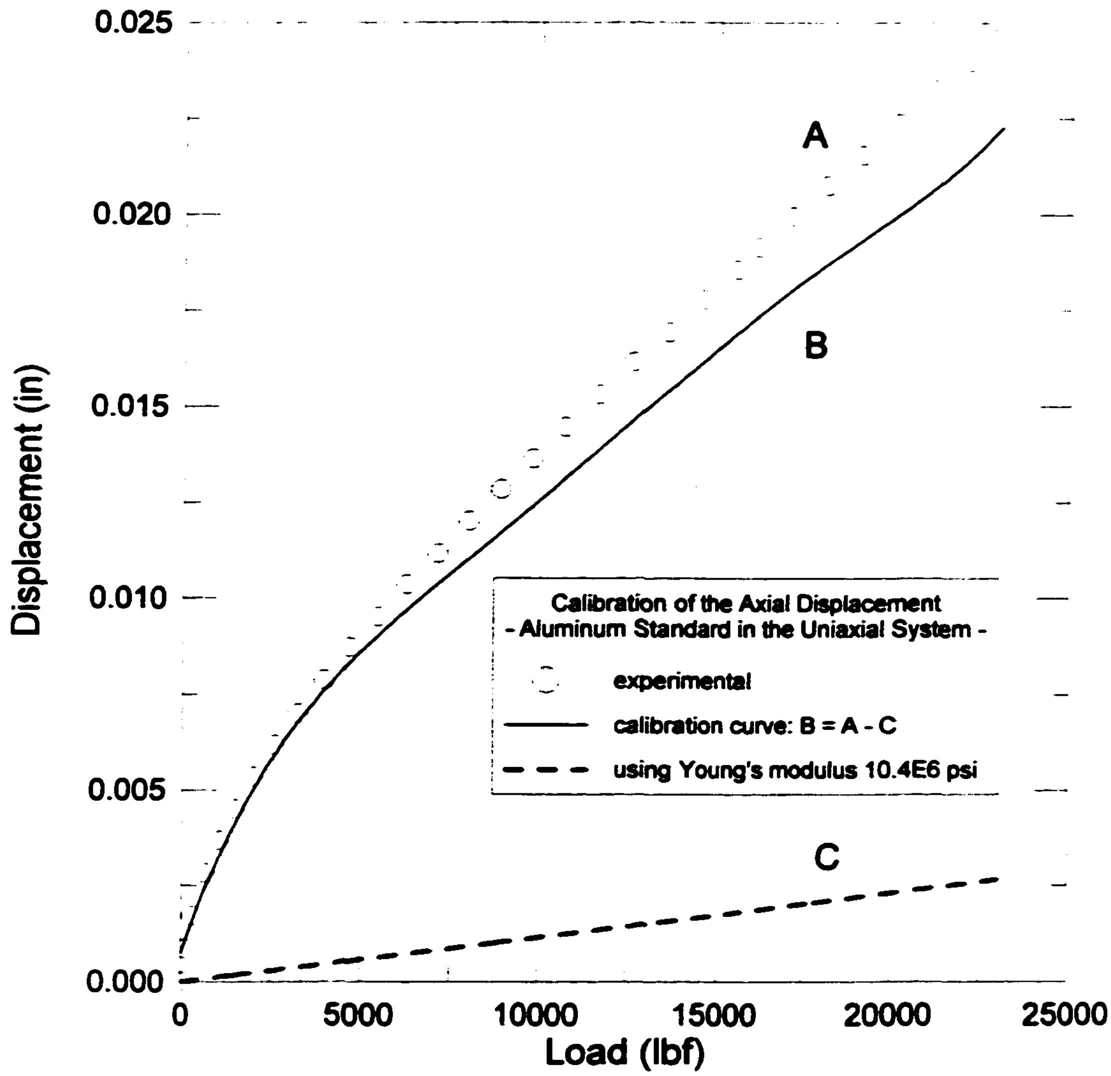

Figure G.2: Axial displacement as a function of load for the uniaxial compression of the aluminum standard.

G.2 Axial Displacement for the Triaxial Compression Tests

The axial displacement in the triaxial tests performed with the MTS 815 system were given by the averaged output of two LVDTs attached to the upper and lower steel caps, as shown in Figure 6.6. The linearity of each LVDT was verified with a special micrometer (Figure G.3), generating the calibration curve shown in Figure G.4. These curves were obtained by the least square method, and the coefficient of determination is also shown in Figure G.4.

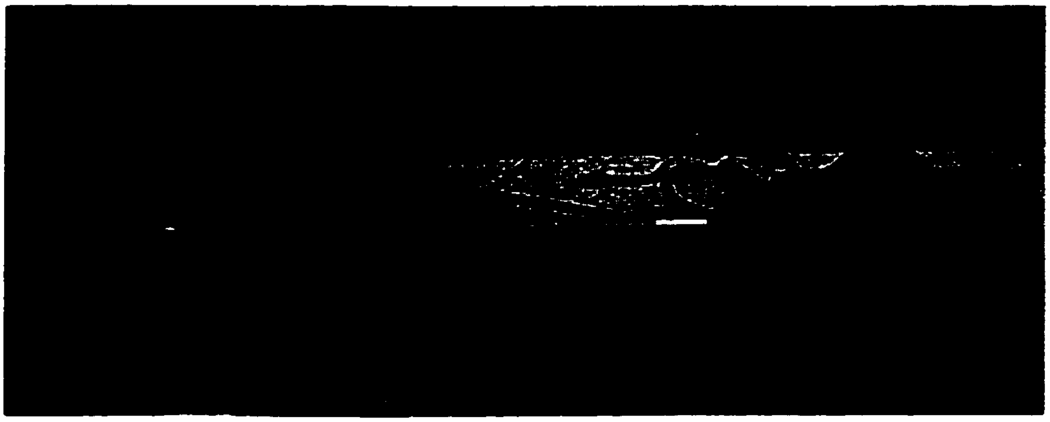

Figure G.3: Calibration of the LVDTs using a high precision electronic Mitutoyo gauge.

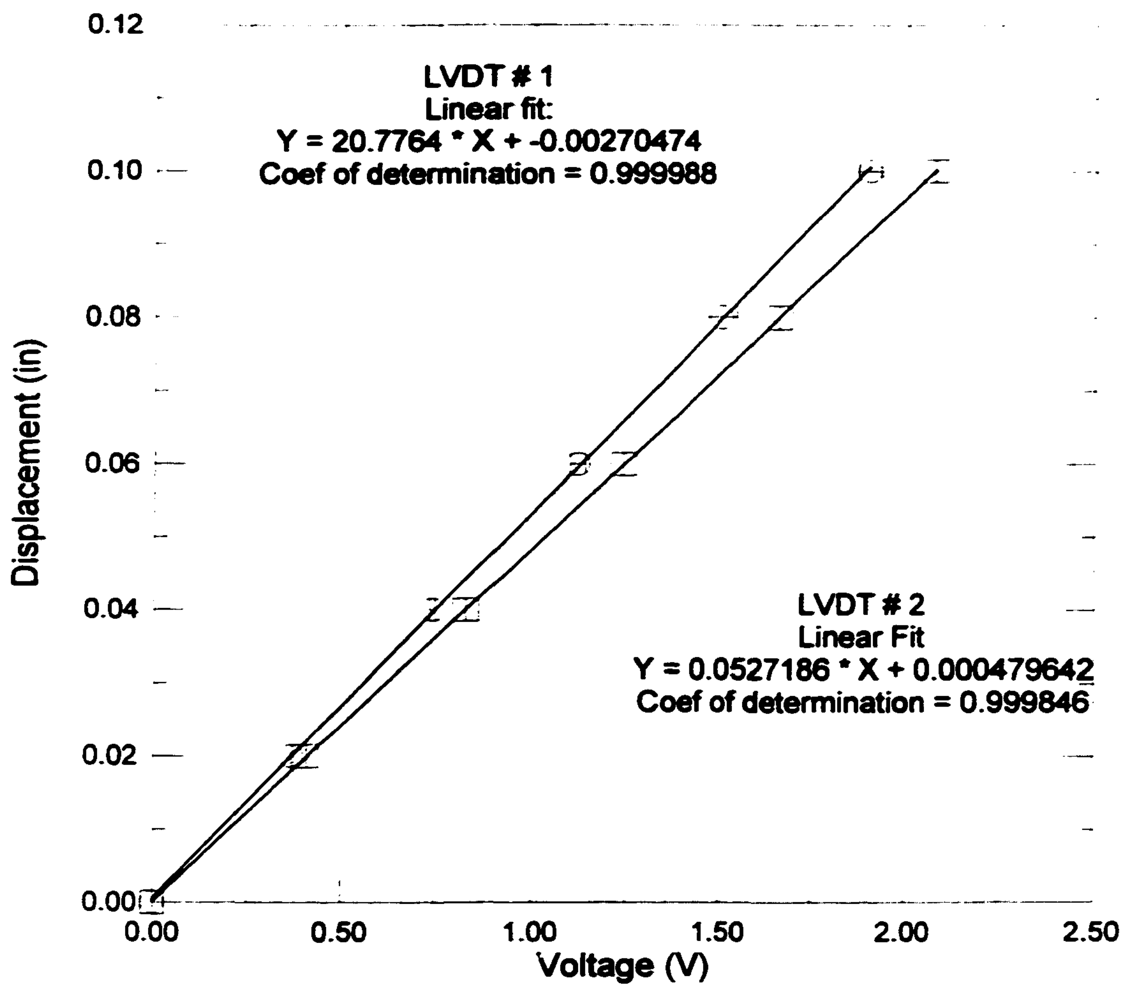

Figure G.4: Calibration of the LVDTs.

The contribution of the testing system to the sample displacement was verified once more with the aluminum standard, following the same procedure used for the uniaxial setup. Figure G.5 shows the stress-strain curve for the aluminum standard in the triaxial setup.

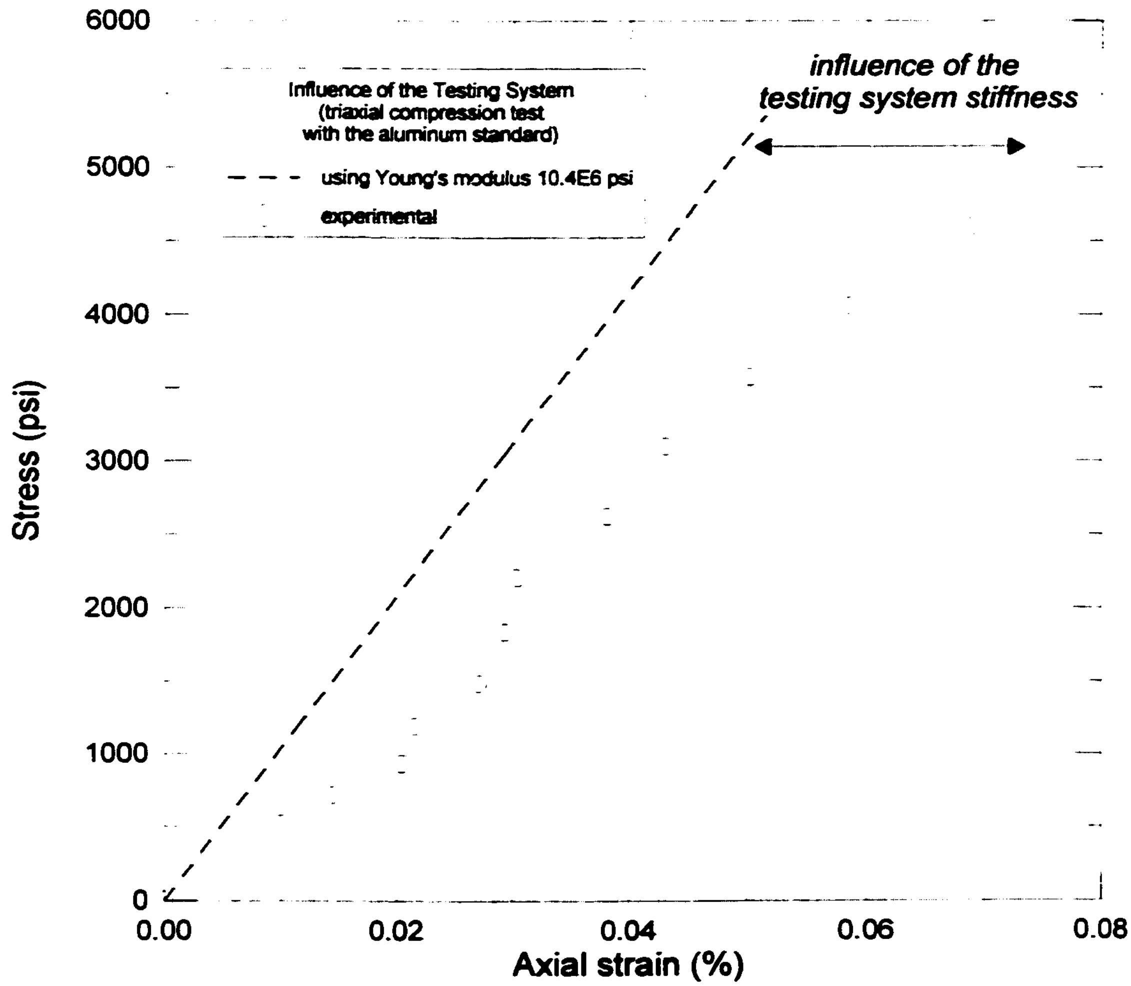

Figure G.5: Stress-strain curves for the triaxial compression of the aluminum sample.

A linear fit was obtained for computing the corrected displacement as a function of the applied load, in the same way it was done for the uniaxial compression test. The linear fit (Figure G.6), is given by:

$$F = 5.49 \times 10^{-8} L + 1.5 \times 10^{-4} \tag{G.3}$$

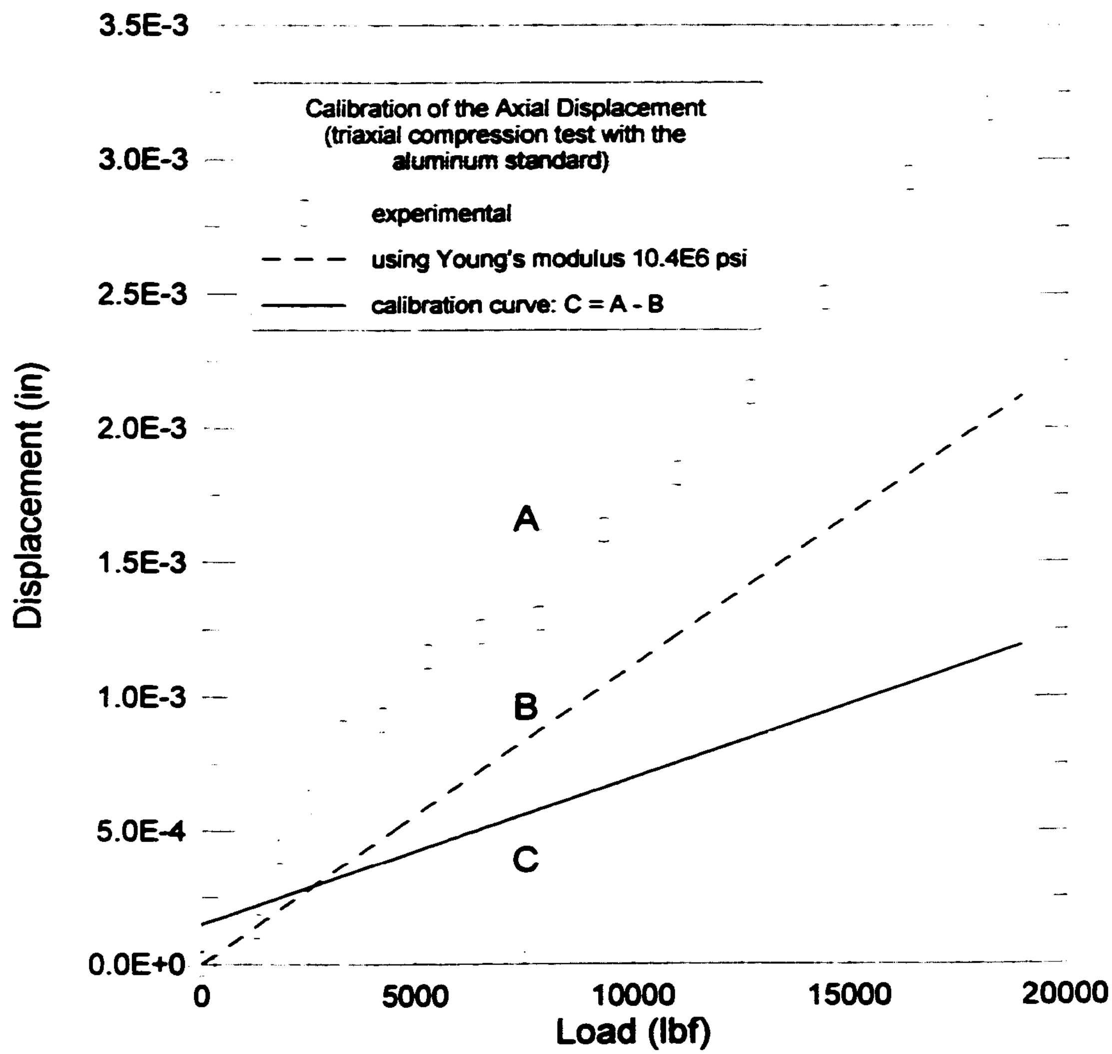

Figure G.6: Linear correction for the displacement measured in the triaxial system (MTS 815) as a function of load.

G.3 Lateral Displacement

The lateral extensometer was also calibrated by running a uniaxial compression test with the aluminum sample. Figure G.7 shows the experimental and the theoretical curves for the lateral strain of the aluminum sample. Comparing the plots it can be seen that the experimental curve is parallel to the theoretical one ($\Delta\varepsilon_{lat}|_{theor} = \Delta\varepsilon_{lat}|_{\exp}$), thus, no correction was necessary for the rock tests. This result was already expected, since the lateral extensometer is directly attached to the rock sample, making the measurements free from the influence of the testing system.

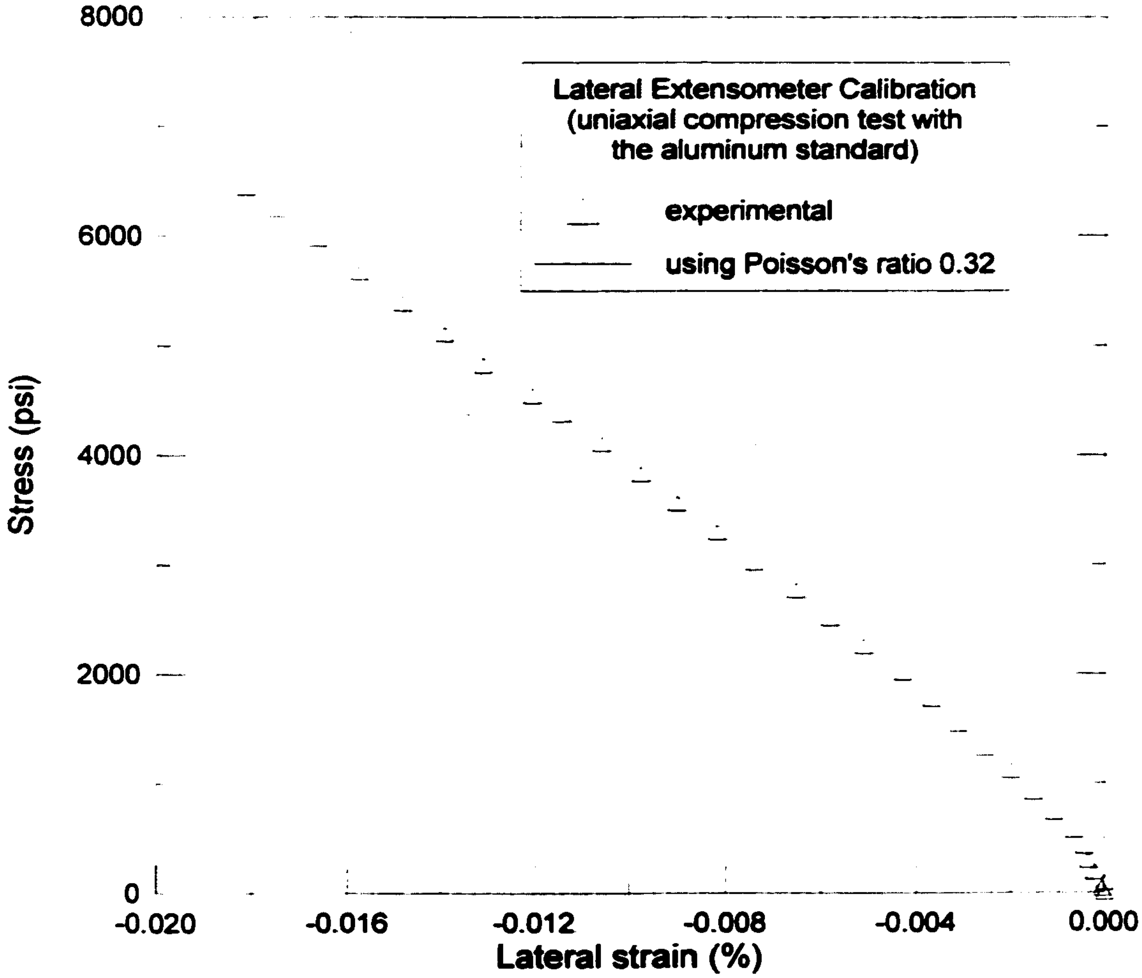

Figure G.7: Stress versus lateral strain for the aluminum sample.